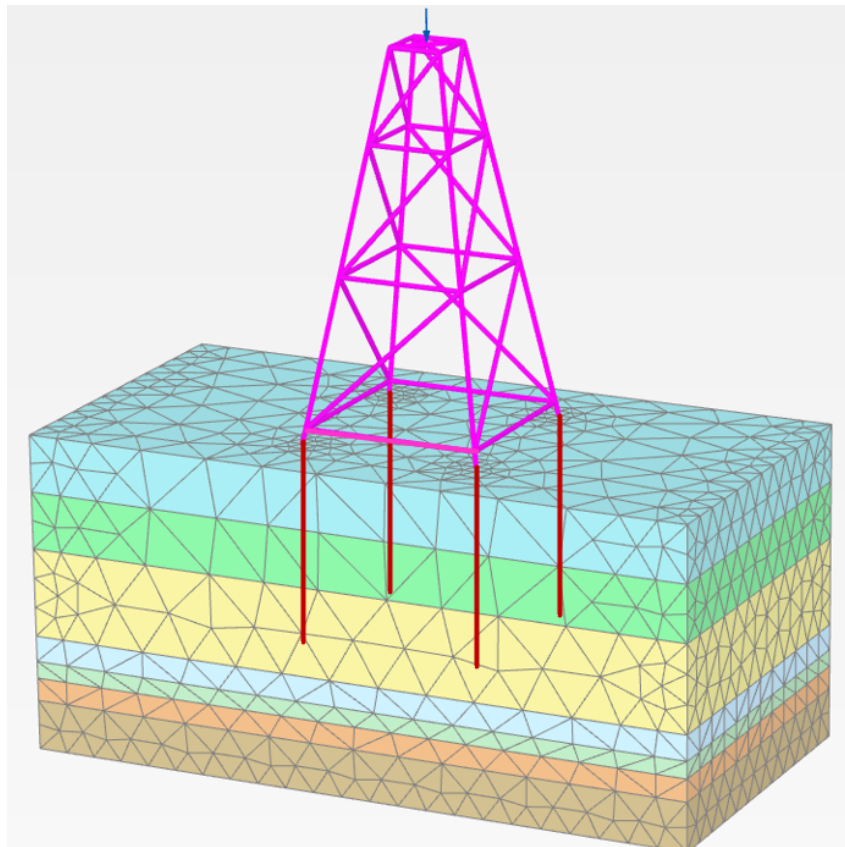


Aalborg University

Numerical Seismic Response Analysis of an Offshore Wind Turbine Foundation

Structural and Civil Engineering



Structural and Civil Engineering
Aalborg University
9th of June 2022



Title:

Numerical Seismic Response Analysis of an
Offshore Wind Turbine Foundation

Topic:

Numerical Seismic Analysis

Project:

Master Thesis

Project period:

1st of September 2021 - 9th of June 2022

Project group:

Casper Schrøder Jensen
Emilie Kongstad Sørensen
Rasmus Emil Vestergaard Sørensen

Supervisor:

Lars Damkilde

Censor:

Jens Peder Ulfkjær

Page number of main report: 98

Total page number: 246

Number of appendices: 11

Synopsis:

Offshore wind farms are being planned and constructed in regions throughout the world prone to strong earthquakes which can be a leading design criteria for an offshore wind turbine (OWT). Wind turbines is a highly dynamic structure due to a slender tower which is connected to a heavy mass at the top consisting of nacelle, rotor and rotating blades. Strong earthquakes result in strong ground shaking which will oscillate the OWT and the ground shaking can lead to soil liquefaction. Ground shaking and soil liquefaction can result in unacceptable large deformations of the OWT foundation and is an important design aspect in seismic active regions. The aim of this project is to investigate seismic analysis procedures according to EN 1998-1 and DNV-RP-0585. The first part of the project concerns the seismic analysis procedures in EN 1998-1 where a simple 2D multistory building is exposed to an earthquake and the analysis procedures are compared and discussed. The second part of the project concerns the seismic analysis procedures in DNV-RP-0585 where an OWT foundation located in Japan is exposed to an earthquake. The OWT foundation is modelled as a jacket substructure with embedded piles in three different ways with increasing model complexity and the response in the models are compared. The first model is very simple with rough assumptions about the soil-structure interaction and the last model is more complex and realistic as a soil volume is modelled. The models are made in the software programs *SeismoStruct* and *Plaxis* where non-linear dynamic analyses of the OWT foundation are performed. An advanced numerical model of the soil profile are made in the software program *DeepSoil* to conduct a Site Seismic Response Analysis (SSRA) for assesment of the depth varying ground motions and change in stiffness properties of the soil which are used to asses the response of the OWT foundation. The initiation of soil liquefaction is investigated and compared for a simple approach and an advanced liquefaction model.

Preface

This master thesis is made during 3rd and 4th semester in the master of Structural and Civil Engineering at Aalborg University by Casper Schrøder Jensen, Emilie Kongstad Sørensen and Rasmus Emil Vestergaard Sørensen.

The aim of the project is to investigate seismic analysis procedures according to EN 1998-1 and DNV-RP-0585 and evaluate assumptions and limitations. The project focuses on numerical analysis using software programs such as *DeepSoil*, *SeismoStruct* and *Plaxis 3D*. The project is divided into two parts; the first part consists of applying EN 1998-1 seismic analysis procedures on a simple 2D multistory building and evaluate the methods and results. The second part consists of applying DNV-RP-0585 seismic analysis procedures on an offshore wind turbine foundation located in Japan and evaluate the seismic hazards such as ground shaking and liquefaction.

The authors would like to thank the supervisor Lars Damkilde, professor at Aalborg University at the Department of Civil Engineering for assistance and guidance throughout the project.

Reading Guide

The report consists of a main report and appendices where underlying theory.

Source references are denoted by the Harvard referencing. The citation is marked as ["Author(s) Surname", "Year"] in text and as **Author(s) Surname, Initial(s)**. *Title. Edition (if not first edition). Place of publication. Publisher, year.* in the literature list.

Figures, tables and equations are quoted in numbers such that figure 2 in chapter 1 will be referred as figure 1.2. Whereas, the equations appear as equation (1.2).

Matrices are denoted with a bold letter and square brackets, e.g. **[K]** and vectors are denoted with a bold letter and curly brackets, e.g. **{u}**.

Aalborg University, 9th of June 2022



Casper Schrøder Jensen
cjense20@student.aau.dk



Emilie Kongstad Sørensen
ekongs20@student.aau.dk



Rasmus Emil Vestergaard Sørensen
revs17@student.aau.dk

Contents

Chapter 1	Introduction	1
1.1	Background	1
1.2	Problem Formulation	4
1.3	Report Structure	4
1.4	Project Limitations	7
Chapter 2	Basis for Seismic Analysis Procedures	8
2.1	Earthquake Characteristics	8
2.2	Seismic Hazards	9
2.3	Seismic Analysis Procedures in EN 1998-1	10
2.4	Accelerogram	12
2.5	Response Spectrum	14
2.6	Recorded and Artificial Accelerograms	15
2.7	Non-linearity	18
2.7.1	Non-linear Response Spectrum	21
I	Seismic Response Analysis of Multistory Steel Frame Building	
Chapter 3	Application of EN 1998-1 Seismic Analysis Methods	24
3.1	Lateral Force Method	24
3.2	Modal Response Spectrum Analysis	26
3.3	Non-linear Static Pushover Analysis	28
3.4	Non-linear Time History Analysis	31
3.5	Multistory Steel Frame Building	32
3.6	Response Comparison of Multistory Building	34
3.7	Conclusion	38
II	Seismic Response Analysis of Offshore Wind Turbine Foundation	
Chapter 4	Seismic Hazard Assessment	40
4.1	Wind Farm Site	40
4.2	Geotechnical Conditions	41
4.3	Jacket Substructure	42
4.4	Probabilistic Seismic Hazard Analysis	44
4.4.1	Identifying Earthquake Sources	45
4.4.2	Uncertainty of Earthquake Location	46
4.4.3	Uncertainty of Earthquake Size	47
4.4.4	Uncertainty of Ground Motion Intensity	47

4.4.5	Combining All Uncertainties	48
4.4.6	Design Peak Ground Acceleration	49
4.4.7	De-aggregation	50
4.4.8	Site Specific Design Response Spectrum	50
4.5	Summary	51
Chapter 5	Site Seismic Response Analysis	54
5.1	Approaches	57
5.1.1	Equivalent Linear Approach	58
5.1.2	Non-linear Approach	58
5.2	Input Parameters	59
5.2.1	Soil Profile	59
5.2.2	Shear Modulus Reduction and Damping Curves	60
5.2.3	Constitutive Soil Model	60
5.2.4	Excess Porewater Pressure Generation Model	62
5.3	Numerical Model	62
5.4	Response Comparison of Non-linear Soil Models	63
5.5	Results	66
5.6	Summary	67
Chapter 6	Liquefaction	68
6.1	Liquefaction Evaluation	68
6.2	Summary	71
Chapter 7	Modelling Approaches	72
7.1	Numerical Model 1: Jacket Substructure on Rigid Base	73
7.2	Numerical Model 2: Jacket Substructure on Embedded Piles with Soil-pile Springs	74
7.2.1	Soil-pile Interaction	75
7.3	Numerical Model 3: Jacket Substructure on Embedded Piles with Soil Volume	80
7.3.1	Soil-pile Interaction	80
7.3.2	Soil Constitutive Model	81
7.3.3	Model Size	81
7.3.4	Boundary Conditions	82
7.4	Results	83
7.4.1	Response Comparison of Offshore Wind Turbine Foundation	85
7.5	Ground Improvement	93
7.6	Summary	96
Chapter 8	Conclusion	97
III	Appendix	
Appendix A	Earthquake Characteristics	106

Appendix B	Seismic Design Tools	111
Appendix C	Principles of Seismic Design According to EN 1998-1	126
Appendix D	Seismic Analysis Methods According to EN 1998-1	133
Appendix E	Response of Multistory Steel Frame Building	152
Appendix F	Seismic Hazard Analysis	164
Appendix G	Site Seismic Response Analysis	177
Appendix H	Geotechnical Site Conditions	199
Appendix I	Input Parameters for Numerical Models	207
Appendix J	P-y Curves for Laterally Loaded Piles	225
Appendix K	Liquefaction Hazard Analysis	228

1 | Introduction

1.1 Background

In the past decades there has become an increased focus on the climate effect of CO₂-emission caused by burning fossil fuels for power production, industry, buildings, transportation and others. In 2015 this led to the Paris agreement at the COP21 (The 21st Conference of the Parties) meeting with the pledge to reduce the global CO₂-emission, to limit the rise in global temperature to a maximum 1.5°C. Furthermore, the International Energy Agency has recently published "Net Zero by 2050: A Roadmap for the Global Energy Sector" [International Energy Agency, 2021] for the COP26 meeting to strengthen the international effort and cooperation to become global CO₂-neutral by 2050 which will acquire a rapid increase in the renewable energy. The increase in renewable energy has already begun and since 2010 wind energy is the energy source that has increased the most according to the report "Future of Wind, 2019" by The International Renewable Energy Agency (IRENA), as shown on figure 1.1.

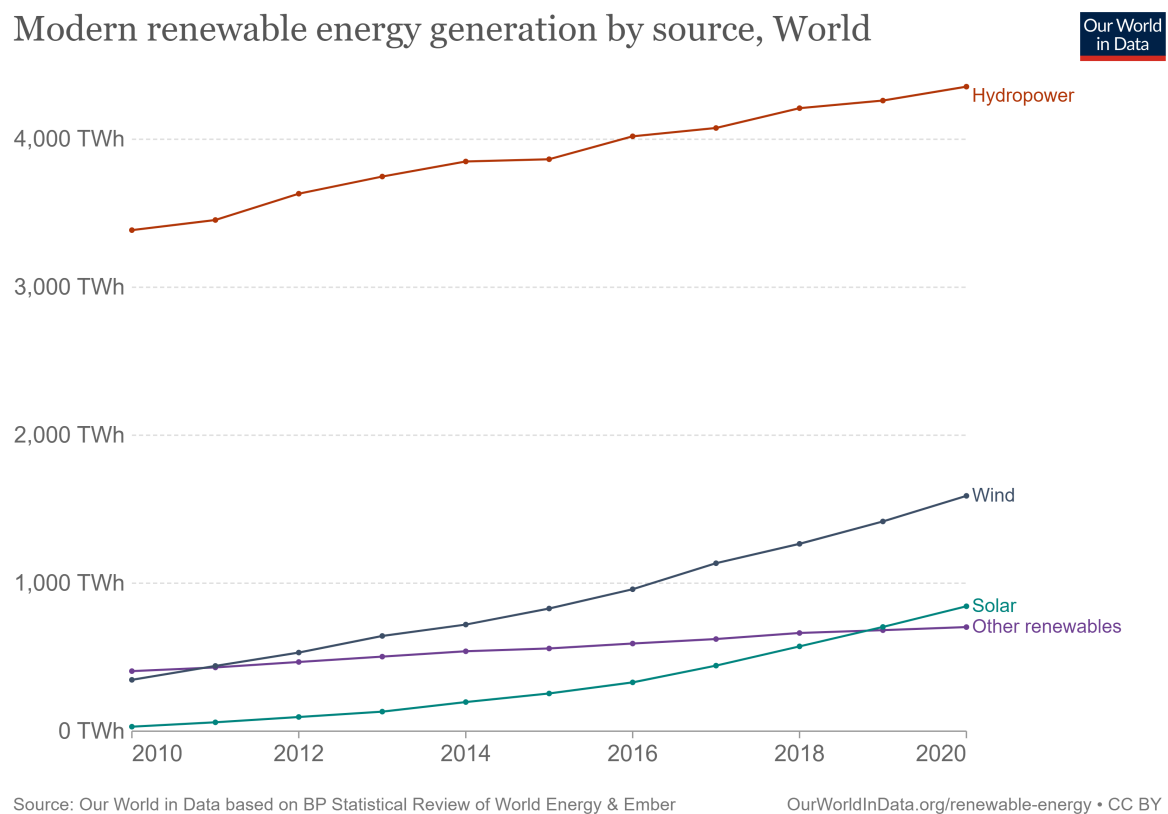


Figure 1.1: Modern renewable energy generation by source worldwide since 2010 [IRENA, 2019].

As wind energy is the fastest developing renewable energy, there is a large potential for development of wind turbines. Furthermore, the wind energy predictions from [IRENA, 2019] are continuously increasing which will result in an increased demand for onshore and offshore wind turbines in the coming years as shown on figure 1.2.

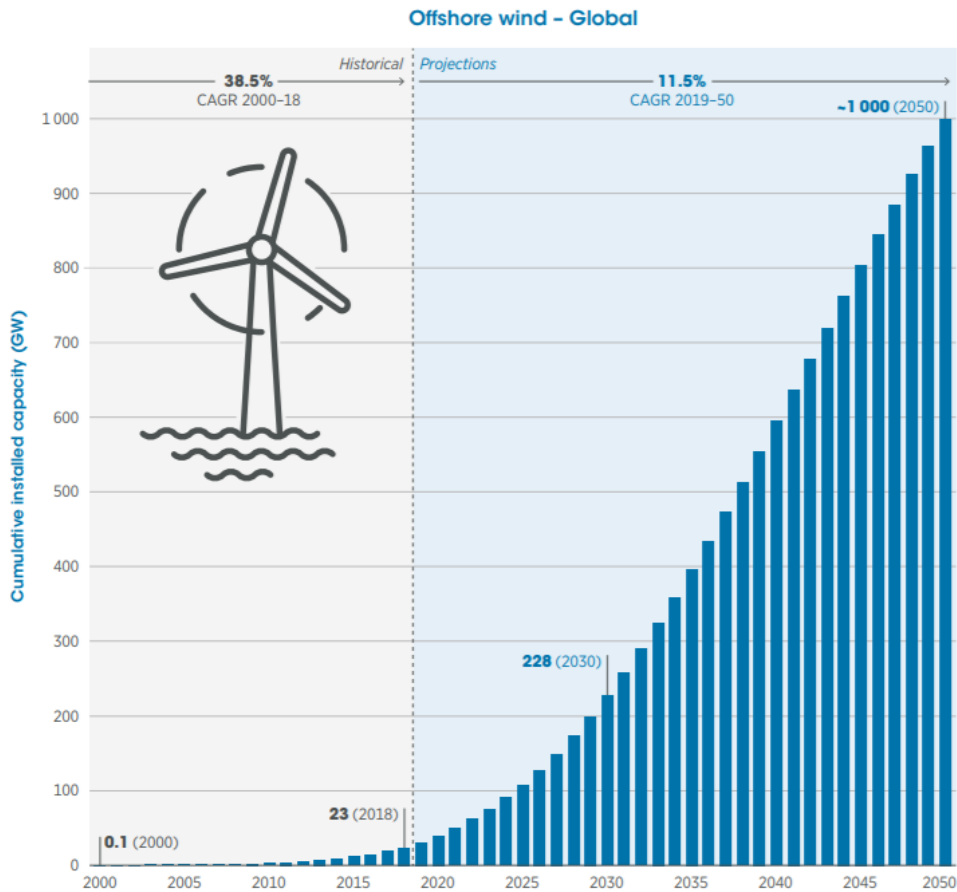


Figure 1.2: Predicted installed offshore capacity globally. Offshore wind power would grow to nearly 1,000 GW by year 2050, [IRENA, 2019].

Globally Asia has been predicted to have the largest wind capacity installed by 2050 with more than 50% of all onshore global installations and more than 60% of all offshore global wind installations, [IRENA, 2019].

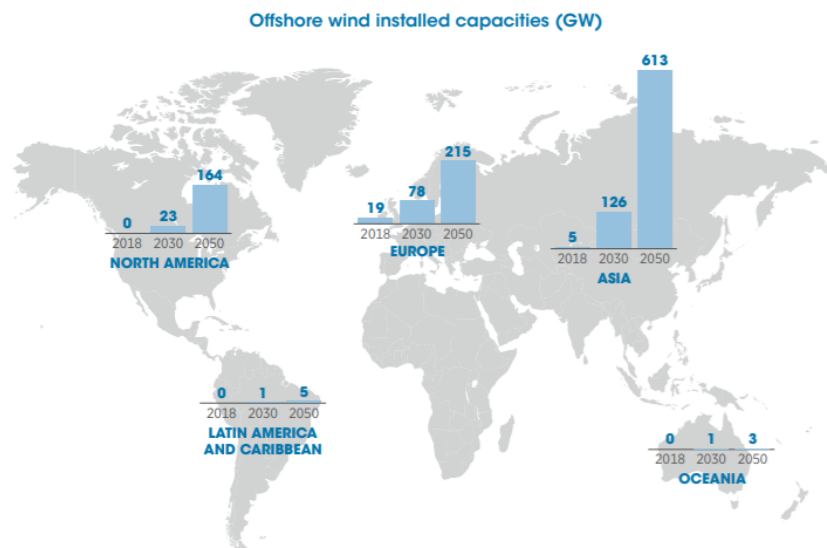


Figure 1.3: Asia would dominate global offshore wind power installations by 2050, [IRENA, 2019].

Japan is one of the countries in Asia that has a large potential for development of offshore wind turbines due to its geographical location as it is surrounded by the ocean. Furthermore, future development is realistic as Japan has set the goal for a net zero of CO₂-emission by 2050, [Ministry of Economics, Trade and Industry, 2021]. As mountains cover over 80% of the land mass, [Anne K. Petry, 2021], and transportation to a mountainous site and maintenance of the turbines are difficult offshore wind turbines have a larger potential in Japan compared to onshore wind turbines.

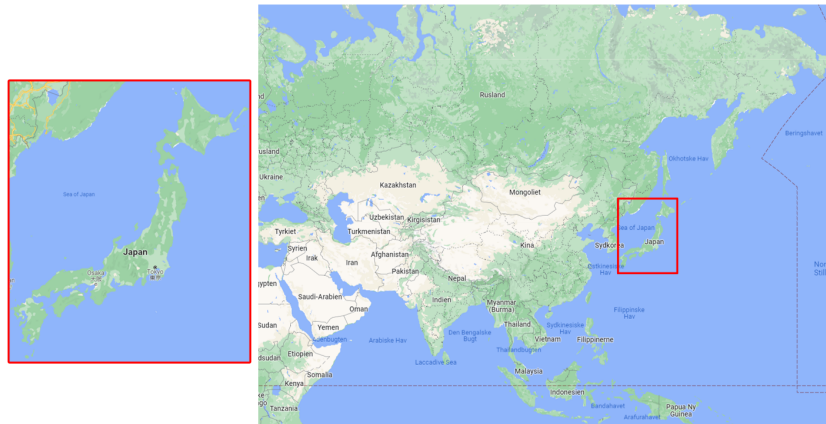


Figure 1.4: Location of Japan on the world map.

Despite Japan's ideal location for construction of offshore wind turbines the area is also exposed to a variety of natural disasters, majority of which exists due to frequent seismic activity in the region, illustrated on figure 1.5. These frequent occurrences of seismic activities are the major cause of seismic hazards such as ground shaking, soil liquefaction, landslides and tsunamis, which are further explained in appendix A. Within the scope of this project only ground shaking and soil liquefaction are investigated.

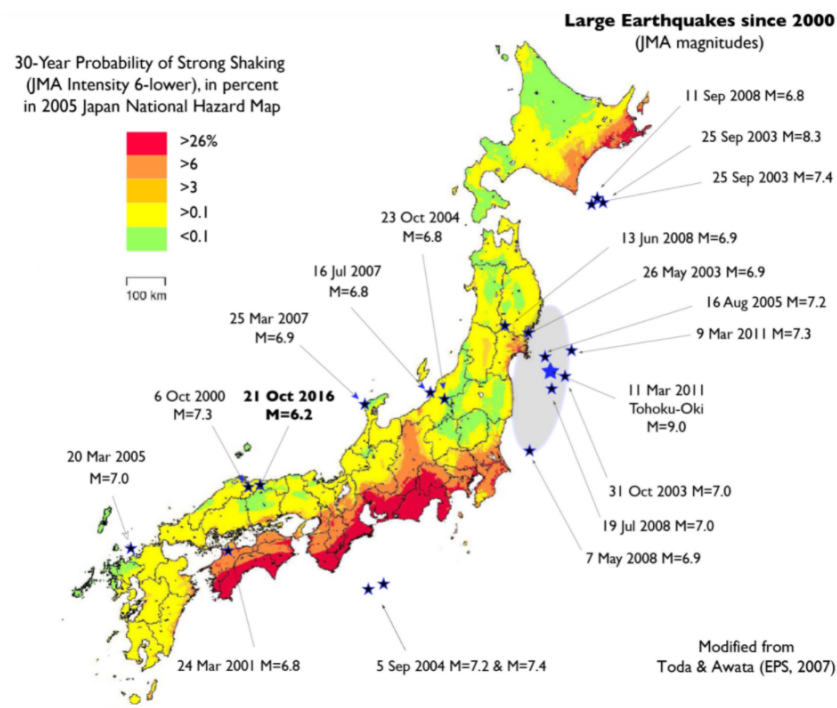


Figure 1.5: Epicenters of large earthquakes since 2000, [Ross Stein and David Jacobson by Temblor, 2016].

1.2 Problem Formulation

It is essential that the durability of offshore wind turbine foundations are sufficiently strong to withstand major seismic activity and the seismic hazards that follow. In order to analyse the seismic response of an offshore wind turbine foundations the following points are wished to be answered:

- How are earthquake loads acting on structures simulated?
- How is soil liquefaction evaluated and incorporated in the numerical models of an offshore wind turbine foundation?
- How can different numerical models with increasing complexity capture the dynamic behaviour of an offshore wind turbine foundation during an earthquake?

In order to answer the problem statements a report with the following structure is made.

1.3 Report Structure

Chapter 2:

- The relevant earthquake characteristics as well as the hazards associated with an earthquake such as ground shaking and liquefaction are briefly explained.
- The seismic design methods and tools proposed by EN 1998-1 are explained as well as the non-linearity aspect when performing a seismic analysis.

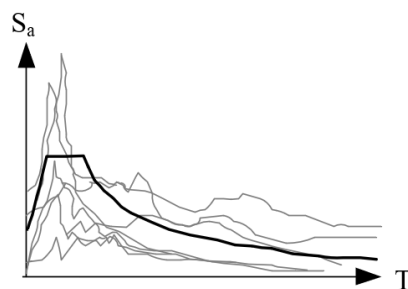


Figure 1.6: Seismic design tool in EN 1998-1.

Part 1

The first part of the project revolves around the seismic loading and response of a simple steel frame building according to EN 1998-1.

Chapter 3:

- The seismic loading and response of a 2D ten-storey steel frame building, using the static linear and non-linear as well as dynamic non-linear analysis procedures proposed by EN 1998-1, is analysed.
- The analysis procedures are compared based on structural response, complexity, computational demands and limitations.

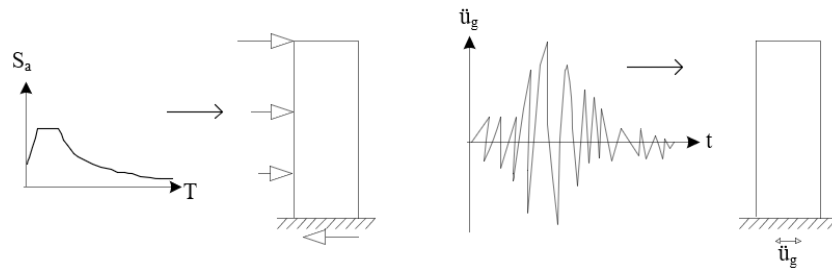


Figure 1.7: Application of EN 1998-1 methods.

Part 2

The next part of the project deals with the seismic loading and response of an offshore wind turbine foundation according to DNV-RP-0585.

Chapter 4:

- A wind farm site location, geotechnical site conditions and jacket substructure is defined.
- A site-specific design earthquake is obtained through a Probabilistic Seismic Hazard Analysis (PSHA) in order to obtain the ground motions at the bedrock beneath the offshore wind turbine foundation.

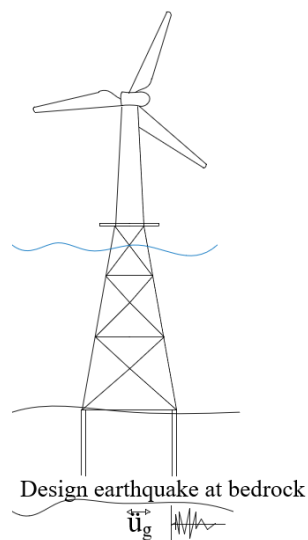


Figure 1.8: Site specific seismic hazard assessment to obtain design earthquake.

Chapter 5:

- The propagation of seismic waves from bedrock to mudline on the wind turbine site is obtained through a 1D Site Seismic Response Analysis (SSRA) in order to obtain the free-field depth-varying ground response during the design earthquake.
- The earthquake loading acting on the offshore wind turbine foundation can be determined.

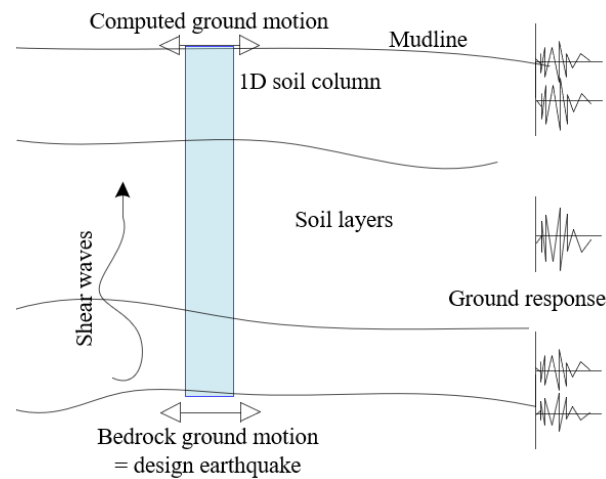


Figure 1.9: Site specific ground response during design earthquake.

Chapter 6:

- Firstly the soil liquefaction phenomenon as well as the factors that affect a soil to behave as a liquid and what the consequences to structures can be are introduced.
- It is evaluated whether or not liquefaction is initiated in the soil layers based on a stress-based approach utilising results from the SSRA.

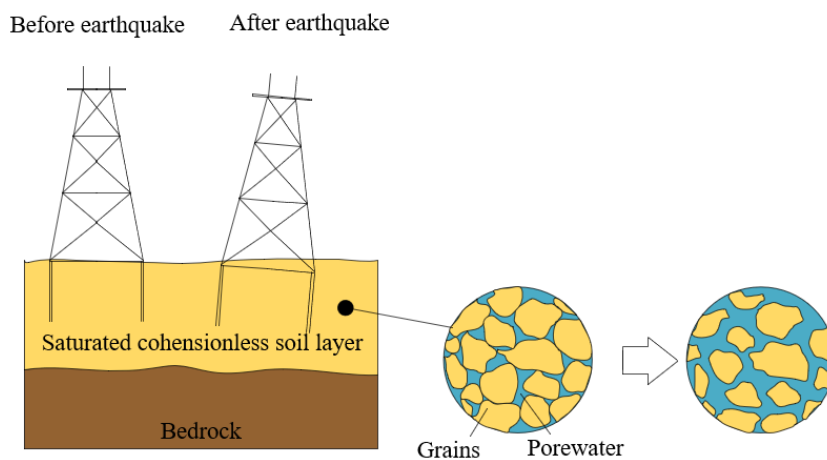


Figure 1.10: Liquefaction evaluation.

Chapter 7:

- Three different modelling approaches with increasing complexity are investigated and compared amongst each other.
- The 1st model consist of a rigid soil-pile interaction model with no soil damping and no change in soil stiffness where ground motions excite the structure at the ground surface.
- The 2nd model is a soil-pile interaction model where the embedded piles below the jacket substructure are modelled as beams with non-linear springs that are excited by depth-varying ground motions from SSRA.
- The 3rd model is a soil volume model with ground motions acting on the soil volume boundary with an advanced liquefaction soil model.

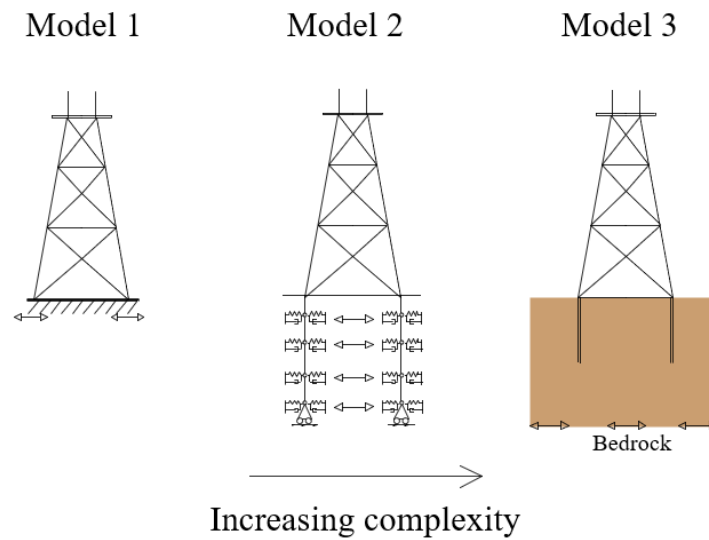


Figure 1.11: Different modelling approaches.

Chapter 8:

- A conclusion of the report.

1.4 Project Limitations

The aim of this project is to investigate seismic analysis procedures according to EN 1998-1 and DNV-RP-0585. Within the scope of this project structural design is not included, as it is the seismic analysis procedures that are investigated leading to the following limitations:

- Wind loads, hydrodynamic loads and operational loads are not included.
- Design of structural members against ultimate limit state, serviceability limit state and fatigue limit states and accidental limit states are not performed.

2 | Basis for Seismic Analysis Procedures

In this chapter the important earthquake characteristics and seismic hazards are described and the aim is to clarify assumptions, tools and methods in order to perform a seismic structural analysis according to [EN1998-1, 2004].

2.1 Earthquake Characteristics

As discussed in chapter 1 there is an increased need for offshore wind turbines in Japan, which is located in a region with high seismic activity or high risk of strong earthquakes. Earthquakes are ranked among the most devastating natural disasters on the planet and it is impossible to prevent them from happening. However, it is possible to mitigate the effects from earthquakes on people, buildings and other structures, [Kramer, 1996], and therefore the seismic effects need to be included in the design of an offshore wind turbine foundation located in a seismic active region. An earthquake is described as passage of seismic waves from a source of disturbance, and when it comes to defining an earthquake there are three main characteristics; earthquake type, size and location which will be described briefly in the following and in further detail in appendix A section A.1.

Earthquake type

The earthquake type describes the occurrence of an earthquake. This is essential as knowing the source of an earthquake could help to identify future seismic activity. There are several different causes as to why earthquakes are generated, however the most common reason is due to the slow continuous movement of the tectonic plates. These types of earthquakes occur due to abrupt breaking and sliding between the tectonic plates and is the most destructive type of earthquakes. [Kramer, 1996].

Earthquake size

The earthquake size or more commonly denoted the earthquake magnitude is a quantitative measurement of the earthquake size. Within the scope of this project the earthquakes are evaluated based on the moment magnitude M_w scale which is a measure of the energy released during an earthquake from the source of disturbance, [Kramer, 1996].

Earthquake location

Earthquakes can occur at several locations around a site but are only measured at measurement stations. The most used parameter when it comes to defining the location of an earthquake relative to a specific site is its *epicentral distance* which is the horizontal distance from the point at which rupture begins to the site, see appendix A section A.1.

2.2 Seismic Hazards

The discipline of earthquake engineering is under constant development with the purpose of finding solutions to issues posed by earthquakes and hazards associated with earthquakes, called seismic hazards, which are described in further detail in appendix A section A.2. Seismic hazards are dangerous phenomena that can occur during or after an earthquake, and are highly dependent on location, topography, geology, groundwater conditions and earthquake characteristics, [Kramer, 1996]. Within the scope of this project only two seismic hazards are investigated which are ground shaking and liquefaction. The two failure modes caused by an earthquake are structural failure (red building) and soil failure (below grey building), illustrated on figure 2.1.

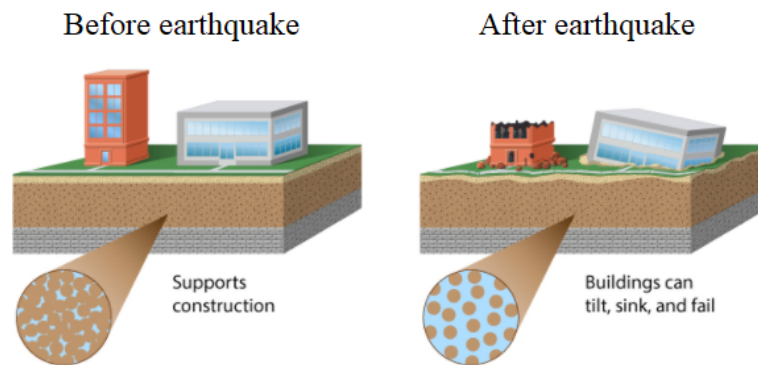


Figure 2.1: Failure modes; structural and soil failure, [Institute, 2018].

Ground shaking

When an earthquake occurs, seismic waves travel rapidly through the earth's crust, and when the waves reach the ground surface they produce shaking which may last seconds to minutes [Kramer, 1996]. This can cause immense damage to surrounding structures. The strength and duration of ground shaking highly depend on location and earthquake magnitude. Among the different seismic phenomena ground shaking is considered the most important as all other seismic hazards are caused by ground shaking, [Kramer, 1996].

Liquefaction

Liquefaction is initiated when saturated cohesionless soil particles are separated from each other and mixed with water by ground shaking. This reduces the load bearing capacity of the soil, and as a result structures can sink into the ground or tilt and remain stuck when the earthquake stops. Liquefaction is highly dependent on geology and groundwater conditions, as it frequently occurs for sandy saturated soils, [Kramer, 1996]. Offshore structures founded in the seabed indeed have the risk of liquefaction when an earthquake occurs as the soil deposit on the seabed has the ability to mix with water. If the soil around the wind turbine foundation appears to flow as a fluid, the consequences can be that the wind turbine will undergo very large vertical and horizontal deformations or even overturn.

2.3 Seismic Analysis Procedures in EN 1998-1

It is essential to mitigate the effects these seismic hazards have on a structure to ensure structural integrity, and therefore a seismic analysis is carried out on the structure. In [EN1998-1, 2004] four methods are specified in order to design the structure against earthquake loading, where there are two linear and two non-linear methods listed below:

The linear methods are:

- Lateral Force Method
- Modal Response Spectrum Analysis.

The non-linear methods are:

- Non-linear Static Pushover Analysis
- Non-linear Time History Analysis.

In a linear method the stiffness of the structure is constant regardless of the deformation state of the structure. In a non-linear method the stiffness will change dependent on the deformation of the structure, hence the assumption of a linear relationship is not applicable unlike the linear methods.

Linear methods

The lateral force method is the most simple and least computationally demanding method, as it only requires the first eigenperiod, mass of the structure and a peak acceleration of the structure during the earthquake, which is obtained by a response spectrum (explained in section 2.5). It is a traditional method, due to lack of computational power in the past. The modal response spectrum analysis is very similar to the lateral force method, here only more eigenmodes are considered which leads to more precise results. Both methods result in a maximum static response, such as base reactions and story displacements, and are found from the linear static equilibrium equation in equation (2.1).

$$[\mathbf{K}] \{\mathbf{u}\} = \{\mathbf{P}\} \quad (2.1)$$

where

$[\mathbf{K}]$	Global stiffness matrix [N/m]
$\{\mathbf{u}\}$	Global displacement vector [m]
$\{\mathbf{P}\}$	Global load vector [N].

It should be noted that within the scope of this project non-linear aspects, such as material and geometric non-linearity, which will be explained in section 2.7, are approximately incorporated in lateral force method and modal response spectrum analysis through the behaviour factor explained in section 2.7. The linear methods are illustrated in figure 2.2.

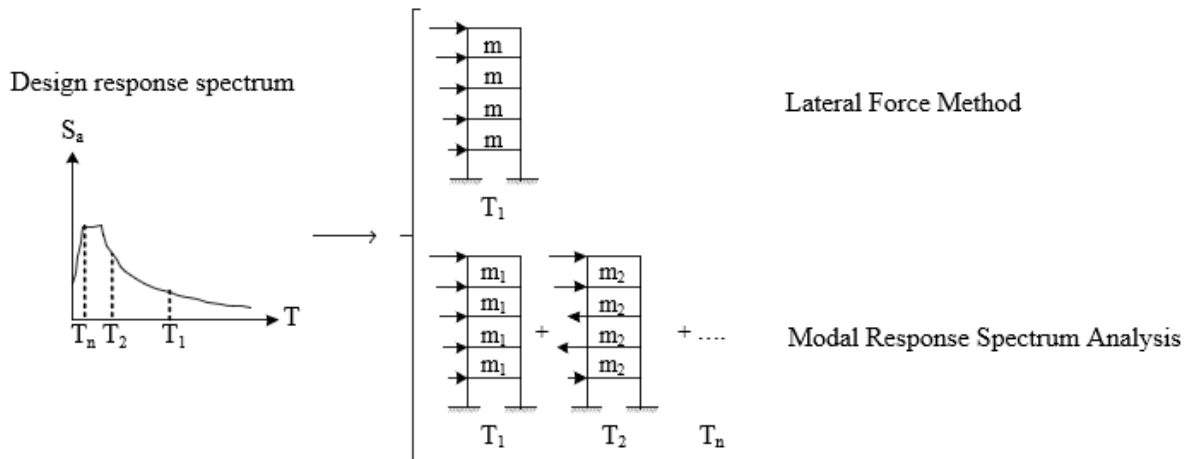


Figure 2.2: Linear methods in EN 1998-1.

Non-linear methods

The non-linear static pushover analysis is a more complex and computationally demanding method than the linear methods, as it requires a monotonic loading analysis with non-linearity effects to acquire a capacity curve and response spectra. The method gives a better understanding of the non-linear structural behaviour, but is still based on response spectra. The maximum static response is obtained from the non-linear static equilibrium equation in equation (2.2) where the stiffness of the system is dependent on the displacement.

$$[\mathbf{K}(\mathbf{u})]\{\mathbf{u}\} = \{\mathbf{P}\} \quad (2.2)$$

The non-linear time history analysis is the most complex and most computationally demanding method, as it requires time integration to solve the equation of motion in equation (2.3). Non-linearity effects are accounted for and the earthquake motion is represented by a time history accelerogram instead of a response spectrum.

$$[\mathbf{M}]\{\ddot{\mathbf{u}}\} + [\mathbf{C}]\{\dot{\mathbf{u}}\} + [\mathbf{K}(\mathbf{u})]\{\mathbf{u}\} = \{\mathbf{P}(\mathbf{u}, t)\} \quad (2.3)$$

where

$[\mathbf{M}]$	Mass matrix [kg]
$[\mathbf{C}]$	Damping matrix [Ns/m]
$[\mathbf{K}]$	Stiffness matrix [N/m]
$\{\ddot{\mathbf{u}}\}, \{\dot{\mathbf{u}}\}, \{\mathbf{u}\}$	Vector of nodal acceleration [m/s ²], velocity [m/s] and displacement [m]
$\{\mathbf{P}\}$	Global load vector [N].

The method is a newer method, due to the increase of computational power nowadays and gives the most realistic behaviour of a structure during an earthquake. In figure 2.3 are the non-linear methods shown.

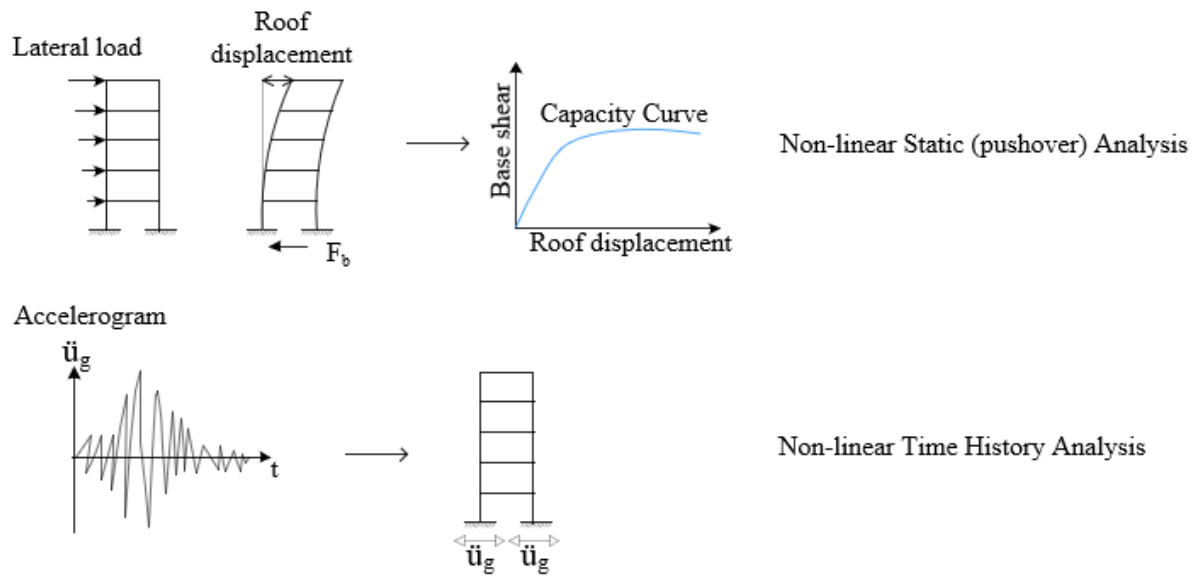


Figure 2.3: Non-linear methods in EN 1998-1.

The four methods are described in further details in chapter 3, where assumptions, limitations and procedure are explained and the methods are compared through an analysis of a simple 2D ten-story steel frame building. In the following are the seismic design tools that are needed in order to analyse a structure according to the EN 1998-1 methods explained.

2.4 Accelerogram

By recording the ground shaking of past earthquakes acceleration time histories also known as accelerograms can be obtained and potentially utilised. Ground shaking is complicated and has six components in total, three components of translation and three components of rotation. Often the rotation components are neglected and three orthogonal transverse components, two horizontal and one vertical component, are measured in acceleration-time histories. Three earthquakes near the South Coast of Honshu in Japan are considered in the design of the multistory steel frame building in chapter 3, these can be seen in table 2.1 and the location of epicenter and earthquake magnitude can be seen in figure 2.4.

Table 2.1: Data of selected ground motion.

Earthquake name	Date	Station Name	Station Country	Magnitude Mw
Miyagi-Oki	2003-05-26	KiKnet station MYGH10	Japan	7.0
Near the East Coast of Honshu	2021-02-13	KiKnet station MYGH10	Japan	7.1
Near the East Coast of Honshu	2021-03-20	KiKnet station MYGH10	Japan	7.0

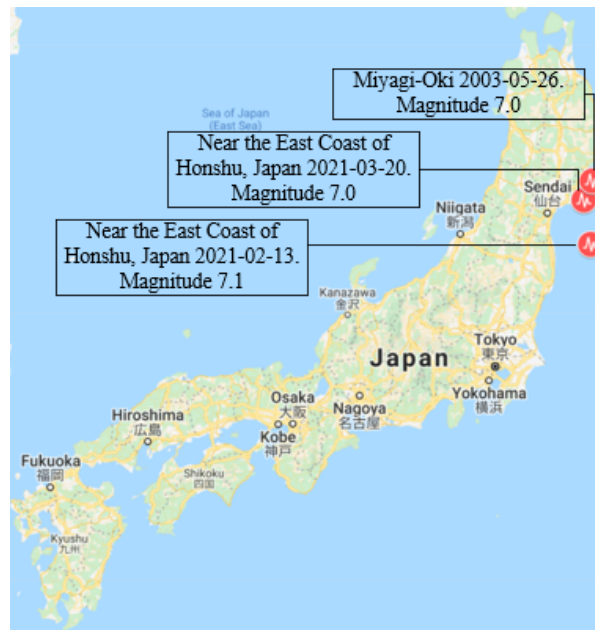


Figure 2.4: Location of earthquakes near the South Coast of Honshu, Japan.

The ground acceleration during the earthquake in Miyagi-Oki, Japan 2003-05-26 can be seen in figure 2.5 and the other ground accelerations can be seen in appendix B section B.4 figure B.7 and B.8.

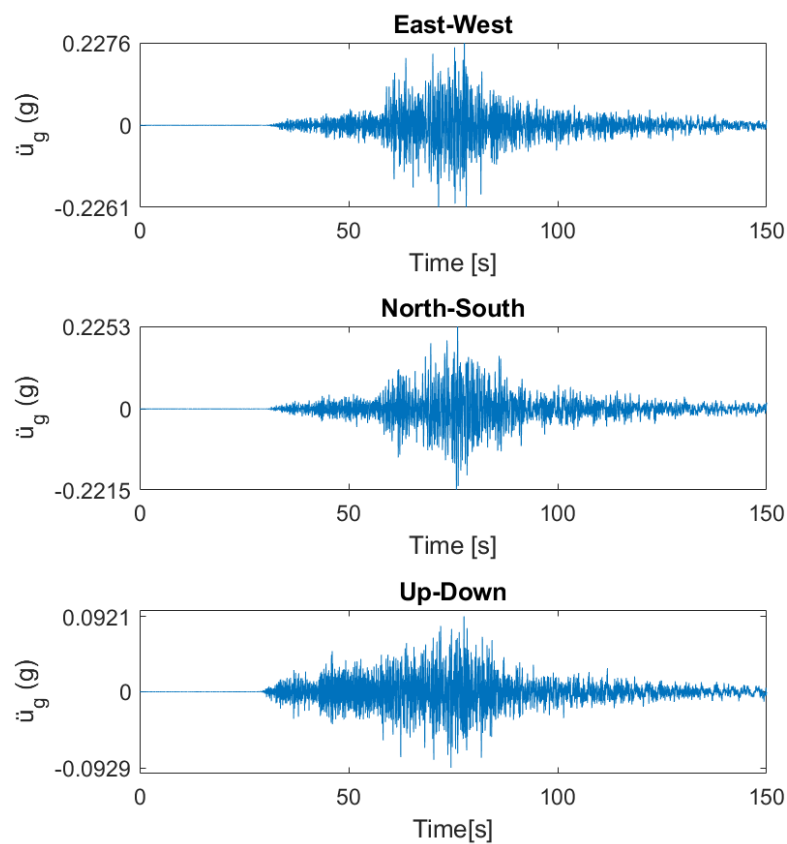


Figure 2.5: Accelerogram for the earthquake Miyagi-Oki, Japan 2003-05-26 with a magnitude of 7.0. Database: [CESMD, 2022].

These accelerograms are a direct measure of what happens in the ground during the earthquake and are very applicable when a structure's response is analysed using time history analysis methods. Past recorded earthquakes with different locations, soil conditions and magnitudes have been used to construct corresponding response spectra for structures with different damping which alternatively can be used as a design tool in the lateral force method, the modal response spectrum analysis and the non-linear static pushover method. The principle for constructing a response spectrum is described in the following section.

2.5 Response Spectrum

The response spectrum is constructed by analysing a wide span of linear single degree of freedom (SDOF) systems, with different natural periods, that are exposed to the same earthquake. By finding the maximum response for each system, which could be displacement, velocity or acceleration, and smoothing out the response of a SDOF to a number of different accelerograms a response spectrum can be constructed as illustrated in figure 2.6.

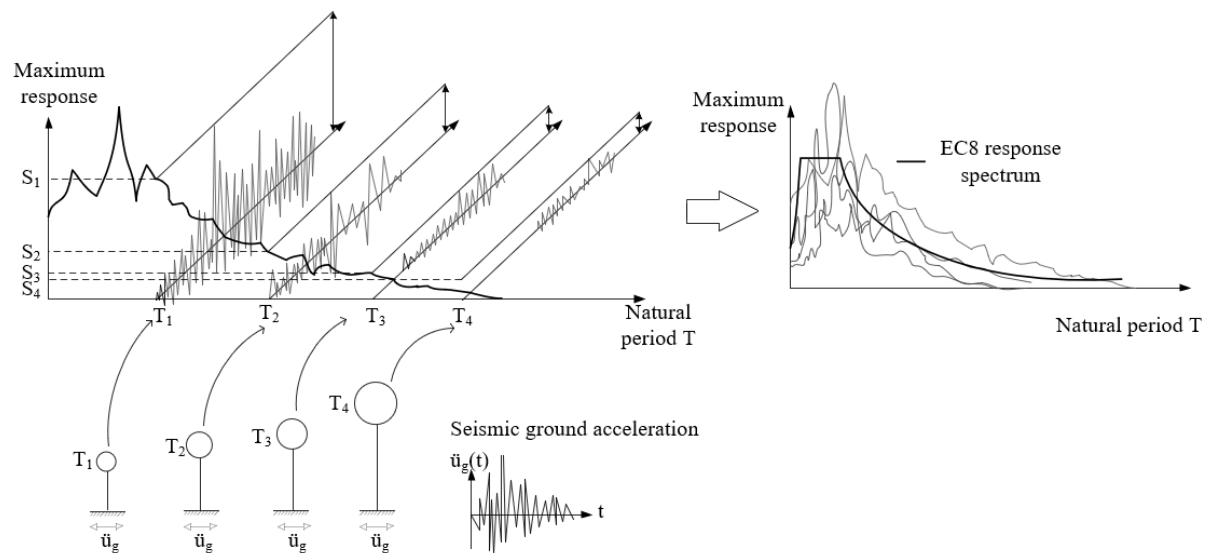


Figure 2.6: From accelerogram of earthquake to response spectrum, [Vrochidou et al., 2014].

The response spectrum is a very useful design tool as future earthquake ground motions are unknown and contains information about the maximum response of a SDOF system depending on its natural period. In EN 1998-1 the response spectrum is also called an elastic response spectrum and can be obtained when the ground type and the seismic activity in the location are known. In figure 2.7 the spectrum for the chosen site can be seen where the assumptions in order to create the spectrum are:

- Medium loose sand or soft to firm clay (soil type type D in table B.2)
- Reference peak ground acceleration of $a_{gR} = 0.4g$ (10% exceedance in 50 years), see zonation map in figure B.3
- Medium importance for public safety (importance class II with an importance factor of $\gamma_1 = 1$)
- Location of high seismic activity (type 1)
- 5% structural damping.

The procedure of how to obtain the response spectra is described in further detail in appendix B section B.2.

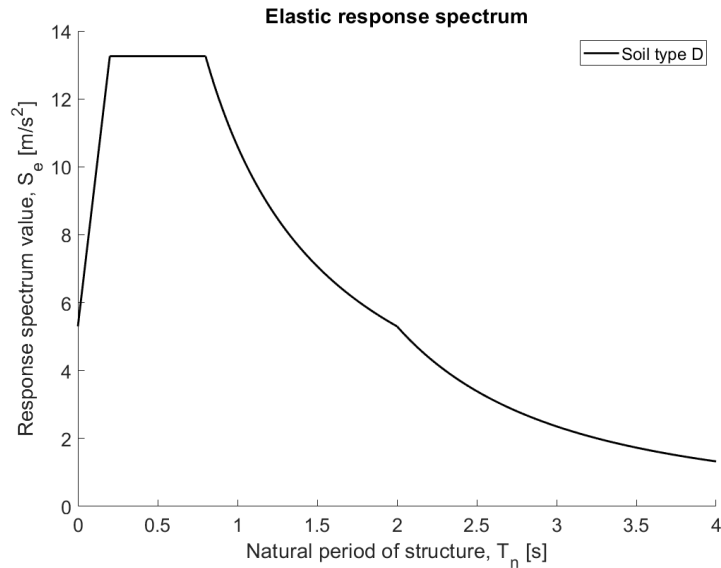


Figure 2.7: Elastic design response spectrum, [EN1998-1, 2004].

Accelerograms compatible to the response spectrum are a useful tool utilised in conjunction with the non-linear time history analysis to obtain an accurate response of the structure in question. Because the response spectrum is constructed by smoothing out the response of a SDOF to a number of different accelerograms, it follows that an infinite number of accelerograms could match the response spectrum, [Elghazouli, 2017]. For this reason, [EN1998-1, 2004] specifies that at least 3 different artificial or recorded accelerograms shall be used and the one that gives the most onerous structural response should be used. However, if at least 7 different accelerograms are used in order to obtain the structural response, the average of all results can be used. In the following the procedure to obtain recorded and artificial accelerograms are described.

2.6 Recorded and Artificial Accelerograms

When non-linear time history analysis is implemented time histories should be obtained and used as input for this analysis, where either recorded or artificial accelerograms are used according to [EN1998-1, 2004]. The type of accelerogram chosen is dependent on the information available and application of the accelerograms. When a sufficient amount of information on recorded accelerograms with similar nature at the specific site are available, recorded accelerograms are utilised, however if the available information is insufficient, artificial accelerograms may be used. Furthermore, the accelerograms used should be relevant to the expected earthquakes at the specific site, meaning recorded or artificial accelerograms should produce similar responses to the expected earthquakes. The procedure of obtaining the recorded and artificial accelerogram are described below respectively.

Recorded accelerograms

The preferred type of accelerogram to be utilised is the recorded accelerogram if recorded accelerograms are chosen appropriately. This is because it has several similarities and

characteristics to an expected earthquake in regards to magnitude and location, and therefore the use of recorded accelerograms require sufficient amount of measured earthquakes at similar sites and magnitudes.

The accelerograms are obtained from a strong motion database such as "Center for Engineering Strong Motion Data" [CESMD, 2022]. From the strong motion database a variety of earthquake data can be obtained from seismic stations located all around the world. These recordings include measurement of acceleration time history in the vertical and two horizontal directions along with magnitude and location of the measured earthquake. The response spectrum in g for the East-West component for the earthquake in Miyagi-Oki 2003-05-26, as presented in figure 2.5, is illustrated in figure 2.8.

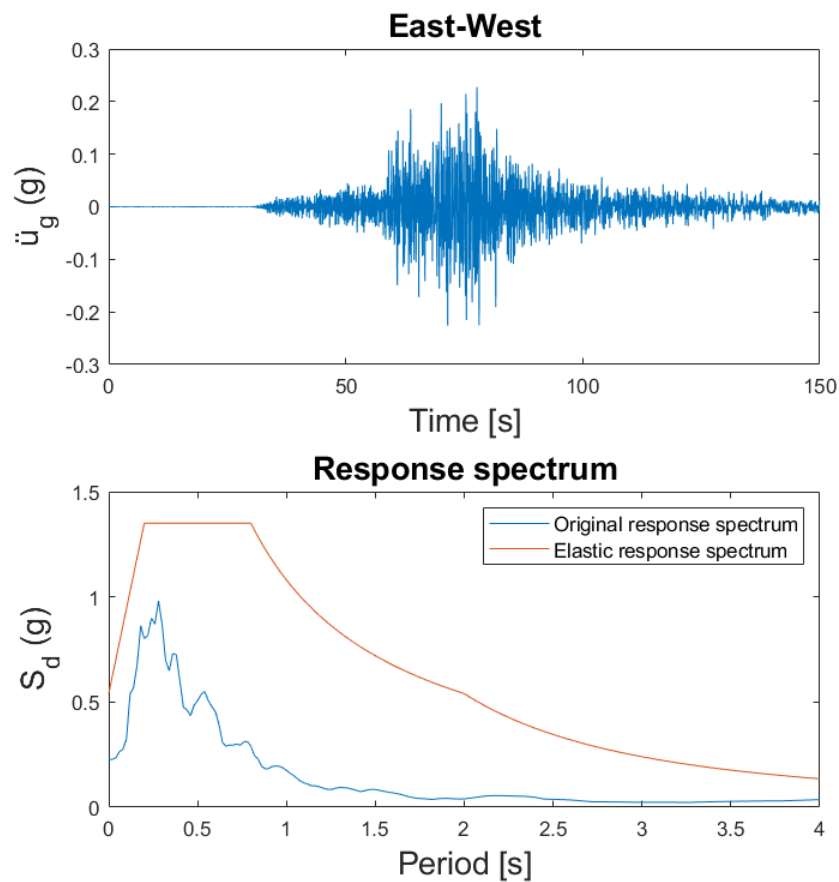


Figure 2.8: Accelerogram and response spectrum for the earthquake Miyagi-Oki, 2003-05-26 Japan with a magnitude of 7.0.

To ensure the recorded accelerogram is relevant to the expected earthquakes at the specific site the acceleration time history of the recorded earthquakes is modified to give peak responses similar to the expected earthquakes to satisfy the requirement that the accelerograms should be relevant to the expected earthquakes. This procedure can be performed through spectral matching with the purpose of matching the earthquake response spectrum to the elastic response spectrum at the given site, see appendix B section B.4.1 for further detailed explanation. The recorded accelerograms are matched by an iterative stepwise procedure in the software program *SeismoMatch*, which results in a modified acceleration time history and corresponding response spectrum illustrated in figure 2.9.

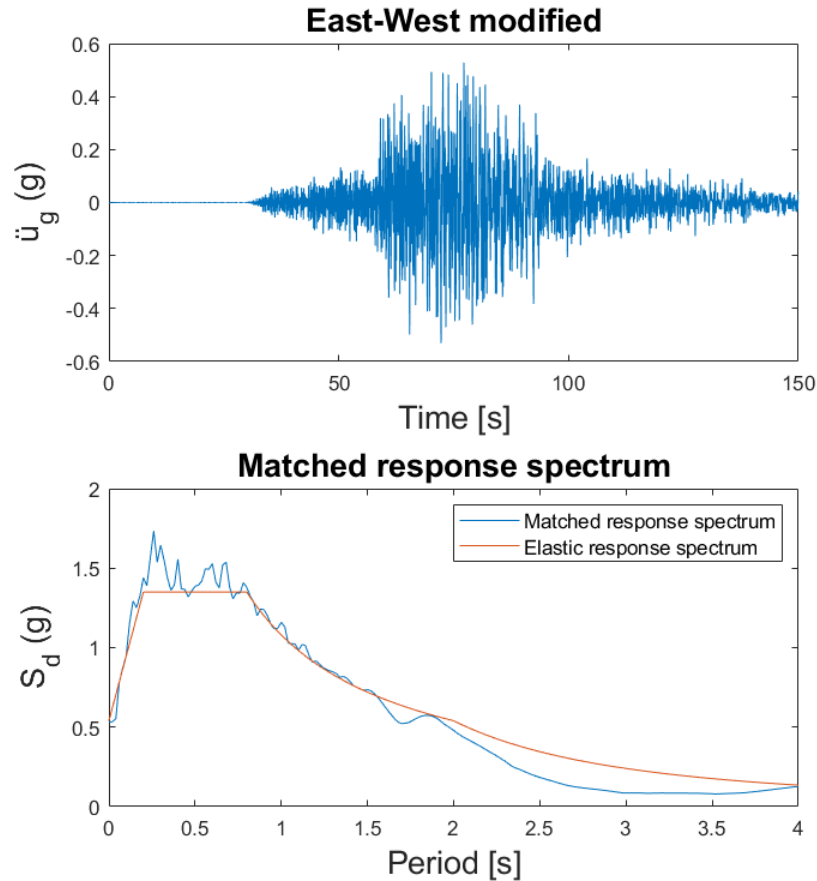


Figure 2.9: Modified accelerogram and response spectrum for the earthquake Miyagi-Oki, 2003-05-26 Japan.

Artificial accelerograms

In the absence of a sufficient amount of data artificial accelerograms need to be generated. Artificial accelerograms are generated computationally from the elastic response spectrum at the given site. The artificial accelerogram is generated in the software program *SeismoArtif* through a stepwise iterative procedure, which is further explained in appendix B section B.4.2, resulting in an artificially generated accelerogram whose response spectrum matches the elastic response spectrum relatively well.

Whether recorded or artificial accelerograms are used in the non-linear time history analysis both accelerograms are modified such that their response spectrum is almost identical to the elastic response spectrum, however in reality the structure will not behave linear elastic and therefore non-linearities should be taken into account.

2.7 Non-linearity

What characterizes a non-linear behaviour is the change in stiffness and loads which is dependent on the deformation, [Cook et al., 2002]. Non-linearity covers:

- Geometric non-linearity is when a structure experiences very large deformations which have to be taken into account in the equilibrium equations because equilibrium in the deformed position is very different from equilibrium in the undeformed position.
- Material non-linearity is non-linear elasticity, hyper elasticity, plasticity and creep which mean that the material strength depends on the stress or strain state in the material. [Cook et al., 2002].
- Contact non-linearity is when two or more structural parts are pulling, pushing or sliding against each other which results in change in stiffness of the involved parts.

Geometric non-linearities

For geometric non-linearity one could consider the column in figure 2.10 that is exposed to small displacements, large displacements and displacements somewhere in between, which is referred to as the $P-\Delta$ effect. The $P-\Delta$ effect allows to approximate the deformed shape so only translation of the column top is considered in the equilibrium equations. It is a practical solution that does not take much time. Depending on the size of P and Δ the moment contribution may be significant or insignificant. [P-Delta effect, 2019].

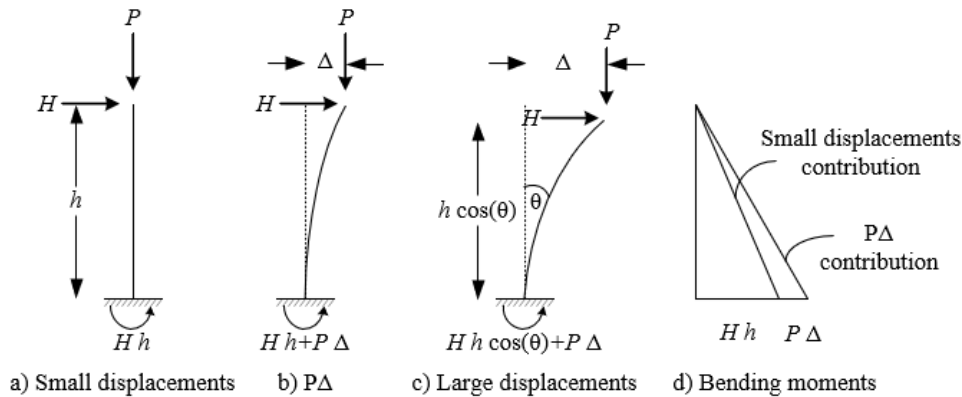
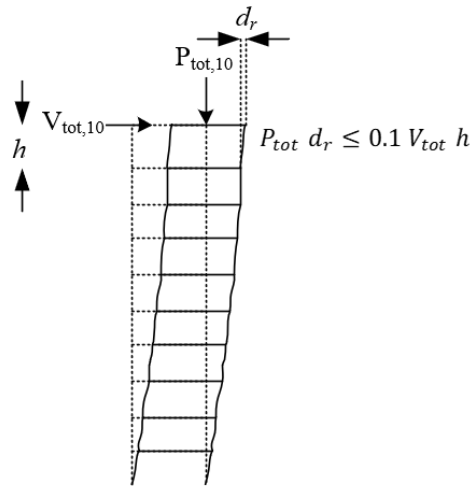


Figure 2.10: Geometric non-linearity.

According to [EN1998-1, 2004] the $P-\Delta$ effect can be neglected if the moment contribution from $P-\Delta$ effects does not exceed 10% of the moment contribution from small displacements, see the bending moment diagram in figure 2.10 d). This is secured by an interstory drift sensitivity coefficient, θ , which is given as:

$$\theta = \frac{P_{tot} d_r}{V_{tot} h} \leq 0.1 \quad (2.4)$$

For a multi story building equation (2.4) should be secured for each story as illustrated in figure 2.11.

Figure 2.11: $P-\Delta$ effect.

If $P-\Delta$ effects exceed 10% of the moment contribution the geometric non-linearities can be approximated by increasing each relevant story force by a factor equal to $1/(1 - \theta)$.

Material non-linearities

For material non-linearity one could consider a brittle and a ductile material as shown in figure 2.12. The brittle material behaves almost linearly until its ultimate strength where the material will fail and it is therefore not necessary to make a non-linear analysis for such a material behaviour. For the ductile material the material starts to behave non-linear after its yield point and it is therefore necessary to perform a non-linear analysis.

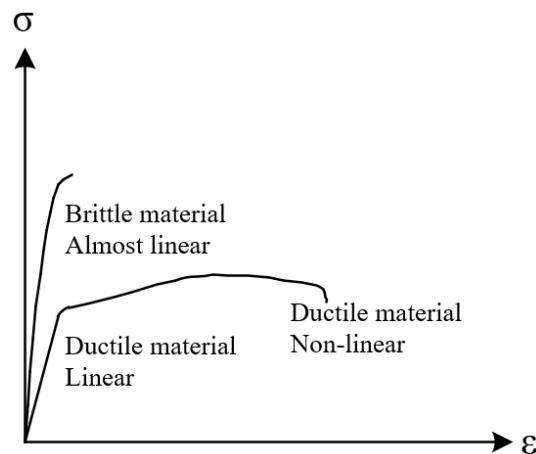


Figure 2.12: Material non-linearity.

A suitable constitutive model to account for material non-linearities in the numerical model of the multistory steel frame building is applied. The structural members in the building are of structural steel S275 with Young's modulus of $E = 210$ GPa. A bi-linear stress-strain model in figure 2.13 with kinematic strain hardening is used to model the elastic and plastic behaviour of the structural elements.

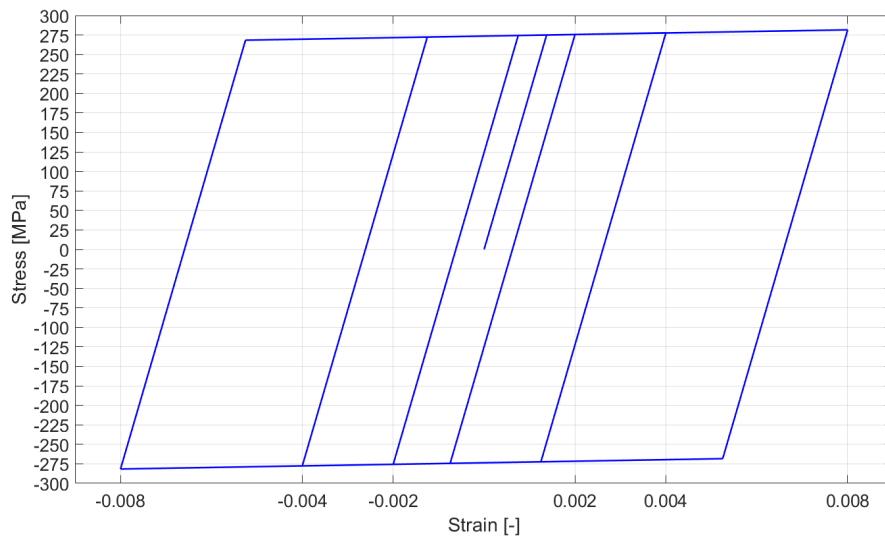


Figure 2.13: Bilinear kinematic hardening model for steel S275.

Contact non-linearities

For contact non-linearity one could consider a column that is linearly deformed until the column has contact with other parts of the structure or surrounding structures as shown in figure 2.14. When the structure gets in contact with other parts there will be an instantaneous change in the deformation of the structure.

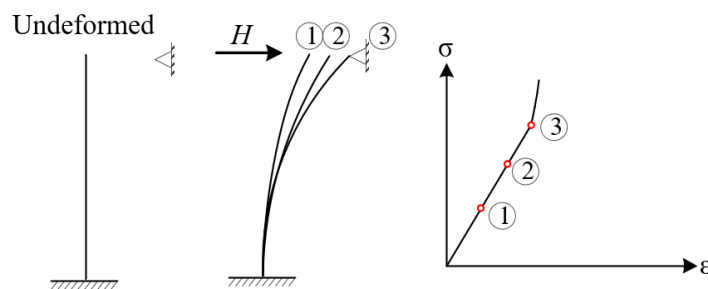


Figure 2.14: Contact non-linearity.

Within the scope of this project contact non-linearity is not incorporated within the numerical model of the multistory building as it is not expected that structural elements will be in contact with surrounding structures. However, contact non-linearities between soil and piles are taken into consideration in the numerical model of the windturbine foundation.

In regard to the response spectra it is possible to consider material non-linearity in a so called non-linear response spectrum which will be described in the following.

2.7.1 Non-linear Response Spectrum

In several earthquakes inelasticity in the structure will occur and the elastic response spectrum will result in too conservative spectral acceleration values. The ductility, i.e. the structure's ability to withstand deformations beyond yielding, [Elghazouli, 2017], can be taken into account by a behavior factor, q , that reduces the forces in the structure. The behavior factor makes it possible to analyse inelastic structures by use of elastic methods. Thus, the behaviour factor has limitations on the regularity of the structure, i.e. the inelasticity is expected to be uniformly distributed along the height of the structure where the deformation shape will be similar to an elastic structure, see appendix D. Furthermore, it should be ensured that the structure does not fail by a brittle failure before a ductile failure, otherwise the response is not ductile. The behaviour factor according to [EN1998-1, 2004] be found as the ratio between the maximum elastic strength, $F_{el.max}$, and the base shear force at which the first element starts to yield, F_{el} , as shown in figure 2.15.

$$q = \frac{F_{el.max}}{F_{el}}$$

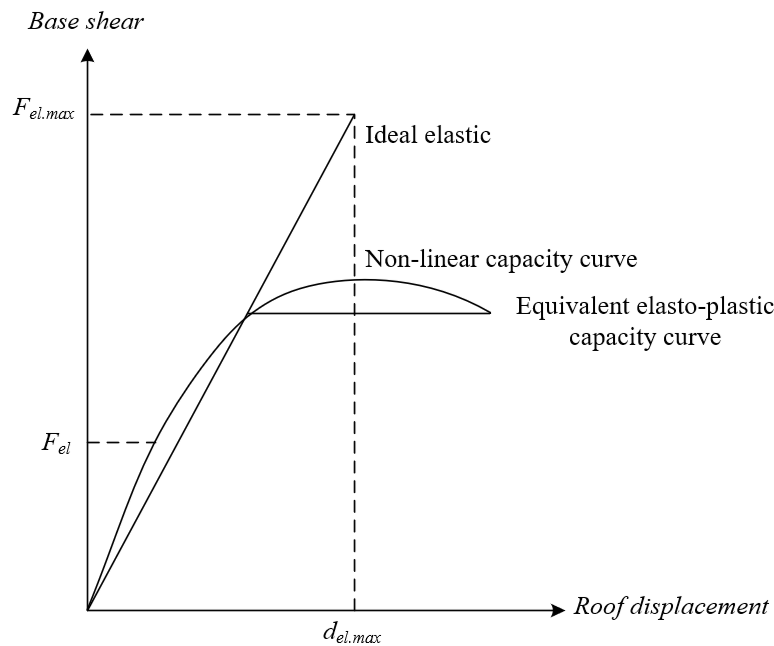


Figure 2.15: Behaviour factor, q .

In EN 1998-1 the ductility-modified spectrum is called a design spectrum and the assumptions in order to create the spectra in figure 2.16 are listed and can be seen in details in appendix B section B.3:

- Medium loose sand or soft to firm clay (soil type type D)
- Behaviour factor of $q = 1$, equal to elastic response spectrum
- Behaviour factor of $q = 2$, describing the behaviour of an inverted pendulum
- Behaviour factor of $q = 4$, describing the behaviour of a moment resisting frame, [EN1998-1, 2004].

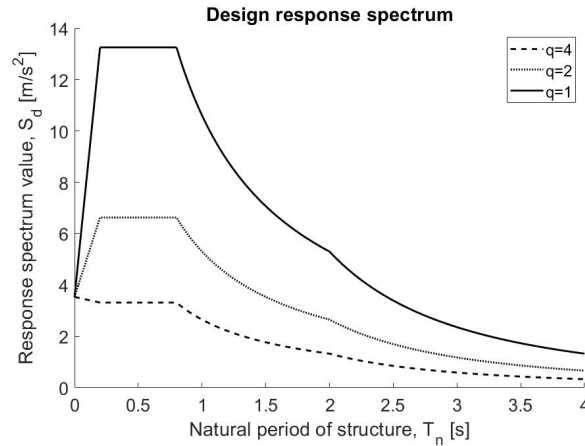


Figure 2.16: Inelastic design response spectrum, [EN1998-1, 2004].

It should be remembered that the response spectra in figure 2.7 and 2.16 are representing a SDOF system. In most cases structures have much more than a single degree of freedom and therefore have to be modelled as multi-degree-of-freedom (MDOF) systems. Later in the modal response spectrum analysis, it will be explained that it is possible to consider the response in several vibration modes as a SDOF system and then combining the responses to obtain the response of a MDOF system. Caution should be applied if the structure develops plastic deformations as the response of each mode only can be summarised if the inelasticity is assumed to be uniformly distributed, i.e. the plastic deformation is not only concentrated in local yield points of the structure, [Elghazouli, 2017]. Hence, summation of modal response is valid in a structure with uniformly distributed inelasticity and has the same deformation shape as an elastic structure. In cases where plastic deformations are concentrated in local yield points of the structure the design response spectra in figure 2.16 cannot be used and a time history analysis has to be used instead to obtain the response of the structure.

In figure 2.17 it is outlined how the response of a structure can be obtained when a building is in different ranges of elasticity and inelasticity during an earthquake.

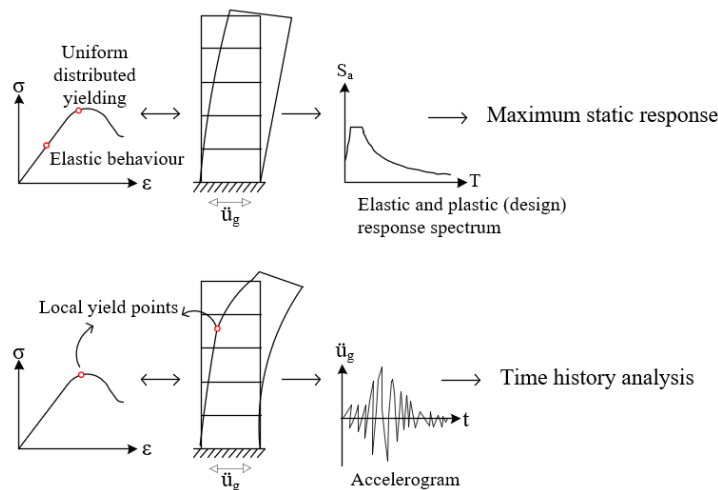


Figure 2.17: Illustration of how the response of a building in different ranges of elasticity and plasticity during an earthquake can be found.

Accelerograms and response spectra are utilised in the structural analysis of a multistory steel frame building in the following chapter.



Seismic Response Analysis of Multistory Steel Frame Building

Chapter 3	Application of EN 1998-1 Seismic Analysis Methods	24
3.1	Lateral Force Method	
3.2	Modal Response Spectrum Analysis	
3.3	Non-linear Static Pushover Analysis	
3.4	Non-linear Time History Analysis	
3.5	Multistory Steel Frame Building	
3.6	Response Comparison of Multistory Building	
3.7	Conclusion	

3 | Application of EN 1998-1 Seismic Analysis Methods

The aim of this chapter is obtain knowledge of the EN 1998-1 seismic analysis procedures, including limitations and differences.

In the following chapter the response of a ten-story building exposed to an earthquake is analyzed by the four methods presented in section 2.3. The different methods are divided into two main parts as shown in figure 3.1. The methods in figure 3.1a and 3.1b top are based on the response spectrum, as described in section 2.5, where a maximum static response can be obtained. The method in figure 3.1b bottom is based on the accelerogram, also as described in section 2.5, where the response can be obtained as a time history series.

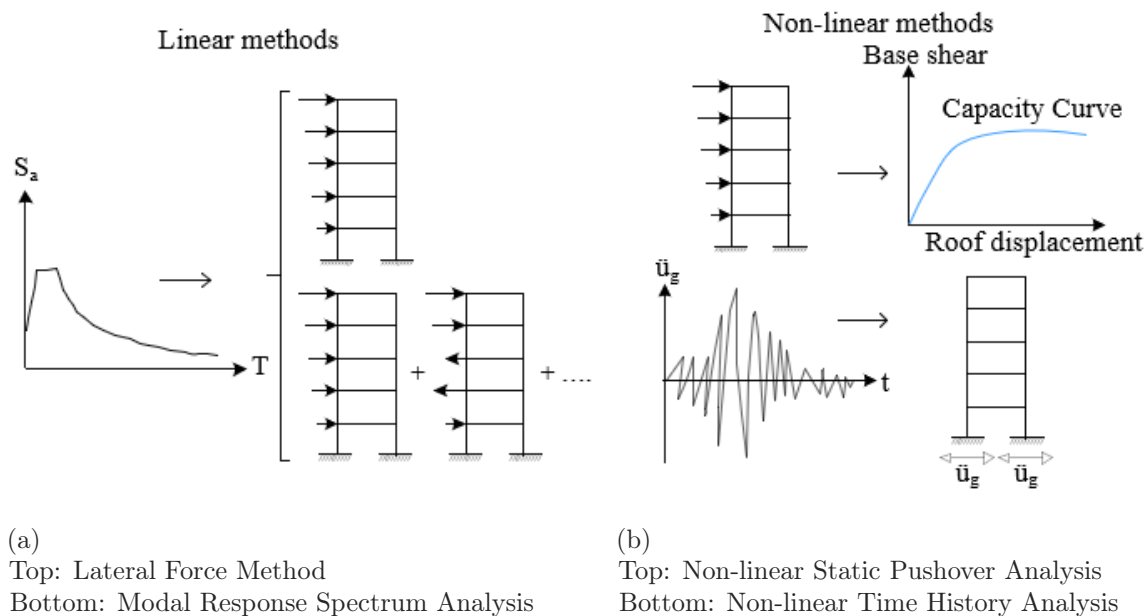


Figure 3.1: Illustration of the different methods.

3.1 Lateral Force Method

The lateral force method can be used as initial calculations on a structure subjected to minor dynamic oscillations. It is used to estimate the equivalent static load on a structure excited by an earthquake and can only be applied as long as it can be reasonably assumed that the structure is dominated by a single eigenmode, [Elghazouli, 2017], which often is the first eigenmode. According to EN 1998-1 [EN1998-1, 2004] it has to be ensured that the structural behaviour will be more quasi-static than dynamic, in other words, the method requires the structure to be so stiff that the response can be considered quasi-static with little dynamic oscillations. Furthermore, the structure needs to meet the criteria for regularity in elevation which means that there is only little variation in stiffness and mass in elevation of the structure so that the dynamic behavior does not suddenly change.

Step 1

The procedure is to first obtain the acceleration of the structure during the earthquake by the design response spectrum and then find the maximum base shear force as illustrated on figure 3.2.

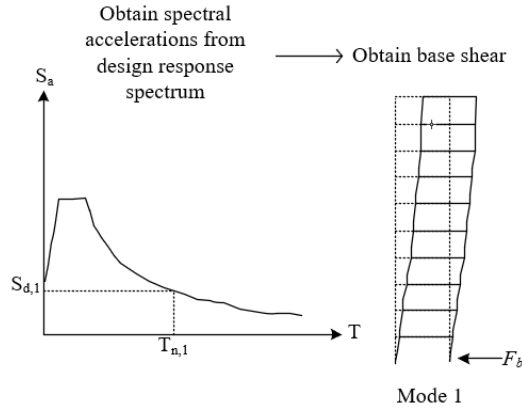


Figure 3.2: Obtain spectral acceleration and base shear.

The maximum base shear force can be calculated by equation (3.1).

$$F_b = S_d(T_1) m \lambda \tag{3.1}$$

where

$S_d(T_1)$	Design spectrum value at period T_1
m	Total mass of the structure
λ	Correction factor that accounts for an effective modal mass for the first mode which is 15% smaller than the total mass of the building.

Step 2

The next thing is to find the story forces and corresponding maximum static response as illustrated on figure 3.3.

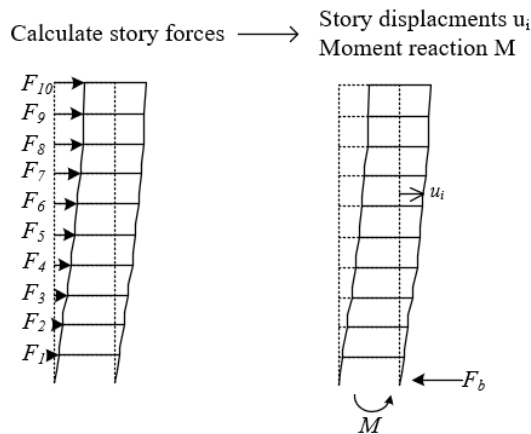


Figure 3.3: Obtain story forces and maximum static response.

The story forces can be calculated by equation (3.2).

$$F_i = F_b \frac{s_i m_i}{\sum_{i=1}^j (s_i m_i)} \quad (3.2)$$

where

F_i	Horizontal seismic force in story i
m_i	Mass in story i
s_i	The modal displacement of story i in the first modeshape
j	The number of stories.

The material and geometric non-linearities can be included but the non-linearities are only approximated. The material non-linearity is taken into account by the behaviour factor and the geometric non-linearity, in terms of P - Δ effect, can be taken into account by increasing the story forces, as described in section 2.7. Therefore, this method has some limitations which are summarised; only one mode is considered and the response has to be considered quasi-static, non-linearities (geometric and material) are only approximated. For a more detailed explanation of the method, see appendix D.1.

3.2 Modal Response Spectrum Analysis

For a flexible structure, which is less stiff and more dynamic, the modal response spectrum analysis can be used as an alternative to the lateral force method. Modal analysis is a method of determining the dynamic characteristics of a structure in terms of eigenfrequencies and modeshapes, and use them to determine the dynamic behaviour of the structure. It is an approximate method, but the more modes considered, the more exact the method will be. However, the method is often utilised due to its low computational requirements, but the solution is only given for the selected modal responses.

Step 1

The first thing is to obtain the eigenperiods, the acceleration of the structure during the earthquake and then maximum base shear force for each considered mode as illustrated on figure 3.4.

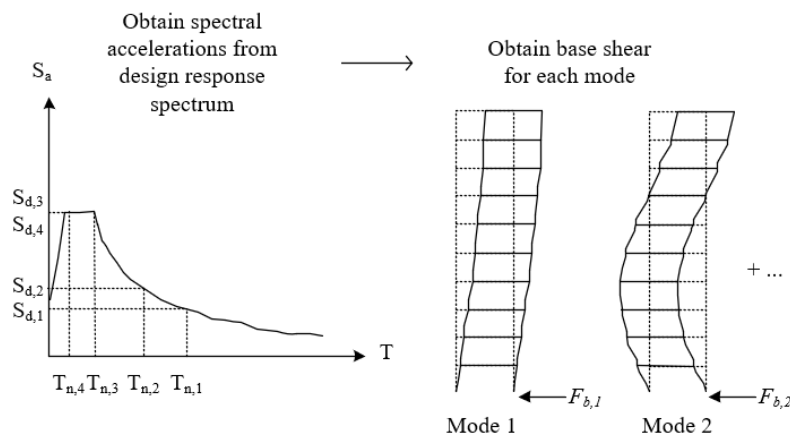


Figure 3.4: Obtain spectral acceleration and base shear force for each considered mode.

The maximum base shear force for each mode is seen in equation (3.3).

$$F_{bn} = S_{dn}(T_n) m_n \tag{3.3}$$

where

S_{dn}		Spectral acceleration for mode n
T_n		Eigen period for mode n
m_n		Modal mass for mode n .

Step 2

The next thing is to find the maximum story forces and response for each considered mode and lastly, the total response can be found as illustrated on figure 3.5

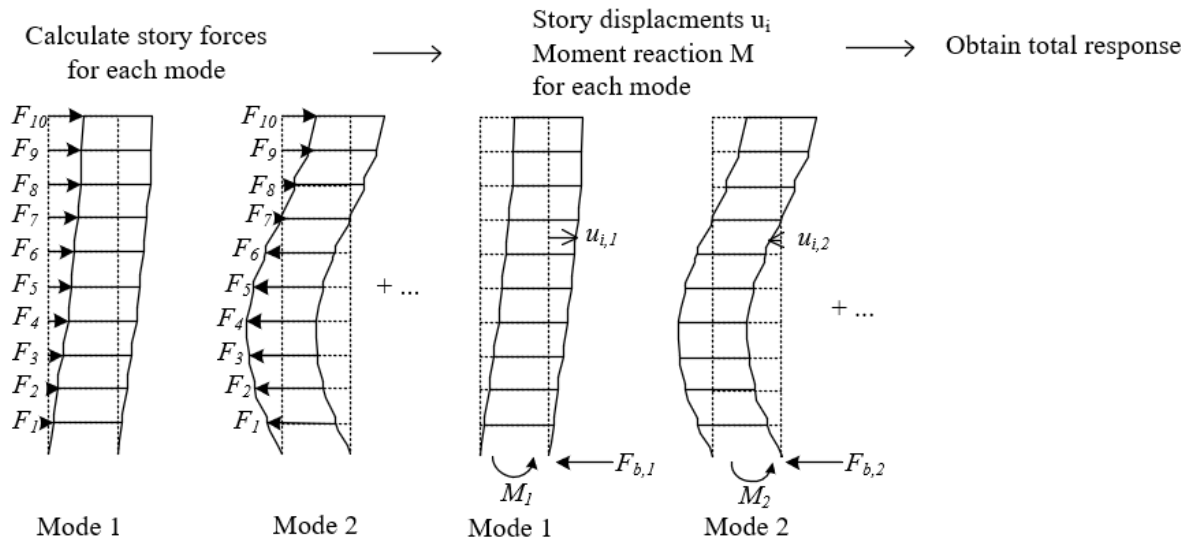


Figure 3.5: Obtain story forces and maximum static response for each considered mode.

The maximum story forces for every mode is calculated using equation (3.4).

$$F_{in} = F_{bn} \frac{s_{in} m_{in}}{\sum_{i=1}^j (s_{in} m_{in})} \tag{3.4}$$

where

F_{in}		Horizontal seismic force in story i for mode n
F_{bn}		Base shear for mode n
m_{in}		Mass in story i for mode n
s_{in}		The modal displacement of story i for mode n
j		The number of stories.

It is unlikely that the maximum response for each mode happens at the same time and therefore is the total response combined by using the square root of the sum of squares (SRSS) method in

equation (3.5).

$$r_o = \sqrt{\sum_{n=1}^N r_{io}^2} \quad (3.5)$$

where

$$\begin{array}{l|l} r_o & \text{Total response} \\ r_{io} & \text{Response from mode } i \end{array}$$

The limitations of this method are the same kind as for the lateral force method, only in this method several modes can be considered. For a more detailed explanation of the method, see appendix D.2.

3.3 Non-linear Static Pushover Analysis

This method is more advanced than the linear analysis methods and ductility modified response spectra because the collapse mechanism of the structure is calculated in a non-linear analysis instead of assumed to be a uniform ductility failure, [Elghazouli, 2017]. The method has a higher computational requirement than the lateral force method and modal response spectrum analysis, but it will give a more realistic structural behaviour due to material non-linearities.

Step 1

The first part is to apply a lateral load in a load pattern and increase the lateral load by load increments until the structure forms a failure mechanism. A “uniform” load pattern with lateral forces proportional to the story masses and a “modal” load pattern that follows the first modeshape with lateral forces proportional to the product of the mass matrix by the modal vector is applied to the building and the most unfavourable one should be chosen for the design. The method can be inaccurate if the assumed load pattern is incorrect, and therefore it is important to choose a load pattern corresponding to the dynamic properties of the structure. A proper load pattern takes contributions from significant mode shapes into account and furthermore has to consider a non-fixed load pattern if the structure has local yield points. The load pattern is applied in the numerical model and the displacement at the upper story during monotonic loading is calculated, from which the capacity curve can be constructed as a relation between base shear force and roof displacement, which is illustrated on figure 3.6.

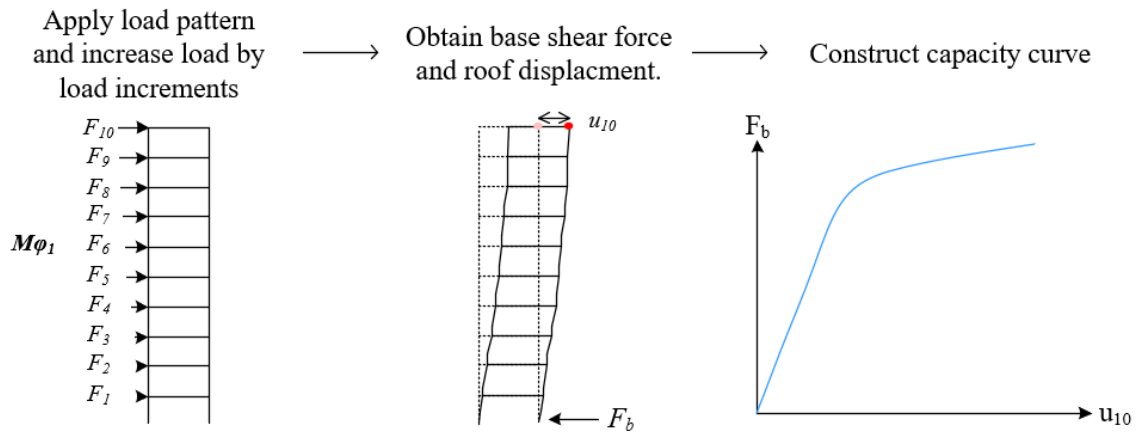


Figure 3.6: Steps for construction of capacity curve.

Step 2

The second part is to determine the demands imposed by the earthquake on the structure by obtaining response spectra for certain damage levels according to EN 1998-1 (damage limitation, significant damage and near collapse) as shown in figure 3.7. The limit state corresponding to the elastic response spectrum in figure 2.7 is significant damage (a 10% probability of exceedance in 50 years corresponding to a return period of 475 years) which is chosen for the design.

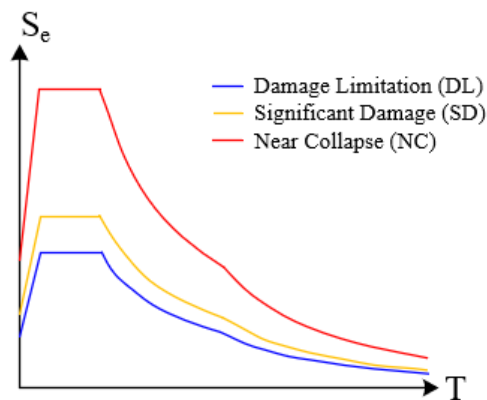


Figure 3.7: Response spectra for damage levels.

Step 3

The last step is to convert the capacity curve into an idealized elastic perfectly-plastic capacity curve, and to convert the response spectrum into a demand curve. The target displacement which is the peak inelastic displacement that the structure is expected to reach during the design earthquake, d_t^* , can then be obtained by the procedure in figure 3.8.

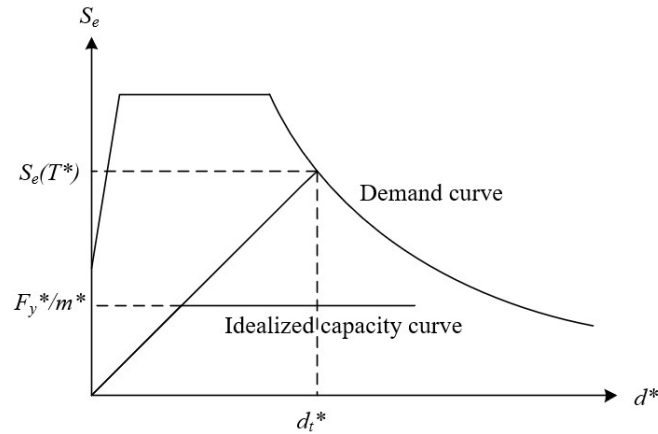


Figure 3.8: Determination of target displacements from idealized capacity and demand curves, [Elghazouli, 2017].

The target displacement for the relevant damage level is obtained and plotted on the capacity curve to obtain the base shear that a future earthquake is expected to push the structure and the level of yielding can be evaluated. A non-linear static analysis can then be performed for the target displacement to obtain the structural response as shown on figure 3.9.

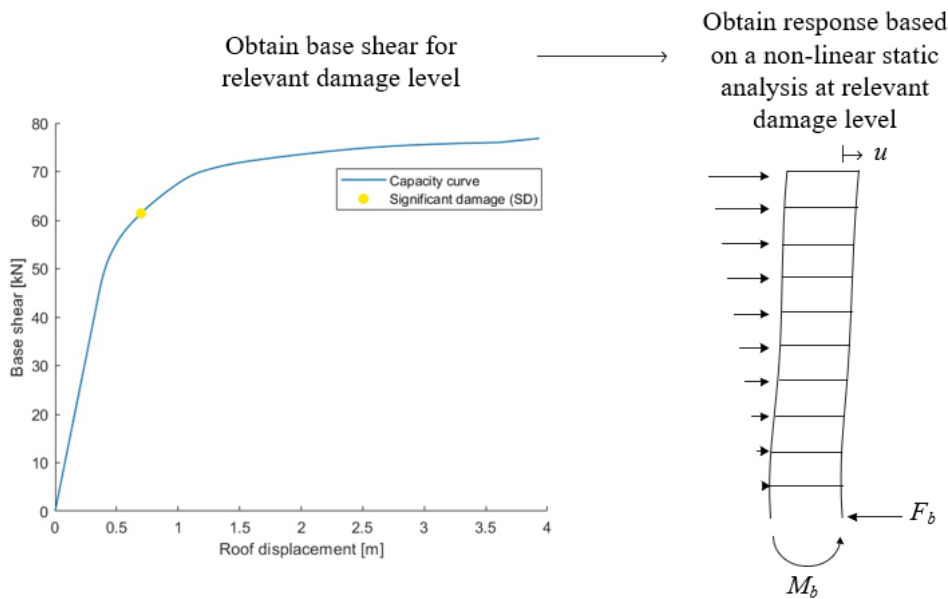


Figure 3.9: Target displacement and corresponding base shear for a load pattern that follows the first modeshape.

A pushover analysis is carried out for each fixed load pattern, the “uniform” and the “modal” load pattern. The desired response quantities, i.e. base shear, base moment and story displacements are calculated for the first 4 modeshapes and combined using the SRSS rule for the “modal” load pattern.

The procedure for applying non-linear static pushover analysis is explained in details in appendix D.3.

3.4 Non-linear Time History Analysis

A non-linear time history is used if the dynamic response of the system is beyond the linearly elastic range and is also applicable if the structure has nonclassical damping which for an example could be the case in a soil-pile system where soil and structure have significantly different levels of damping, [Chopra, 2007]. In both cases is the modal analysis no longer applicable as the modal equations cannot be uncoupled - for nonclassical damping because the damping matrix is no longer diagonal and for non-linear systems because the modal equations are coupled when the structure is beyond yielding.

The dynamic equation is solved numerically where initial conditions, such as displacement, velocity and acceleration at $t = 0$, are known. Because the stiffness and perhaps loads as well depend on the deformation of the structure, the dynamic equation has to be solved by an iterative procedure because the deformation $\{\mathbf{u}\}$ cannot be immediately solved for because stiffness and loads, $[\mathbf{K}]$ and $\{\mathbf{P}\}$ is not known in advance as they depend on $\{\mathbf{u}\}$, [Cook et al., 2002].

$$[\mathbf{M}]\{\ddot{\mathbf{u}}\} + [\mathbf{C}]\{\dot{\mathbf{u}}\} + [\mathbf{K}(\mathbf{u})]\{\mathbf{u}\} = \{\mathbf{P}(\mathbf{u}, t)\}$$

The solution is obtained using a stepwise procedure called direct integration method where the time at $n + 1$ at the end of a time step is used, [Chopra, 2007]. For this analysis Newmark's integration method is used to solve the dynamic equation.

In the time history analysis a model is analysed under an accelerogram that represents the behaviour of a wide span of past earthquakes, as the accelerogram's frequency content matches the design spectrum, [Elghazouli, 2017]. Because future earthquake ground motions are unknown and can have complete different behaviour such as peak acceleration and time duration as shown on figure 3.10 and 3.11, three matched accelerograms are chosen. The selection of appropriate accelerograms is more time consuming than the use of design response spectra because it requires a larger database of available recorded ground motions because the ground motions have to be compatible with the local seismicity and ground conditions in order to give a realistic representation of the earthquake.

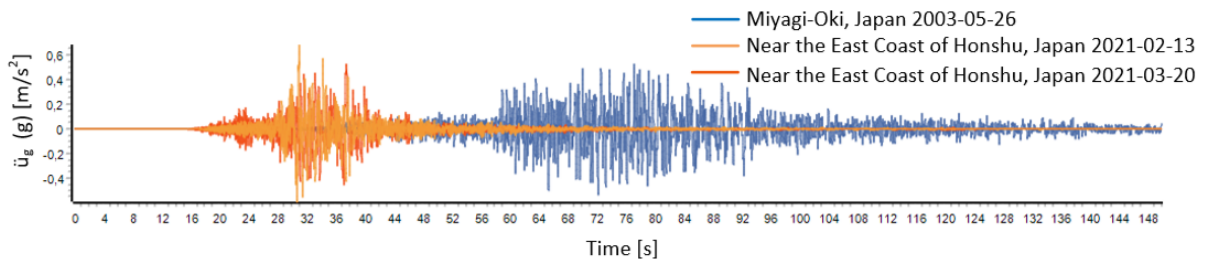


Figure 3.10: Matched accelerograms. Matching in commercial software: *SeismoMatch*.

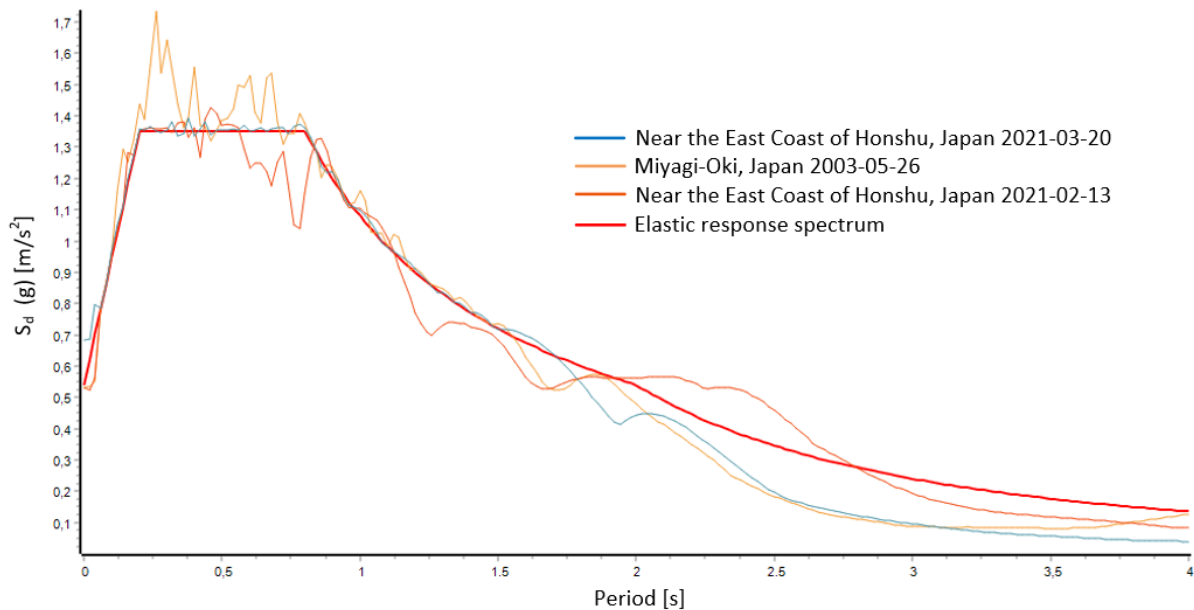


Figure 3.11: Matched response spectra. Matching in commercial software: *SeismoMatch*.

To perform the non-linear static pushover analysis and the non-linear time history analysis the finite element program *SeismoStruct* is used. The program is capable of predicting the large displacement behaviour of space frames under static or dynamic loading and takes into account both geometric and material non-linearities. The general modelling input for both methods are:

- Bilinear constitutive model as shown in figure 2.13
- Inelastic force-based frame element type (infrmFB), which is a 3D beam-column element type capable of modelling members of space frames with geometric and material non-linearities.

For non-linear time history analysis further modelling input parameters are specified below:

- Rayleigh damping with mass and stiffness parameters, α and β , found based on eigenperiods and modal damping ratio of $\zeta = 5\%$
- Implicit time integration method with time integration parameters is solved by iterative algorithm: modified Newton-Raphson, see subsection D.4.2 in appendix D

The procedure for applying non-linear time history analysis is explained in details in appendix D.4.

3.5 Multistory Steel Frame Building

A ten-story steel frame, with static system, dimensions and members as illustrated in figure 3.12, is analysed by the different methods to get an understanding of how the methods work and how the comparison between results based on assumptions and approximations in the methods are. The model is regular in plan and elevation and can therefore be modelled as a planar 2D model, which is described in further details in appendix C.1. The soil-pile interaction is assumed to be rigid illustrated with fixed supports in column ends.

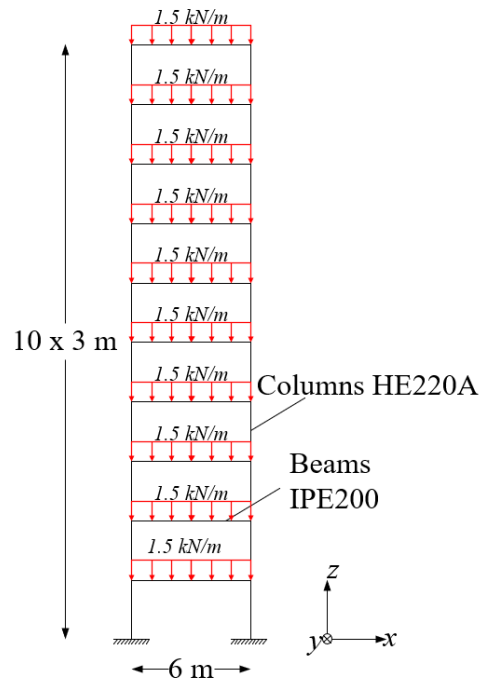


Figure 3.12: Static system of the structural model. A rigid support between soil and structure is assumed.

Behaviour Factor

In order to assign the behaviour factor, q , as described in section 2.7, the steel frame is assumed to be:

- A moment resisting frame in which the desired failure mechanism is to develop plastic hinges in the beam ends rather than in the column ends, called beam/strong column concept which provides favorable performance in comparison to strong beam/weak column behaviour, EN 1998-1 [EN1998-1, 2004], as illustrated in figure 3.13.
- Designed as a dissipative structure with a medium ductility class (DCM).

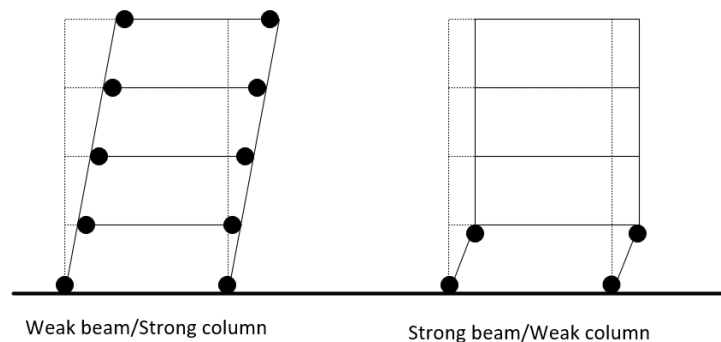


Figure 3.13: Weak beam/strong column and strong beam/weak column behaviour.

The behaviour factor is assigned to $q = 4$ and all the requirements in order to assign q is described in details in appendix C.3.

3.6 Response Comparison of Multistory Building

The maximum response, which include base shear, base moment and lateral displacements of the multistory building obtained in each method is compared to each other. The results from the four methods can be seen in details in appendix E. The following are compared:

- Lateral force method, modal response spectrum analysis, non-linear static analysis vs. non-linear time history analysis.

The base shear and base moment for each method is illustrated in figure 3.14.

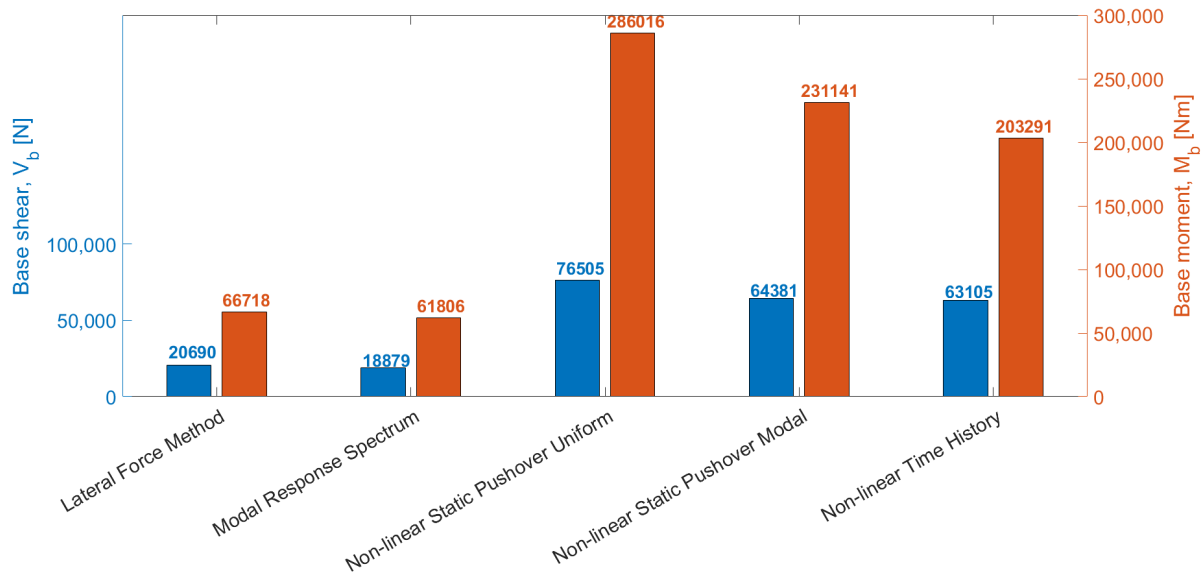


Figure 3.14: Base shear and moment for the four methods.

From the results it can be seen that the response found from lateral force and modal response spectrum methods are generally underestimated compared to the time history analysis. A leading factor that explains this large difference is the behaviour factor which reduces the response spectrum values used in lateral force and modal response spectrum methods significantly as shown in figure 2.16. It is therefore tempting to question whether a behaviour factor $q = 4$ is realistic for the structure during the earthquake. Because the results from lateral force and modal response spectrum methods underestimate the response of the building compared to non-linear time history analysis it can not be guaranteed that the assumption of global ductile failure and satisfactory energy dissipation is secured. The large difference could be due to the building behaving elastically up to near collapse and not having global ductile failure as assumed through the behaviour factor of $q = 4$. Furthermore, the interstory drift sensitivity coefficient θ and the strong column/weak beam concept secure enough stability against second order (P- Δ) effects, which lead to large lateral strength, could be an explanation of the low energy dissipation during the earthquake with 10% probability of exceedance in 50 years, [Costanzo et al., 2019].

The structural behaviour factor is therefore calculated based on the capacity curve which is constructed in the pushover analysis instead of using an assumed value. The capacity curve and equivalent elasto-plastic capacity curve for the multistory building is shown in figure 3.15. The structural behaviour factor during the earthquake with 10% probability of exceedance in 50 years for the multistory building is found to be considerable below the assumed behaviour factor

of $q = 4$. This means that the earthquake energy is not dissipated due to global ductile failure as first assumed and the response of the building will in reality be larger. It can be seen from the figure that the base shear during the earthquake, $F_{el,max}$, is at a point on the capacity curve where the building has not developed large plastic deformations yet and is placed far away from the maximum base shear strength of the building at around 75 kN. If the earthquake instead develops base shear corresponding to the strength of the building the assumption of $q = 4$ would be more realistic.

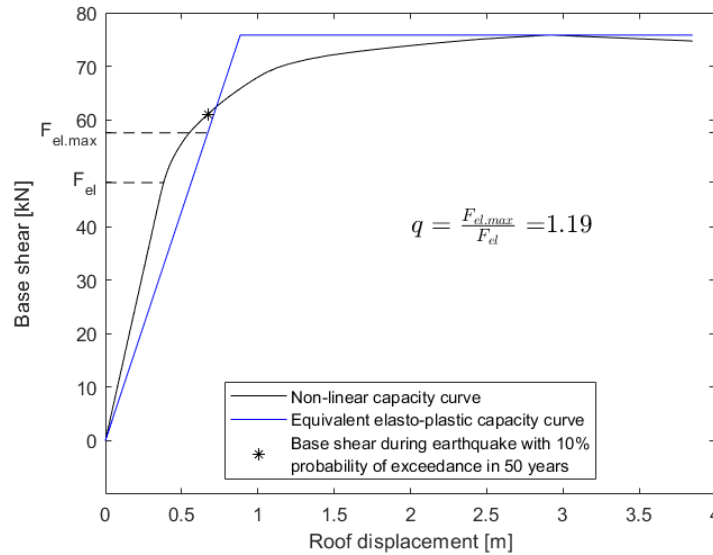


Figure 3.15: Capacity curve to obtain behaviour factor, q . F_{el} marks the base shear at first yield point and $F_{el,max}$ marks the base shear for an earthquake with 10% prob. of exceedance in 50 years on the equivalent elastic perfectly-plastic curve.

The behaviour factor is found by the ratio between the base shear developed during an earthquake with 10% prob. of exceedance in 50 years and the base shear at the first yield point, as shown at figure 3.16.

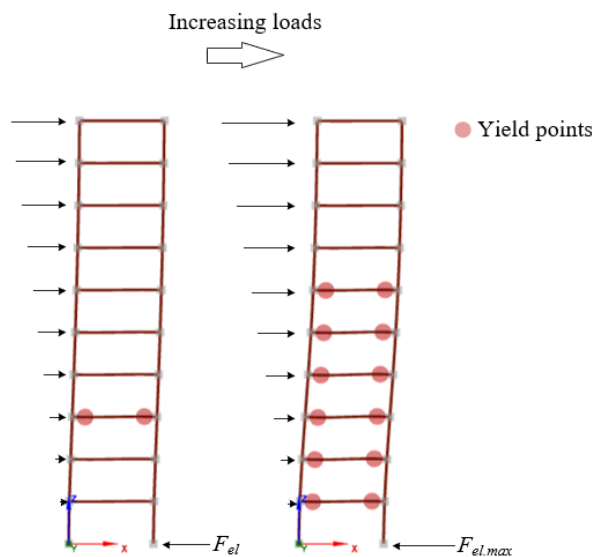
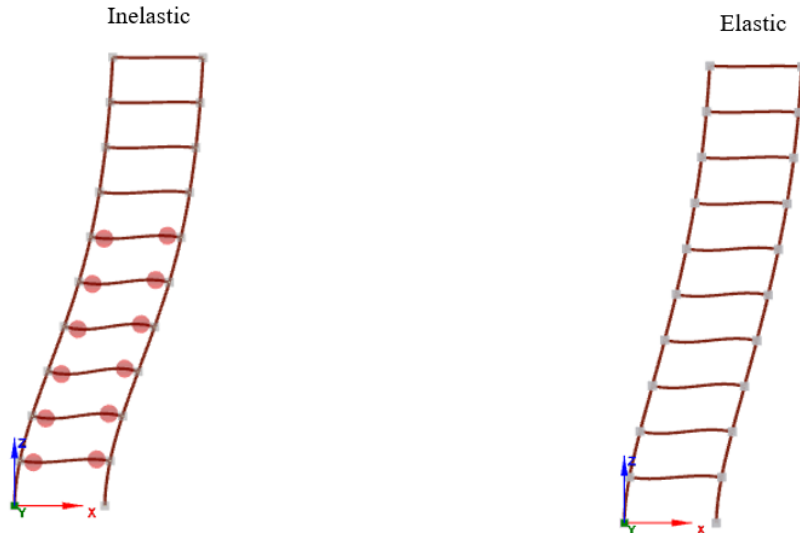


Figure 3.16: The base shear at first yield point, F_{el} , and the base shear and yield points developed during an earthquake with 10% prob. of exceedance in 50 years.

Figure 3.17 illustrates the deformed shape at the point where the base shear during the earthquake with 10% prob. of exceedance in 50 years is reached for an inelastic material with bi-linear stress-strain curve and an elastic material. It is noted that the deformed shape of the plastic structure in 3.17a is similar to the elastic one in 3.17b which indicates that yielding is evenly distributed throughout the structure and the ductility-modified response spectrum with q is suitable to use.



(a) Inelastic material: kinematic hardening in stress-strain relationship

(b) Elastic material

Figure 3.17: Deformed shape vector.

The base shear and base moment found from the lateral force and modal response spectrum analysis with a behaviour factor of $q = 1.19$ can be seen in figure 3.18 to give considerably higher correlation with the non-linear time history analysis.

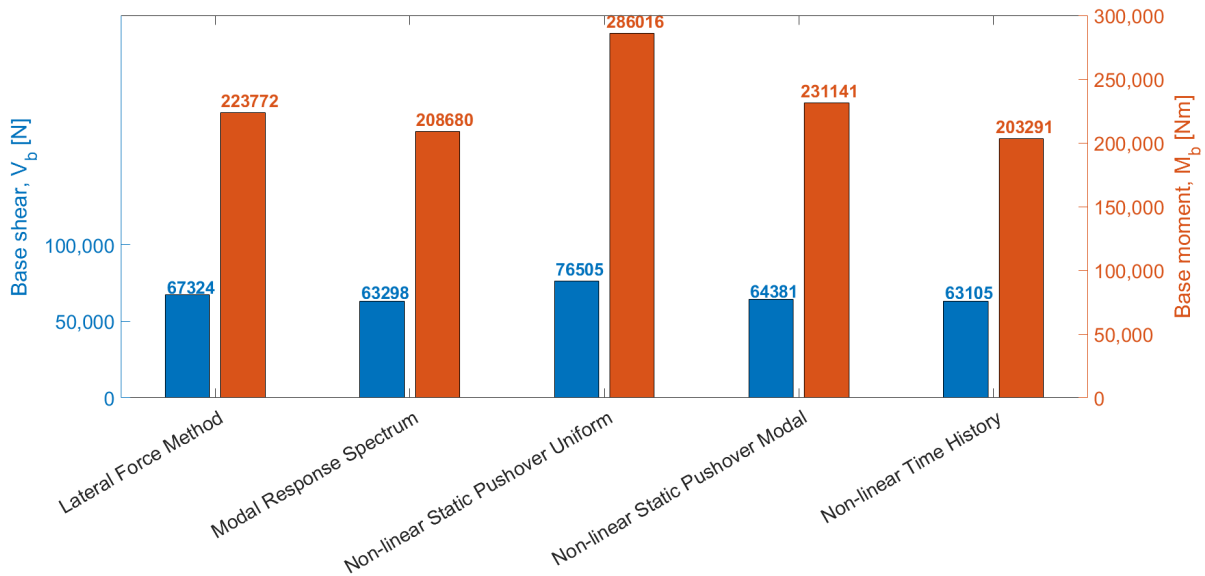


Figure 3.18: Updated base shear in lateral force method and modal response spectrum analysis with $q = 1.19$.

The lateral story displacements from the different methods are illustrated in figure 3.19. The story displacements in the lateral force and modal response spectrum analysis are found by multiplying the elastic displacements, found based on a static linear analysis, by the behaviour factor of $q = 1.19$, as stated in EN 1998-1 [EN1998-1, 2004].

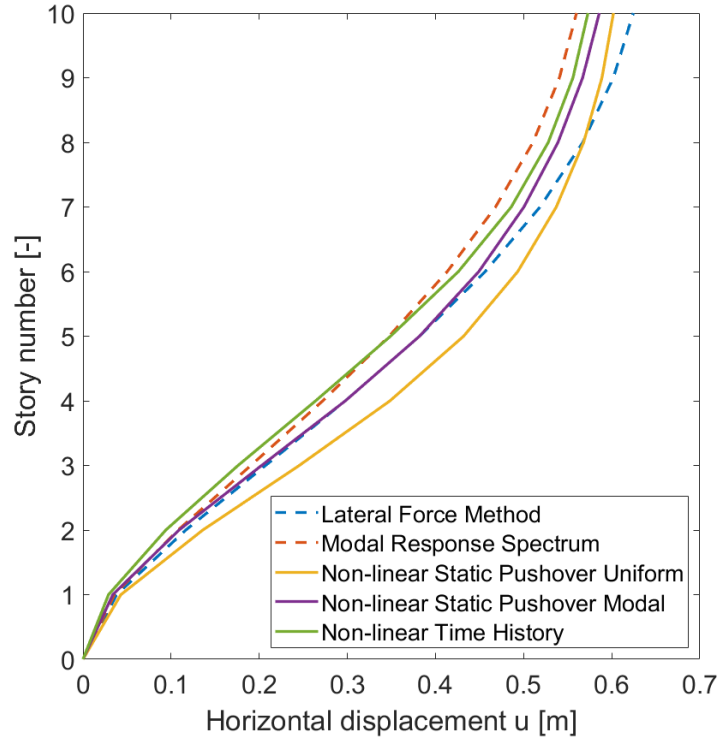


Figure 3.19: Story displacements in lateral force method and modal response spectrum analysis with $q = 1.19$.

From table 3.1 it can be seen that the lateral force method and modal response analysis in general gives conservative estimates of base shear and base moment compared to the non-linear time history analysis. The more modes considered yields more accurate estimates of base reactions (around 3% in deviation compared to the time history analysis). The non-linear static pushover analysis with a “uniform” load pattern gives very conservative estimates of base reactions which is due to the very simplified way of describing the dynamic properties of the building. However, the “modal” load pattern gives higher correlation of base reactions compared to the time history analysis as four modeshapes that represent the dynamic behaviour well are included.

Table 3.1: Deviation from non-linear time history analysis.

	Deviation from non-linear time history analysis [%]			
	Lateral force method	Modal response spectrum analysis	Non-linear static pushover analysis uniform	Non-linear static pushover analysis modal
Base shear	6.7	3.1	21.2	2.0
Base moment	10.1	2.7	40.7	13.7
Roof displacement	9.0	-2.3	5.1	2.3

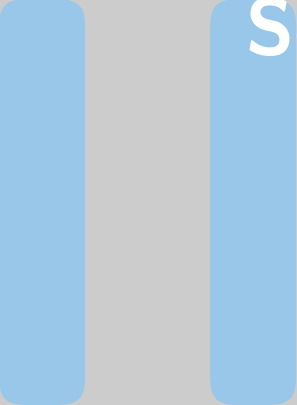
3.7 Conclusion

It can be concluded that the assumption of $q = 4$ and high energy dissipation is not satisfied and the multistory building behaves mostly elastically with low yielding (figure 3.15) which explains why the results from the linear methods differ from the non-linear methods. An updated behaviour factor of $q = 1.19$ gives more comparable base reactions in figure 3.18 and it can be concluded that the lateral force method gives the most conservative estimate of base shear.

Conclusive remarks on the different methods are given:

- The lateral force method can determine the response of a structure if it can be assumed that the structure behaves quasi-static and tend to oscillate in a single mode. From a modal analysis it is concluded that the structure does not oscillate in a single mode as only 77% of the total mass is included in the first eigenmode (see results from modal analysis in figure E.3). The structure is more flexible and the dynamic behaviour is better described by several modes where the modal response spectrum analysis can be used. When using the design spectrum and behavior factor it has to be ensured that the building has a uniform distribution of yielding, otherwise the design spectrum, and therefore these methods, cannot be used. It is verified in figure 3.17 that the building has a uniform distribution of yielding which is why both lateral force method and the modal response spectrum analysis give reasonable results.
- The non-linear static pushover analysis gives a more realistic non-linear behaviour as the failure mechanism is no longer assumed but calculated in the capacity curve. However, the uncertainty lies in the assumed load pattern where the “uniform” load pattern gives very conservative base reactions. Several modes describing the load pattern is included which yields more accurate results. The target displacement and hereby the response is found based on the demand curve which is constructed from the elastic response spectrum rather than an accelerogram which makes the method faster and more simple than the non-linear time history analysis. However, the static pushover analysis is less accurate compared to the time history analysis because the method compromises the dynamic behaviour by evaluating the response in a static analysis.
- The non-linear time history analysis is the most precise method but also the most time consuming as the dynamic equation has to be solved by an iterative procedure (due to change in stiffness) at each time step, and several accelerograms should be considered in the analysis due to the fact that future earthquake ground motions are unknown and can have complete different duration and amplitude. However, the method does not have any limitations and is preferred for offshore structures as the dynamic impact is large and have to be fully captured.

In this first part of the project Eurocode 8 seismic analysis procedures have been applied on a multistory building and the response has been evaluated. In the next part are the seismic analysis procedures developed in DNV-RP-0585 applied on an offshore wind turbine foundation located in Japan where seismic hazards such as ground shaking and liquefaction are evaluated.



Seismic Response Analysis of Offshore Wind Turbine Foundation

Chapter 4	Seismic Hazard Assessment	40
4.1	Wind Farm Site	
4.2	Geotechnical Conditions	
4.3	Jacket Substructure	
4.4	Probabilistic Seismic Hazard Analysis	
4.5	Summary	
Chapter 5	Site Seismic Response Analysis	54
5.1	Approaches	
5.2	Input Parameters	
5.3	Numerical Model	
5.4	Response Comparison of Non-linear Soil Models	
5.5	Results	
5.6	Summary	
Chapter 6	Liquefaction	68
6.1	Liquefaction Evaluation	
6.2	Summary	
Chapter 7	Modelling Approaches	72
7.1	Numerical Model 1: Jacket Substructure on Rigid Base	
7.2	Numerical Model 2: Jacket Substructure on Embedded Piles with Soil-pile Springs	
7.3	Numerical Model 3: Jacket Substructure on Embedded Piles with Soil Volume	
7.4	Results	
7.5	Ground Improvement	
7.6	Summary	
Chapter 8	Conclusion	97

4 | Seismic Hazard Assessment

In the second part of the project are the seismic effects on an offshore wind turbine foundation analysed using [DNV-RP-0585, 2021] as a framework. A planned wind farm located near the south coast of Japan is chosen, the geotechnical conditions are assumed and a foundation structure is chosen. Firstly, a probabilistic seismic hazard analysis (PSHA) must be performed to determine the design earthquake in terms of a site specific design response spectrum, target moment magnitude and target distance to earthquake source. On the basis of a design/target earthquake, an appropriate earthquake accelerogram from the past is chosen. By spectral matching the accelerogram to the design spectrum, the site specific ground motions are obtained. The site specific ground motions must then be analysed through a seismic site response analysis (SSRA) to assess the depth-varying ground motions and behaviour of the soil layers during the earthquake. The depth-varying ground motions are used in a numerical model of the wind turbine foundation in order to assess the seismic effects. Several numerical models with increasing complexity will be analysed in a non-linear time history analysis to assess the seismic effects and the structural responses will be compared and discussed.

In this chapter are the wind farm site, geotechnical conditions and foundation structure presented the aim, procedure and results of the probabilistic seismic hazard analysis are presented.

4.1 Wind Farm Site

The chosen site is located near the south coast of Japan where a wind farm is in the early planning stage according to [4C-Offshore, 2022] as shown at figure 4.1.

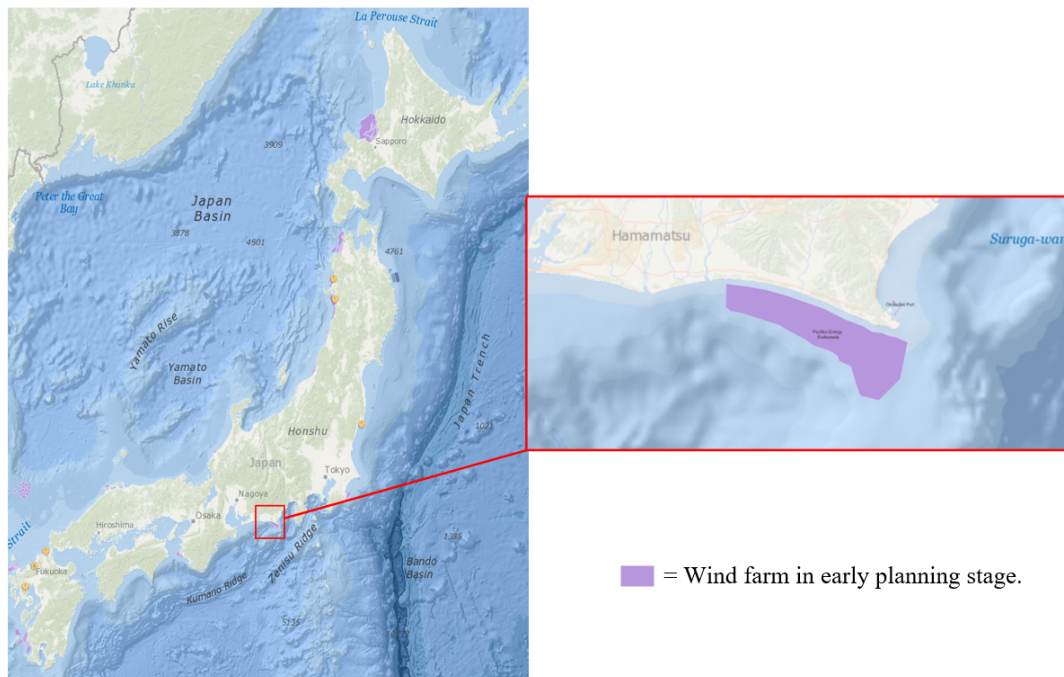


Figure 4.1: Site location in Japan, [4C-Offshore, 2022].

For the wind farm the following informations are given:

- Wind farm capacity = 650 MW
- Minimum 54 number of turbines
- Foundation type = grounded: not specified
- Distance from shore = 1 km
- Water depth = 15-50 m.

The wind turbines at the site are chosen to be a Vestas V164-8.0 MW turbine.

4.2 Geotechnical Conditions

The geotechnical conditions for the site is assessed based on available standard penetration test (SPT) data shown at figure 4.2 from a site with similar characteristics. The geotechnical conditions will be used in a seismic site response analysis to construct the soil layering, soil model as well as shear modulus reduction and damping curves, from which the depth-varying ground motions from the bedrock to the seabed can be determined. The bedrock is the soil layer beneath the site where the average shear wave velocity is 360 m/s or above and is deposits of very dense sand, gravel, very stiff clay or rock, [Kuo et al., 2021].

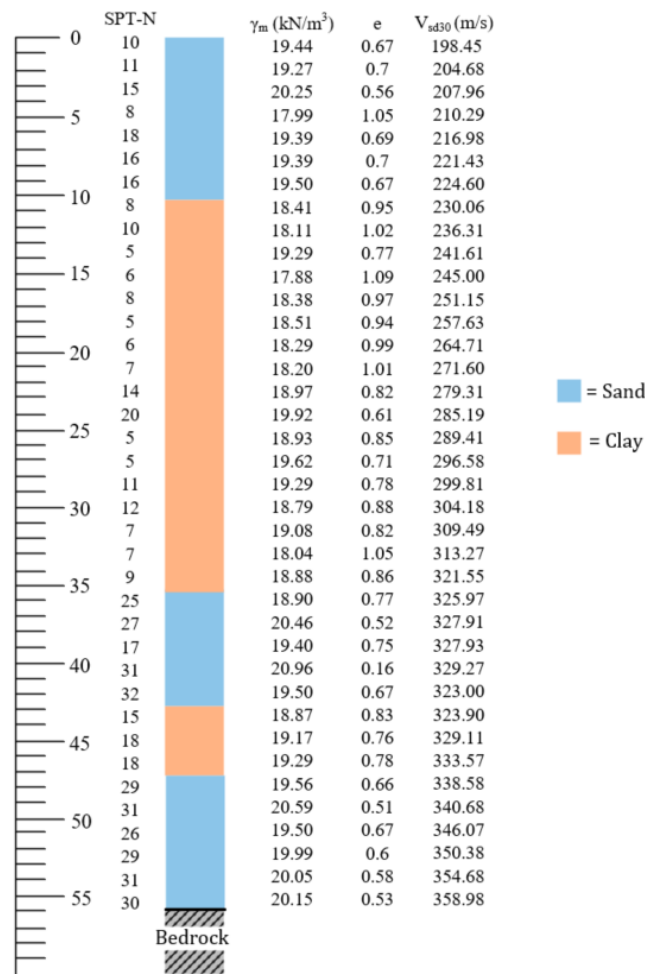


Figure 4.2: Soil data at location of foundation, [Kuo et al., 2021].

where

SPT-N	Number of blows per 0.304 meters
γ_m	Saturated unit weight [kN/m ³]
e	Void ratio [-]
V_{sd30}	Average shear wave velocity in the upper 30 meters [m/s].

The mean soil parameters in each soil layer is obtained based on the SPT and are calculated in appendix H and summarised in table 4.1.

Table 4.1: Soil parameters.

Layer no	Soil type	Depth [m]	Description	γ_m [kN/m ³]	e [-]	V_{sd30} [m/s]	D_r [%]	ϕ' [°]	s_u [kPa]	OCR [-]	PI [%]	LL [%]
1	Sand	0 - 10	Loose	19.32	0.72	212	24.6	34.1	-	-	-	-
2.1	Clay	10 - 20	Medium stiff	18.43	0.96	258	-	-	25.3	3.02	11.1	35.3
2.2		20 - 35.5	Medium stiff	18.91	0.85	281	-	-	39.5	2.24	14.1	39.4
3.1	Sand	35.5 - 40	Medium dense	19.59	0.68	310	51.4	38.0*	-	-	-	-
3.2		40 - 43	Medium dense	20.23	0.42	320	65.1	38.2*	-	-	-	-
4	Clay	43 - 47	Stiff	19.11	0.79	329	-	-	83.3	2.36	25.9	55.7
5	Sand	47 - 55.65	Medium dense	19.94	0.59	348	61.9	38.9*	-	-	-	-
-	Bedrock	55.65 -				>360						

*These values correspond to the peak friction angle ϕ'_p

4.3 Jacket Substructure

There is a water depth of 50 m at the site and therefore a traditional four legged jacket substructure with Z-bracings is investigated as the ground based wind turbine foundation in this project with structural members and specifications as shown in figure 4.3 and table 4.2.

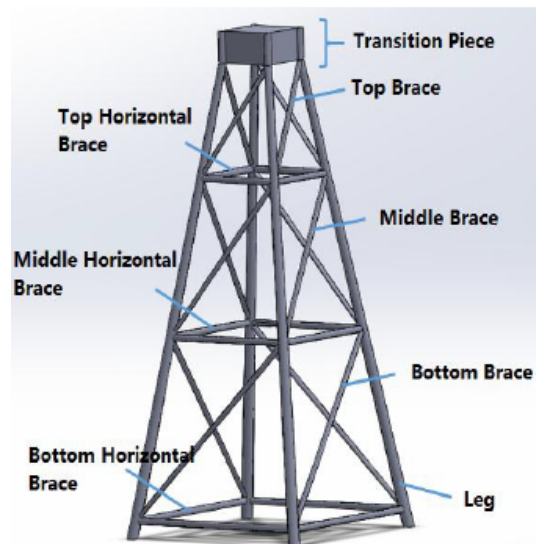


Figure 4.3: Structural members in a jacket substructure, [Chen et al., 2016].

Table 4.2: Jacket substructure specifications.

Total height	66.00 m
Length of leg	67.97 m
Length of top braze	20.07 m
Length of middle brace	28.94 m
Length of bottom brace	37.18 m
Length of top horizontal brace	14.58 m
Length of middle horizontal brace	22.24 m
Length of bottom horizontal brace	31.13 m
Thickness of brace	0.03 m
Thickness of leg	0.04 m
Diameter of brace	0.90 m
Diameter of leg	1.80 m

According to [DNV-RP-0585, 2021] a site-specific seismic hazard analysis should be performed as the site is located in an area with high seismicity. The reason being that for areas with high seismicity structures have a high likelihood of being exposed to destructive earthquakes therefore site-specific characteristics ought to be chosen based on local site conditions as opposed to generalized regional maps to determine the design earthquake. The first thing to do is to assess the seismicity based on the exposure level and site seismic zone from regional maps in [ISO 19901-2, 2017]. For the site and structure the following site seismic zone and exposure level are acquired:

- Seismic zone is 4 due to the 1.0 s horizontal spectral acceleration, $S_{a,map}(1.0)$ from regional maps in [ISO 19901-2, 2017] being above $0.45g$ for the site.
- Exposure level is L2 due to a wind turbine being categorized as unmanned structure, which are only manned at the minimum amount of time possible, but there are societal losses and possibility of significant economic losses.

The level of seismicity are determined from the seismic risk category, SRC. The table used for determination of seismic risk category are shown on table 4.3.

Table 4.3: Seismic risk category, SRC, [ISO 19901-2, 2017].

Site seismic zone	Exposure level		
	L1	L2	L3
0	SRC 1	SRC 1	SRC 1
1	SRC 3	SRC 2	SRC 2
2	SRC 4	SRC 2	SRC 2
3	SRC 4	SRC 3	SRC 2
4	SRC 4	SRC 4	SRC 3

<i>SRC1</i>	Very low seismicity
<i>SRC2</i>	Low seismicity
<i>SRC3</i>	Moderate seismicity
<i>SRC4</i>	High seismicity.

From table 4.3 it can be concluded that the seismic risk category is 4 and hereby high seismicity. Therefore, the site has to be investigated through a time domain analysis based on the target earthquake obtained from PSHA according to DNV-RP-0585 [2021].

4.4 Probabilistic Seismic Hazard Analysis

PSHA is a method to determine the site-specific seismic hazards and is the preferred method for evaluating the hazards on an offshore wind turbine, [DNV-RP-0585, 2021]. PSHA incorporates seismic source and ground motion uncertainties, which also makes it more realistic than a deterministic method, which is described in detail in appendix F.

The purpose of the PSHA is to obtain a site-specific target/design earthquake in terms of magnitude and source-to-site distance, and a target response spectrum. The site-specific design response spectrum is the response spectrum at the bedrock beneath the site, which accounts for the wave propagation from the source fault to the bedrock. The target magnitude and target source-to-site distance are used to select an accelerogram from an earlier earthquake with similar magnitude and source-to-site distance. Figure 4.4 shows the procedure of PSHA where uncertainties such as earthquake size (magnitude), earthquake location (source-to-site distance) and uncertainties regarding the ground motions at the site are input parameters and a target earthquake (site-specific response spectrum, target magnitude and target distance) are the output parameters.

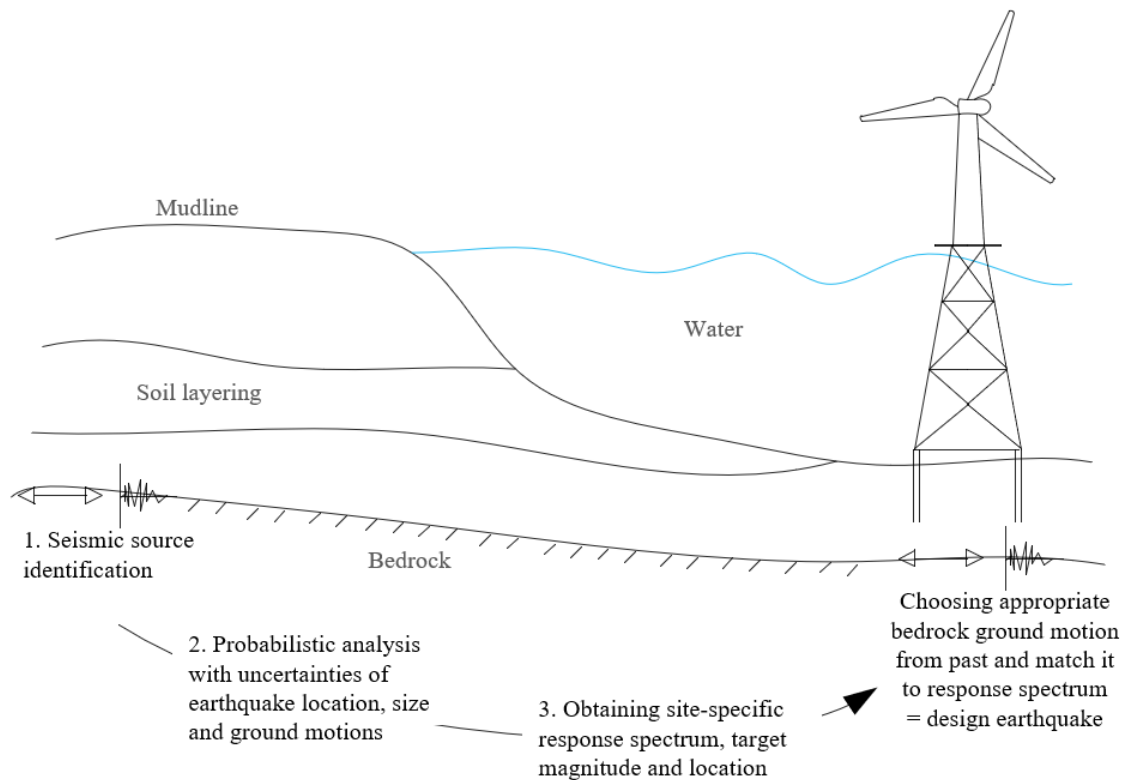


Figure 4.4: Procedure of the PSHA.

The first thing in a PSHA is to identify the earthquake sources that are capable of producing strong ground motions at the site. Afterwards, the procedure steps listed below are followed.

- Step 1: Uncertainty of earthquake location
- Step 2: Uncertainty of earthquake size
- Step 3: Uncertainty of the intensity of the ground motions at the site
- Step 4: Combining all uncertainties.

4.4.1 Identifying Earthquake Sources

Identifying the earthquake sources capable of producing damaging ground motions is the most complicated and troubling part of the PSHA. Normally, a geophysicist will develop a source fault map for the site and surrounding area which are the basis for future PSHA. In this project a source fault map is developed based on the IRIS Earthquake Browser [IRIS, 2021] which is an online database of 5.8 million recorded earthquakes. The recorded earthquakes within a coverage radius of 200 km from the center of the site and a magnitude range between 4 and 9 are collected in the PSHA, which is shown at figure 4.5.

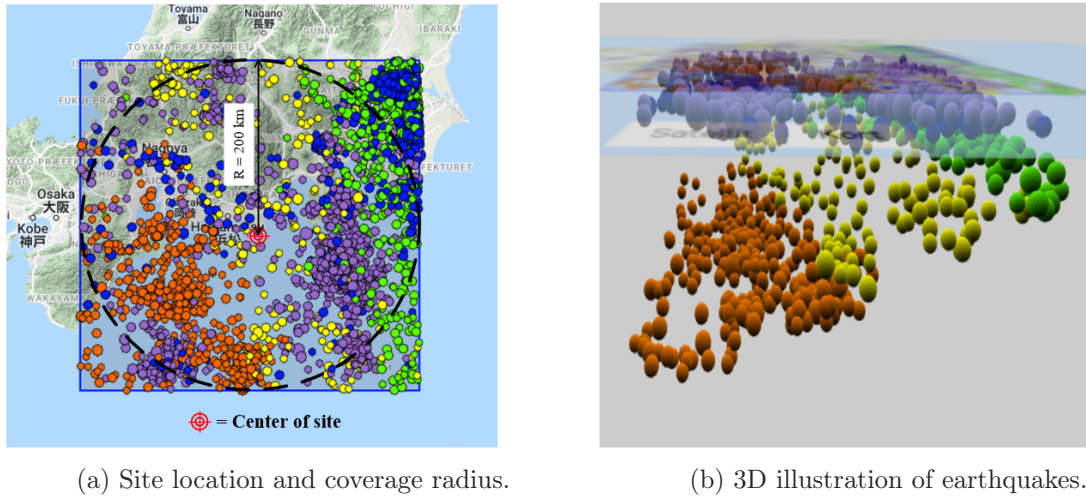


Figure 4.5: Earthquakes from IRIS Earthquake Browser. The colors indicate different depths of the earthquakes [IRIS, 2021].

The earthquake epicenters with blue and purple dots stem from crustal events and the green, yellow and orange dots stem from deep events. The earthquake sources are identified as either a line source or an area source. Two area sources and two line sources have been modelled in a source fault map as shown in figure 4.6. The area sources are characterized by a high concentration of crustal events and the line sources are characterized by earthquakes located more or less on a line.

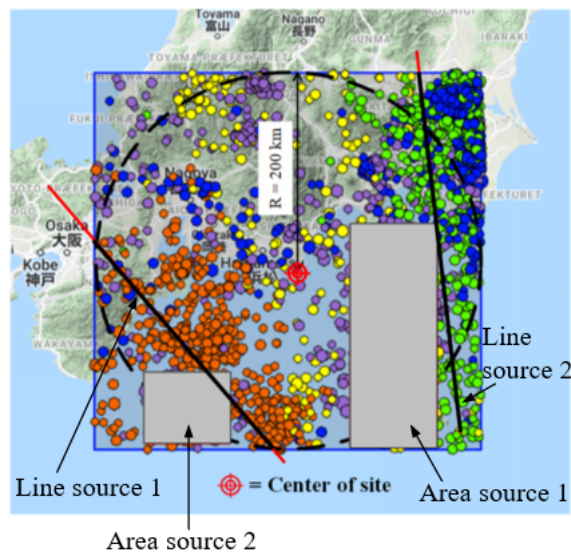


Figure 4.6: Earthquake sources - area and line sources.

When the source fault map has been composed and the information about occurrence of earthquakes and distances for each source has been achieved the uncertainty modelling of magnitude, distance and intensity of the ground motions can be determined and used to compose the total probability for annual rate of exceedance to achieve a site-specific peak ground acceleration and design response spectrum.

4.4.2 Uncertainty of Earthquake Location

To account for the earthquake location uncertainty, a probability function for an earthquake occurring on each source is determined based on the assumption that there is a uniform likelihood that the earthquake will happen in every possible location at the source. This is a valid assumption since earthquakes are known to occur located somewhere at the sources from the database, but exactly where is uncertain. At figure 4.7 the cumulative distribution function for each source in the area around the site are shown.

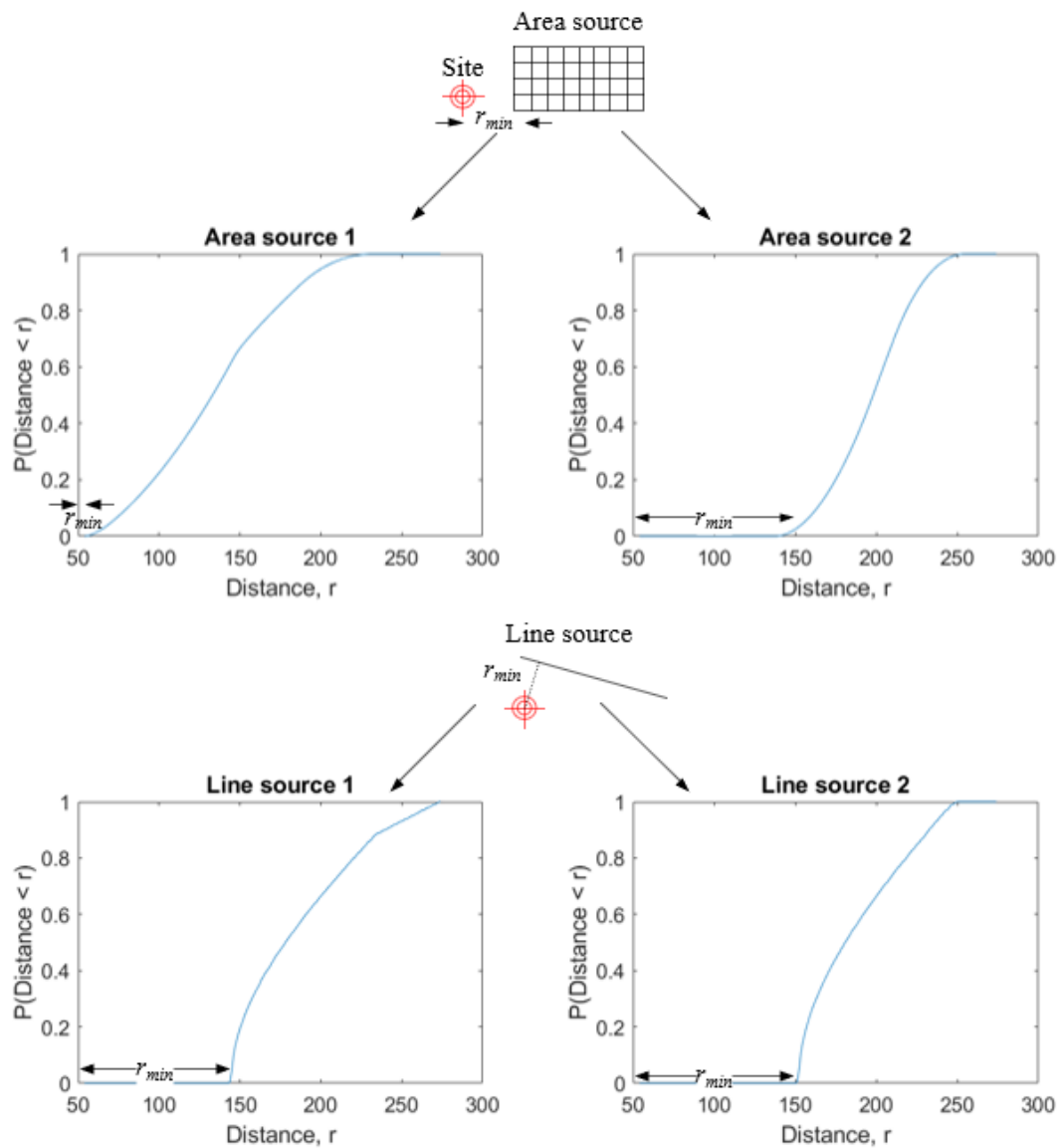


Figure 4.7: Distribution of source-to-site distances.

4.4.3 Uncertainty of Earthquake Size

The probability function for the annual rate of exceeding a given magnitude is found. It is assumed that recurrence law obtained from past earthquakes is appropriate for prediction of future earthquakes and the bounded Gutenberg-Richter Recurrence Laws are used which state that there is a linear relationship between the logarithm to the annual rate of exceedance and the earthquake magnitude. The recurrence law is taking into account that sources are only capable of producing up to a given magnitude which can be found from the earthquake history at the sources. This is a reliable way to model the earthquake magnitude uncertainties, since it considers historical data, known relationship between magnitude and annual rate of exceedance and also takes the physical capability of the faults into account. At figure 4.8 the annual rate of exceedance for each source is shown.

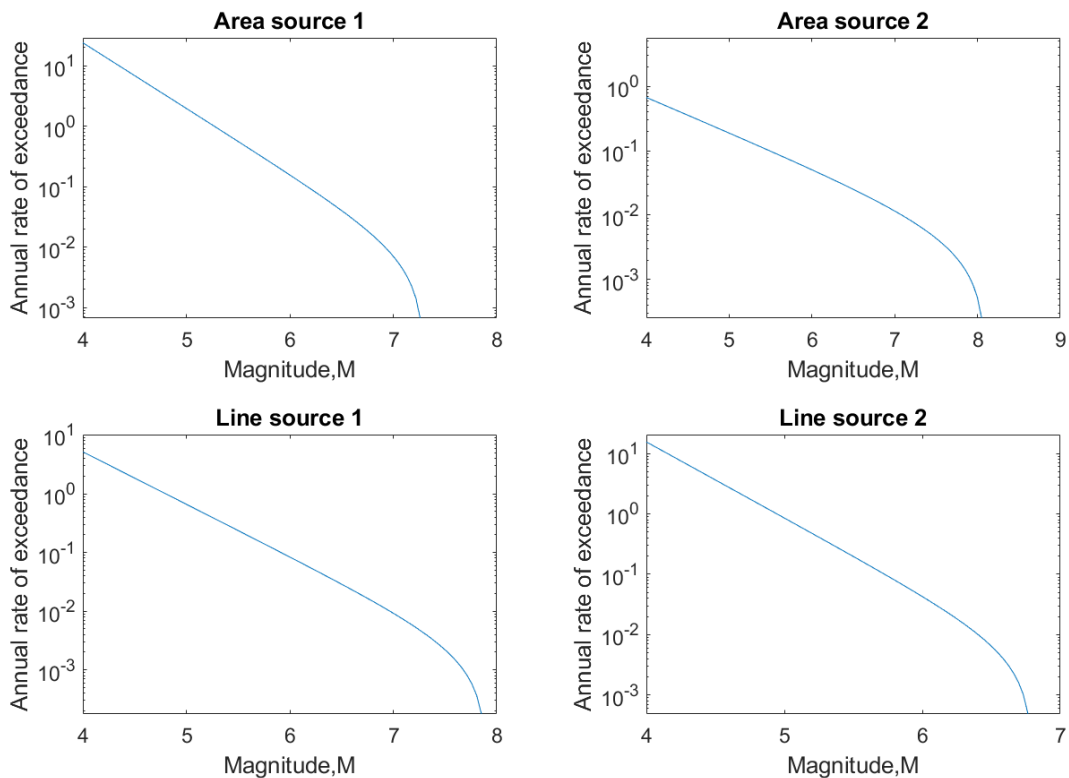


Figure 4.8: Distribution of earthquake magnitudes with a bounded upper limit which states the maximum magnitude that the source is capable of producing.

4.4.4 Uncertainty of Ground Motion Intensity

To consider the uncertainty of the intensity of ground motions at the site an attenuation relationship, also known as ground motion prediction equations (GMPE), are used. The attenuation relationship predict the ground motions at the site based on magnitude of earthquake, source-to-site distance, spreading of seismic waves, the area over fault rupture, soil damping and source or site characteristics. There have been developed a lot of attenuation relationships which varies in complexity to model the intensity of ground motions. The GMPE's by [Si and Midorikawa, 1999] used in this project is shown in appendix F is the same as used for national Japanese hazard maps. The GMPE's account for magnitude of earthquake, source-to-site distance, spreading of seismic waves, the area over which fault rupture and soil damping. It is a

good model for this project as it requires the magnitude, source-to-site distance and regression coefficients obtained from fitting to historical earthquake data. It is possible to use the chosen GMPE's with limited knowledge of the fault size and earthquake source. At figure 4.9 the GMPE for different magnitude of shallow earthquakes are shown. It can be seen that the peak ground acceleration (PGA) attenuates with source-to-site distance.

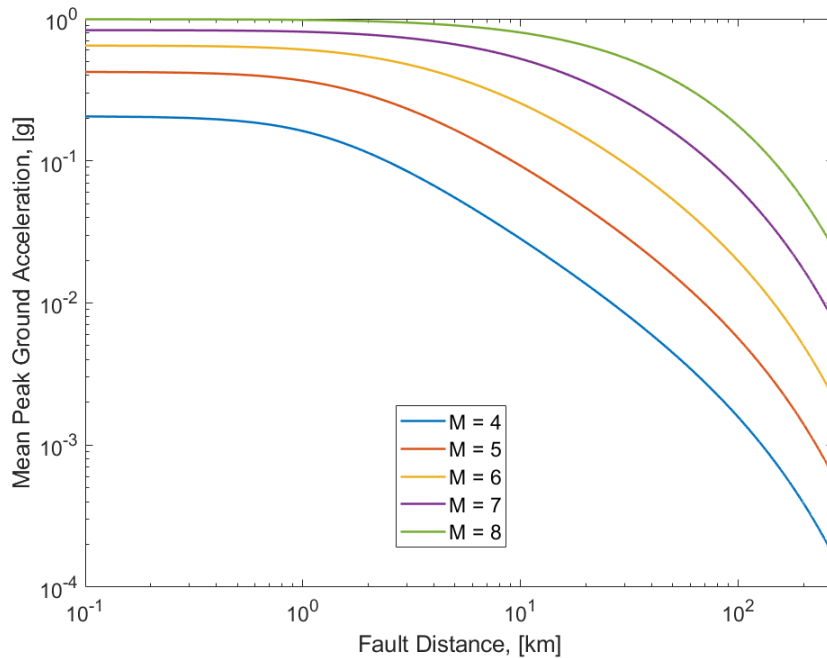


Figure 4.9: Distribution of peak ground acceleration (PGA) as a function of source-to-site distance.

From the GMPE there have been obtained errors between predicted and observed values which gives a standard deviation. For each magnitude and source-to-site distance there can be made a normal probability density function, which can be used to obtain the probability of exceedance for the chosen PGA.

4.4.5 Combining All Uncertainties

It is of interest to obtain the mean PGA for a wide range of earthquakes so that all uncertainties (location, size and intensity of ground motions) are accounted for. The total probability theorem can be used by combining all the uncertainties to obtain the mean annual rate of exceedance for a chosen PGA. This is done by summing up the mean annual rate of exceeding the minimum earthquake magnitude, ν , multiplied by the summation of various magnitudes and distances of the probability of exceeding a chosen PGA given a magnitude and distance combined with the probability of occurrence for that magnitude and distance. This is shown in equation (4.1).

$$\lambda_{y^*} = \sum_{i=1}^{N_s} \nu_i \sum_{j=1}^{N_m} \sum_{k=1}^{N_r} P[Y > y^* | m_j, r_k] P[M = m_j] P[R = r_k] \quad (4.1)$$

where

N_s	Number of different earthquake sources
λ_{y^*}	Mean annual rate of exceedance
ν_i	Mean annual rate of exceeding the minimum earthquake magnitude
N_m	Number of different earthquake magnitudes
N_r	Number of different source-to-site distances
$P[Y > y^* m_j, r_k]$	Probability of exceeding PGA given a magnitude and distance
$P[M = m_j]$	Probability of occurrence for magnitude
$P[R = r_k]$	Probability of occurrence for distance.

4.4.6 Design Peak Ground Acceleration

By performing the above PSHA for PGA's from 0.01 g to 1 g and obtaining the mean annual rate of exceedance, λ_{y^*} for each PGA a seismic hazard curve can be constructed. By picking a mean annual rate of exceedance of $\lambda_m = 0.0021$ corresponding to a return period of 475 years, which is the return period that is used for the design earthquake, the target/design PGA can be obtained as shown at figure 4.10 to $PGA_t = 0.7g$.

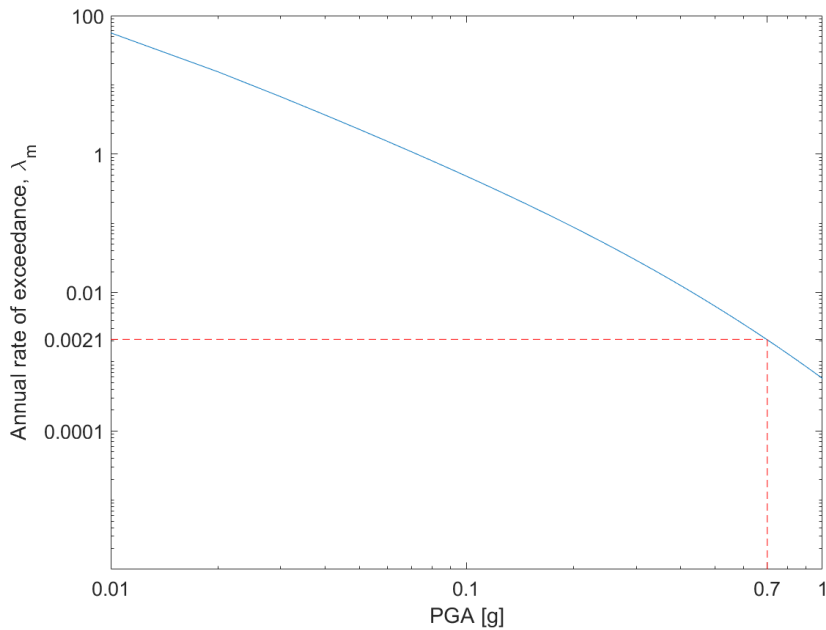


Figure 4.10: Design peak ground acceleration from hazard curve.

The site specific design PGA is used to describe the seismicity at the site and to make a de-aggregation analysis in order to obtain the seismic hazard contribution.

4.4.7 De-aggregation

Previously design earthquakes intensity also known as the PGA has been determined, the earthquakes size and location that contributes most to seismic hazard should be found. According to [DNV-RP-0585, 2021] the earthquake event that contributes the most to the seismic hazard at the site shall be found by de-aggregating the data down to individual earthquake events. This is important as an existing ground motion accelerogram with a relevant magnitude (± 0.5 of target magnitude) and similar site-to-source distance shall be selected to design the wind turbine foundation. The de-aggregation analysis for the site is shown at figure 4.11.

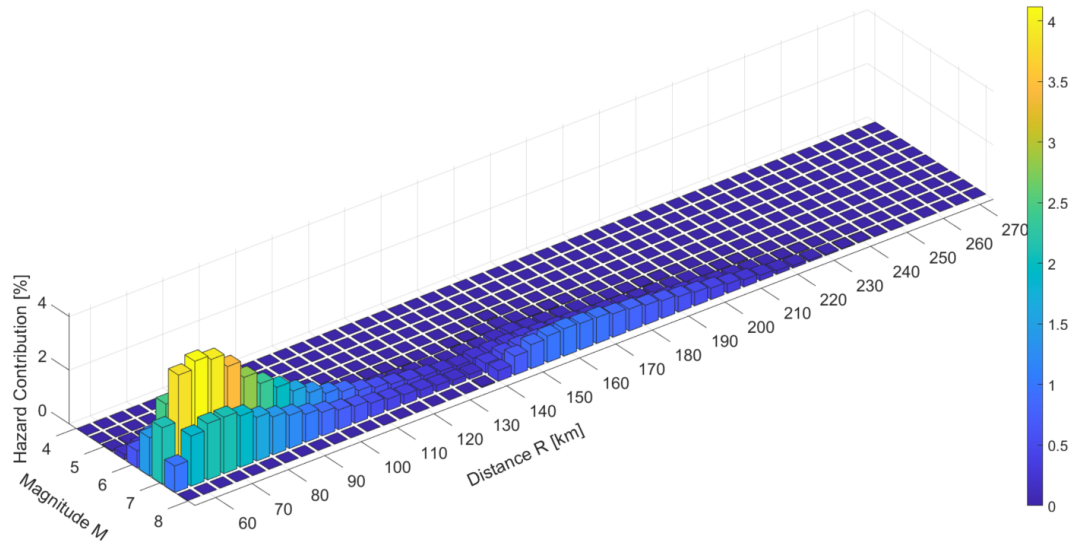


Figure 4.11: Site-specific de-aggregation for $\text{PGA} = 0.7 \text{ g}$.

From the de-aggregation the magnitude and distance where the hazard contribution is highest can be obtained and the target magnitude and distance are determined and shown in the following table.

Table 4.4: Result for de-aggregation of target magnitude and target source-to-site distance-

M_t	7.0
R_t	64 km

The results of the de-aggregation are used to select an earthquake accelerogram from the past with similar magnitude and source-to-site distance.

4.4.8 Site Specific Design Response Spectrum

The hazard curve used to determine the design PGA is based on ground motion prediction equations (GMPE's) with regression coefficients corresponding to a period of 0 s, which is the ground motions. In appendix G at figure F.8 regression coefficients for periods from 0.05 s to 5.0 s can be substituted in the GMPE's in the PSHA to achieve a hazard curve and peak ground acceleration at each period. This results in the site specific design response spectrum as shown at figure 4.12.

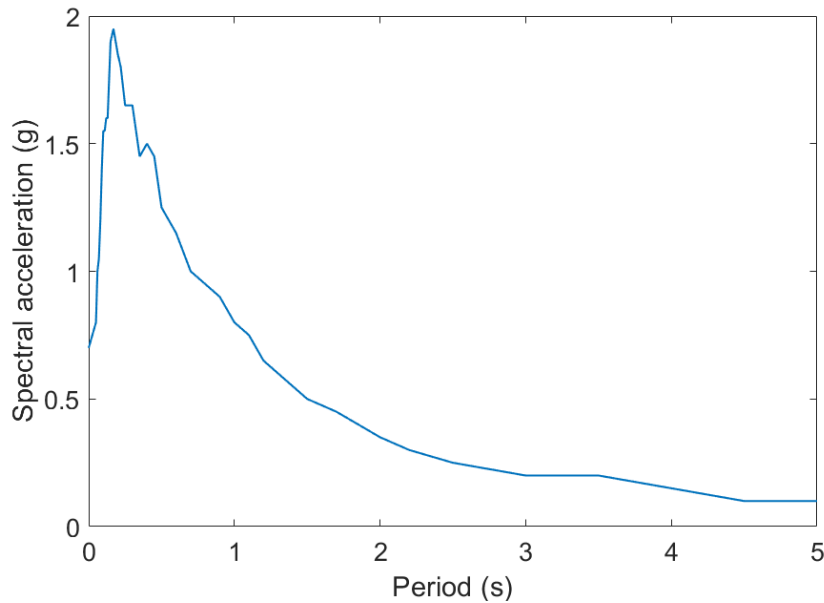


Figure 4.12: Design response spectrum with a 0.0021 annual rate of exceedance = 475 years return period.

The design response spectrum is used when selecting earthquake ground motions that are used for the seismic design. According to [DNV-RP-0585, 2021] earthquake accelerograms are selected to represent the engineering bedrock motion underneath the wind farm site based on the design response spectrum. This means that the design response spectrum will be used as the target spectrum in spectral matching for acquisition of the accelerogram to the time history analysis.

4.5 Summary

Results from the PSHA and de-aggregation are shown in table 4.5. The results are used to define the seismicity at the site and for selection of ground motions.

Table 4.5: Results from PSHA.

PGA_t	0.7 g
M_t	7.0
R_t	64 km

[DNV-RP-0585, 2021] specifies the following for selection of ground motions:

- The chosen earthquake magnitudes should be within ± 0.5 magnitude units of the target magnitude, M_t .
- The distances to the fault should be similar, in particular for near-fault wind farm sites, R_t .
- The ground conditions of the selected earthquake motion records should be broadly similar to those of the wind farm site.
- Near-source effects such as earthquake directivity should be considered if applicable for the wind farm site.
- Other relevant attributes such as non-stationary characteristics, earthquake duration, peak ground acceleration magnitude and spectral content and shape should also be considered.

From the above guidelines, historical earthquake ground motions are selected with a magnitude of $6.5 - 7.5M_w$ and a distance to fault as close to 64 km as possible. The ground conditions of the selected earthquake motion record can not be similar to those of the wind farm site due to the stations being placed onshore and the wind farm is offshore. The direction of the earthquake waves are not considered in the ground motion amplitude since the geometry of the fault and the propagation of the seismic waves cannot be obtained. The spectral content and shape is considered through spectral matching as explained in section 2.6 and appendix C.

At figure 4.13 the location of the selected earthquake and center of the site are shown.



Figure 4.13: Location of selected earthquake and center of wind farm site.

The accelerograms for North-South and East-West directions from a recording station from the database [CESMD, 2022] are selected as the ground motions, which match the guidelines for magnitude and source-to-site distance. Furthermore, the spectral content and shape of the response spectrum are adjusted to match the design response spectrum for the site at figure 4.12. After the spectral matching the modified accelerograms can be obtained for each direction, these are shown at figure 4.14 and are the input bedrock ground motions for the Site Seismic Response Analysis (SSRA) in chapter 5.

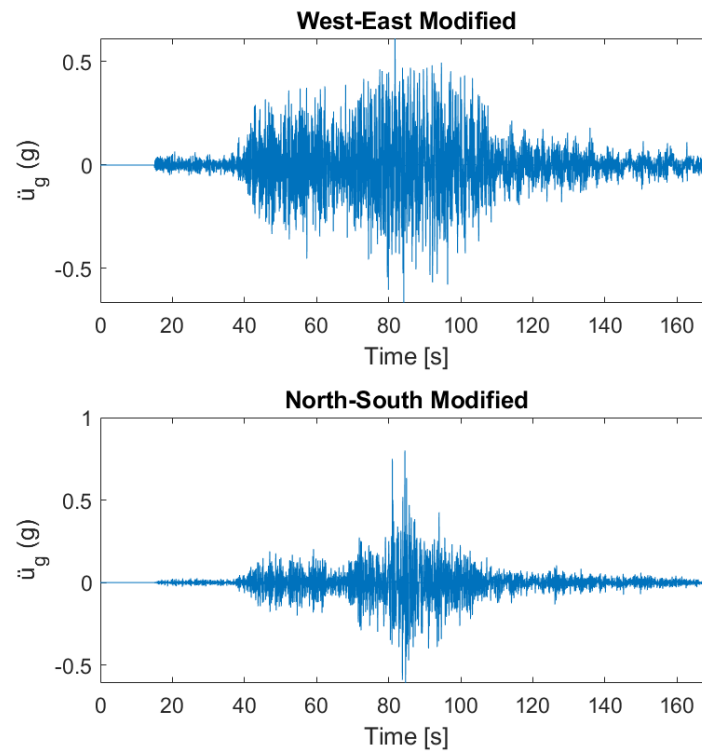


Figure 4.14: Input bedrock ground motions for SSRA.

5 | Site Seismic Response Analysis

The aim of this chapter is to obtain depth-varying ground motions and ground response such as stresses and strains in the soil and change in stiffness properties of the soil during the design earthquake.

In the previous chapter the design earthquake has been obtained at bedrock and now the bedrock ground motions are used in a site seismic response analysis (SSRA) to predict the depth-varying free-field ground motions at the site as shown in figure 5.1. The ground response is for a free-field soil column and the soil-pile interaction is not considered in a SSRA. The depth-varying ground motions are important to know when the wind turbine foundation is analyzed later in a numerical model in chapter 7.

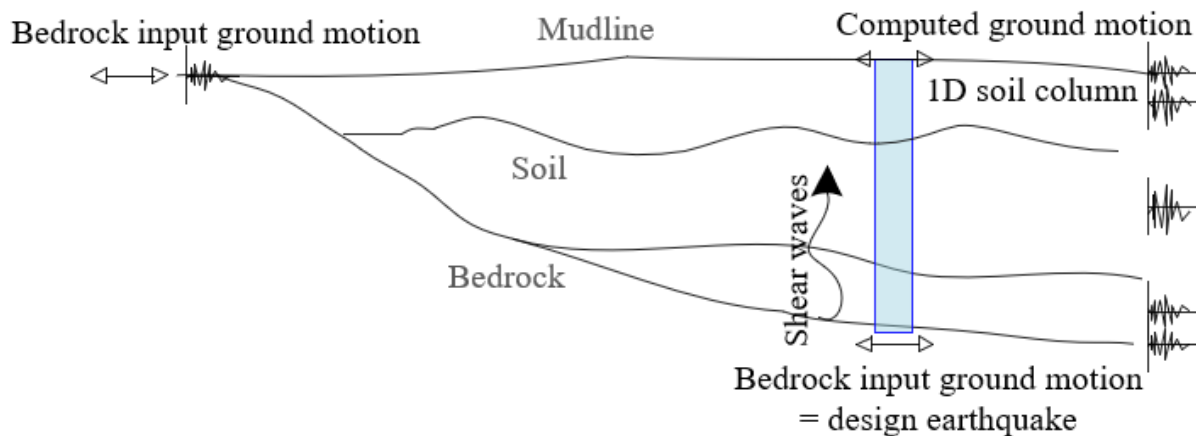


Figure 5.1: Graphical illustration of 1D SSRA.

The SSRA gives site specific ground motions compared to the response spectrum as described in section 2.5. The main differences between obtaining the ground motions in the response spectrum method and the SSRA are listed below.

Response spectrum:

- Gives maximum spectral acceleration at ground surface or in structure for chosen natural period
- The seismic hazard is based on a reference value of PGA from a seismic hazard map
- The soil characteristics are approximated roughly through a chosen soil type, e.g. rock, dense/loose sand, stiff/soft clay.

SSRA:

- Gives depth-varying ground accelerations and ground response as a time history
- Seismic hazard is site specific through the PSHA where a design earthquake time history is found
- The soil characteristics are taken into account in the SSRA in soil constitutive models obtained by site investigations.

The SSRA can further be used to evaluate stresses and strains in the soil layers and evaluate whether or not soil layers tend to liquefy and what the liquefaction hazards might be. The SSRA will in the following be described and the results are presented in the end of the chapter.

Throughout this project a 1D SSRA is utilised to obtain ground response. This may be used if 2D or 3D effects are not significant at the site meaning little to no bedrock slope, mostly homogeneous soil layers, little to no sloping of soil layers, no presence of hills, cliffs, ridges and or basin edges near the vicinity of the site and no interaction with other embedded structures, [DNV-RP-0585, 2021]. When these conditions are fulfilled a 1D-SSRA is sufficient, furthermore it is assumed that all boundaries are horizontal and extend infinitely in the horizontal direction, and that response of the soil is mainly caused by shear waves propagating in the vertical direction, see figure 5.2.

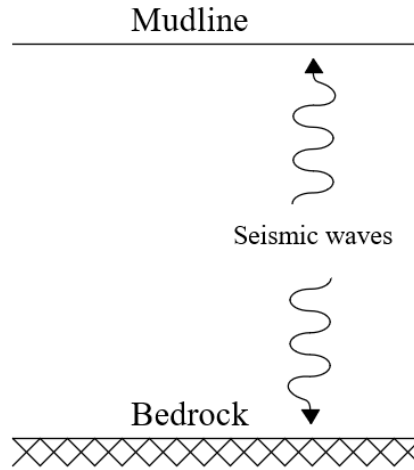


Figure 5.2: Illustration of 1D SSRA seismic wave propagation.

The SSRA is performed in the software program *DeepSoil* which is capable of performing a 1D-SSRA using one of three approaches:

- 1D non-linear time domain analysis with or without excess pore water pressure generation
- 1D equivalent linear frequency domain analysis
- 1D linear time frequency domain analysis.

The approaches listed differ in whether or not a frequency domain solution or a time domain solution is obtained and the solution principle for them is given below respectively and described in detail in appendix G section G.1.

Frequency domain solution

The frequency domain solution procedure is the computationally fastest and simplest procedure compared to the time domain solution procedure. The reason for the frequency domain solution being computationally faster is that bedrock input motion can be directly computed into an ground output motion in whatever depth is wanted, through the use of a transfer function $F(\omega)$. The transfer function is a function obtained based on the analytical solution to the ground response u in the wave equation (5.1), see also appendix G.1.

$$\rho \frac{\partial^2 u}{\partial t^2} = G \frac{\partial^2 u}{\partial z^2} + \eta \frac{\partial^3 u}{\partial z^2 \partial t} \quad (5.1)$$

where

u	Displacement [m]
z	Depth [m]
t	Time [s]
G	Shear modulus [kPa]
ρ	Soil density [kg/m^3]
η	Soil viscosity [-].

The solution to the wave equation gives the ground displacement $u(z,t)$ and is then used to find the transfer function at any given point from $z = H$ to $z = 0$, see figure 5.3.

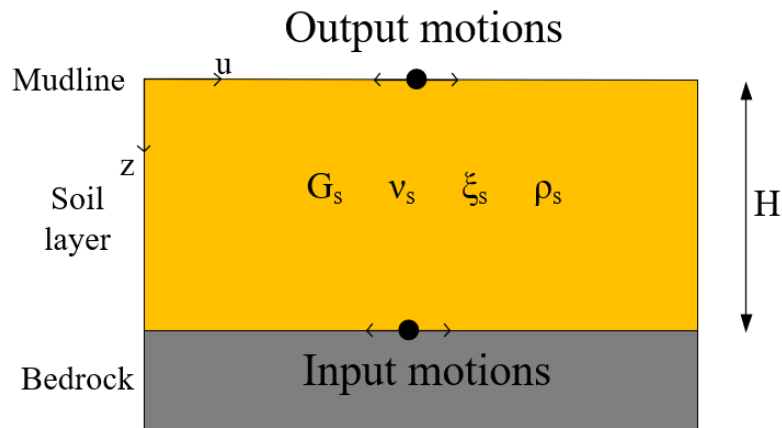


Figure 5.3: Linear elastic soil of thickness H underlain by rigid bedrock.

The transfer function is used to determine the ground response by multiplying the bedrock input motion with the transfer function as shown in figure 5.4. This approach however is only applicable for constant shear modulus G_s , shear wave velocity ν_s , damping ratio ξ_s and density ρ_s . The ground motion is transformed into the frequency domain by Fast Fourier Transform and the solution is then rewritten in the time domain by Inverse Fast Fourier Transform.

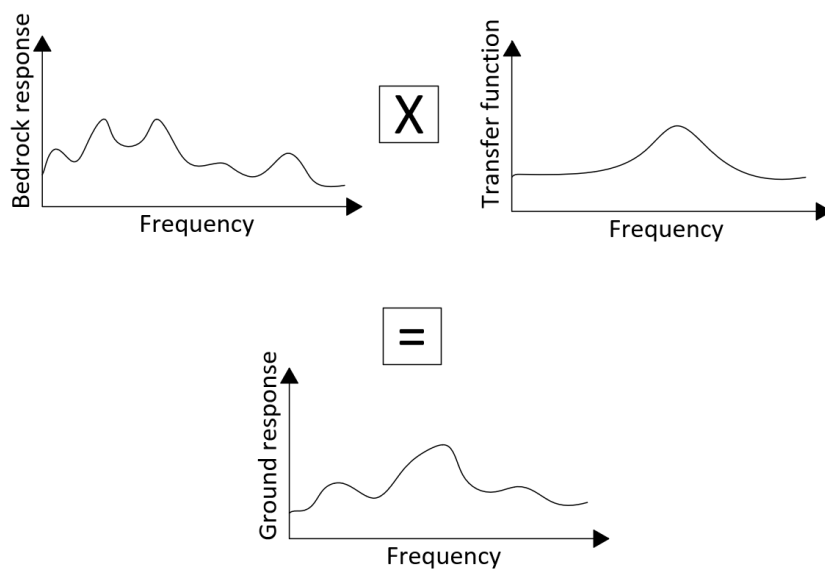


Figure 5.4: Frequency domain approach to obtain ground response by multiplying the input bedrock motion by the transfer function.

Time domain solution

The time domain solution is more complicated than the frequency domain solution method, however what it lacks in computational time it gains in accuracy as this solution method can better account for soil non-linearity. The non-linear response is analyzed using implicit numerical integration to solve the equation of motion as shown in equation (5.2), see also appendix G.1.

$$[\mathbf{M}]\{\ddot{\mathbf{u}}\} + [\mathbf{C}(\mathbf{u})]\{\dot{\mathbf{u}}\} + [\mathbf{K}(\mathbf{u})]\{\mathbf{u}\} = -[\mathbf{M}]\{\mathbf{1}\}\ddot{u}_g \quad (5.2)$$

where

$[\mathbf{M}]$	Mass matrix [kg]
$[\mathbf{C}]$	Damping matrix [Ns/m]
$[\mathbf{K}]$	Stiffness matrix [N/m]
$\{\ddot{\mathbf{u}}\}, \{\dot{\mathbf{u}}\}, \{\mathbf{u}\}$	Vector of nodal acceleration [m/s ²], velocity [m/s] and displacement [m]
$\{\mathbf{1}\}$	Unit vector with ones in nodes where ground motion is applied and in the direction of acceleration [-]
\ddot{u}_g	Input ground motions [m/s ²].

This solution method takes into account the change in soil parameters as a function of shear strain at every time step and has the capability of incorporating generation and dissipation of excess porewater pressure and furthermore it does not require transforming the ground motions into the frequency domain. However, due to its required input parameters as well as computational costs it is only recommended under medium to large strains and/or critical development of excess porewater pressure, and it is always recommended to run an equivalent linear analysis to compare the two.

5.1 Approaches

Among the three approaches, the most commonly used are the equivalent linear frequency domain and non-linear time domain approaches. The linear approach is rarely utilised for a SSRA as it does not account for soil non-linearity in any way, and therefore is only good for very stiff soil with very small ground motions which results in very small strains. The equivalent linear and non-linear approaches account for soil non-linearity in their own ways as shown in figure 5.5.

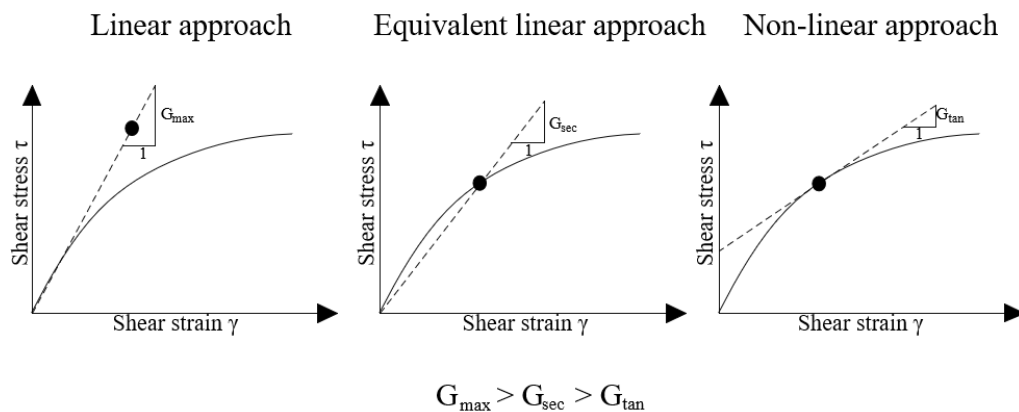


Figure 5.5: Shear modulus utilised for SSRA approaches.

The linear approach uses the initial shear modulus G_{max} and is therefore only applicable for soil undergoing very small shear strains as this stiffness is utilised throughout the entire analysis. The equivalent linear approach accounts for non-linearity in soils through an iterative procedure to obtain the secant shear modulus G_{sec} , this method is alright for small strains, but nevertheless only provides an estimate of the soil stiffness which is utilised throughout the entire analysis. Finally, the non-linear approach utilises the constitutive soil model and takes into account the change in stiffness through the use of the tangent shear modulus G_{tan} , this method is applicable for all strain ranges as it continually takes the change in stiffness into account. The choice of an appropriate SSRA method depends on available information, soil profile, ground motions and the desired accuracy of the results.

5.1.1 Equivalent Linear Approach

The equivalent linear approach is a modification of the linear approach as it only utilises one shear modulus G and one damping ratio ξ for each soil layer throughout the entire analysis. However, the difference between linear and equivalent linear is that the non-linear hysteretic stress-strain behaviour is approximated through equivalent linear soil properties, see appendix G section G.1. It should be remembered that the strain-compatible soil parameters are constant throughout the analysis. The equivalent linear approach utilises the frequency domain solution procedure to compute soil response.

The equivalent linear approach is a fast and simple approach, however it can not be used to represent the changes in soil stiffness over time, furthermore it is only an approximation to the non-linearity of soil and should be used with caution especially for soft soils exposed to large ground motions resulting in large shear strains. This is due to the large change in stiffness when soils are exposed to large shear strains. Moreover the equivalent linear approach does not include the development and dissipation of excess porewater pressure which could cause liquefaction.

In comparison to the non-linear approach the equivalent linear approach requires much less input, as it only requires shear modulus and damping curves as well as soil density ρ which is described in section 5.2. In conclusion the equivalent linear approach should be used in situations dealing with low strain, stiff soils and negligible pore pressures. However in this project both an equivalent linear and non-linear SSRA is run to compare the results of both methods.

5.1.2 Non-linear Approach

The non-linear approach is an approach where the actual non-linearity of soil is considered using direct numerical integration. This method considers the change in soil parameters as a function of shear strain from the constitutive model unlike the equivalent linear method, furthermore it can incorporate development of excess porewater pressure (PWP), through a PWP generation model which is described in section 5.2. However, a PWP generation model requires thorough lab and/or site testing to verify results.

Due to the large requirements and uncertainties when choosing a constitutive soil model and porewater pressure model the non-linear SSRA is run along with an equivalent linear SSRA to compare the output of the two methods. The non-linear SSRA should only be used when dealing with large strain, soft soils, influential pore pressures and when sufficient lab and/or

site testing is available to verify the soil constitutive models and excess porewater pressure generation models.

5.2 Input Parameters

To run the numerical models in the software program *DeepSoil* a sufficient amount of input parameters are required to run the analysis. The amount of parameters required heavily depend on the SSRA approach chosen. Every approach listed may or may not require either of the following listed input parameters:

- Soil profile
- Shear modulus reduction and damping curves
- Constitutive soil model
- Excess pore pressure generation model.

The linear approach requires the least amount of input and non-linear approach requires the most amount of input parameters as shown in table 5.1.

Table 5.1: Required input parameters for the different approaches, (x) input is optional.

	Linear	Equivalent linear	Non-linear
Soil profile	x	x	x
Shear modulus reduction and damping curves	-	x	x
Constitutive soil model	-	-	x
Excess PWP model	-	-	(x)

5.2.1 Soil Profile

The initial input in *DeepSoil* besides the SSRA approach is the soil profile, where soil stratigraphy, layer thickness, shear wave velocity ν_s , density ρ and damping ratio ξ of the soil layers are inserted, see figure 5.6.

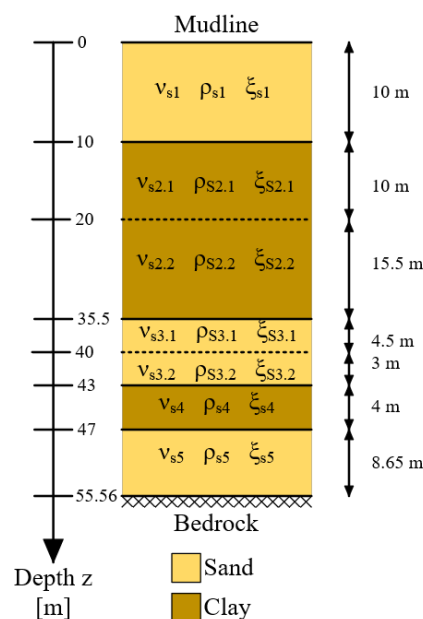


Figure 5.6: Soil profile at the wind farm.

The small-strain shear modulus G_{max} in each soil layer is obtained from the relation between shear wave velocity and density, see equation (5.3).

$$\nu_s = \sqrt{\frac{G}{\rho}} \quad (5.3)$$

For the linear approach shear wave velocity ν_s , damping ratio ξ and shear modulus G input is constant throughout the entire analysis. Within this analysis the water table in *DeepSoil* is defined at the surface of the soil profile/mudline, see figure 5.6. Ignoring the extra confinement pressure from the water table from mudline to sea surface will lead to further development of excess porewater pressure and is assessed to be on the safe side with regard to development of excess porewater pressure.

5.2.2 Shear Modulus Reduction and Damping Curves

When soil is exposed to large strains it will loose its stiffness as shown in figure 5.7 where the shear modulus decreases. On the contrary the damping of the soil increase when the soil is exposed to large strains due to hysteretic damping of the soil during cyclic loading. These relationships are taking into account in equivalent linear and non-linear approach where shear modulus reduction and damping curves, as shown in figure 5.7, are required as input parameters.

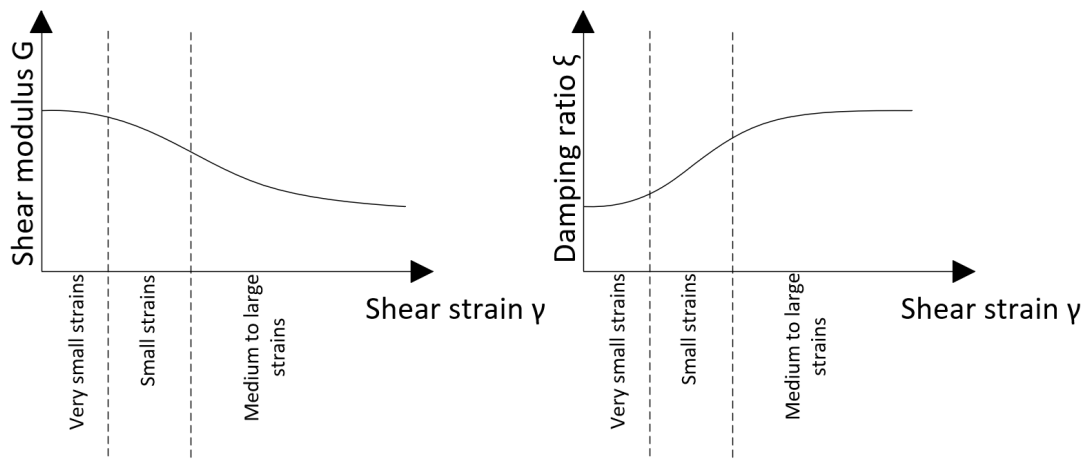


Figure 5.7: Illustration of shear modulus reduction and damping curve.

These curves are usually determined from empirical relationships and within the context of this project the relationship proposed by [Roblee and Chiou, 2004] called the "Geo-Index Model" is used as stated in appendix G in equation (G.24) and (G.25). The relationships are applicable on all soils with the exception of rock, thick gravel deposits, very high plasticity soils ($PI > 50$) and highly overconsolidated soil ($OCR > 4$). The model takes into account the confinement pressure and soil classification as shown in appendix G table G.2.

5.2.3 Constitutive Soil Model

For the non-linear SSRA approach a constitutive soil model has to be chosen. The constitutive soil model establishes the stress-strain relationship for the soil, and within the bounds of this

project the generalized quadratic/hyperbolic (GQ/H) model in G equation (G.33) available in *DeepSoil* are used. The soil model is fitted to the shear modulus reduction and damping curves.

The GQ/H model takes into account a shear strength at failure, τ_{max} , so that shear stress corrections are made at large strains and the development of shear stresses is controlled. The soil model is described further in appendix G.3.

The soil model is used together with the extended Masing rules with soil damping control to capture the loading re-loading behaviour of soil during earthquake motions as shown in figure 5.8 which is further described in appendix G.4.

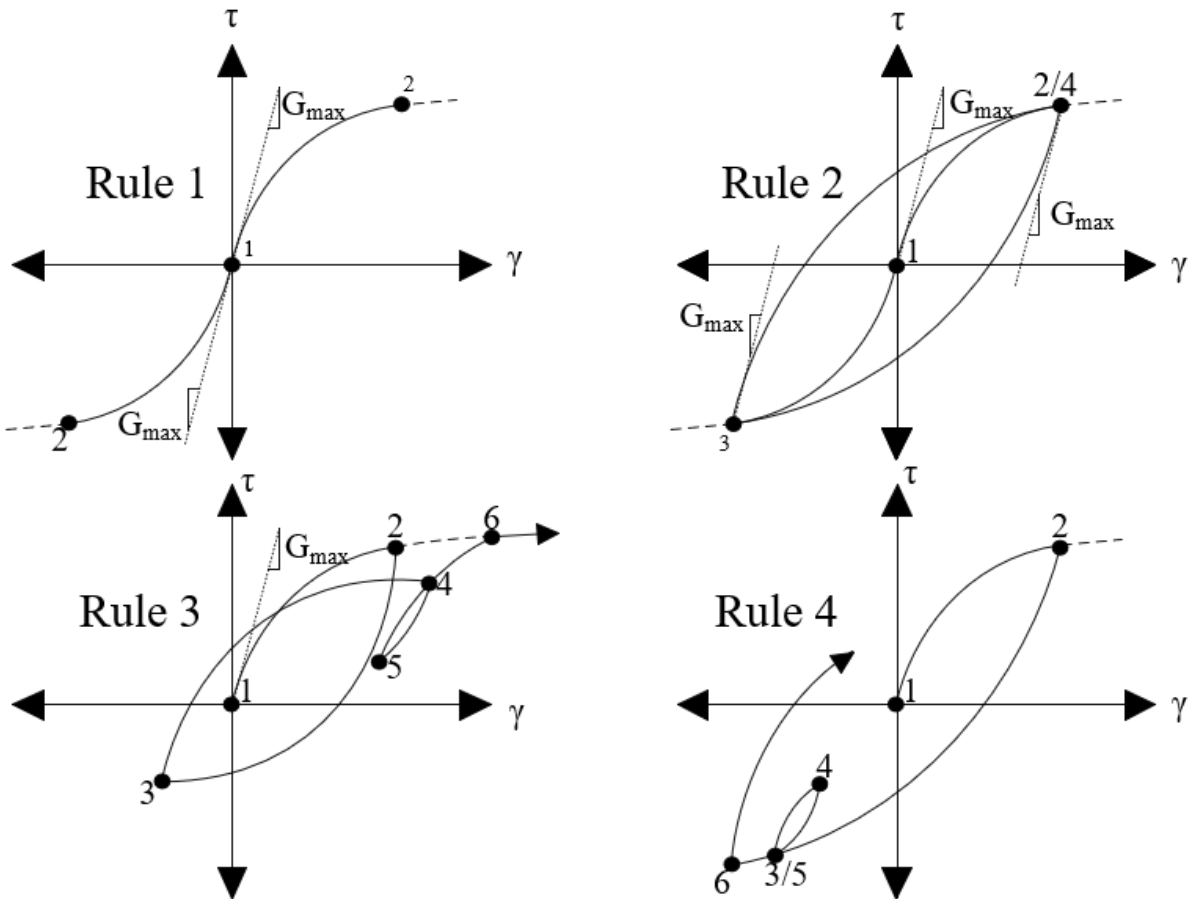


Figure 5.8: Extended Masing rules for loading reloading behaviour of material.

However, at large strains it is known that Masing behaviour produces overestimated hysteretic damping and therefore a non-Masing behaviour can be chosen which controls the soil damping at large strains.

If excess porewater pressure generation and dissipation is considered this affects the shear stress-strain behaviour of the soil and is incorporated into the constitutive soil model through soil stiffness and strength degradation/hardening parameters which is further described in appendix G.3. The larger excess porewater pressure the more stiffness and strength loss which lead to degradation parameters below 1.

5.2.4 Excess Porewater Pressure Generation Model

An optional input for the non-linear SSRA approach is the porewater pressure (PWP) generation model, which is capable of modelling the development of excess porewater pressure. Modelling of excess porewater pressure could be crucial in seismic design as an increase in porewater pressure leads to a decrease in soil strength, and if a critical amount of porewater pressure is developed the soil will liquefy. Development of excess porewater pressure is quantified by the excess pore pressure ratio r_u which is given as:

$$r_u = \frac{u_N^*}{\sigma'_v} \quad (5.4)$$

where u_N^* is the excess pore pressure and σ'_v is the effective vertical stress. When this ratio reaches one the soil has lost all its strength and has reached full liquefaction where the soil fully behaves like a liquid. However within this analysis a maximum allowable excess pore pressure ratio of 0.95 is chosen. Excess pore pressure ratio is calculated from empirical relations and differ whether or not it is a cohesionless or a cohesive soil, shown respectively in equation (G.34) and (G.36) in appendix G.

The PWP generation model is further explained in appendix G.5.

5.3 Numerical Model

As previously mentioned the SSRA is performed in the software program *DeepSoil* which can either utilise a frequency or time domain approach to obtain ground response. Within the time domain approach *DeepSoil* utilises lumped mass model, with seismic wave propagation in the vertical direction whose number of degrees of freedom (DOF) depends on the soil layering as well as the depths where ground response is sought. An illustration of the lumped mass model for a soil profile is illustrated in figure 5.9.

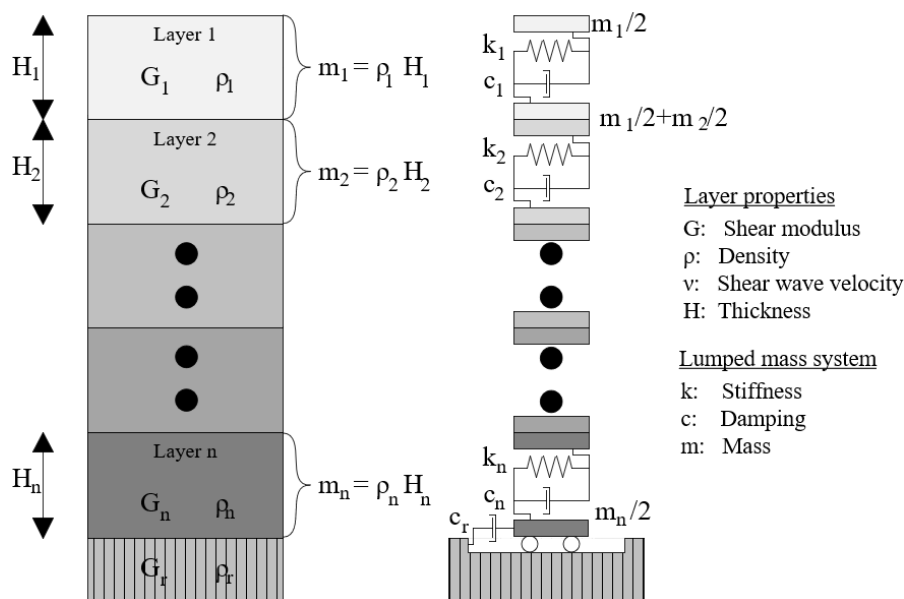


Figure 5.9: Illustration of lumped mass model for a soil profile with stiffness k and viscous damping c .

5.4 Response Comparison of Non-linear Soil Models

Four soil models available in *DeepSoil* are investigated, and the purpose is to examine the characteristics in each model and to get insight to which consequences the model selection has on the soil response. The models used in *DeepSoil* are the hyperbolic/pressure-dependent modified Kondner-Zelasko (MKZ) model and the generalized quadratic/hyperbolic (GQ/H) model with Masing (shear modulus reduction) and non-Masing (shear modulus reduction and controlled soil damping):

1. Modified Kondner-Zelasko with non-Masing-rules (MKZ MRDF)
2. Modified Kondner-Zelasko with Masing-rules (MKZ MR)
3. Generalized Quadratic Hyperbolic with Masing-rules (GQH MR)
4. Generalized Quadratic Hyperbolic with non-Masing-rules (GQH MRDF).

The MKZ model is very well representative of the small-strain behaviour while large strain behaviour often develops over- or underestimated shear stresses which could lead to generating shear stresses that exceeds the soil shear strength and therefore the soil will fail and the shear stresses produced could be incorrect. The GQ/H controls the shear stresses developed in the soil by an input of shear strength.

The response in the middle of each layering is compared between the models. The spectral acceleration (SA) for all soil layers can be seen in figure 5.10 where a comparable result between the four models can be seen as the SA for each model tend to peak at similar periods. Similarity between the models can also be observed at large periods with deamplification of soil SA, meaning that the SA will decrease as the soil gets softer (has a higher period).

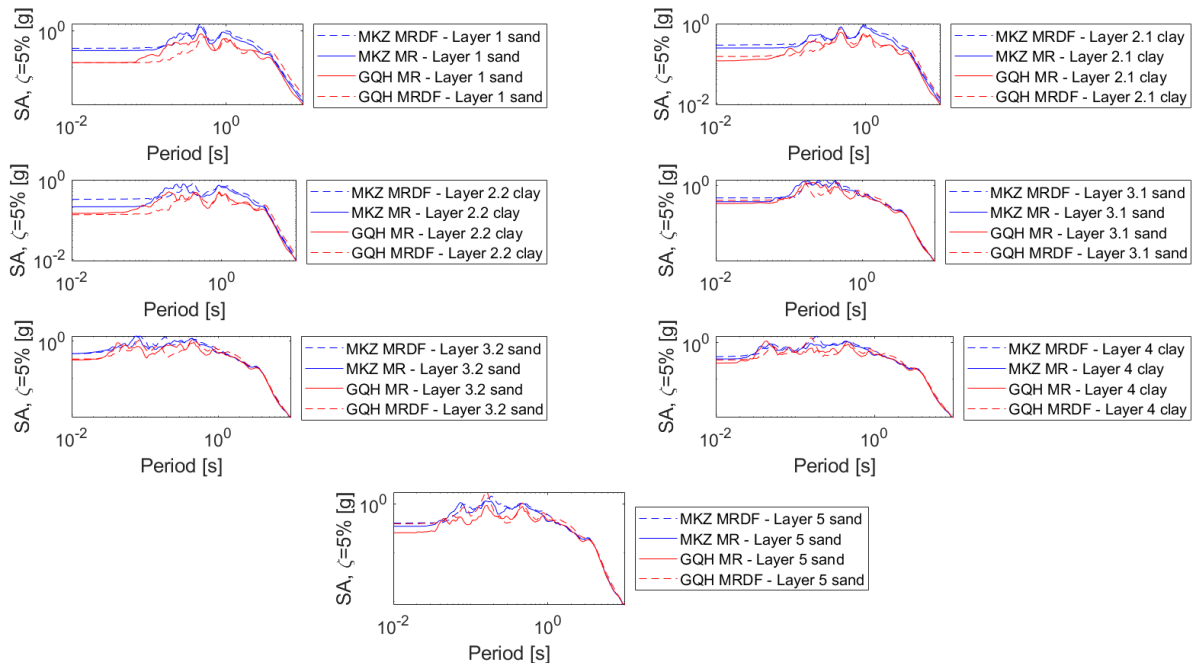


Figure 5.10: Spectral acceleration (SA) for all non-linear soil models for each soil layer.

The depth-varying peak ground acceleration (PGA) and shear strains can be seen in figure 5.11 and 5.12 where the Non-masing behaviour (MRDF) in general gives larger response than the Masing behaviour (MR). This is as expected since MRDF has damping control to match the target damping curve and the hysteretic damping loop is constrained which will lead to a larger response than for MR.

From figure 5.11 it can be seen that the MKZ model in general develops larger PGA's than the GQ/H model. This is because the MKZ model tend to overestimate the shear strength of the soil and models the soil too stiff, and as the ground motions from bedrock can be more directly transferred to soil layers when the soil is modelled stiffer than if the soil is modelled softer this will lead to overestimated PGA's compared to the PGA's estimated in the GQ/H model.

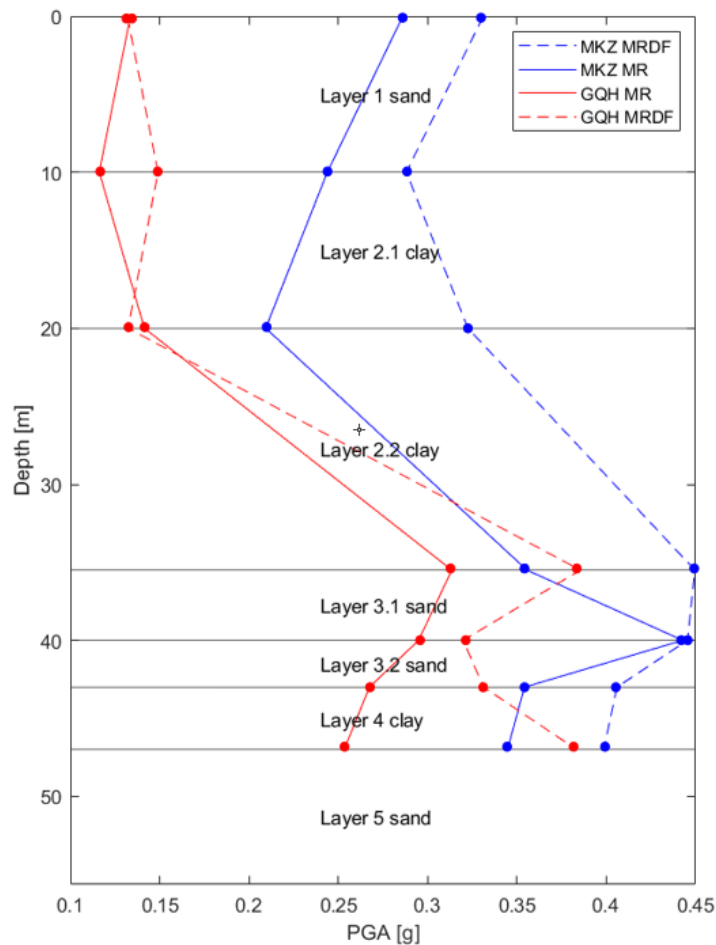


Figure 5.11: Peak ground acceleration (PGA) for all non-linear soil models.

From figure 5.12 it can be seen that larger strains are developed in the GQ/H model compared to the MKZ model. This could be due to a plastic behaviour of the soil in the GQ/H model which is supported in figure 5.13 where the soil has reached plasticity in most depths as the Mohr-Coulomb shear strength for sand and the constant undrained shear strength for clay layers are reached for the GQ/H model. The shear stress in the GQ/H model is bounded by the shear strength which is inputted in the middle of each layer and *DeepSoil* assumes that shear strength increases linearly between each layer's middle. It can be seen that shear stresses in MKZ are exceeding the shear strength at all depths and therefore this model develops unrealistic shear stresses.

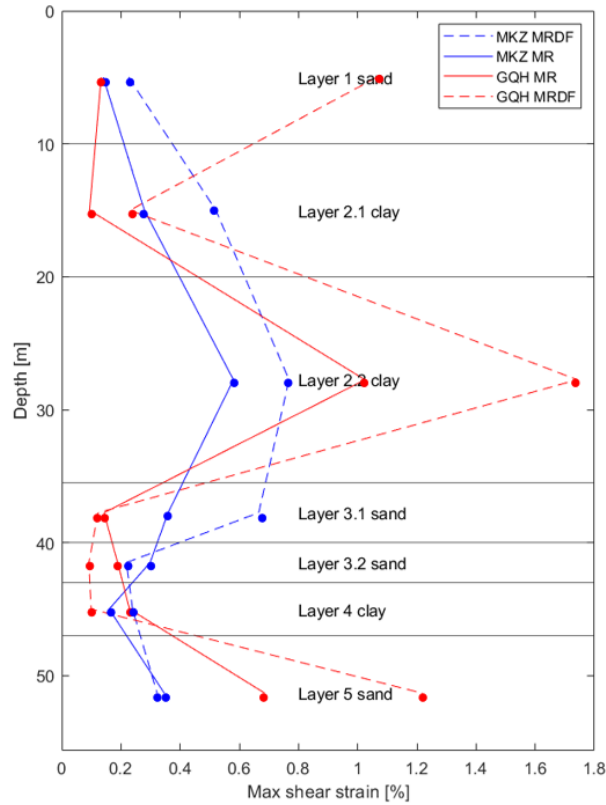


Figure 5.12: Maximum shear strain for all non-linear soil models.

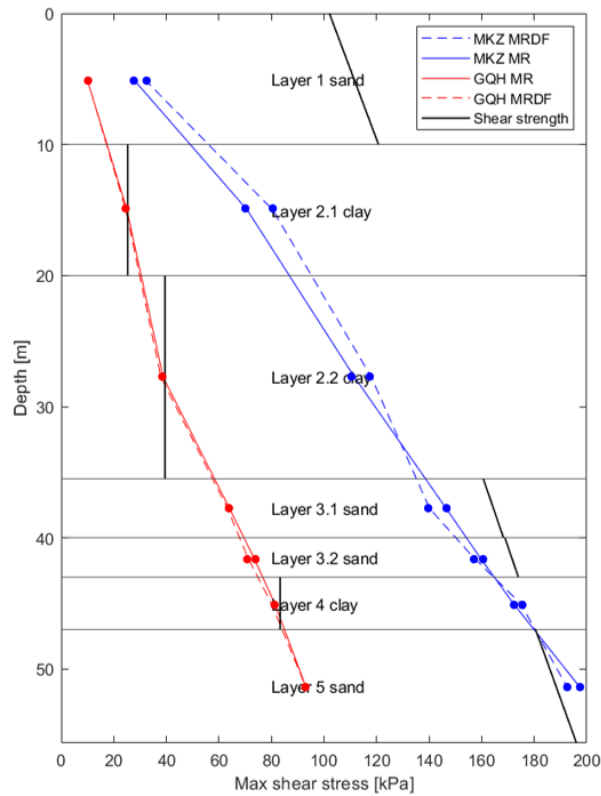


Figure 5.13: Maximum shear stress for all non-linear soil models.

It is concluded from the response comparison that a GQ/H model with shear strength control together with non-Masing with damping control is better suited for the SSRA for the soil profile given at the wind farm site as this leads to more realistic shear stresses.

5.5 Results

Among the equivalent linear and non-linear approach the ground response time history at variable depths are obtained among other ground response parameters such as:

- Maximum acceleration
- Maximum shear strain
- Maximum shear stress ratio $\frac{\tau_{max}}{\sigma'_v}$
- Maximum excess porewater pressure ratio $\frac{u_{max}^*}{\sigma'_v}$

These maximum parameters from each respective time history at variable depths in soil layers are presented in figure 4.2 and input bedrock motions are presented in figure 4.14. The following results are only shown for the design earthquake in the East-West direction (upper part of figure 4.14).

The maximum depth-varying response is shown in figure 5.14. From figure 5.14 a) it can be seen that the ground motions from bedrock are deamplified from soil damping up to the mudline. From figure 5.14 b) it can be seen that the shear strain becomes very large in layer 2.2 clay and layer 5 sand which is correlated to high PWP ratios. From figure 5.14 c) it can be seen that the shear stress estimated by equivalent linear is larger which is explained as the soil is modelled stiffer in the equivalent model due to a larger shear modulus ($G_{sec} > G_{tan}$ figure 5.5) than in the non-linear model. This is generally correlated to the larger strains in the equivalent linear except in those layers with very high porewater pressure ratios which is correlated to larger strains in the non-linear approach.

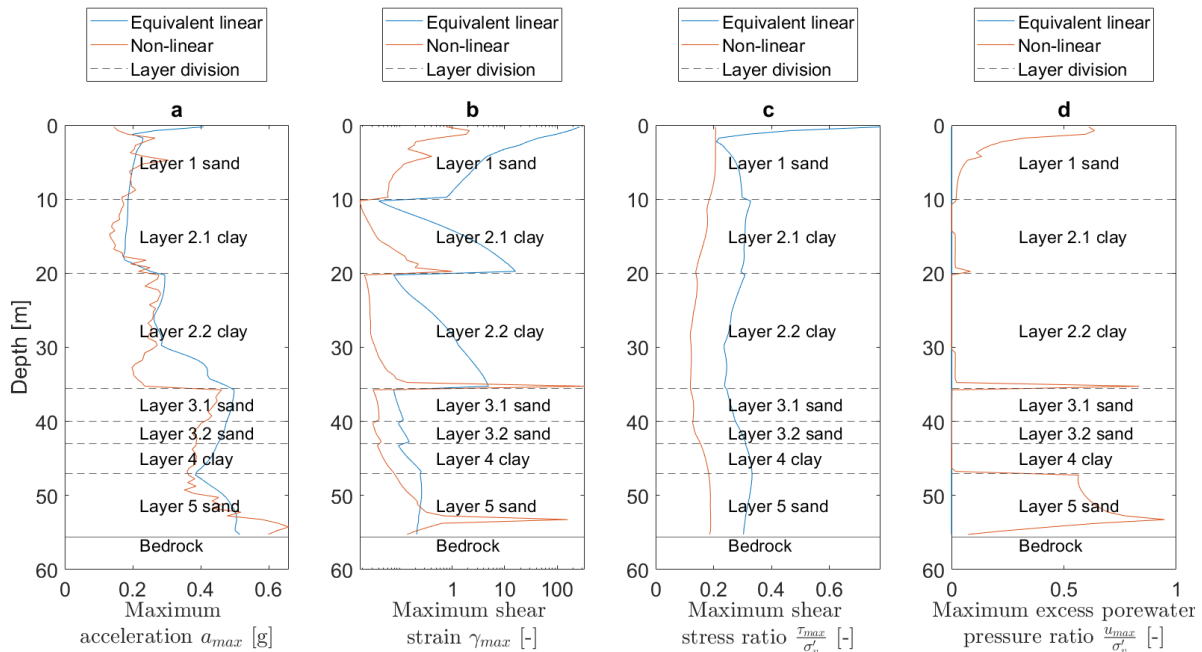


Figure 5.14: Depth-varying maximum response; ground acceleration, shear strain, shear stress ratio and PWP ratio for earthquake in East-West direction.

The minimum depth-varying soil stiffness and strength degradation parameters are shown in figure 5.15 and are obtained through equation (G.31) and (G.32). They are highly correlated to the generation of excess porewater pressure ratio as presented in figure 5.14 d). Where large

excess porewater pressure is generated the degradation parameters decrease as the porewater pressure softens the soil.

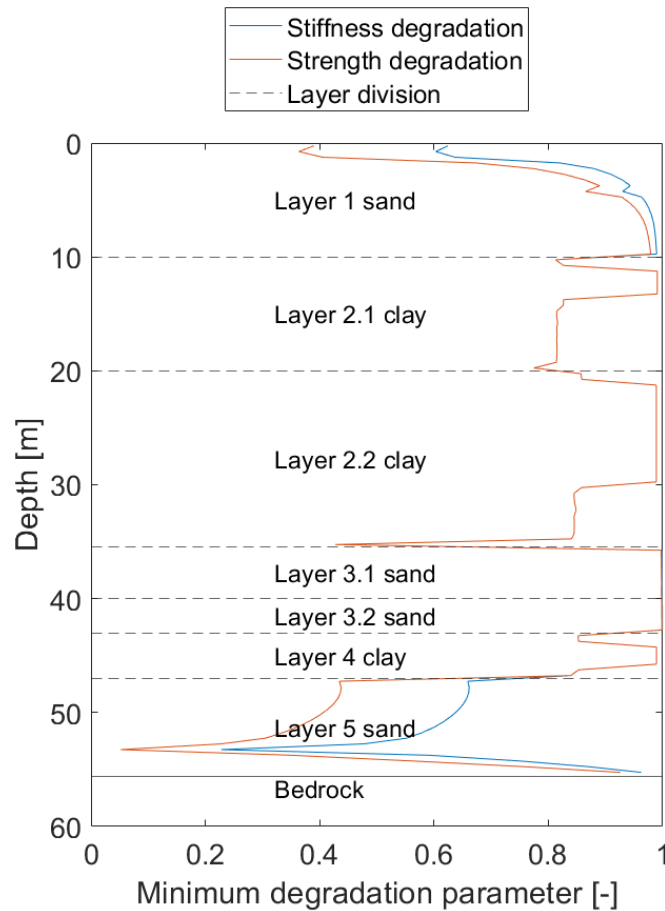


Figure 5.15: Minimum depth-varying soil stiffness and strength degradation for earthquake in East-West direction.

5.6 Summary

The ground response that will be used in chapter 7 to investigate the structural response of the wind turbine foundation in the numerical model include the depth-varying acceleration time histories and minimum depth-varying soil stiffness and strength degradation parameters from figure 5.15.

The results obtained from the SSRA are utilised in the next chapter for evaluation of liquefaction in the cohesionless soil layers, and the liquefaction evaluation is compared with the excess porewater pressure ratio obtained in the SSRA, see figure 5.14.

6 | Liquefaction

The aim of this chapter is to evaluate whether or not liquefaction is initiated in some of the soil layers based on a simple stress-based approach.

During a rapid motion saturated soil is considered to be in an undrained condition because the porewater does not have enough time to dissipate. In a loose to medium dense cohesionless soil, that tends to densify during shaking, an increase in porewater pressure will develop which cannot rapidly dissipate and this will lead to a decrease in effective stresses which in turn may cause the soil to behave as a fluid. The strength of a soil is heavily dictated by the effective stress which is defined as the stress caused by the contact between soil particles. When a soil liquefies the grain contact area decreases thereby decreasing the effective stress and as a result the soil loses majority of its strength as shown in figure 6.1.

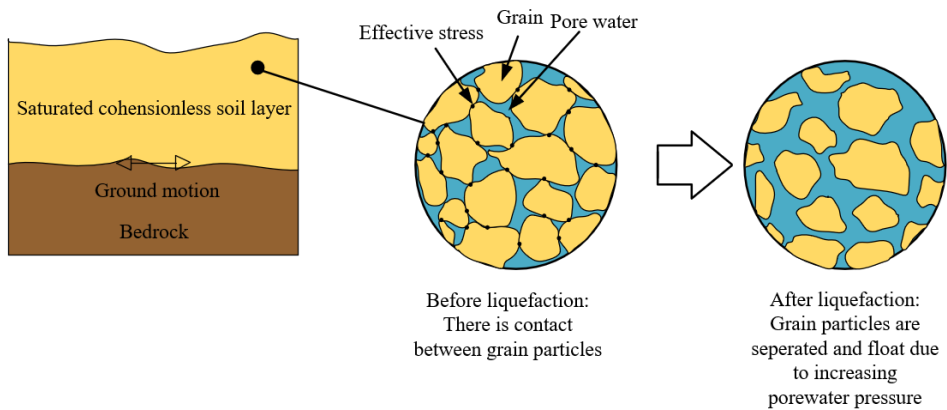


Figure 6.1: The characterization of liquefied soil.

6.1 Liquefaction Evaluation

It is important to consider the risk of liquefaction in cohesionless saturated soil layers and take the necessary precautions if necessary. When evaluating a site for liquefaction aspects like susceptibility, initiation and effects ought to be considered in the mentioned order. A liquefaction evaluation can be composed of three questions attaining to the three aspects previously the process is illustrated in figure 6.2

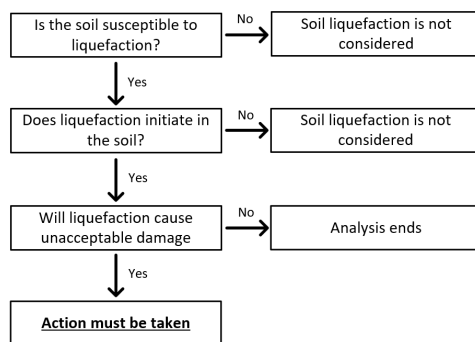


Figure 6.2: Liquefaction evaluation process diagram.

It should be noted that the liquefaction evaluation utilises results from the SSRA which does not include soil-pile interaction but merely a free-field ground motion on a soil column. Therefore this analysis only concludes whether or not the soil profile liquefies on its own when exposed to the design earthquake.

Liquefaction susceptibility

Firstly it is necessary to assess whether or not a soil layer is susceptible to liquefaction, and if so secondly whether or not liquefaction is initiated during the ground shaking and lastly what the liquefaction effects might be. Liquefaction susceptibility in soil is assessed through historical maps showing events of liquefied soil as the one shown in figure 6.3. It can be seen that several locations near the site have liquefied in the past and it is concluded that liquefaction can occur again.

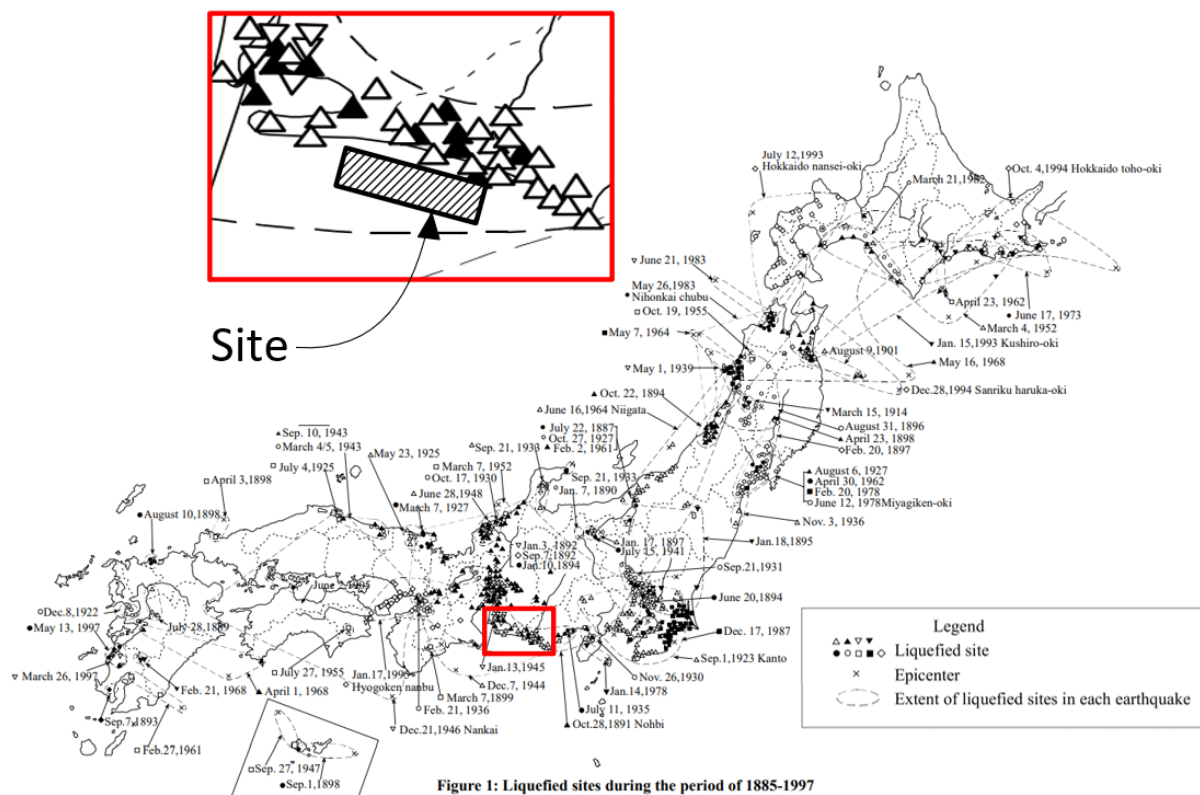


Figure 1: Liquefied sites during the period of 1885-1997

Figure 6.3: Map of liquefied sites in Japan in the period 1885-1997, [Wakamatsu, 1997]. The site investigated in this project is zoomed in.

Liquefaction susceptibility is also assessed based on the soil type and compacts of the soil, where cohesive soils (sands) can liquefy if their compactness is classified as being either loose or medium dense both of which is the case in layer 1, 3 and 5 see chapter 4 table 4.1. It can therefore be concluded that layer 1, 3 and 5 - sand all are susceptible to liquefaction.

Liquefaction Initiation

Even though the sand layers all are susceptible to liquefaction does not necessarily mean that liquefaction is initiated during ground shaking. The evaluation of liquefaction initiation is made through a stress-based approach where the earthquake loading is compared to the liquefaction

resistance of the soil. The earthquake loading and liquefaction resistance are both expressed in terms of cyclic shear stresses and are obtained from the SSRA and SPT results. The stress based approach is chosen due to its simplicity as only the earthquake loading and soil resistance are compared to determine whether or not the soil liquefies.

The shear stresses determined in each layer from the SSRA are characterized as transient and irregular from the earthquake loading and the stress-based approach requires a conversion of the irregular shear stress time history to an equivalent number of uniform stress cycles. It has been discovered by [Seed et al., 1975] that a cyclic shear stress, τ_{cyc} , which generates similar excess porewater pressure as a shear stress history from recorded earthquake motions is 65 % of the maximum shear stress, τ_{max} , from the irregular shear stress time history as shown in figure 6.4.

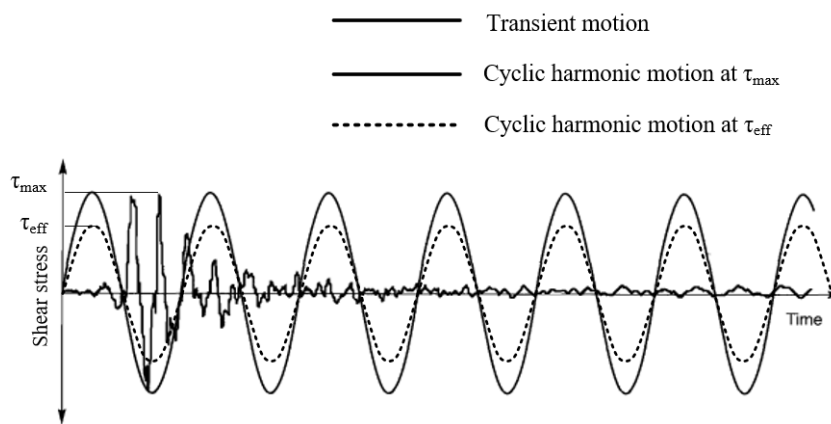


Figure 6.4: Illustration of transient earthquake motion along with a cyclic harmonic motion with peak stress τ_{max} and an equivalent cyclic harmonic motion to the transient motion with peak stress τ_{eff} [Kramer, 1996].

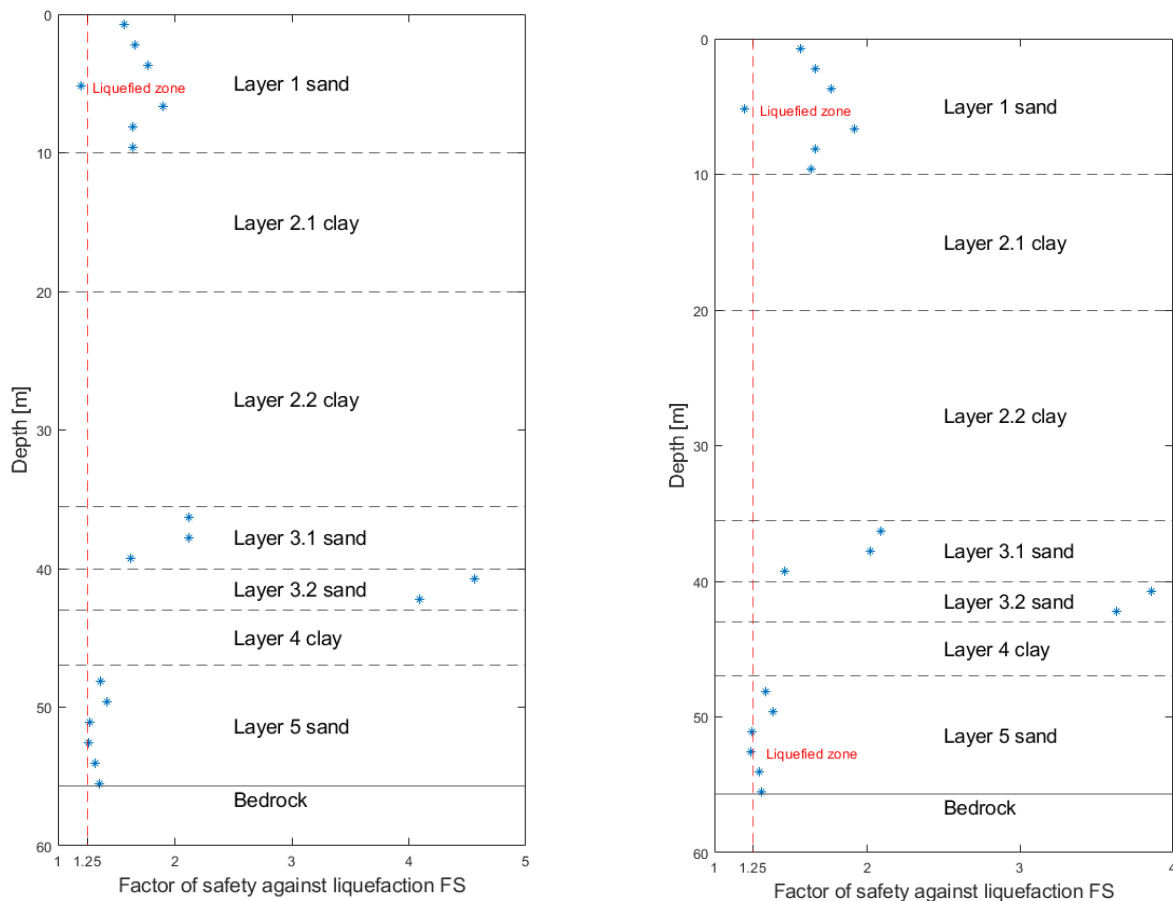
The earthquake loading expressed in terms of cyclic shear stresses is called the cyclic shear stress ratio (CSR) and is obtained through the maximum depth-varying shear stress ratios through SSRA in figure 5.14 c). The CSR is then found as:

$$CSR = 0.65 \frac{\tau_{max}}{\sigma'_v}$$

The soil liquefaction resistance is correlated to the SPT blow count through an empirical relationship developed by [Idriss and Boulanger, 2010] described in appendix K.2 equation (K.6) is used to obtain the soil liquefaction resistance in terms of cyclic shear stresses which is called the cyclic resistance ratio, CRR .

When the CSR and CRR are obtained a factor of safety against liquefaction, FS , is found and liquefaction is initiated if FS is below 1.25, according to [DNV-RP-0585, 2021] an increased factor of safety is recommended due to the uncertainty of the stress-based method. The FS is obtained for every SPT measurement in layers 1, 3 and 5 - sand for the design earthquake in the East-West and North-South direction using equation (6.1) and results are shown in figure 6.5a and 6.5b respectively.

$$FS = \frac{CRR}{CSR} \tag{6.1}$$



(a) Depth-varying factor of safety against liquefaction for design earthquake in East-West direction

(b) Depth-varying factor of safety against liquefaction for design earthquake in North-South direction

Figure 6.5

It is concluded that liquefaction is initiated in layer 1 and 5 - sand. Compared to figure 5.14 in chapter 5, layer 1 and 5 develop high porewater pressures which correspond well with results of FS in those layers. Layer 3 - sand has high FS which makes sense when compared to figure 5.14 in chapter 5 as no excess porewater is developed in sand layer 3.

6.2 Summary

Liquefaction evaluation has been made by considering the soil's susceptibility to liquefaction, and whether or not liquefaction is initiated during ground motions. It has been evaluated that layer 1 and 5 - sand both have zones with liquefied soil during the design earthquakes in the North-South direction and in layer 1 in the East-West direction and North-South direction. In the next chapter the offshore wind turbine jacket substructure with embedded piles is investigated in 3 different models with increasing complexity and the response of the structure are compared among each other. It should be noted that the liquefaction evaluation does not consider soil-pile interaction but merely a free-field ground motion on a soil column and therefore the liquefaction results are on the non-conservative side. However it should be noted that the liquefaction evaluation in Plaxis will be based on the excess pore pressure ratio whereas the liquefaction evaluation in this chapter is based on a simple stress-based approach.

7 | Modelling Approaches

The aim of this chapter is to investigate 3 different numerical models of the wind turbine foundation with increasing complexity and compare the responses. The simple liquefaction evaluation approach in chapter 6 is compared to results from an advanced liquefaction model made in Plaxis. Ground improvements are made in liquefied soil layers in order to assess the soil properties that affect the liquefaction resistance.

When carrying out a seismic time domain analysis the appropriate modelling approach should be chosen among fully integrated modelling approach and superelement modelling approaches according to [DNV-RP-0585, 2021], as shown at figure 7.1. The choice of approach in this project is based on a focus on the wind turbine foundation and not on the tower, blades and nacelle, which is why the superelement model is chosen.

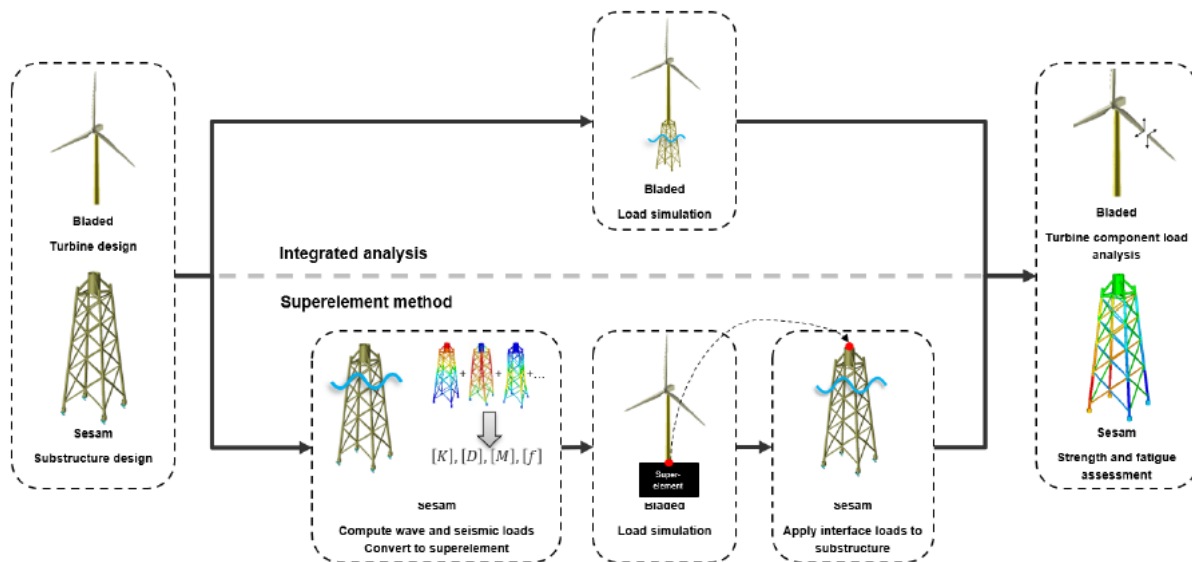


Figure 7.1: Workflow, fully integrated and superelement approach, [DNV-RP-0585, 2021].

The offshore wind turbine jacket substructure is investigated in 3 different models with increasing complexity and the responses of the structure are compared. The 3 models are exposed to ground motions as shown chapter 4 figure 4.14. The 1st model consists of a jacket substructure exposed to earthquake loading at the mudline with a fixed base to support the jacket legs. The 2nd model consists of the jacket substructure founded on embedded piles with depth-varying earthquake loading where piecewise-linear springs represent the soil-pile interaction. The 3rd model consists of the jacket substructure founded on embedded piles with surrounding soil volume that is exposed to earthquake loading at the bottom boundary as shown in figure 7.2.

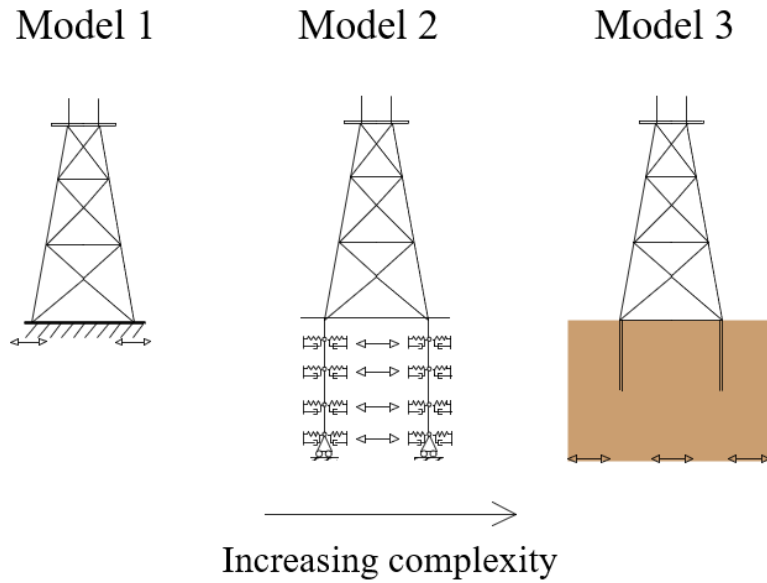


Figure 7.2: Concept of 3 different numerical models with increasing complexity investigated.

7.1 Numerical Model 1: Jacket Substructure on Rigid Base

The jacket substructure is exposed to ground motions at the mudline with a fixed base to support the jacket legs. The main assumption of the fixed base model is that the soil layers are as stiff as the bedrock so that ground motions at bedrock propagate to the mudline without any amplification or deamplification, see figure 7.3. The embedded piles are assumed to be rigid and to move simultaneously with the surrounding soil and can therefore be left out of the model.

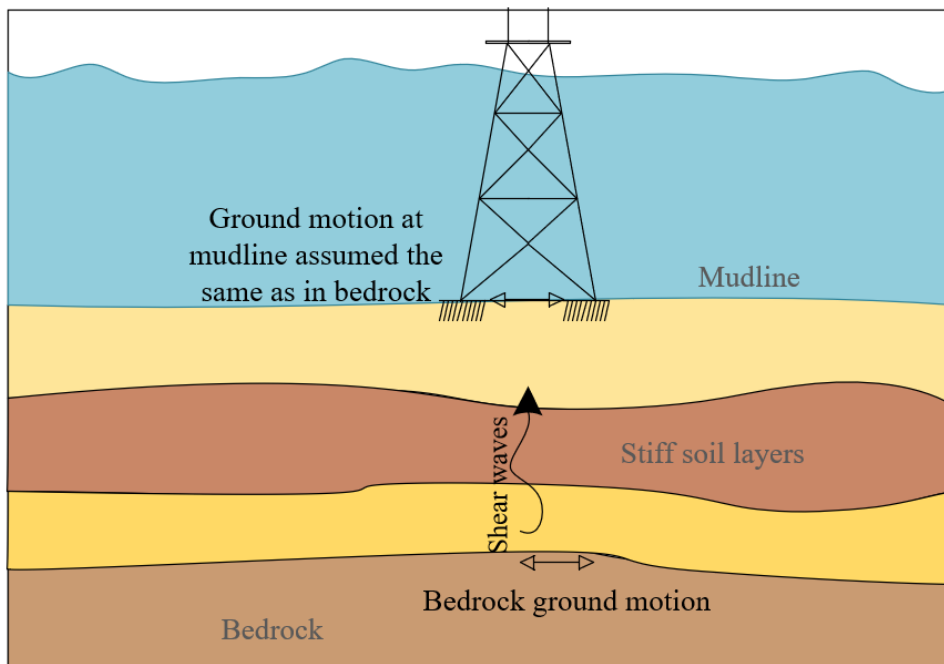


Figure 7.3: Numerical model 1: Rigid base.

The numerical model is made in the program *SeismoStruct* and the main assumptions regarding structural members, damping and turbine load are:

- Moment resistant connection between braces and jacket legs
- Structural steel S275 with bi-linear stress-strain model with kinematic hardening as presented earlier in figure 2.13
- Jacket members with Young's modulus of $E = 210$ GPa
- Structural jacket members as presented in table 4.2
- Steel structural damping = 1 %, [DNV-RP-0585, 2021]
- Hydrodynamic damping = 0.75 %, [DNV-RP-0585, 2021]
- Rayleigh structural damping found from eigenvalue analysis with modal damping ratio of $\zeta = 5\%$
- 1st and 2nd natural period of jacket substructure $T_{n1} = 0.71$ s and $T_{n2} = 0.28$ s
- Soil damping = 0 %
- Self-weight of wind turbine, V164-8.0 MW = 18,530 kN.

7.2 Numerical Model 2: Jacket Substructure on Embedded Piles with Soil-pile Springs

The soil is assumed to have a certain stiffness and damping opposite to the 1st model which is represented as non-linear springs. The depth-varying ground motions found in chapter 5 are used as input ground motions along the embedded piles as shown in figure 7.4.

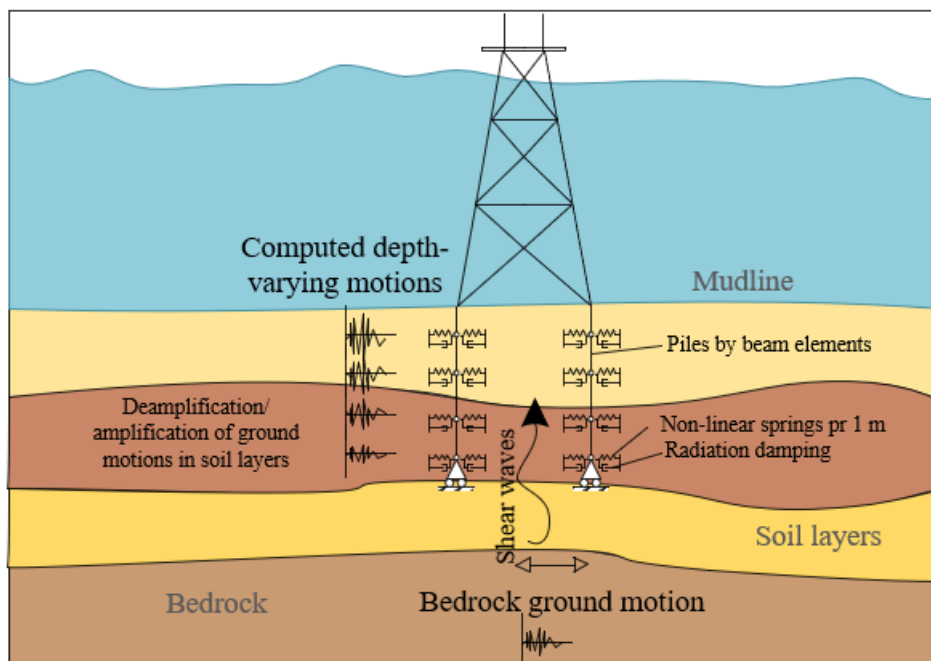


Figure 7.4: Numerical Model 2: Embedded piles with soil-pile springs.

The numerical model is made in *SeismoStruct* and the main assumptions regarding structural jacket members are the same as for model 1 and further assumptions are:

- Moment resistant connection between jacket legs and embedded piles
- Piles are modelled as beam elements with structural steel S275 with bi-linear stress-strain

model with kinematic hardening as presented chapter 2 figure 2.13

- Piles and jacket members with Young's modulus of $E = 210 \text{ GPa}$
- Piles with diameter of 2 m, wall thickness of 30 mm and length of 30 m
- Structural damping = 1 %
- Hydrodynamic damping = 0.75 %
- Rayleigh structural damping with mass and stiffness parameters, α and β , found from eigenvalue analysis with modal damping ratio of $\zeta = 5\%$
- 1st and 2nd natural period of jacket substructure and embedded piles $T_{n1} = 0.98\text{s}$ and $T_{n2} = 0.31\text{s}$
- Soil damping from radiation damping and hysteretic damping.

7.2.1 Soil-pile Interaction

The site specific depth-varying earthquake ground motions for soil layers were determined in the SSRA for a free-field case and now the soil-pile interaction evaluated where the relative displacements between soil and pile due to free-field ground motions are estimated. The soil-pile interaction is evaluated by using a number of non-linear springs to represent the soil response of the lateral loaded pile foundation and non-linear damping in parallel with the springs. The non-linear behaviour of the springs are represented by p-y curves from [DNV-RP-0126, 2016] that describe the soil resistance, p , against lateral deflection, y , see appendix J.

The pile is modelled as a beam element that is discretized into 1 m elements connected by nodes which are attached to two support springs, where one p-y curve represent each spring, see figure 7.5. The springs are excited by the free-field ground motions at the ends and is modelled to have an initial displacement from the horizontal earth pressure.

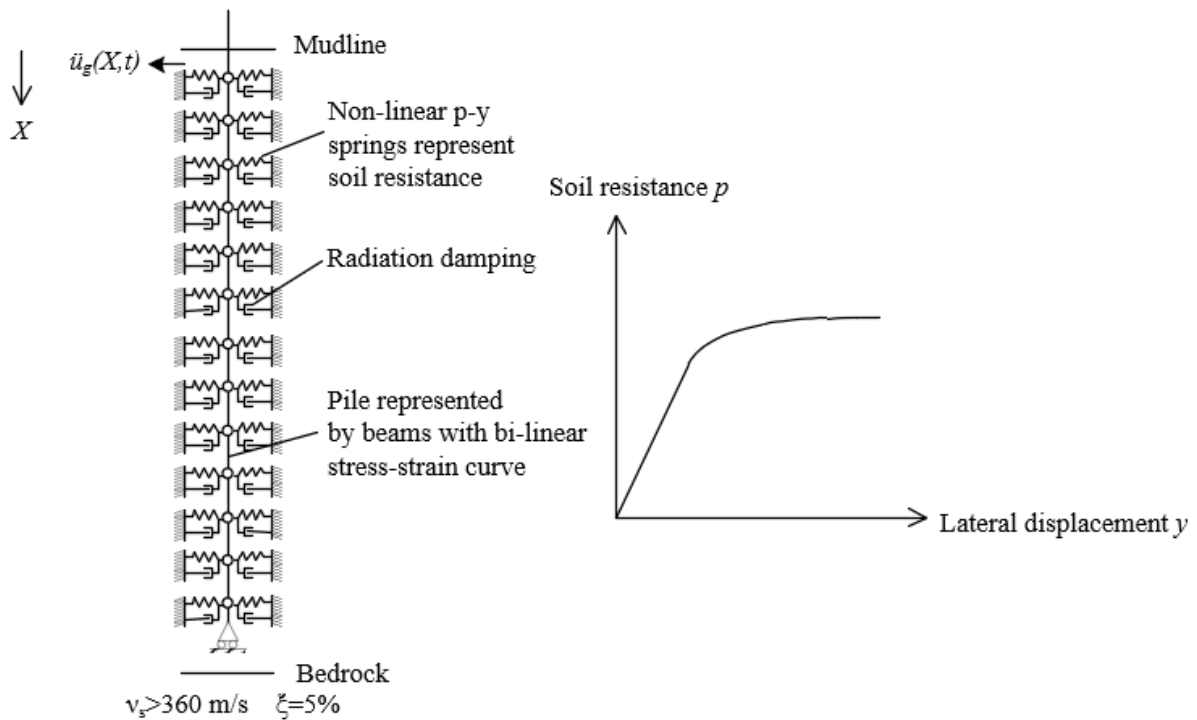


Figure 7.5: p-y analysis.

Stiffness

The non-linear p-y springs are implemented in *SeismoStruct* by fitting the non-linear p-y curves for each 1 m to four line segments with input parameters as shown in figure 7.6. The unloading and reloading is defined by the stiffness and strength degradation parameters that were obtained in the SSRA.

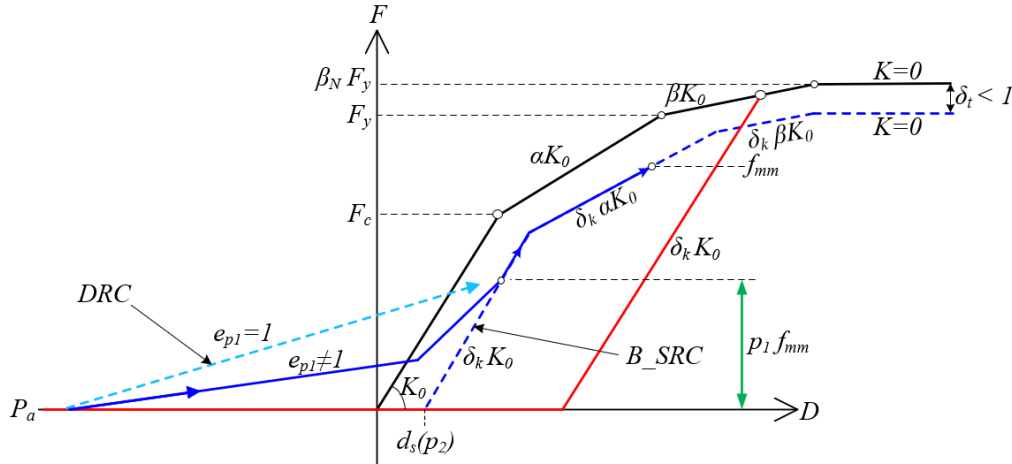


Figure 7.6: Fitted p-y curve (black curve) with unloading (red curve) and reloading (blue curve), [SeismoStruct, 2022] user manual.

K_0	Initial stiffness [kN/m]
F_y	Yield soil strength [kN]
F_c	Soil strength after 1st turning point as a ratio to F_y [-]
α	Stiffness ratio after 1st turning point [-]
β	Yielding stiffness ratio [-]
β_N	Ultimate soil strength factor in proportion to F_y [-]
f_{mm}	Direct reload point
<i>DRC</i>	Direct reload curve
<i>B_SRC</i>	Base standard reload curve
d_s	Starting displacement of <i>B_SRC</i> [m]
P_a	Minimum force ratio in proportion to F_y [-]
p_1	Gap force parameter [-]
p_2	Soil cave-in parameter [-]
e_{p1}	DRC starting stiffness ratio [-]
δ_k	Stiffness degradation/hardening parameter [-]
δ_t	Strength degradation/hardening parameter [-].

The p-y curves and corresponding curve fitting is shown for a spring in the middle of each layer in figure 7.7. The implementation procedure is further described in appendix I section I.3.

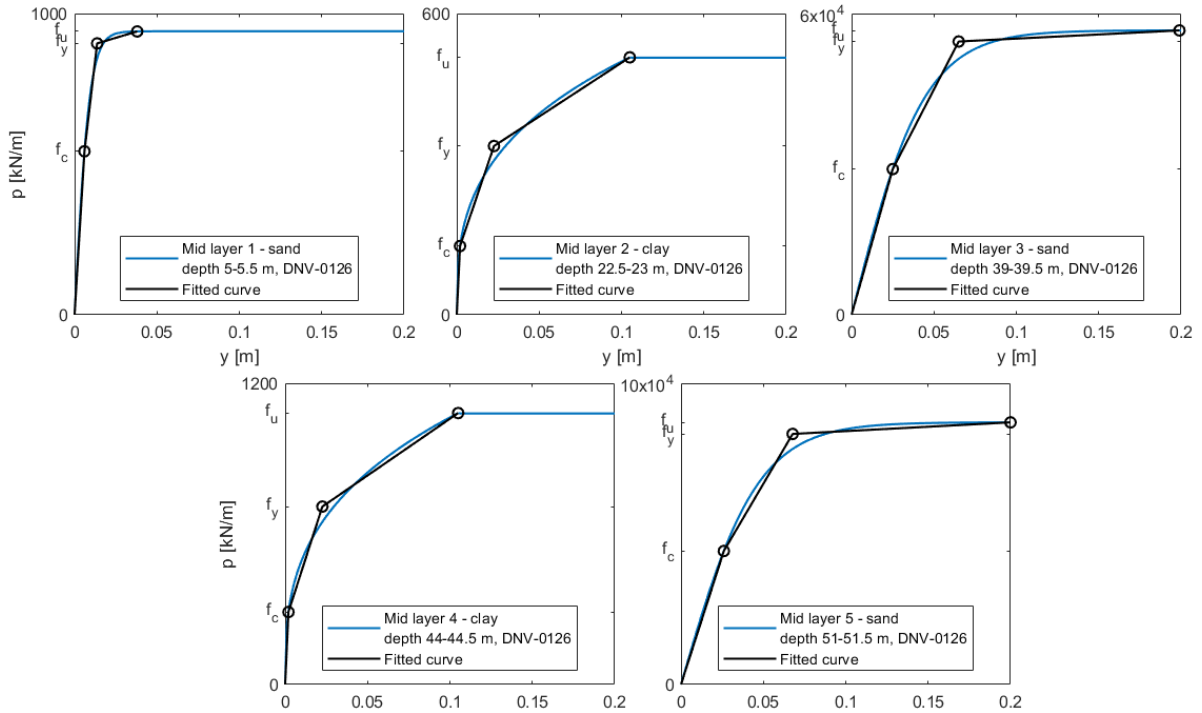


Figure 7.7: p - y curve fitting.

Soil stiffness and strength degradation

The soil-pile interaction model takes the soil stiffness and strength degradation due to generation of pore water pressure and soil softening during cyclic loading into account by the degradation parameters, δ_k, δ_t , which were obtained from SSRA in chapter 5 figure 5.15.

Cyclic S-N curve parameters

The soil-pile interaction model further takes into account the liquefaction resistance by inputting parameters for the cyclic resistance S-N curve for the soil layers. The S-N curve describes the maximum shear stress versus number of load cycles until failure. Failure is defined when the porewater pressure (PWP) exceeds 95% of the effective stress (PWP ratio $r_u = 0.95$). The S-N curves are obtained by exciting a 10 meter soil layer with properties as given in table 4.1 by an acceleration time series of different amplitudes with a frequency of 0.1 Hz in *DeepSoil*. The maximum shear stress versus the number of load cycles until failure are plotted which give the corresponding S-N curve for the specific soil layer as shown in figure 7.8. The input ground motions and corresponding response of layer 1 - sand in order to obtain the SN curve can be seen in appendix I.3.

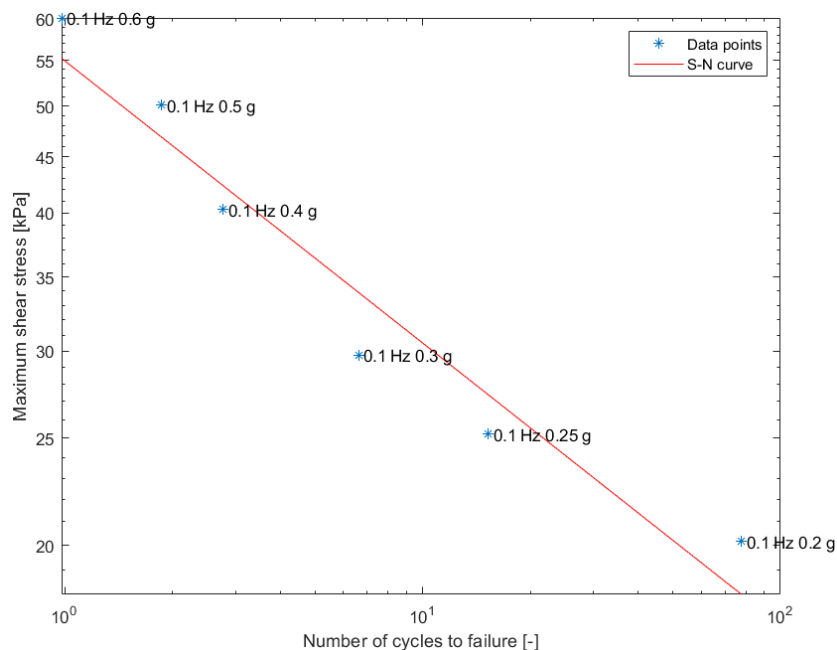


Figure 7.8: S-N curve for layer 1 - sand.

Pile movement in slack zone

The soil-pile interaction model further takes the permanent displacement of the soil away from the pile, which is called the slack zone, into account. When the pile is laterally displaced a gap can be developed between soil and pile. The gap is assumed to be within the first 1/3 of the pile where the confinement of the soil is small. When the pile moves in the slack zone the soil-pile interaction is modelled with a direct reload curve (DRC) as shown in figure 7.6. In *SeismoStruct* the DRC is controlled by a DRC stiffness ratio, e_{p1} , where a value of 0 is representing a pure gap, which could be the case for stiff clay, and a value of 1 is representing a soil gap that is filled with soil immediately, which could be the case for dry sands. In this project, the DRC stiffness ratio, e_{p1} , in all soil layers is assumed to increase linearly from 0 (pure gap) to 1 (backfill of soil) in the first 1/3 of the pile and to be 1 in the lower 2/3 of the pile due to confinement of soil, [Allotey and Nagggar, 2008]. *SeismoStruct* also requires a soil cave-in parameter where a value of 0 means no soil cave-in. The soil cave-in parameter, p_2 , is taken to be 0 at the pile head and increase linearly to 5 in the first 1/3 of the pile based on results from cyclic load tests on piles by [Allotey, 2006]. In figure 7.9 the effects of DRC stiffness ratio, e_{p1} , and soil cave-in parameter, p_2 , are shown on the backbone curve.

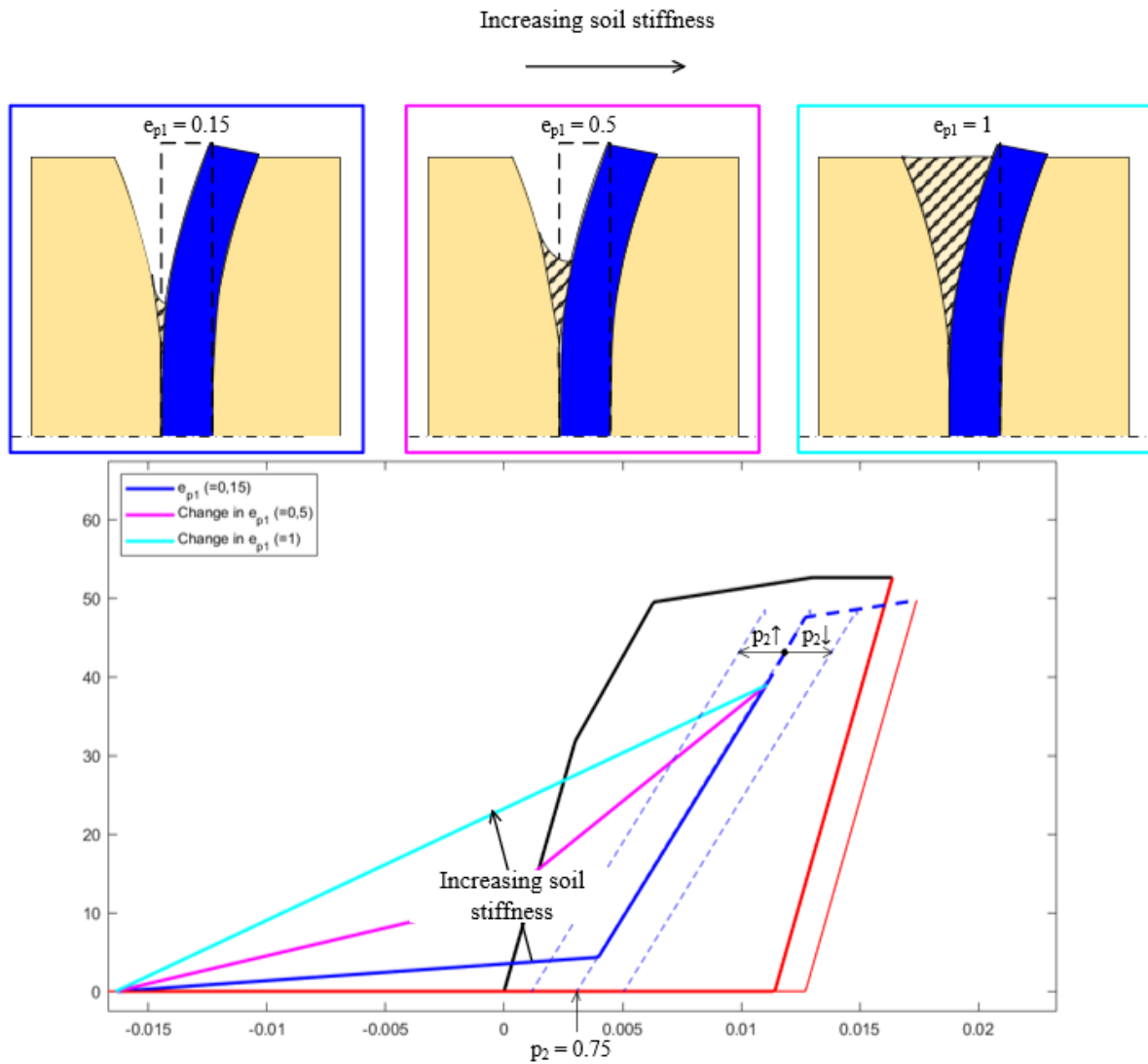


Figure 7.9: Effect of soil gap parameters on the reloading curves.

Radiation and hysteretic damping

The soil-pile damping consists of hysteretic damping and radiation damping where the hysteretic damping usually is the major reason for energy dissipation during an earthquake. However, radiation damping can also occur from waves radiating outwards from the contact surface between soil and pile when the pile foundation moves back and fourth under cyclic loading. Radiation damping is included in the model by assigning a stiffness-proportional damper in parallel with each spring. The more non-linear behaviour the smaller is the contribution from radiation damping and the main damping will be due to hysteretic damping. For larger shear strains in the soil, the soil stiffness reduces and the hysteretic damping increases and becomes the main damping in the soil-pile interaction model. The hysteretic damping is included through the non-linear force-displacement p - y curve defined in each spring along the pile length. The radiation damping ratio is calculated in appendix I section I.3.3 and is below 0.2 % and therefore insignificant compared to hysteretic damping.

7.3 Numerical Model 3: Jacket Substructure on Embedded Piles with Soil Volume

For the 3rd model of the jacket substructure a soil volume is exposed to bedrock ground motions along the bottom boundary as illustrated on figure 7.10.

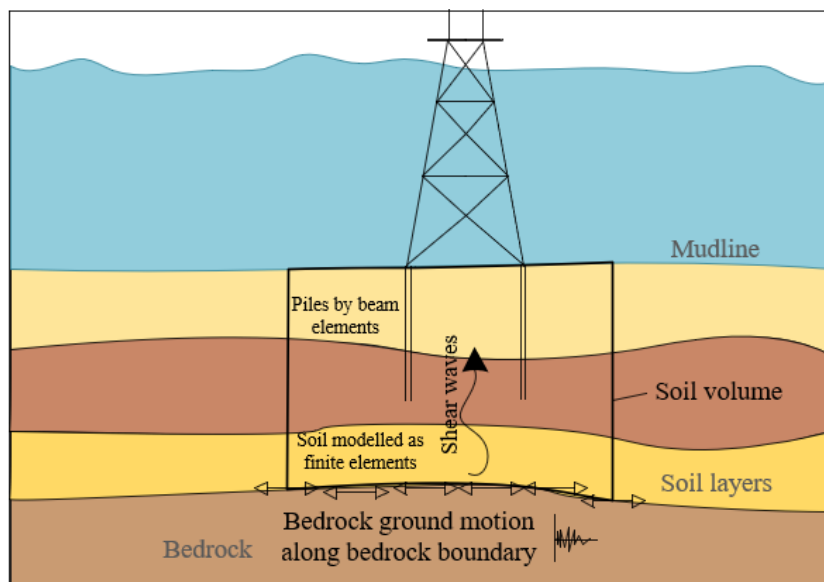


Figure 7.10: Numerical Model 3: Soil volume.

The numerical model is made in *Plaxis* and the main assumptions regarding structural members, structural for jacket substructure and piles are the same as for model 1 and 2 as well as structural and hydrodynamic damping and further assumptions are:

- Structural members in jacket substructure and piles are modelled as embedded beams (beam elements) with each node having 6 degrees of freedom (DOF) 3 translatory and 3 rotational DOF.
- Soil elements are modelled as three-dimensional 10 noded tetrahedral elements with 3 DOF in each node with 3 translatory DOF.
- Pile group behaviour is taken into account, however the group effects are insignificant as the spacing between piles are above 8 times the pile diameter, [DNV-RP-0126, 2016].
- Soil damping from radiation damping and hysteretic damping.

7.3.1 Soil-pile Interaction

The contact surface between soil and pile is not fully rigid but is weaker with relative displacements along the pile length between surrounding soil and pile surface from soil slipping/gapping. The interface is modelled with node pairs where one node belongs to the pile beam element and the other belongs to the soil. The interaction between the node pairs is modelled with two elastic-perfectly plastic Mohr-Coulomb springs; one to model the slip displacement and one to model the gap displacement. A zero tension criterion is assigned to the springs, i.e. instead of tension developing a soil gap between pile and soil occurs. The strength parameters (friction angle and cohesion) in the interface between soil-pile are assigned a strength reduction factor that depends on the pile material and installation method, which is set to 2/3, [Plaxis, 2021b].

7.3.2 Soil Constitutive Model

The constitutive behaviour of soil layers is modelled with a hardening soil model with small-strain stiffness in clay layers and a liquefaction model in sand layers.

Hardening soil model with small-strain stiffness

The hardening soil model with small-strain stiffness in *Plaxis* (HS small) is a soil model with a hyperbolic stress-strain relationship as described in chapter 5 section 5.2 that captures the strain-dependent stiffness in terms of shear modulus reduction curves and hysteretic damping with Masing behaviour, see figure 5.7.

Liquefaction soil model

The liquefaction model in *Plaxis* (UBC3D-PLM constitutive model) incorporates generation of porewater pressure in cyclic loading which may lead to liquefaction where degradation of stiffness and strength is accounted for during the cyclic loading. The input parameters in *Plaxis* for the soil constitutive models can be seen in appendix I.4.

7.3.3 Model Size

As a 3D numerical simulation with advanced constitutive soil models are computationally demanding it is advantageous to decrease the size of the model as much as possible, without compromising the computability of the model, so the calculation time decreases as much as possible. Therefore it has been concluded that a soil volume with width, length and height of 80 m, 120 m and 55.65 m (distance from mudline to bedrock) have been chosen as illustrated in figure 7.11. The earthquake ground motion is acting in the length direction.

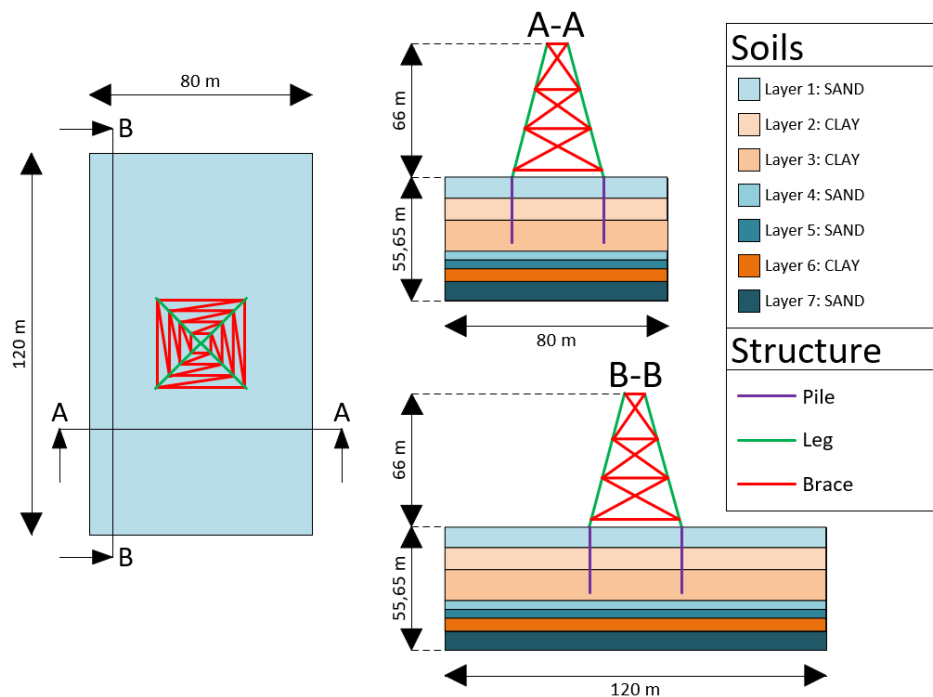


Figure 7.11: Illustration of numerical model in *Plaxis*.

The size of the model is essential when it comes to computability as it requires more elements when generating the mesh.

7.3.4 Boundary Conditions

The numerical model requires static and dynamic boundary conditions to be defined along the model boundaries as illustrated in figure 7.12 and 7.13.

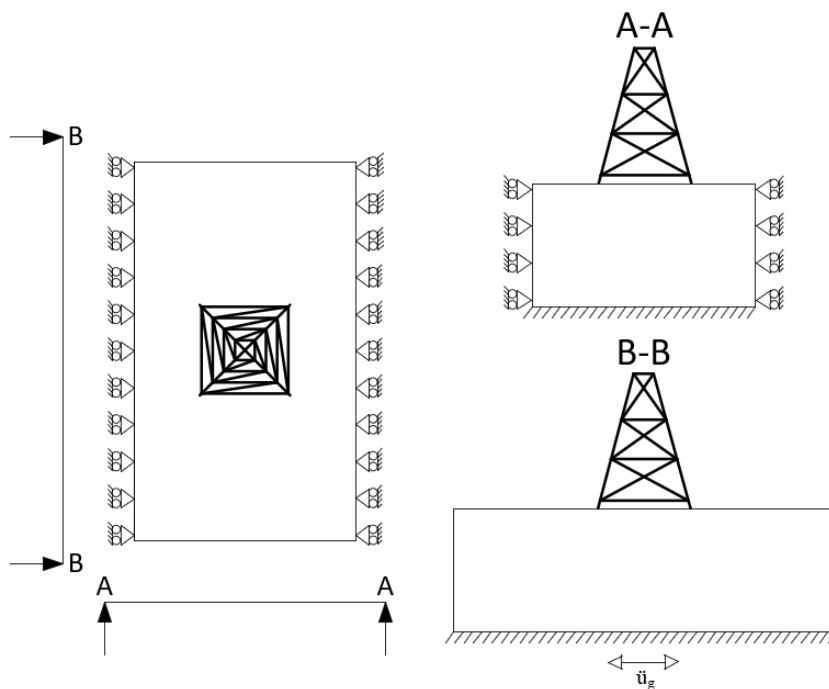


Figure 7.12: Illustration of static boundaries in *Plaxis* model.

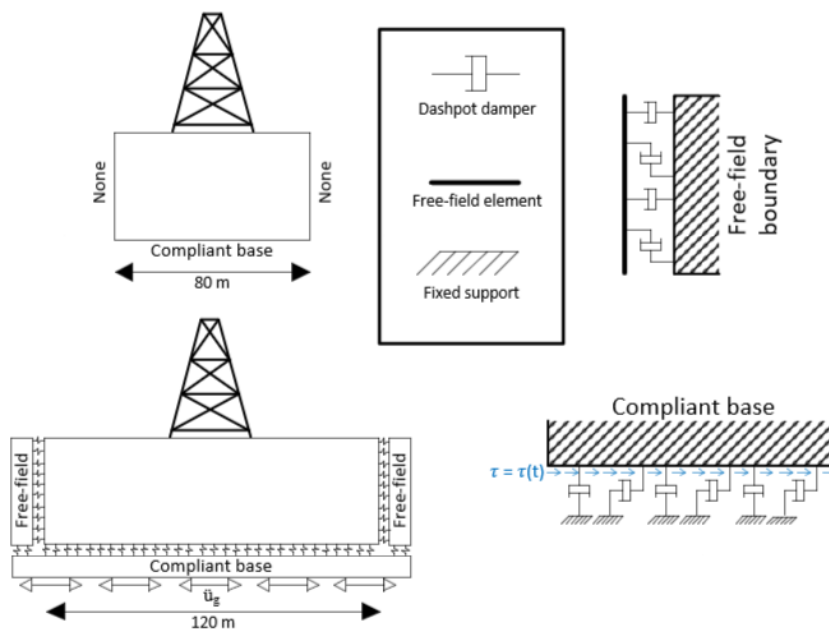


Figure 7.13: Illustration of dynamic boundaries in *Plaxis* model.

When running a numerical calculation *Plaxis* applies boundary conditions depending on whether or not a dynamic or static analysis is utilised. When a dynamic analysis is utilized dynamic boundary conditions are used and vice versa. The dynamic boundaries applied in the *Plaxis* model are described beneath:

Free-field boundary

Free-field boundaries are added to the soil volume sides and simulates the propagation of waves into the free-field. The waves reflected by the piles are absorbed by the dashpot dampers as shown in figure 7.13. The free-field elements are elements with the same soil properties as the soil inside the volume and they transfer the free-field motion to the soil volume by equivalent normal and shear stresses as a time history.

None

When no dynamic boundary conditions are applied to a model boundary the static boundary conditions are applied in the dynamic analysis for that boundary.

Compliant base

The compliant base boundary condition consist of a viscous boundary and prescribed displacement history. The prescribed displacement history is transferred to the soil volume through applied shear stresses and the dashpot dampers ensure absorption of incoming waves to prevent reflection back into the model and allow upward propagation of waves from the bedrock.

7.4 Results

The 3 numerical models have been analysed with the assumptions and setups as mentioned in the previous sections. For each model the relative horizontal displacement between the interface node and the base of the jacket substructure in the x and y direction is found, as shown in 7.14.

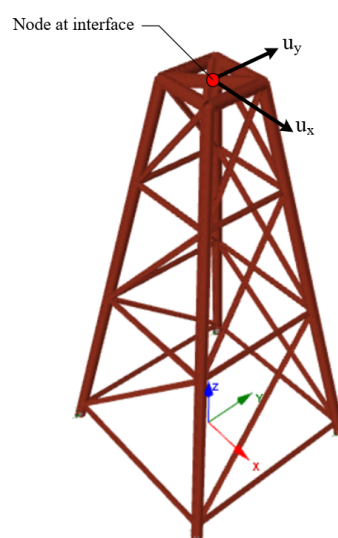
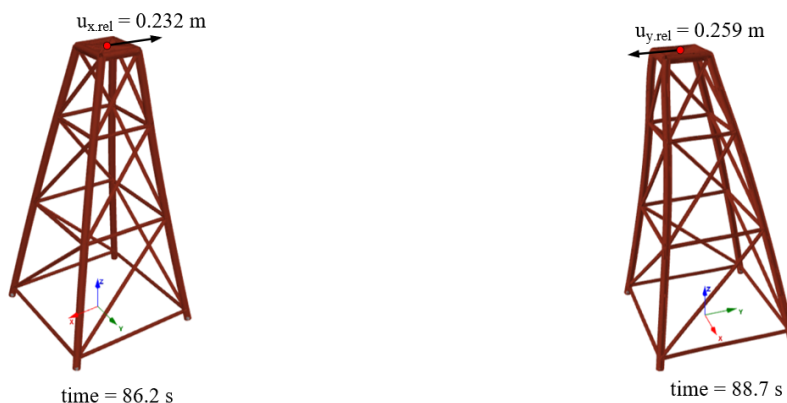


Figure 7.14: Relative displacements, u_x and u_y , between interface node and bottom of jacket legs.

Numerical Model 1: Jacket Substructure on Rigid Base

The maximum relative horizontal displacements at the interface node in the x -direction (earthquake in East-West direction) and y -direction (earthquake in North-South direction) are shown at figure 7.15 and in table 7.1.



(a) Displacement in x (earthquake in East-West) (b) Displacement in y (earthquake in North-South)

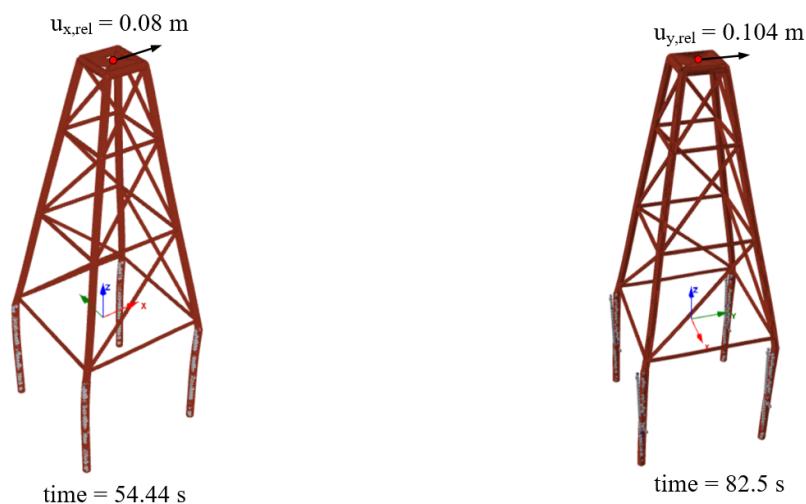
Figure 7.15: Relative maximum horizontal displacement at interface node.

Table 7.1: Horizontal displacement in x and y -direction.

	u_x	u_y
$E_d = E_{Edy}$	-	0.259 m
$E_d = E_{Edx}$	0.232 m	-

Numerical Model 2: Jacket Substructure on Embedded Piles with Soil-pile Springs

The horizontal displacement from East-West and North-South direction of the earthquake is shown in figure 7.16a and 7.16b respectively.



(a) Displacement in x (earthquake in East-West) (b) Displacement in y (earthquake in North-South)

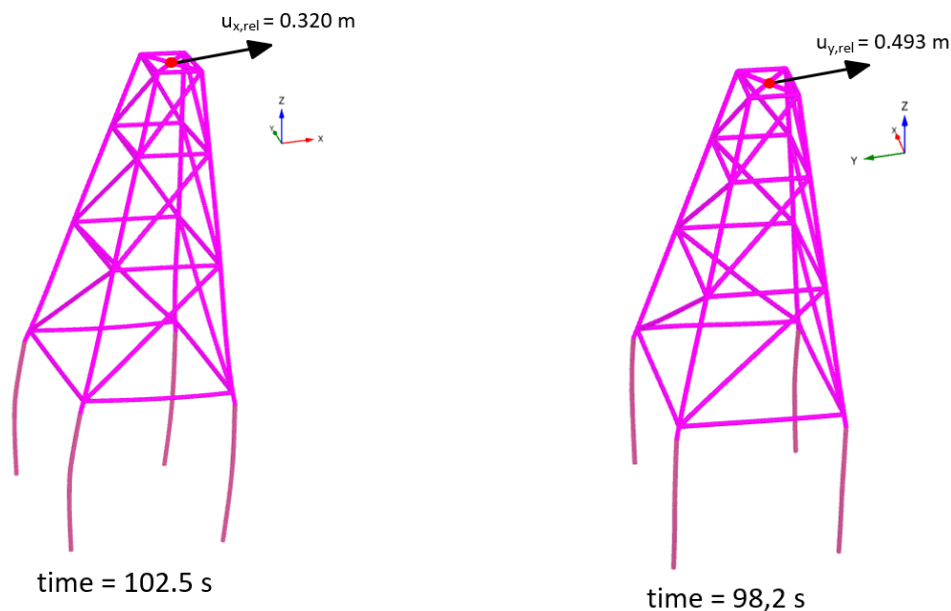
Figure 7.16: Relative maximum horizontal displacement at interface node.

Table 7.2: Horizontal displacement in x and y -direction.

	u_x	u_y
$E_d = E_{Edy}$	-	0.104 m
$E_d = E_{Edx}$	0.080 m	-

Numerical Model 3: Jacket Substructure on Embedded Piles with Soil Volume

The horizontal displacement from the East-West and North-South direction of the earthquake is shown in figure 7.17a and 7.17b respectively.



(a) Displacement in x (earthquake in East-West) (b) Displacement in y (earthquake in North-South)

Figure 7.17: Relative maximum horizontal displacement at interface node.

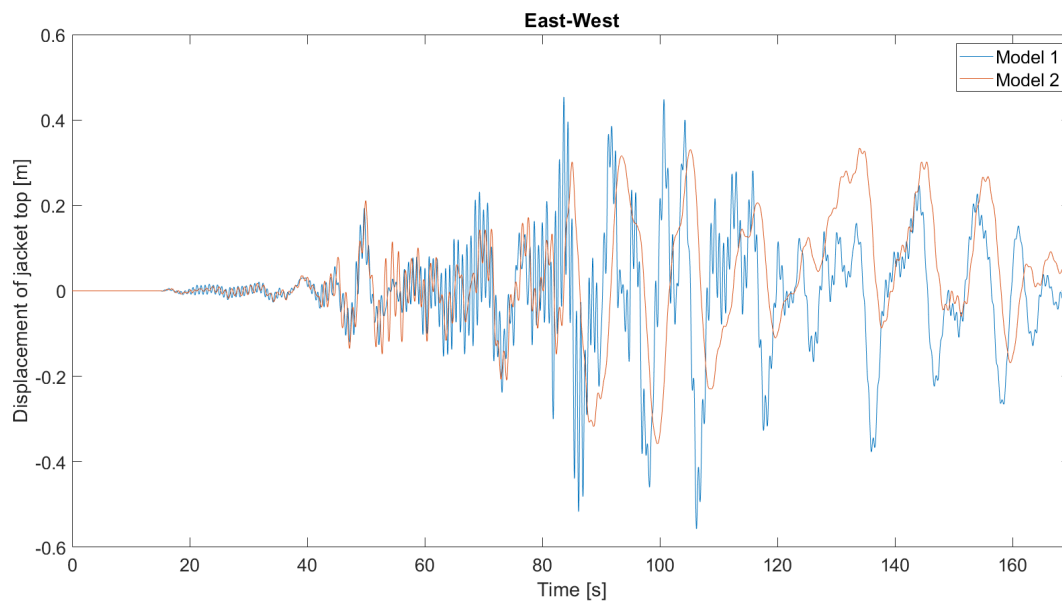
Table 7.3: Horizontal displacement in y -direction for model 3.

	u_x	u_y
$E_d = E_{Edy}$	-	0.493 m
$E_d = E_{Edx}$	0.320 m	-

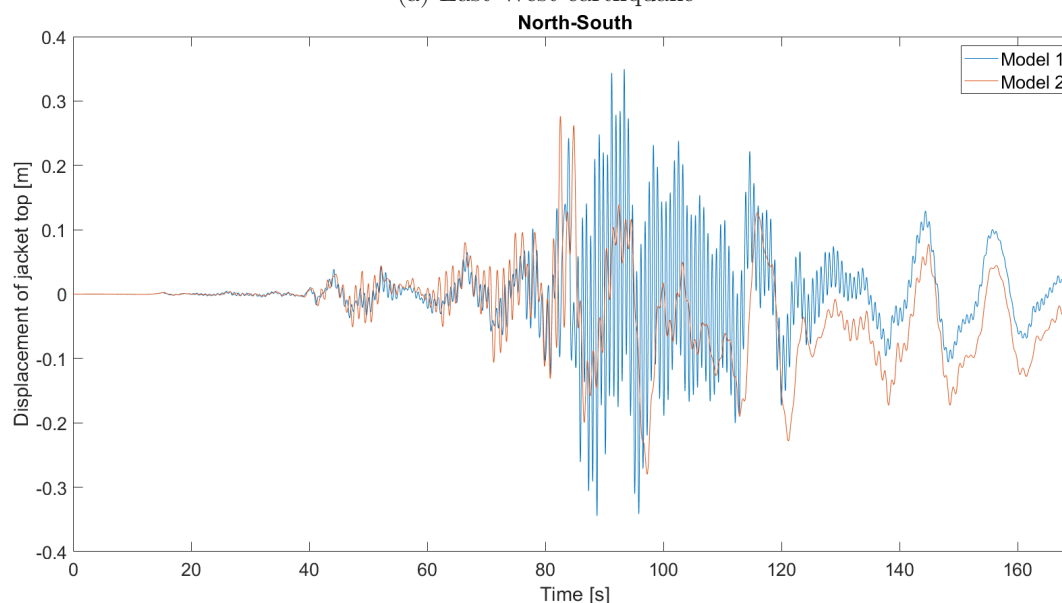
7.4.1 Response Comparison of Offshore Wind Turbine Foundation

Model 1 & 2

The total horizontal displacement of the top at the jacket substructure are compared between model 1 & 2 in figure 7.18.



(a) East-West earthquake



(b) North-South earthquake

Figure 7.18: Total horizontal displacement of jacket top.

It can be seen that model 1 has larger displacements than model 2. This is explained as the jacket base in model 1 moves simultaneously with the ground motions whereas model 2 has a delayed, damped response as soil damping is incorporated in the soil-pile interaction springs. The soil damping in model 2 results in a more 'smooth' response as the jacket substructure does not oscillate with the same amount of cycles as in model 1. Furthermore, model 2 is excited at every spring along the embedded piles with deamplified depth-varying ground motions (see figure 5.14 a)) compared to the ground motions acting on model 1 which also contributes to smaller displacements in model 2 than in model 1. It can be concluded that the assumption of a rigid soil-pile interaction is not realistic as the response of the structure in the two models gives considerable different results.

Model 2 & 3

The numerical simulation of model 3 in *Plaxis* for East-West and North-South earthquakes are stopped at an earlier time step than the the duration of the input motions due to computational time and storage space. From figure 7.18a and 7.18b it can be seen that the time for maximum displacement in the time history has been passed for both earthquakes, and therefore it is acceptable to stop the dynamic calculation in *Plaxis* at earlier time steps as shown on figure 7.19.

For model 2 the depth-varying ground motions acting on the soil-pile springs along the embedded piles are found in SSRA. For model 3 the design earthquake ground motions from PSHA are applied as prescript displacement at the compliant base boundary in *Plaxis* and transferred further to the soil volume as shear stresses. Therefore, the input bedrock ground motions in *Plaxis* and the ground motions at a node at bedrock in *Plaxis* are compared to see if they have similar motions. It can be seen at figure 7.19 that the motions are corresponding well. There is a little difference between the input motion in *Plaxis* and the motion at a node at bedrock, due to the bedrock motions in *Plaxis* being applied to the compliant base boundary and transferred to the soil-volume as shear stress.

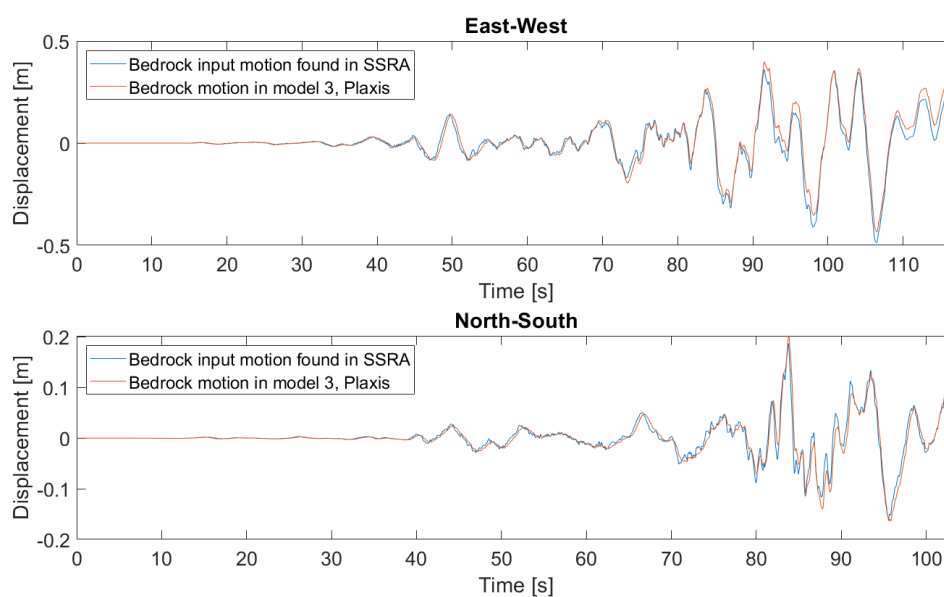


Figure 7.19: Time history for ground motions at bedrock.

Furthermore, the ground motions in the upper soil layer from a free-field SSRA and from *Plaxis* are compared in figure 7.20 and 7.21 to see the effect of site response through the soil profile from bedrock to the upper soil layer. To minimize interference from the piles and to get motions as close to free-field motions as possible, the ground motions in *Plaxis* are found at nodes away from the piles. Furthermore, the ground motions at the upper soil layer are compared with the excess pore water pressure ratio for the soil layer in depth of 35.50 m, since it can be seen from the development of liquefaction points in *Plaxis* that the ground motions starts to deviate more as the liquefaction develops throughout the soil layer in depth of 35.50 m, which can be seen at figure 7.22 and 7.23.

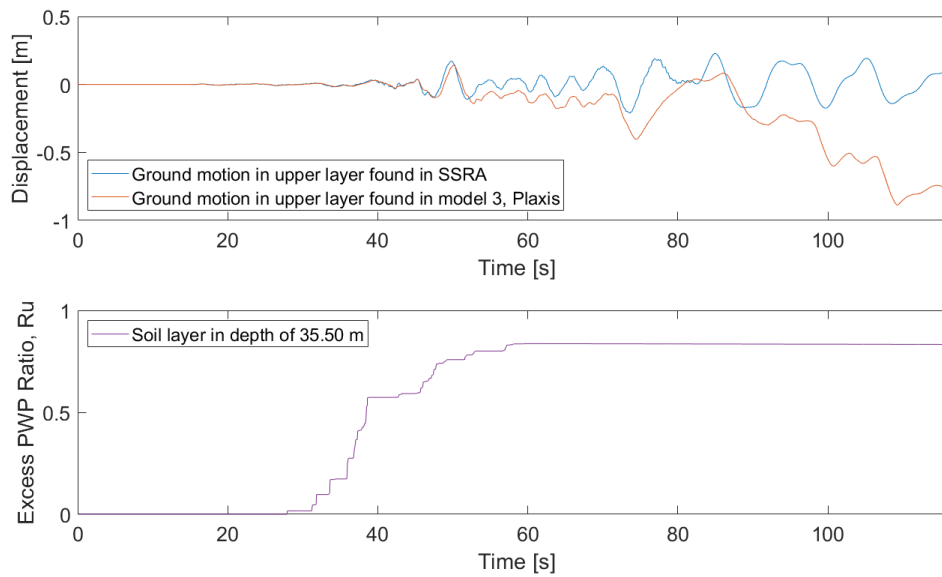


Figure 7.20: Time history for ground motions and PWP ratio at upper soil layer for East-West.

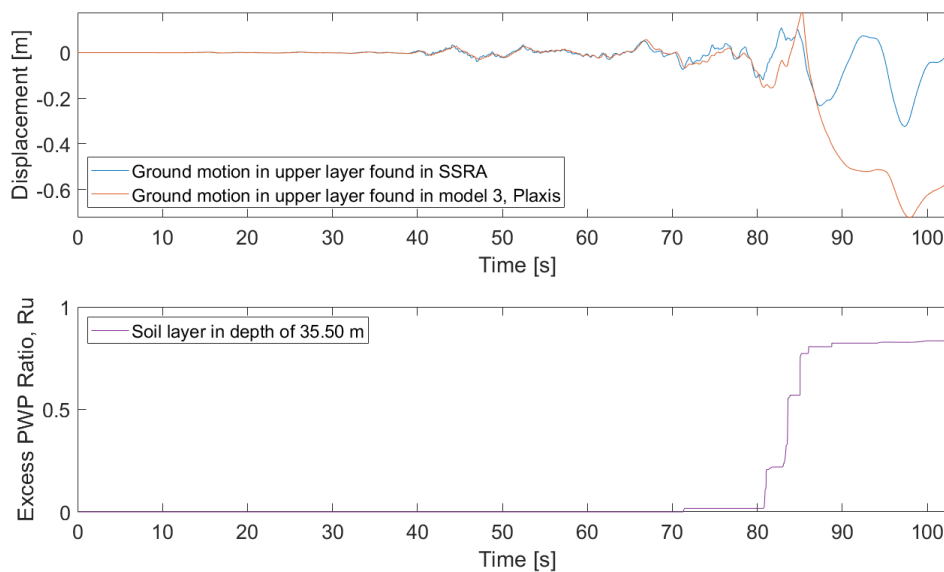


Figure 7.21: Time history for ground motions and PWP ratio at upper soil layer for North-South.

It can be seen that the ground motions in the upper soil layer correspond and have similarities for the first part of the time history, but suddenly starts to deviate where the *Plaxis* model starts to have large displacement. This is because the sand layer beneath the piles in a depth of 35.50 m has fully liquefied in the *Plaxis* model. This can also be seen from the development of excess pore water pressure ratio in the soil layer at the depth of 35.50 m.

The displacement at the bottom of the jacket substructure is compared for the two models with corresponding liquefaction zones for a number of time steps.

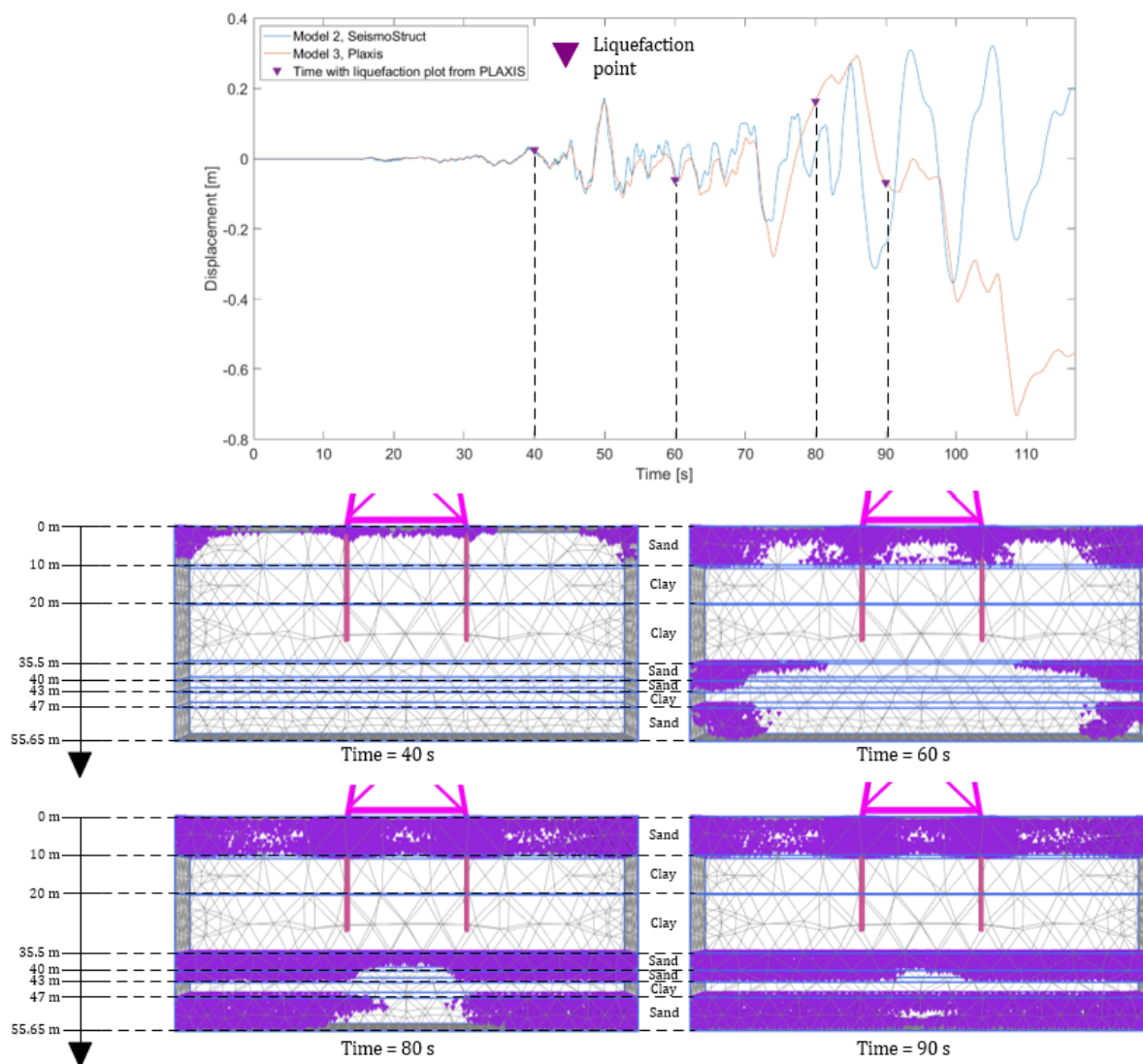


Figure 7.22: Time history for motions at bottom of jacket substructure for East-West and development of liquefaction points with porewater pressure ratio $r_u \geq 0.95$.

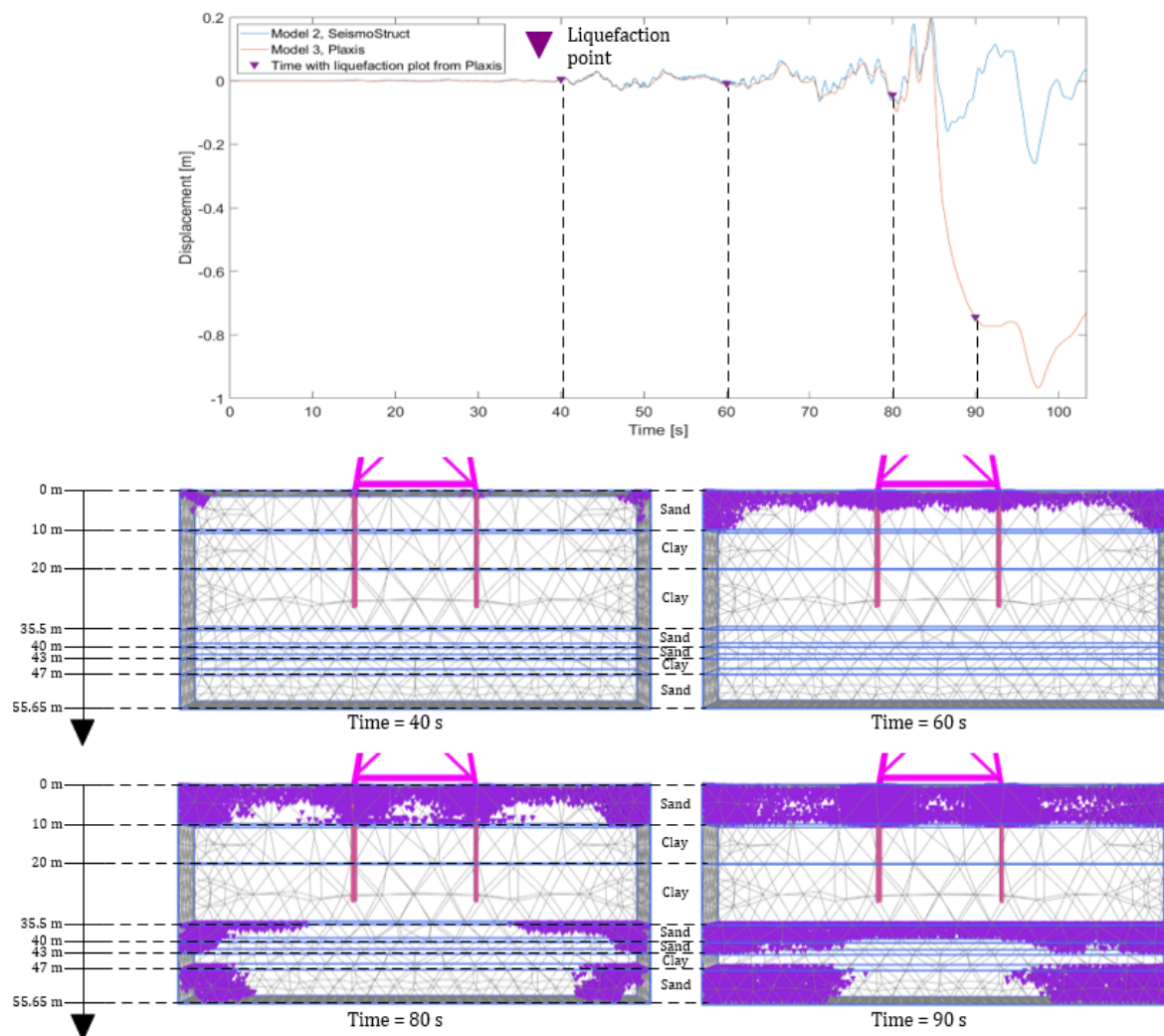
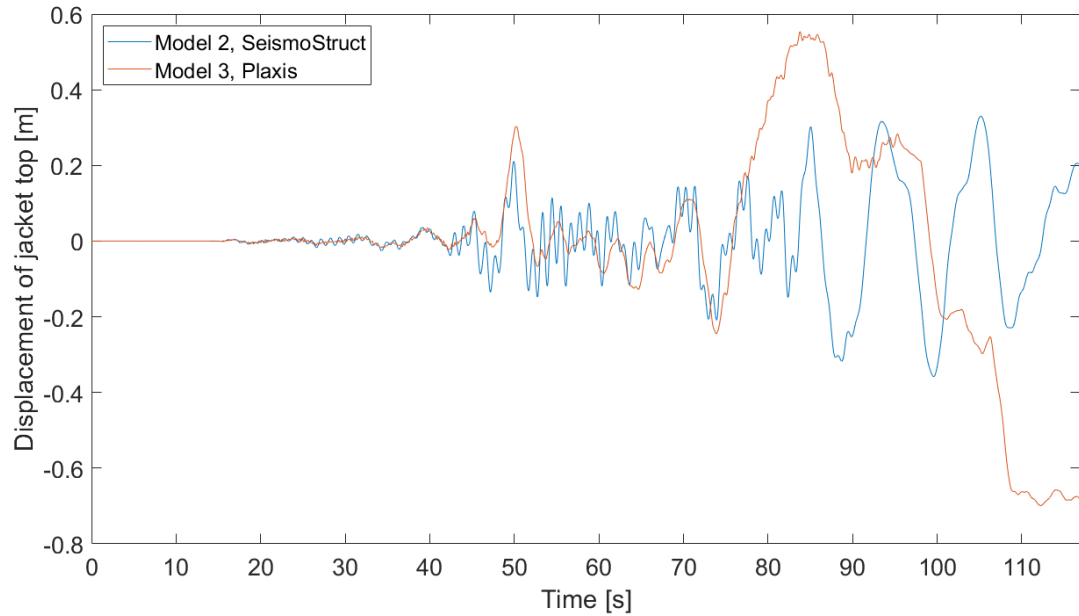


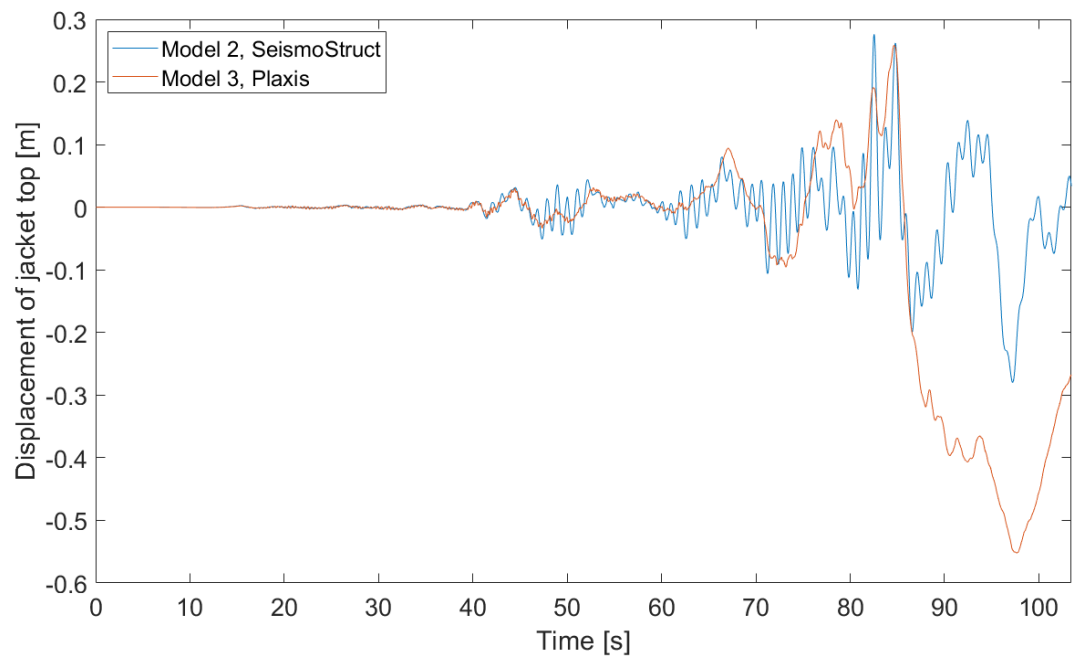
Figure 7.23: Time history for motions at bottom of jacket substructure for North-South and development of liquefaction points with porewater pressure ratio $r_u \geq 0.95$.

As for the ground motions it can be seen that there are correspondence and similarities in the start of the time history, but that the response starts to deviate at a time where liquefaction in the *Plaxis* becomes fully developed in the lower sand layers. From this it is clear that the difference in displacement enlarge as the liquefaction points develops throughout the soil layer at the depth of 35.50 m.

The displacement at the top of the jacket substructure is shown at figure 7.24 where it can be seen that the horizontal displacement in model 2 and model 3 are similar in overall behaviour before liquefaction initiates in model 3.



(a) East-West earthquake

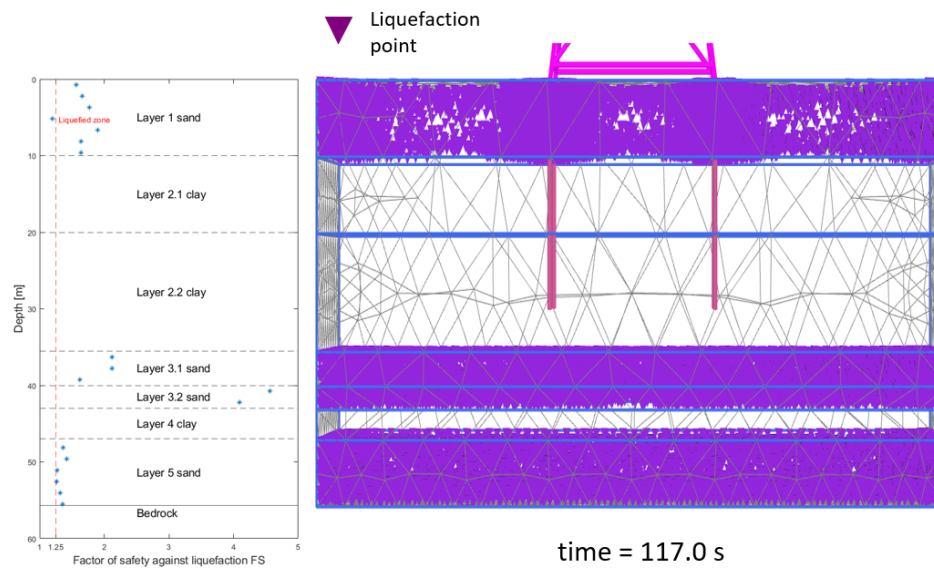


(b) North-South earthquake

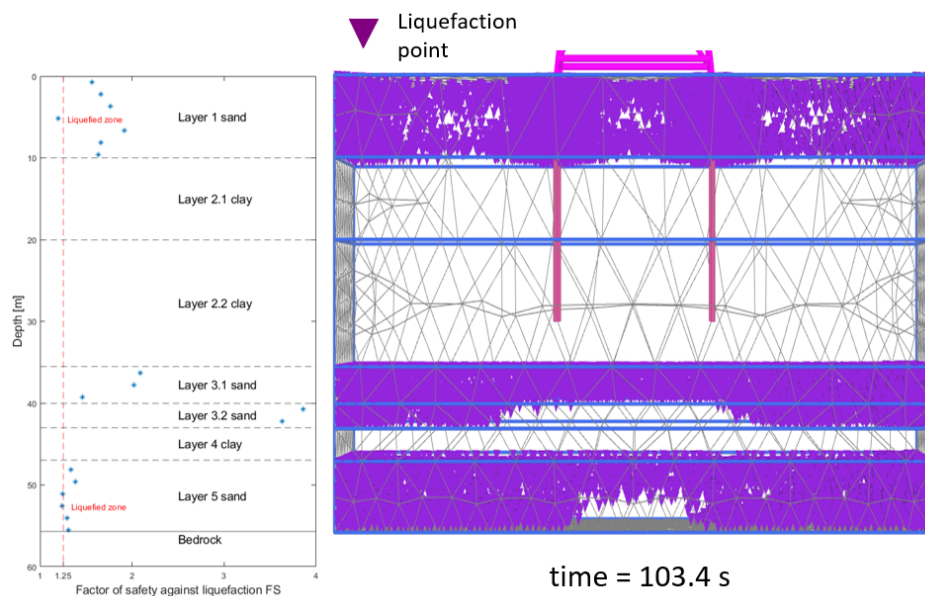
Figure 7.24: Total horizontal displacement of jacket top.

Stress based-based approach & advanced liquefaction model

As mentioned in chapter 6 the liquefaction initiation evaluated from factor of safety (FS) obtained from the stress-based approach through the SSRA and the development of liquefaction in model 3 in *Plaxis* are compared for the two earthquakes, as shown at figure 7.25a and 7.25b.



(a) East-West earthquake



(b) North-South earthquake

Figure 7.25: Comparison of liquefaction initiation for FS by stress-based approach and model 3, *Plaxis*.

It can be seen from figure 7.25a and 7.25b that the liquefaction in the model 3, *Plaxis* does develop more widely than calculated from the FS by stress-based approach. This difference is due to the embedded piles being included in *Plaxis* where it is observed that the liquefaction points starts to rapid develop around. Furthermore, liquefaction is observed to develop from the vertical soil volume boundaries and then spreads through model 3 which may be due to the model not being large enough.

7.5 Ground Improvement

The unacceptable large soil movements due to liquefaction in the top sand layer can be solved by ground improvement techniques. As the soil's stiffness and strength is dependent on the contact surface between grains it is obvious that a denser sand is stiffer than a looser sand. Therefore, densifying a sand is a very effective way of improving its resistance against liquefaction. The top sand layer is loose and the tendency to generate excess porewater will decrease when the sand is more compact. A technique to densifying sandy soils offshore is dynamic compaction or vibro compaction, [Hamidi et al., 2013]. Dynamic compaction is a technique where a heavy weight is dropped on the surface which lead the loose soil's grains to liquefy and rearrange in a denser way, see figure 7.26a. Vibro compaction is a technique where a vibrator is penetrated into the ground and the energy from the vibration makes the sand denser. More sand fill is added on the surface to compensate for the decrease in soil volume, see figure 7.26b.

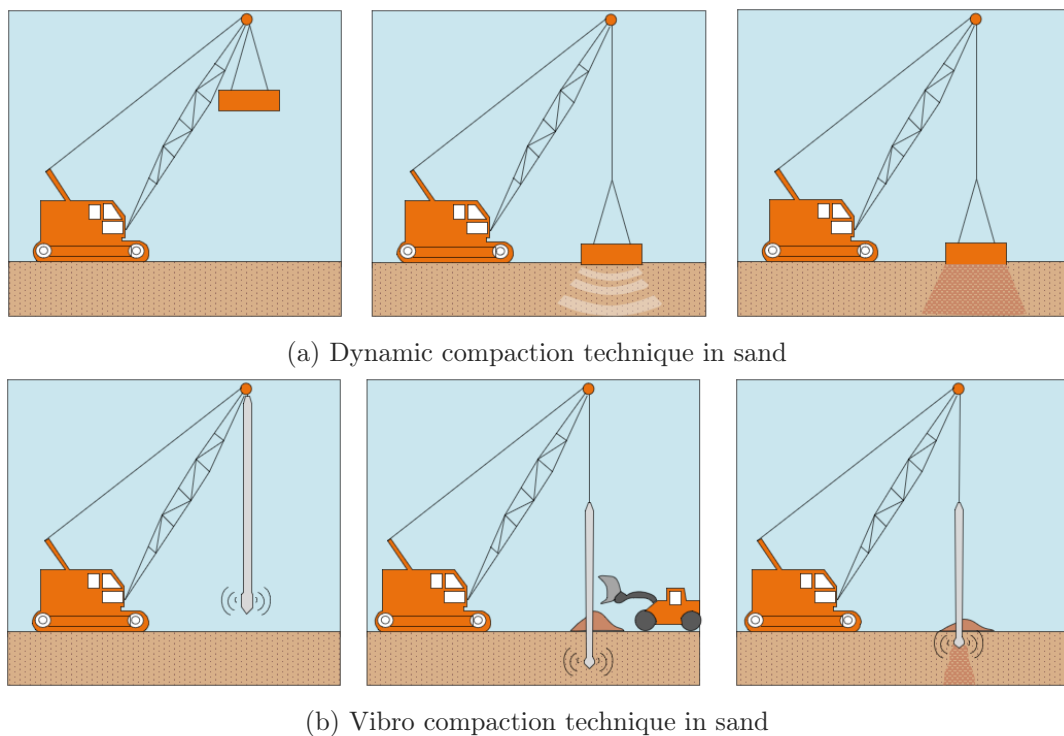


Figure 7.26: Ground improvement techniques.

The effects by compacting the top sand layer is investigated in an numerical model.

Numerical model 3 with ground improvement

The numerical model is made similar to model 3 except from a change in soil parameters in the top sand layer. The compactness of the first layer is made very dense with a corresponding to a normalized blowcount of $N_{1,60}=45$ which influences the stiffness and strength input parameters in *Plaxis*, which are seen in appendix I section I.5.

The structural response of the jacket substructure with implemented ground improvement for the upper layer is only investigated for the North-South direction as the change in response is assumed to follow a similar pattern for the East-West direction. The relative displacement of

the jacket substructure top compared to the displacement of embedded beams at mudline are illustrated on figure 7.27.

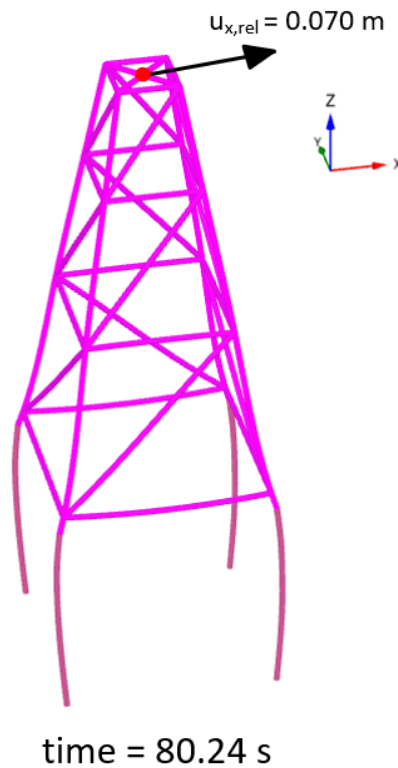


Figure 7.27: Relative displacements, $u_{x,rel}$ at interface node for earthquake in North-South direction.

Ground improvement by densification of the upper sand layer decreases the relative displacement in the x-direction (North-South) from 0.320 m (see figure 7.17a) to 0.07 m, which indicates that the densification of the uppermost soil layer has positive results on the relative displacement. Lastly, the response at the bottom of the jacket substructure in model 3 with implemented ground improvement is compared with the response at the bottom of the jacket substructure as well as liquefaction development in model 3, see figure 7.28.

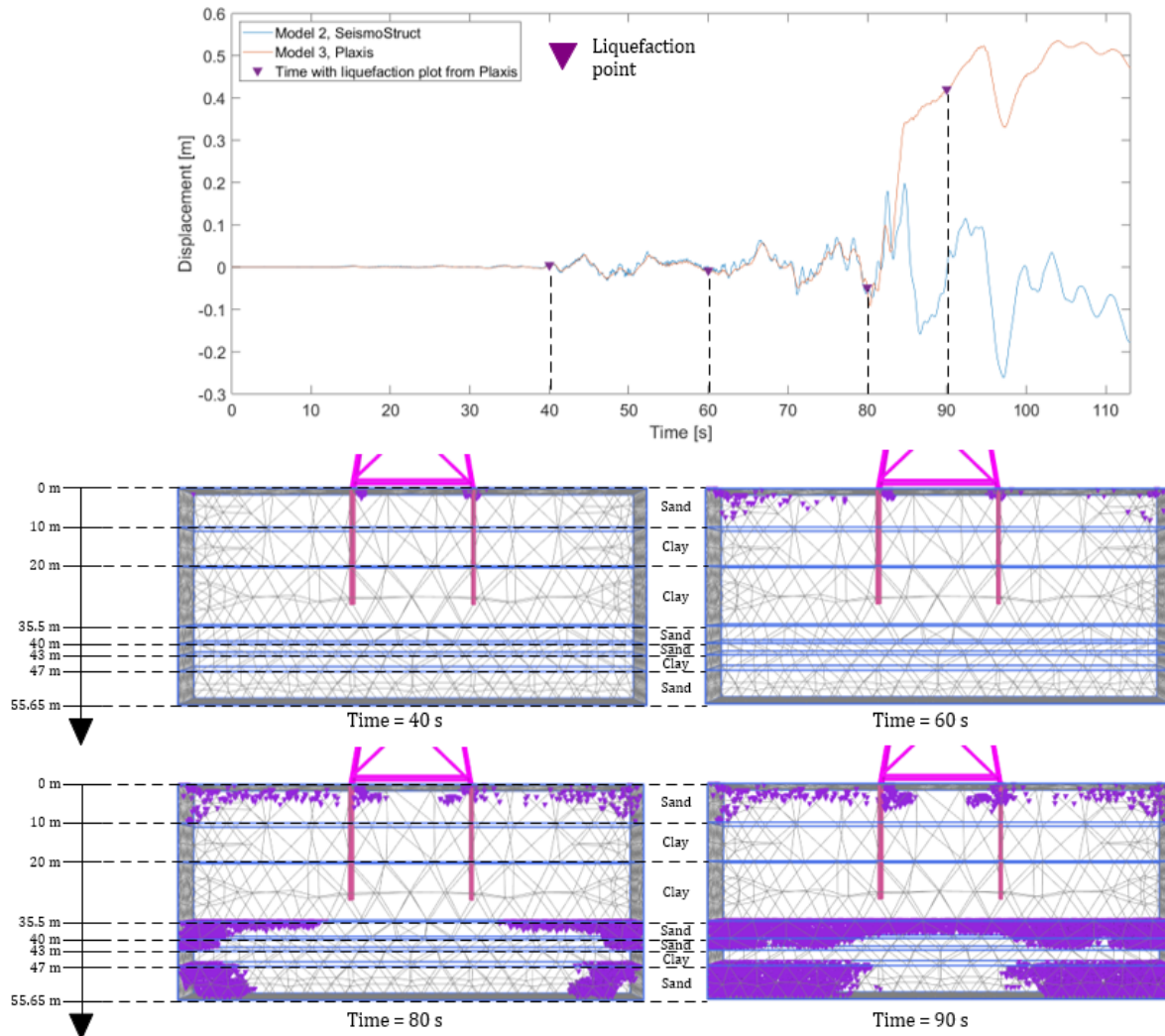


Figure 7.28: Time history for motions at bottom of jacket substructure for North-South and development of liquefaction points with porewater pressure ratio $r_u \geq 0.95$ when ground improvement has been performed for the upper layer.

It is concluded when comparing model 3 with an earthquake in the North-South direction with and without ground improvement illustrated on figure 7.21 and 7.28 that the number of developed liquefaction points have changed significantly in the upper sand layer. However the number of liquefaction points in the lower sand layers remain largely unchanged and will still rapidly develop and somewhere between 80-90 seconds liquefaction is fully developed in one of the sand layers leading to the same large deviation in displacement response of the jacket substructure. It is therefore concluded that the deviation in absolute displacement at the bottom of the jacket substructure between model 2 and 3 is caused by liquefaction of the lower sand layers.

7.6 Summary

The dynamic response of the 3 models have been found for the design earthquake in East-West and North-South directions. Model 1 is fast to model as the jacket substructure is assumed to be a fixed base where the soil layers are assumed to be as stiff as the bedrock so that ground motion propagate from bedrock to mudline without any amplification or deamplification and furthermore are the embedded piles assumed to move rigid and simultaneously with the surrounding soil. It is concluded that the fixed base assumption yields too conservative displacements of the jacket substructure and that a model with soil-pile interaction is better suited to describe the dynamic behaviour. The soil-pile interaction model is incorporated in model 2 in *SeismoStruct*, which is a bit more computationally demanding than model 1 as the model size is increased with embedded piles and furthermore has input acceleration time histories acting on soil-pile springs along the piles. Model 2 however captures the soil hysteretic behaviour in terms of soil damping and strength reduction which gives a better dynamic behaviour than model 1. The soil-pile springs in model 2 are defined by a whole lot of parameters in order to capture the dynamic soil behaviour realistic. The parameters are among other strength and stiffness degradation, cyclic resistance S-N curves, which are obtained through the SSRA. Model 3 in *Plaxis* is the most computational demanding model as a soil volume with advanced soil models is included. However, the soil-pile interaction is automatically incorporated in *Plaxis* when the soil constitutive models are defined. Model 3 captures the dynamic behaviour fully but requires a large soil volume as it is observed that liquefaction is fully developed, starting from the vertical boundaries and then spreads throughout the model. Model 3 with ground improvements has smaller relative displacements, due to prevention of liquefaction in the upper sand layer, however the total displacement still becomes large due to fully development of liquefaction in the lower sand layers.

8 | Conclusion

In this project an offshore wind turbine foundation's seismic response has been analysed in a non-linear time history using different types of numerical models. In the first part of the project the simulation of earthquake loading on a 2D ten-storey steel frame building using different seismic analysis procedures according to EN 1998-1 have been investigated.

It is concluded that the two linear, static methods, called lateral force method and modal response spectrum analysis, give a possibility of calculating the seismic loading requiring little computational demand and are simple to use. The methods have a simple, approximate way of incorporating material non-linear behaviour. However, it is concluded that this simple incorporation of material non-linearity assumes high energy dissipation during the earthquake loading, which is not the case as the structure behaves mostly elastic with low yielding. This assumption results in non-conservative responses and therefore the linear methods should be used with caution pertaining to the incorporation of material non-linearity. Furthermore, for the non-linearity to be incorporated uniformly distribution of yielding should be upheld. Therefore, the non-linear methods which include the non-linear static pushover method and the non-linear time history analysis are preferred in order to obtain the response of the ten-storey building. The non-linear static pushover method gives reasonable response for the 2D ten-storey steel frame building compared to the non-linear time history analysis and can easily be applied for simple structures with a predictable load pattern. However, for more advanced and dynamic structures, where the the dynamic behaviour cannot be compromised by evaluating the response in a static analysis, the non-linear time history analysis is the best suited despite it being the most complex and computationally demanding method.

The second part of the project revolves around the seismic analysis of an offshore wind turbine jacket foundation, located near the South Coast of Honshu in Japan, according to DNV-RP-0585. Firstly, a design earthquake at bedrock is found based on a Probabilistic Seismic Hazard Analysis (PSHA) that accounts for uncertainties of earthquake size, location, intensity and spectral properties at the site. It is concluded that the design earthquake with a return period of 475 years has a magnitude $M_w = 7.0$ with a site-to-source distance of $R = 64$ km and a Peak Ground Acceleration (PGA) of $PGA = 0.7$ g. Using this a recorded earthquake accelerogram has been chosen as the design earthquake.

Following this the design earthquake at bedrock is utilised to perform a Site Seismic Response Analysis (SSRA) in order to obtain the depth-varying ground response at the site. The output of the SSRA is depth-varying ground response over time such as stresses, strains, accelerations and excess porewater pressure ratio, where it is concluded that the soil layers deamplify the propagating waves from bedrock. It is also concluded that there is a high development of excess porewater pressure in some of the soil layers which might cause liquefaction to occur.

The ground response from the SSRA is utilised to perform a simple stress-based approach for liquefaction evaluation. It is concluded that the upper and lower sand layer are at high risk of liquefying during the design earthquake.

Lastly three different modelling approaches with increasing complexity are investigated and compared amongst each other. The 1st model consist of a rigid soil-pile interaction model with

no soil damping and no change in soil stiffness where ground motions excite the structure at the ground surface. It is concluded that the model yields too conservative deformations of the jacket substructure and that the assumption of a rigid soil-pile interaction is unreasonable. The 2nd model is a soil-pile interaction model where the embedded piles below the jacket substructure are modelled as beams with piecewise linear springs that are excited by depth-varying ground motions from SSRA. The 2nd model yields more reasonable results than the 1st model as it incorporates the soil-pile interaction by applying piecewise linear p-y curves along the embedded piles as well as strength and stiffness degradation and soil damping. Liquefaction is approximately incorporated through the stiffness and strength degradation results and the cyclic resistance S-N curves from the SSRA in the piecewise linear springs. The 3rd model is a soil volume model with ground motions acting on the bottom boundary of the soil volume with an advanced liquefaction soil model for sand and hardening model with shear modulus reduction for clay. The 3rd model yields larger displacements of the jacket substructure due to the lower sand layers being almost fully liquefied halfway through the dynamic analysis. However, before the lower sand layers are fully liquefied the displacement of the jacket substructure is similar to the 2nd model why it is concluded that both models yields reasonable results for the dynamic behaviour of the offshore wind turbine foundation. The reason why liquefaction becomes fully developed in sand layers may be due to the size of the soil volume in the 3rd model as liquefaction develops from the vertical boundaries in the earthquake direction and a resolution would be to make a larger model.

Literature

2022 GEM Foundation and Partners, 2022. 2022 GEM Foundation and Partners. *Global Seismic Hazard Map.*

<https://maps.openquake.org/map/global-seismic-hazard-map/#6/36.467/135.804>, 2022. Opened: 07/02/2022.

4C-Offshore, 2022. 4C-Offshore. *Global Offshore Renewable Map.*

<https://map.4coffshore.com/offshorewind/>, 2022. Opened: 14/03/2022.

Allotey and Naggar, 2008. N. Allotey and M. Hesham El Naggar. *A Numerical Study Into Lateral Cyclic Nonlinear soil-pile Response.*

https://www.researchgate.net/publication/233686097_A_numerical_study_into_lateral_cyclic_nonlinear_soil-pile_response#fullTextFileContent, 2008.

Allotey, 2006. N. K. Allotey. *Nonlinear Soil-structure Interaction in Performance-based Design*, 2006. Ph.D thesis University of Western Ontario London.

Ambersariya, 2019. Deepak Ambersariya. *Types of Earthquakes | Four Major Types.*

<https://inventionsky.com/four-major-types-of-earthquakes/>, 2019. Opened: 22/12/2021.

Anne K. Petry, 2021. Anne K. Petry. *Geography of Japan.*

<https://fsi-live.s3.us-west-1.amazonaws.com/s3fs-public/geo.pdf>, 2021. Opened: 18/11/2021.

Ansys, 2020. Ansys. *Mode Participation Factor and Effective Mass.*

<https://courses.ansys.com/index.php/courses/modal-analysis/lessons/mode-participation-factor-and-effective-mass-lesson-4/>, 2020. Opened: 31/01/2022.

Asia Wind Energy Association, 2021. Asia Wind Energy Association. *Japan.*

<https://www.asiawind.org/research-data/market-overview/japan/>, 2021. Opened: 18/11/2021.

Baker, 2013. Jack W. Baker. *Introduction to Probabilistic Seismic Hazard Analysis.* Jack W. Baker, Second edition, 2013.

Budhu, 2010. Muni Budhu. *Soil mechanics and foundation.* John Wiley & sons, INC, 3rd edition, 2010.

Caicedo et al., 2018. Bernardo Caicedo, Cristhian Mendoza, Fernando López and Arcesio Lizcano. *Behavior of diatomaceous soil in lacustrine deposits of Bogotá.* *Journal of Rock Mechanics and Geotechnical Engineering*, 2018. Full Length Article.

Carlton, 2014. Brian Carlton. *An Improved Description of the Seismic Response of Sites with High Plasticity Soils, Organic Clays, and Deep Soft Soil Deposits.* University of California, Berkeley), 2014. https://digitalassets.lib.berkeley.edu/etd/ucb/text/Carlton_berkeley_0028E_14137.pdf.

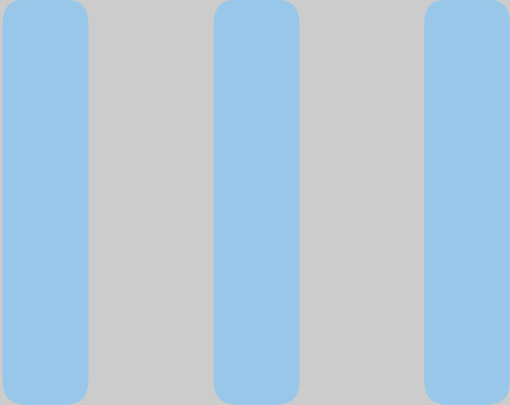
- CESMD, 2022.** CESMD. *Center for Engineering Strong Motion Data.*
<https://www.strongmotioncenter.org/>, 2022. Opened: 02/02/2022.
- Chen et al., 2016.** I-Wen Chen, Bao-Leng Wong, Yu-Hung Lin, Shiu-Wu Chau and Hsin-Haou Huang. *Design and Analysis of Jacket Substructures for Offshore Wind Turbines.* MDPI, 2016. <https://www.mdpi.com/1996-1073/9/4/264>.
- Chopra, 2007.** Anil K. Chopra. *Dynamics of Structures. Theory and Application to Earthquake Engineering.* Pearson Education, 2007.
- Collier and Alblas, 2018.** W. Collier and L.M. Alblas. *Reducing Cost in Jacket Design: Comparing the Integrated and Superelement Approach.*
https://www.dnv.com/Images/Reducing-cost-in-jacket-design-Comparing-the-integrated-and-superelement-approach_tcm8-149174.pdf, 2018. Opened: 29/03/2022.
- Cook et al., 2002.** Robert D. Cook, David S. Malkus, Michael E. Plesha and Robert J. Witt. *Concepts and Applications of Finite Element Analysis.* John Wiley & Sons, INC, Fourth edition, 2002.
- Costanzo et al., 2019.** Silvia Costanzo, Roberto Tartaglia, Gianmaria Di Lorenzo and Attilio De Martino. *Seismic Behaviour of EC8-Compliant Moment Resisting and Concentrically Braced Frames.* MDPI - Buildings, 2019.
<https://www.mdpi.com/2075-5309/9/9/196>.
- Damkilde, 2019.** Lars Damkilde. *Introduction to Structural Dynamics.* Aalborg University, 2019.
- DeepSoil, 2020.** DeepSoil. *A Computer Program for 1D Equivalent Linear and Nonlinear Site Response Analysis.*
http://deepsoil.cee.illinois.edu/Files/DEEPSOIL_User_Manual_v7.pdf, 2020.
User Manual version 7.0.
- DNV-RP-0126, 2016.** DNV-RP-0126. *Support Structures for Wind Turbines DNVGL-ST-0126.* DNV, 2016.
- DNV-RP-0585, 2021.** DNV-RP-0585. *Seismic Design of Wind Power Plants DNV-RP-0585.* DNV, 2021.
- Dobry et al., 1982.** R. Dobry, R.S. Ladd, F.Y. Yokel, R.M. Chung and D. Powell. *Prediction of Pore Water Pressure Buildup and Liquefaction of Sands During Earthquakes by the Cyclic Strain Method.* National Bureau of Standards Building Science Series 138, 1982.
- Elghazouli, 2017.** Ahmed Y. Elghazouli. *Seismic Design of Buildings to Eurocode 8.* Taylor & Francis Group, 2017.
- EN1998-1, 2004.** EN1998-1. *Eurocode 8: Design of structures for earthquake resistance - Part 1.* The European Union, 2004.
- EN1998-3, 2005.** EN1998-3. *Eurocode 8: Design of structures for earthquake resistance - Part 3.* The European Union, 2005.
- Gazetas, 1991.** George Gazetas. *Foundation Vibrations.* In: Fang, HY. (eds) *Foundation Engineering Handbook.* Springer, Boston, 1991.

- G.R. and G.C., 1974. Saragoni G.R. and Hart G.C.** *Simulation of artificial earthquakes. Earthquake Engineering-and Structural Dynamics, 1974. vol. 2 pp. 219-267.*
- Groholski et al., 2015. D. R. Groholski, Y.M.A. Hashash, M. Musgrove, J. Harmon and B. Kim.** *Evaluation of 1-D Non-linear Site Response Analysis using a General Quadratic/Hyperbolic Strength-Controlled Constitutive Model. 6th International Conference on Earthquake Geotechnical Engineering, 2015.*
<https://secure.tcc.co.nz/ei/images/ICEGE15%20Papers/Hashash%20269.00.pdf>.
- Hamidi et al., 2013. Babak Hamidi, Jean-Marc Debats, Hamid Nikraz and Serge Varaksin.** *Offshore Ground Improvement Records, 2013. Australian Geomechanics Journal 48(4):111-122. Civil Engineering Department, Curtin University.*
- Idriss and Boulanger, 2008. I. M. Idriss and R. W. Boulanger.** *Soil Liquefaction During Earthquakes. Earthquake Engineering Research Institute, EERI, 2008.*
- Idriss and Boulanger, 2010. I. M. Idriss and R. W. Boulanger.** *SPT-based Liquefaction Triggering Procedures, 2010. UCD/CGM-10/02, Cenfter for Geotechnical Modeling, department of Civil & Environmental Engineering College of Engineering University of California at Davis.*
- Institute, 2018. Southwest Research Institute.** *Liquefaction Consortium To Improve Earthquake Models.* <https://www.swri.org/technology-today/liquefaction-consortium-earthquake-models>, 2018. Opened: 20/12/2021.
- International Energy Agency, 2021. International Energy Agency.** *Net Zero by 2050: A Roadmap for the Global Energy Sector.*
<https://www.iea.org/reports/net-zero-by-2050>, 2021. Opened: 14/09/2021.
- IRENA, 2019. IRENA.** *Future of wind: Deployment, investment, technology, grid integration and socio-economic aspects. A Global Energy Transformation paper, 2019.*
<https://www.irena.org/publications/2019/Oct/Future-of-wind>.
- IRIS, 2021. IRIS.** *IRIS Earthquake Browser.*
<https://ds.iris.edu/ieb/index.html?format=text&nodata=404&starttime=1970-01-01&endtime=2025-01-01&minmag=0&maxmag=10&mindepth=0&maxdepth=900&orderby=time-desc&src=usgs&limit=1000&maxlat=51.40&minlat=-51.40&maxlon=111.71&minlon=-111.71&zm=3&mt=ter>, 2021. Opened: 01/03/2022.
- ISO 19901-2, 2017. ISO 19901-2.** *Petroleum and natural gas industries - Specific requirements for offshore structures - Part 2: Seismic design procedures and criteria. Dansk Standard, 2017.*
- J. et al., 2006a. Hancock J., Watson-Lamprey J., Abrahamson N.A., Bommer J.J. and Markatis A., McCoy E. and Mendis R.** *An improved method of matching response spectra of recorded earthquake ground motion using wavelets. Journal of Earthquake Engineering, Vol. 10 pp. 67-89, 2006a.*
<https://www.tandfonline.com/doi/abs/10.1080/13632460609350629>.
- J. et al., 2006b. Hancock J., Watson-Lamprey J., Abrahamson N.A., Bommer J.J., Markatis A., McCoy E. and Mendis R.** *An improved method of matching*

- response spectra of recorded earthquake ground motion using wavelets. Journal of Earthquake Engineering, 2006b. vol.10, pp.67-89.*
- Jia, 2017. Junbo Jia.** *Modern Earthquake Engineering Offshore and Land-based Structures.* Springer, 2017.
- Kanno et al., 2006. Tatsuo Kanno, Akira Narita, Nobuyuki Morikawa, Hiroyuki Fujiwara and Yoshimitsu Fukushima.** *A New Attenuation Relation for Strong Ground Motion in Japan Based on Recorded Data. Bulletin of the Seismological Society of America, 2006. Vol. 96, No. 3, pp. 879–897.*
- Kramer, 1996. Steven L. Kramer.** *Geotechnical Earthquake Engineering.* Prentice Hall, 1996.
- Kulhawy and Mayne, 1990. F.H. Kulhawy and P.W. Mayne.** *Manual on Estimating Soil Properties For Foundation Design. Cornell University, 1990. Research Project.*
- Kuo et al., 2021. Yu-Shu Kuo, Tzu-Ling Weng, Hui-Ting Hsu, Hsing-Wei Chang, Yun-Chen Lin, Shang-Chun Chang, Ya-Jhu Chuang, Yu-Hsiu Tseng and Yih-Ting Wong.** *A Methodology for Estimating the Position of the Engineering Bedrock for Offshore Wind Farm Seismic Demand in Taiwan. MDPI, 2021.*
<https://www.proquest.com/openview/cd93e83a7be18e0c9f902c5e5b6da30d/1?pq-origsite=gscholar&cbl=2032402>.
- L. and N.A., 2010. Al-Atik L. and Abrahamson N.A.** *An improved method for nonstationary spectral matching. Earthquake Spectra., 2010. Vol. 26, No. 6, pp. 601-617.*
- Matasovic and Ordóñez, 2011. Neven Matasovic and Gustaco A. Ordóñez.** *D-MOD2000 A Computer Program for Seismic Response Analysis of Horizontally Layered Soil Deposits, Earthfill Dams and Solid Waste Landfills.*
<http://www.geomotions.com/Download/D-MOD2000Manual.pdf>, 2011. User Manual.
- Matasovic and Vucetic, 1995. Neven Matasovic and Mladen Vucetic.** *Generalized Cyclic-Degradation-Pore-Pressure Generation Model for Clays.*
https://www.researchgate.net/publication/248878556_Generalized_Cyclic-Degradation-Pore-Pressure_Generation_Model_for_Clays#fullTextFileContent, 1995. *Journal of Geotechnical Engineering, Volume 121 Issue 1.*
- Matasovic and Vucetic, 1993. Neven Matasovic and Mladen Vucetic.** *Cyclic Characterization of Liquefiable Sands.* <https://ascelibrary.org/doi/10.1061/%28ASCE%290733-9410%281993%29119%3A11%281805%29>, 1993. *Journal of Geotechnical Engineering, Volume 119 Issue 11.*
- Ministry of Economics, Trade and Industry, 2021. Ministry of Economics, Trade and Industry.** *TOKYO “BEYOND-ZERO” WEEK.* https://www.meti.go.jp/english/policy/energy_environment/global_warming/roadmap/tokyo_beyond-zero_week/, 2021. Opened: 18/11/2021.
- Międlarz and Bałachowski, 2018. Kamila Międlarz and Lech Bałachowski.** *Determination of p-y curves for offshore piles based on in-situ soil investigations. MATEC Web Conf. Volume 219, 2018, 2018.*
<https://doi.org/10.1051/mateconf/201821905003>.

- Mujtaba et al., 2017. Hassan Mujtaba, Khalid Farooq, Nagaratnam Sivakugan and Braja M. Das. *Evaluation of Relative Density and Friction Angle Based on SPT-N Values, 2017. KSCE Journal of Civil Engineering; Seoul Vol. 22, Iss. 2, (Feb 2018): 572-581.*
- N.A., 1992. Abrahamson N.A. *An Improved Method for Nonstationary Spectral Matching. Seismological Research Letters, 1992. vol.63, no.1, pp.30.*
- Oscar Moreno-Torres and Olson, 2010. Youssef M. A. Hashash Oscar Moreno-Torres and Scott M. Olson. *A Simplified Coupled Soil-Pore Water Pressure Generation for Use in Site Response Analysis. <https://ascelibrary.org/doi/abs/10.1061/41095%28365%29314>, 2010. GeoFlorida 2010: Advances in Analysis, Modeling & Design.*
- P-Delta effect, 2019. P-Delta effect. *P-Delta effect. <https://wiki.csiamerica.com/display/kb/P-Delta+effect>, 2019. Opened: 27/01/2022.*
- Partner Engineering and Science Inc, 2014. Partner Engineering and Science Inc. *US Peak Ground Acceleration Seismic Map. <https://www.partneresi.com/resources/library/peak-ground-acceleration-seismic-map>, 2014. Opened: 24/11/2021.*
- Phien-wej et al., 2012. N. Phien-wej, M. Humza and Z. Zaw Aye. *Numerical Modeling of Diaphragm Wall Behavior in Bangkok Soil Using Hardening Soil Model, 2012. International Society for Soil Mechanics and Geotechnical Engineering (ISSMGE). Geotechnical Aspects of Underground Construction in Soft Ground – Viggiani (ed) © 2012 Taylor and Francis Group, London, ISBN 978-0-415-68367-8.*
- Plaxis, 2021a. Plaxis. *PLAXIS 3D-Material Models Manual. <https://communities.bentley.com/products/geotech-analysis/w/plaxis-soilvision-wiki/46137/manuals---plaxis>, 2021a. Version 22.0.*
- Plaxis, 2021b. Plaxis. *PLAXIS 2D-Reference Manual. <https://communities.bentley.com/products/geotech-analysis/w/plaxis-soilvision-wiki/46137/manuals---plaxis>, 2021b. Version 22.0.*
- Ritchie and Roser, 2020. Hannah Ritchie and Max Roser. *Energy. Our World in Data, 2020. <https://ourworldindata.org/energy>.*
- Roblee and Chiou, 2004. Cliff Roblee and Brian Chiou. *A proposed geindex model for design selection of non-linear properties for site response analyses. Proceedings of the 8th U.S. National Conference on Earthquake Engineering, 2004. https://apps.peer.berkeley.edu/lifelines/Workshop304/pdf/geo_Roblee.pdf.*
- Rodríguez-Marek et al., 2002. Adrián Rodríguez-Marek, Jonathan D. Bray and Norman A. Abrahamson. *An Empirical Geotechnical Seismic Site Response Procedure. Earthquake spectra, 2001-02, 2002.*
- Ross Stein and David Jacobson by Temblor, 2016. Ross Stein and David Jacobson by Temblor. *Damaging Japan earthquake strikes between two recent large shocks. <https://temblor.net/earthquake-insights/damaging-japan-earthquake-strikes-between-two-recent-large-shocks-1638/>, 2016. Opened: 14/09/2021.*

- Seed et al., 1975. H. Bolton Seed, I. M. Idriss, F. Makdisi and N. Banerjee.** *Representation of Irregular Stress Time Histories by Equivalent Uniform Stress Series in Liquefaction Analyses, 1975. EERC 75-29, Earthquake Engineering Research Center, University of California, Berkeley.*
- SeismoStruct, 2022. SeismoStruct.** *A Computer Program for Static and Dynamic Nonlinear Analysis of Framed Structures. <https://seismosoft.com/>, 2022. User Manual.*
- Si and Midorikawa, 1999. Hongjun Si and Saburoh Midorikawa.** *New attenuation relationships for peak ground acceleration and velocity considering effects of fault type and site condition. Journal of Structural and Construction Engineering, AIJ, 523, 63-70, 1999. <https://www.issmge.org/uploads/publications/96/97/IS11-1.pdf>.*
- Tomlinson and Boorman, 2001. M.J. Tomlinson and R. Boorman.** *Foundation Design And Constriction. Longman Group United Kingdom, 2001.*
- Vrochidou et al., 08 2014. Eleni Vrochidou, Petros Alvanitopoulos, I Andreadis, Anaxagoras Elenas and Katerina Mallousi.** *Synthesis of artificial spectrum-compatible seismic accelerograms. Measurement Science and Technology, 25, 2014. doi: 10.1088/0957-0233/25/8/085002.*
- Vucetic and Dobry, 1986. Mladen Vucetic and Ricardo Dobry.** *Pore pressure buildup and liquefaction at level sandy sites during earthquakes. Research report (Rensselaer Polytechnic Institute. Department of Civil Engineering), 1986. no. 86-3.*
- Wakamatsu, 1997. Kazue Wakamatsu.** *LIQUEFACTION HISTORY, 416-1997, IN JAPAN. Institute of Industrial Science, University of Tokyo, 1997.*
- Wang, 1979. W. Wang.** *Some findings in soil liquefaction. Water Conservancy and Hydroelectric Power Scientific Research Institute, Beijing, China, 1979.*



Appendix

Appendix A	Earthquake Characteristics	106
Appendix B	Seismic Design Tools	111
Appendix C	Principles of Seismic Design According to EN 1998-1	126
Appendix D	Seismic Analysis Methods According to EN 1998-1	133
Appendix E	Response of Multistory Steel Frame Building	152
Appendix F	Seismic Hazard Analysis	164
Appendix G	Site Seismic Response Analysis	177
Appendix H	Geotechnical Site Conditions	199
Appendix I	Input Parameters for Numerical Models	207
Appendix J	P-y Curves for Laterally Loaded Piles .	225
Appendix K	Liquefaction Hazard Analysis	228

Appendix A | Earthquake Characteristics

In this appendix the earthquake characteristics are explained in more detail as well as the hazards associated with earthquakes, as well as a description of tectonic earthquakes.

A.1 Earthquake characteristics

An earthquake is characterised as the travelling of seismic waves transmitted in all directions from a disturbance in the earth, or as vibrations of the earth due to release of energy from a ground rupture.

Earthquake type

The cause of the disturbance can be due to a multitude of reasons which include tectonic earthquakes, volcanic earthquakes, explosion earthquakes and collapse earthquakes, which are described below in accordance to [Kramer, 1996].

- Tectonic earthquakes are the most common and destructive type of earthquakes, which occurs when the earth's crust ruptures due to geological forces on neighbouring plates. Their geographical location is usually well known as they frequently occur at tectonic plate boundaries and/or at rupture zones.
- Volcanic earthquakes are the second most well known and destructive earthquake. This type of earthquake usually occurs from a combination of the energy released from volcanic eruption and rupture of tectonic plates, their location is usually also well known.
- Collapse earthquakes is a result of the collapse of mines and underground caverns due to seismic waves caused by explosions. This phenomena is called "mine bursts" which can cause small local earthquakes.
- Explosion earthquakes occurs as a result of detonation of chemical or nuclear devices.

Earthquake size

The earthquake size is measured, denoted and quantified as the earthquake magnitude, produced from seismic waves and measured by seismographs. The earthquake magnitude is a scale on how much energy is released during an earthquake. To quantify measured earthquakes a variety of scales have been developed over time to accurately quantify its size. The most commonly used today is the "Moment Magnitude Scale" which is a scale that quantifies the size of an earthquake based on the amount of energy released. The moment magnitude is obtained from equation (A.1), [Kramer, 1996].

$$M_w = \frac{\log(M_0)}{1.5} - 10.7 \tag{A.1}$$

Where M_0 is the seismic moment which defines how much force is needed to generate the

recorded waves and is obtained from equation A.2.

$$M_0 = \mu D A \quad (\text{A.2})$$

Where μ is the rigidity of the soil, D is the distance the block slips and A is the area of the ruptured zone. These parameters are illustrated on figure A.1.

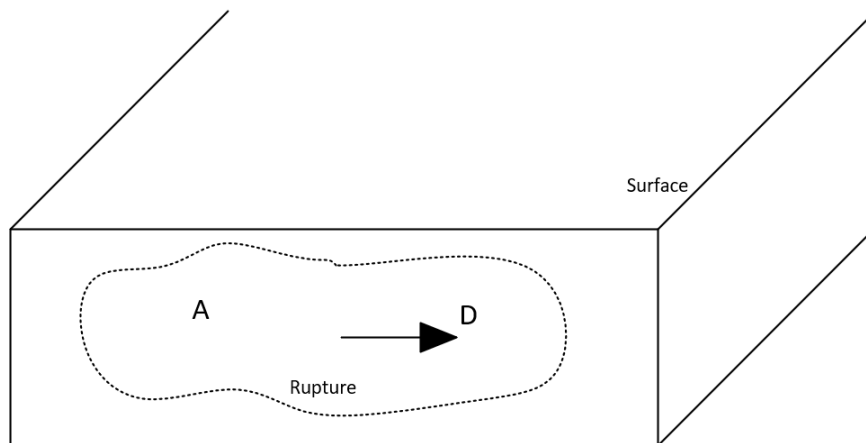


Figure A.1: Sliding of block with rupture zone illustration.

Earthquake location

The last essential factor when it comes to earthquake characteristic is the earthquake location. On a global scale the locations of earthquakes are usually well defined, however locally in a seismic active area it is pretty uncertain where an earthquake will occur, therefore the following notations of earthquake distance is used, [Kramer, 1996].

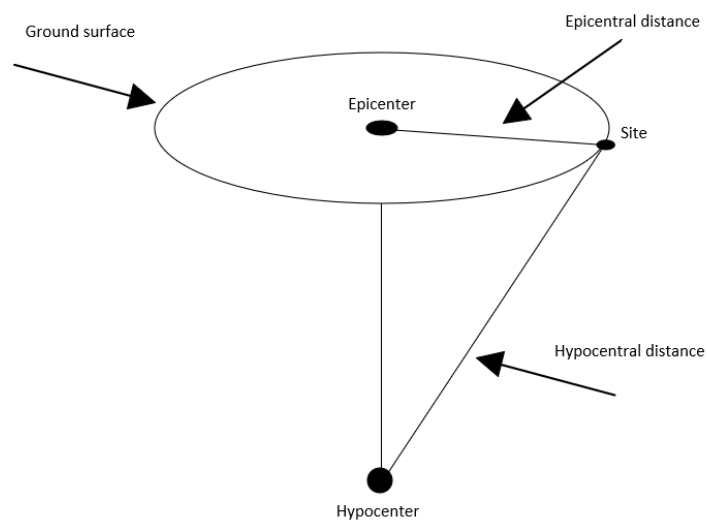


Figure A.2: Notation for earthquake location.

The earthquake originates from the *hypocenter*, which is the point at which an earthquake

begins, the point on the ground surface located directly above the origin of the earthquake is the *epicenter*. The distance between the epicenter and the specific site is known as the *epicentral distance* and the distance between the specific site and hypocenter is known as the *hypocentral distance*. When it comes to defining the specific location of an earthquake usually the epicentral distance is used, as well as the depth of the earthquakes hypocenter.

A.2 Seismic Hazards

Seismic hazards might occur during or after an earthquake has occurred. These hazards can be crucial to the design of structures in seismic active zones, and therefore the most crucial hazards associated with an earthquake are listed below:

Ground shaking

When an earthquake occurs, energy is released and travels by seismic waves through the internal structure of earth until the waves reach the ground surface. The seismic waves cause the ground to start shaking, and depending on the size of the earthquake, the location and characteristics of the site, the ground shaking can vary enormously. The size of ground shaking is very important as this can lead to other seismic hazards, [Kramer, 1996]. As the seismic waves travel through the crust of the earth they enter different types of soil. The ground shaking is highly dependent of the soil type and therefore it is of great importance to evaluate the effect that soil conditions have on ground shaking. In order to design structures against major earthquake damages predictions of ground motions are needed and therefore providing design ground motions are of great importance.

Liquefaction

One of the most critical examples of seismic hazards can occur during ground shaking when a soil deposit is loose and saturated. When a loose saturated soil deposit undergoes crucial cyclic or transient motions the soil will lose majority of its strength and appear to flow as a fluid [Kramer, 1996]. During liquefaction the soil strength is often reduced to the point of being unable to support the structure causing instability. The phenomena is very complicated but framework has made it possible to consider the triggering conditions of liquefaction to appear and procedures for evaluation of hazards led by liquefaction.

Landslides

Another seismic hazard that can occur at sloped surfaces is landsliding. The landslides can be caused by liquefaction or simply because the slope at the soil surface which was previously stable becomes unstable, [Kramer, 1996]. The consequence for offshore structures are the instability of the foundation in the case where a turbine is placed on a unstable slope that begins to slide or if the turbine is placed at the bottom of an unstable slope, which could lead to large sliding soil deposits impacting the foundation with large loads.

Tsunamis

When an earthquake happens in the seabed rapid movement of the seabed releases the energy into the water causing a series of tsunami waves. On the open sea a tsunami wave can travel

great distances at high speeds, but are usually hardly detectable until it reaches the shoreline where the water depth decreases and the wave height increases, [Kramer, 1996]. Tsunami waves can cause tremendous damage to offshore structures due to the enormous wave loads.

A.3 Tectonic earthquakes

The surface of the earth consists of several plates, called the tectonic plates which are shown in figure A.3.

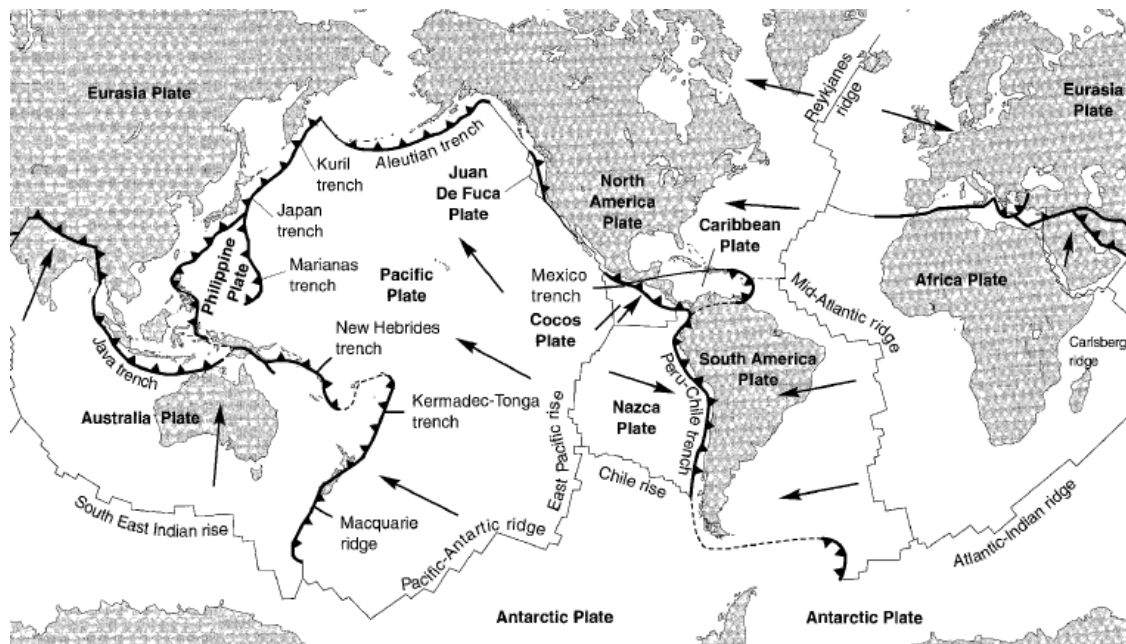


Figure A.3: The major tectonic plates and their movement indicated by large arrows, [Kramer, 1996].

These plates tend to move with respect to each other and occasionally a sudden movement between the boundaries of the tectonic plates causes an earthquake. It is therefore often in the boundaries of the tectonic plates that the strongest earthquakes appear, which can be seen in figure A.4.

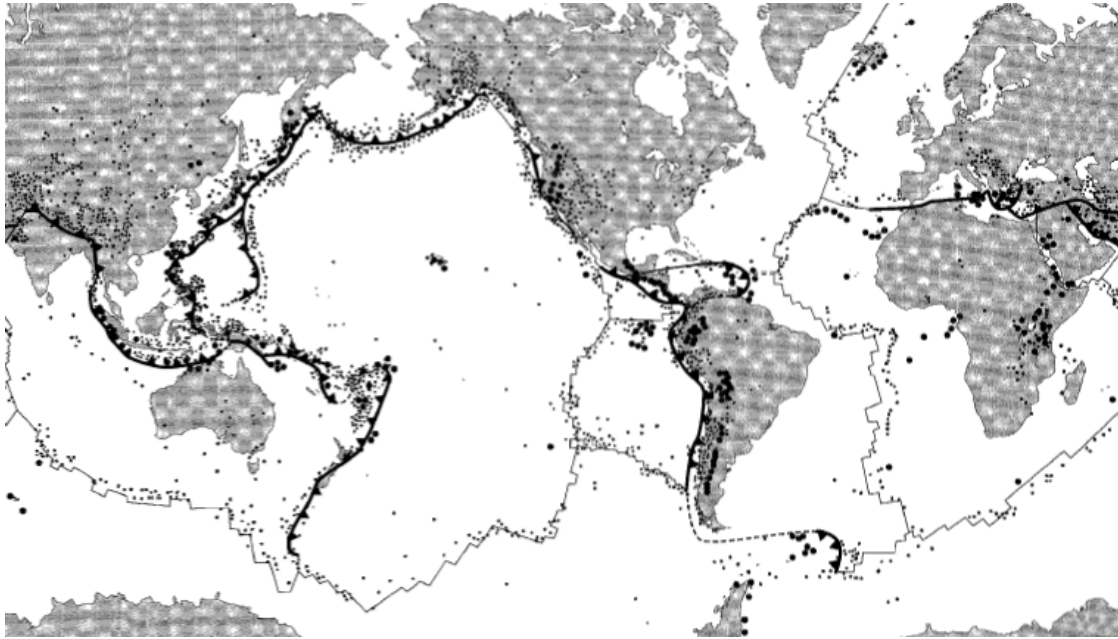


Figure A.4: World wide earthquakes with epicenters marked with black dots, [Kramer, 1996].

Figure A.4 shows that the vast majority of recorded earthquakes occur at plate boundaries which shows that tectonic earthquakes are the most frequently occurring earthquakes.

The tectonic plates can move in different ways with respect to each other which can be seen in figure A.5. The soil below the fault plane is referred to as the foot wall and the soil above the fault plane is referred to as the hanging wall. In figure A.5a the hanging wall moves downwards relative to the foot wall which is called a normal fault. In figure A.5b the opposite happens which is called a reverse fault. These movements, normal fault and reverse fault, that occur along the fault plane is called dip slip movements. In figure A.5c the movement occurs transverse to the fault plane and is called a strike slip movement. Often both movements of dip slip and strike slip occur and is called an oblique fault movement.

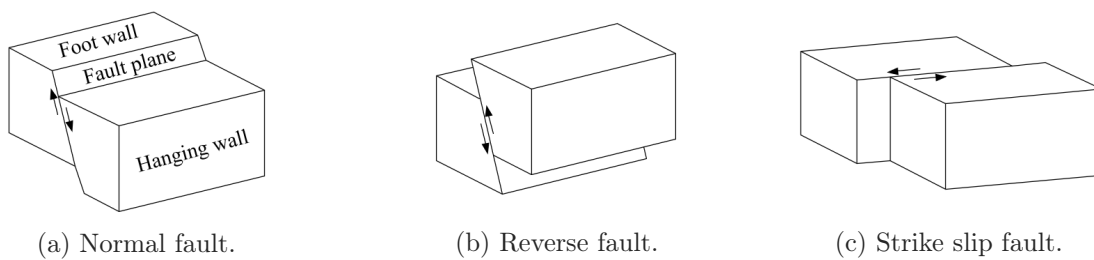


Figure A.5: Different types of fault movements.

A fault plane can involve thousands of square kilometers and the point at where the first seismic waves can be detected is called the *hypocenter* of an earthquake. The closest point on the ground surface is called the *epicenter* and the *focal depth* is the distance between *hypocenter* and *epicenter*.

Appendix B | Seismic Design Tools

In this appendix the seismic design tools used in the EN 1998-1 analysis methods are described such as accelerograms, response spectrum and how to modify or generate an accelerogram such that its response is similar to the response spectrum.

B.1 Accelerograms

Accelerogram is a measure of ground acceleration with respect to time, the measurement are performed by instrumental measurements located at measurement stations. The accelerations are usually expressed as m/s^2 or as a fraction of gravity acceleration (g) and the time is measured in seconds. At figure B.1 some representative accelerograms of earthquake ground motions are shown and illustrate how accelerogram may look like and how different accelerograms can be.

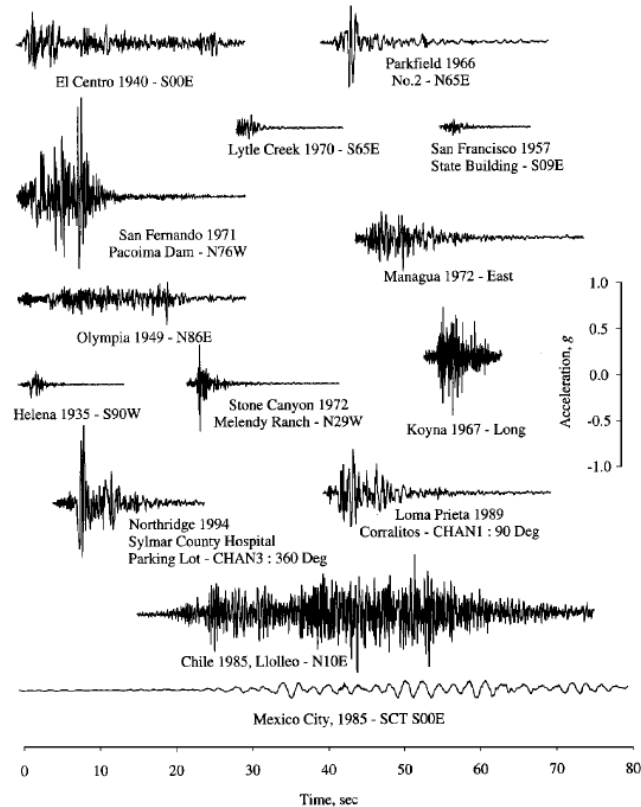


Figure B.1: Accelerograms from several earthquakes, [Chopra, 2007].

Some important characteristics of accelerograms are their peak ground acceleration (PGA), frequency content and duration. Accelerograms are an essential tool used in time history analysis methods for the design of structures undergoing seismic action. However due to the method being computationally demanding and time consuming, the seismic design tool known as the elastic response spectrum has been developed to analyze earthquakes.

B.2 Elastic Response Spectrum

By analysing a wide span of linear single degree of freedom (SDOF) systems, with different natural periods, that are exposed to the same earthquake and finding the maximum response, which could be displacement, velocity or acceleration, a response spectrum can be made. A response spectrum is a very useful design tool as future earthquake ground motions are unknown. The response spectrum contains information about the maximum response of a SDOF system depending on its natural period. To make a design spectrum several spectra for different earthquakes are obtained and by enveloping and smoothening them, a single curve that represent the maximum response of a structure exposed to a number of possible earthquake accelerograms is obtained, [Elghazouli, 2017].

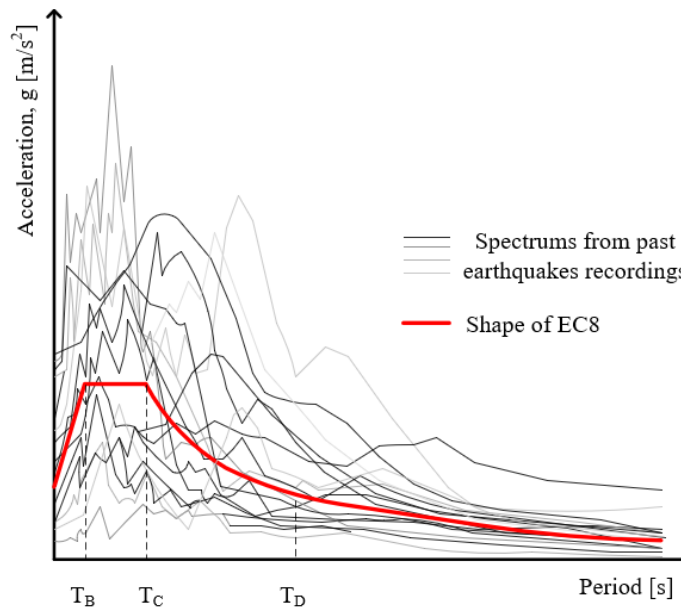


Figure B.2: Response spectrum of representative motions of earthquakes.

The spectral acceleration is the maximum absolute acceleration that the mass experiences. In EN 1998-1 the response spectrum is also called an elastic response spectrum and can be obtained when the ground type and the seismic activity in the location are known. The elastic response spectrum is obtained from the following equation (B.1):

$$\begin{aligned}
 S_e(T) &= a_g \cdot S \cdot \left[1 + \frac{T}{T_B} \cdot (\eta \cdot 2.5 - 1) \right] & \text{for } 0 \leq T \leq T_B \\
 S_e(T) &= a_g \cdot S \cdot \eta \cdot 2.5 & \text{for } T_B \leq T \leq T_C \\
 S_e(T) &= a_g \cdot S \cdot \eta \cdot 2.5 \cdot \frac{T_C}{T} & \text{for } T_C \leq T \leq T_D \\
 S_e(T) &= a_g \cdot S \cdot \eta \cdot 2.5 \cdot \frac{T_C \cdot T_D}{T^2} & \text{for } T_D \leq T \leq 4
 \end{aligned} \tag{B.1}$$

where

S_e	Elastic response spectrum [g]
T	Vibration period of SDOF system [s]
a_g	Design ground acceleration ($a_g = \gamma_1 a_{gR}$) [g]
γ_1	Importance factor [-]
a_{gR}	Reference peak ground acceleration [g]
T_B	Lower limit of constant spectral acceleration branch [s]
T_C	Upper limit of constant spectral acceleration branch [s]
T_D	Value defining the beginning of the constant displacement response range [s]
S	Soil factor [g]
η	Damping correction factor with reference value of $\eta = 1$ for 5% structural damping ratio [-].

The reference peak ground acceleration a_g is obtained from a zonation map based on the geographical location of the specific site which is investigated, see figure B.3.

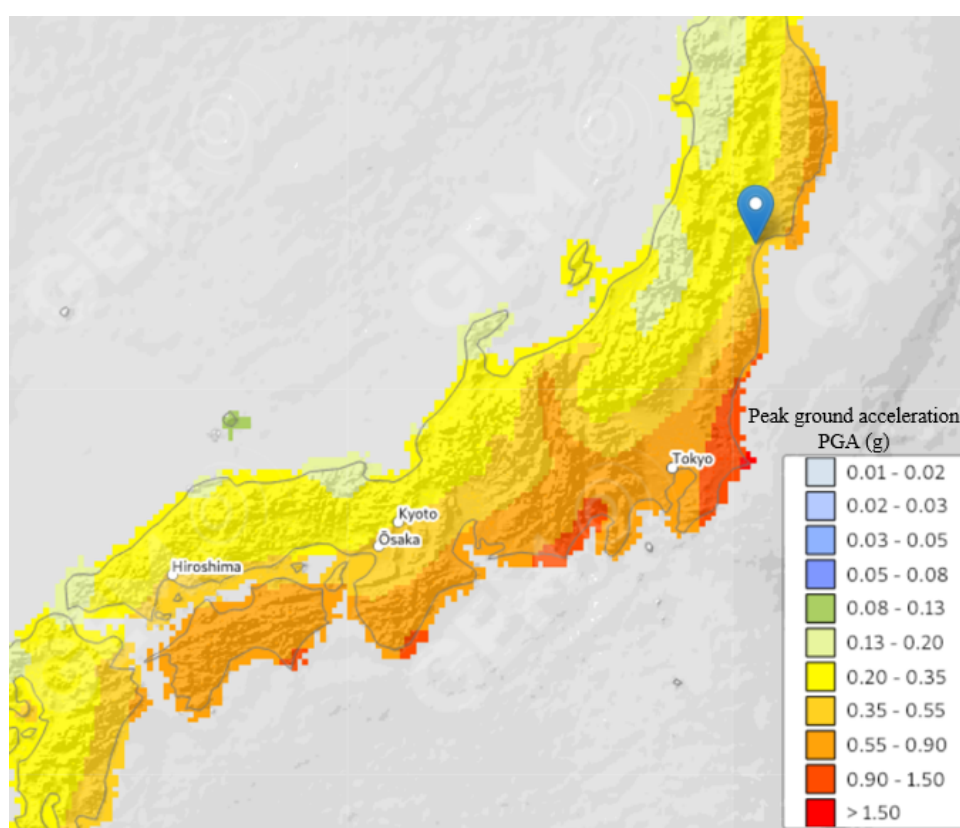


Figure B.3: Zonation map of Japan, [2022 GEM Foundation and Partners, 2022].

The reference peak ground acceleration obtained is a reference peak ground acceleration with a 475 year return period or a 10% probability of exceedance in 50 years. The parameters T_B , T_C , T_D and S are obtained based on the type (shape) of the response spectrum where type 1 describes the response in an area of high seismic activity and type 2 describes the response in an area of low seismic activity and groundtype, see table B.1 and B.2.

Table B.1: Parameters describing the elastic response spectrum.

Type 1					Type 2				
Ground type	S	Tb	Tc	Td	Ground type	S	Tb	Tc	Td
A	1.00	0.15	0.40	2.00	A	1.00	0.05	0.25	1.20
B	1.20	0.15	0.50	2.00	B	1.35	0.05	0.25	1.20
C	1.15	0.20	0.60	2.00	C	1.50	0.10	0.25	1.20
D	1.35	0.20	0.80	2.00	D	1.80	0.10	0.30	1.20
E	1.40	0.15	0.50	2.00	E	1.60	0.05	0.25	1.20

Table B.2: Ground types.

Ground type	Stratigraphic profile
A	Rock or other rock-like geological formation, including at most 5 m of weaker material at the surface.
B	Deposits of very dense sand, gravel, or very stiff clay, at least several tens of metres in thickness, characterised by an gradual increase of mechanical properties with depth.
C	Deep deposits of dense or medium dense sand, gravel or stiff clay with thickness from several tens to many hundreds of metres.
D	Deposits of loose to medium cohesionless soil (with or without some soft cohesive layers), or of predominantly soft to firm cohesive soil.
E	A soil profile consisting of a surface alluvium layer with v_s values of type C or D and thickness varying between about 5 m and 20 m, underlain by stiffer material with $v_s > 800$ m/s.
S_1	Deposits consisting, or containing a layer at least 10 m thick, of soft clays/silts with a high plasticity index ($PI > 40$) and high water content.
S_2	Deposits of liquefiable soils, of sensitive clays, or any other soil profile not included in types A-E or S_1 .

In figure B.4 the spectra can be seen where the assumptions in order to create the spectra are:

- Reference peak ground acceleration of $a_{gR} = 0.4g$ (10% in 50 years exceedance)
- Importance class II with a importance factor of $\gamma_1 = 1$
- Type 1; location of high seismic activity
- 5% structural damping.

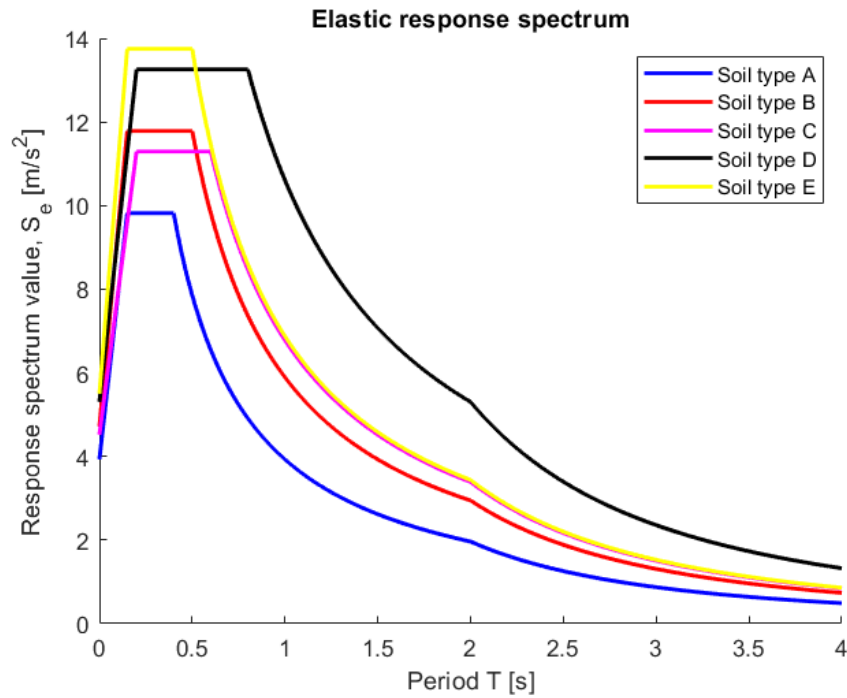


Figure B.4: Elastic design response spectrum for different soil types , [EN1998-1, 2004].

The elastic response spectrum as previously stated is a spectrum made up of the peak response of a linear SDOF system with different vibration periods T . However in reality constructions will typically have a tendency to undergo plastic deformation when exposed to seismic action. In EN 1998-1 plastic redistribution can be dealt with using the so-called design response spectrum, which is described in the following section.

B.3 Design Response Spectrum

In severe earthquakes inelasticity in the structure will occur and the elastic response spectrum will result in too conservative spectral acceleration values. The ductility can be taken into account by a behavior factor, q , that reduces the forces in the structure. The ductility of a material is its capability to undergo plastic deformation without losing its bearing capacity and is calculated as:

$$\mu = \frac{d_{max}}{d_y}$$

Where d_{max} is the structure's maximum displacement, and d_y is the displacement at which yielding initiates. When a structure yields it also has the result of limiting the peak force it must undergo. In [EN1998-1, 2004] this reduction in peak force is carried out through the behaviour factor q . The behaviour factor can be found as the ratio between the peak elastic force in a SDOF system and the force where the system starts to yield, see figure B.5:

$$q = \frac{F_{el}}{F_y}$$

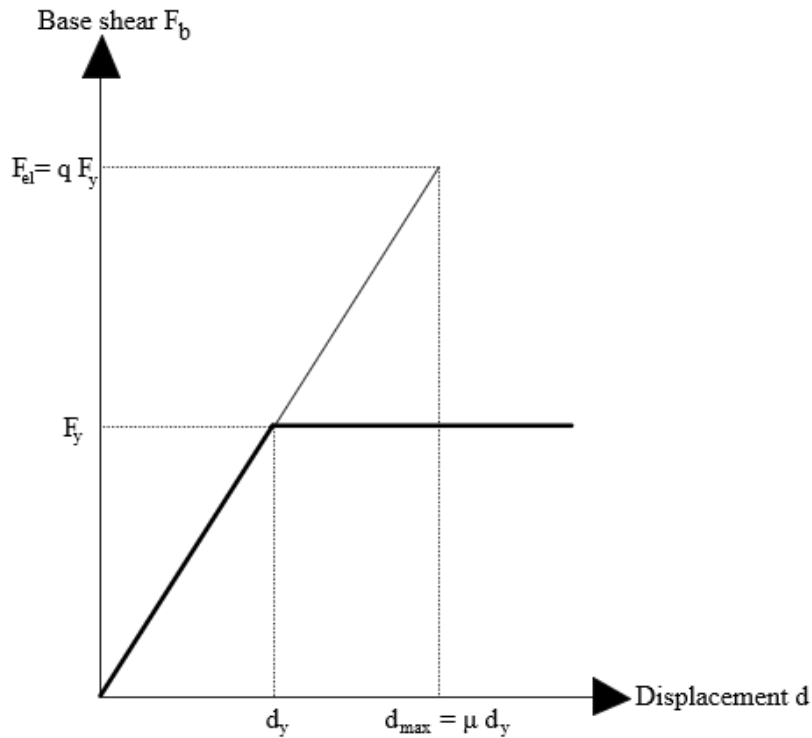


Figure B.5: Ductility and behaviour factor comparison between elastic and inelastic displacements.

The behaviour factor is incorporated through the design spectrum which is a response spectrum that takes the reduction of the peak force into account. The design response spectrum is constructed using equation (B.2).

$$\begin{aligned}
 S_d(T) &= a_g \cdot S \cdot \left[\frac{2}{3} + \frac{T}{T_B} \cdot \left(\frac{2.5}{q} - \frac{2}{3} \right) \right] & \text{for } 0 \leq T \leq T_B \\
 S_d(T) &= a_g \cdot S \cdot \frac{2.5}{q} & \text{for } T_B \leq T \leq T_C \\
 S_d(T) &= a_g \cdot S \cdot \frac{2.5}{q} \cdot \frac{T_C}{T} & \text{for } T_C \leq T \leq T_D \\
 S_d(T) &= a_g \cdot S \cdot \frac{2.5}{q} \cdot \frac{T_C - T_D}{T^2} & \text{for } T_D \leq T \leq 4
 \end{aligned} \tag{B.2}$$

In [EN1998-1, 2004] the behaviour factor q is determined based on ductility class, structural type and cross sectional type, which are all described in appendix C.3. Within the scope of this project a behaviour factor of $q = 4$ is used and the design response spectra for the different ground types are illustrated in figure B.6.

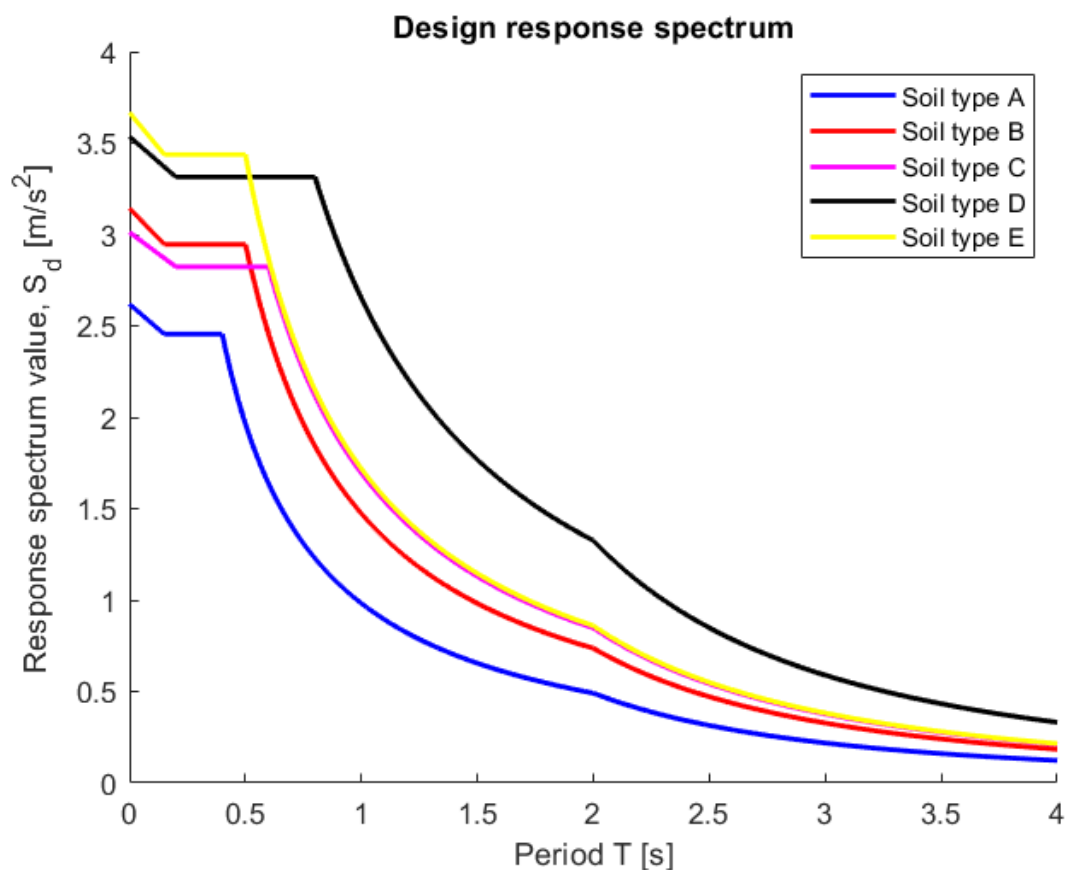


Figure B.6: Inelastic design response spectrum, [EN1998-1, 2004].

It can be seen that for a wide range of larger natural periods the design spectral acceleration, S_d , is a factor of $q = 4$ smaller than the elastic spectral acceleration, S_e . Opposite, for very small natural periods it can be seen that $S_d \approx S_e$, i.e. the ductility does not reduce the design spectral acceleration as a very stiff, or even infinite stiff, structure will not undergo deformations but simply moves with the ground, [Elghazouli, 2017].

B.4 Accelerogram Types

Acceleration time history can be presented by either a recorded or artificial accelerogram and according to [EN1998-1, 2004] the artificial accelerogram may be used in the case of an insufficient amount of data of recorded accelerograms. This is because generated artificial earthquakes do not behave with similar nature to recorded earthquakes. Two accelerograms which are utilised within the scope of this project are illustrated in figure B.7 and B.8.

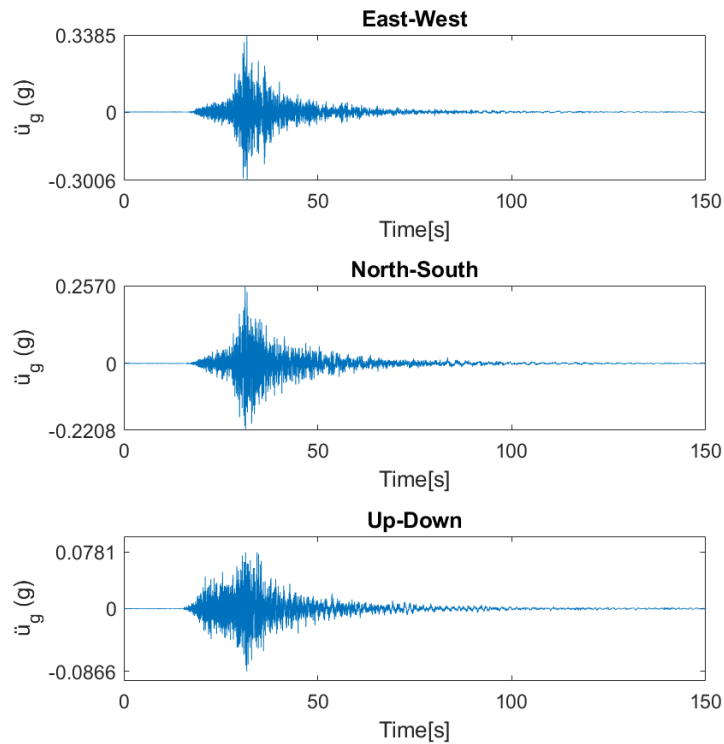


Figure B.7: Accelerogram for the earthquake near the South Coast of Honshu, Japan 2021-03-20 with a magnitude of 7.0. Database: [CESMD, 2022].

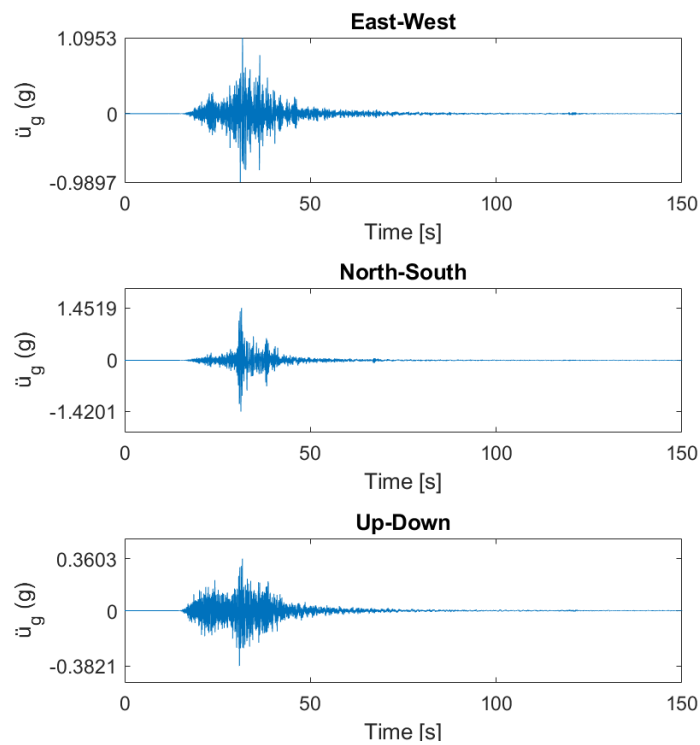


Figure B.8: Accelerogram for the earthquake near the South Coast of Honshu, Japan 2021-02-13 with a magnitude of 7.1. Database: [CESMD, 2022].

B.4.1 Recorded Accelerograms

Recorded accelerograms are obtained from a strong motion database, within the scope of this project the "Center for Strong Motion Engineering Data" [CESMD, 2022] is used. However, according to [EN1998-1, 2004] the recorded accelerograms must be relevant to the specific site and therefore the recorded accelerograms are modified so their response is similar to the elastic response spectrum. This is done through an iterative procedure in the software program *SeismoMatch* that uses wavelet functions to modify the acceleration time series. The procedure within the software program is as follows:

Step 1

Select the acceleration time history $\ddot{u}(t)$ that should be matched from a strongmotion center database.

Step 2

Calculate the earthquake response spectrum by exposing a number of SDOF systems to the acceleration time series and construct the response spectrum as well as the code specified elastic response spectrum. The elastic response spectrum as well as the accelerogram and response spectrum from earthquake from Miyagi-Oki 2003-05-26 Japan is illustrated in figure B.9.

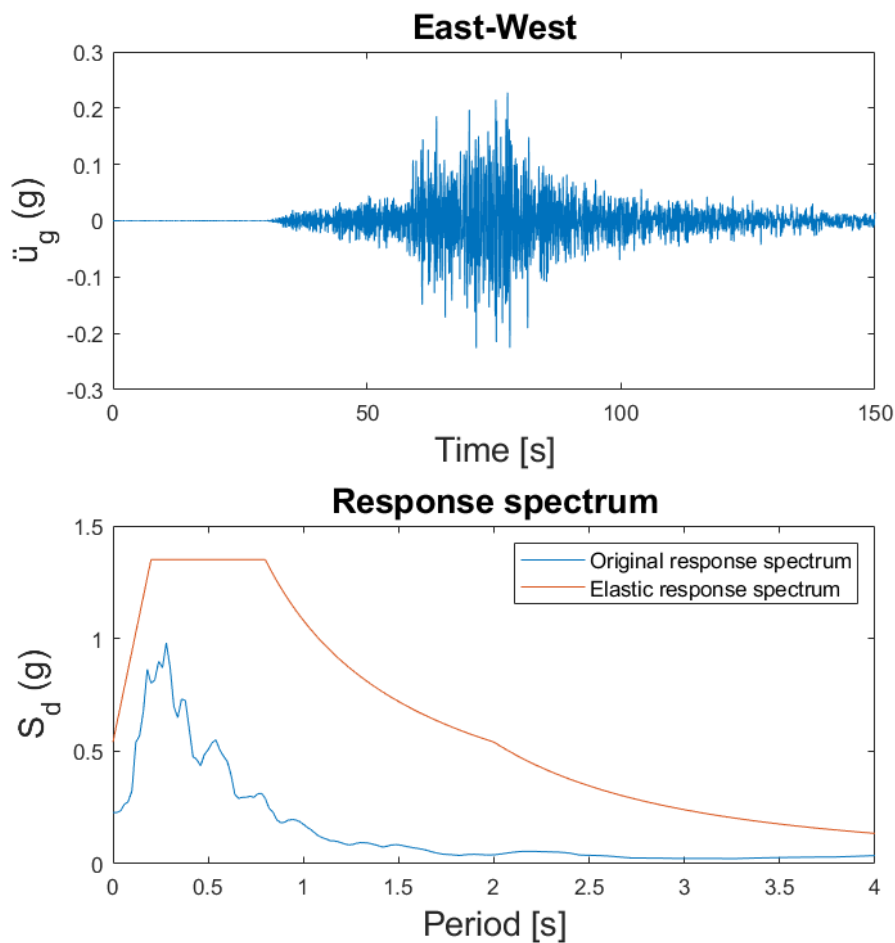


Figure B.9: Accelerogram and response spectrum for the earthquake Miyagi-Oki, 2003-05-26 Japan with a magnitude of 7.0. Software program: *SeismoMatch*.

Step 3

Calculate the spectral misfit $S_{amisfit}$ between the elastic response spectrum $S_{atarget}$ and the earthquake S_{ai} at different periods and evaluate the maximum S_{max} spectral misfit, see figure B.10. If the maximum spectral misfit exceeds 30% wavelet functions spectral matching is performed.

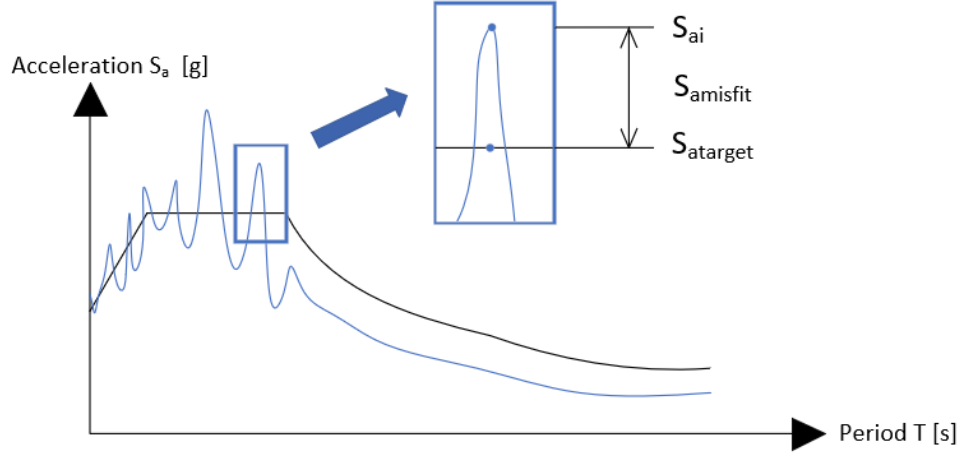


Figure B.10: Illustration of spectral misfit $S_{amisfit}$ between the elastic response spectrum $S_{atarget}$ and earthquake spectrum S_{ai} .

Step 4

Spectral matching is performed using wavelet function to adjust the acceleration time series, so its computed response spectrum matches the target spectrum across the entire frequency range. The commercial program *SeismoMatch* uses the wavelets algorithm proposed by [N.A., 1992] and [J. et al., 2006b]. The acceleration time history is modified using equation (B.3)

$$\ddot{u}^r(t) = \ddot{u}^{r-1}(t) + \sum_{j=1}^N b_j \psi_j(t) \quad (\text{B.3})$$

Where

$\ddot{u}^r(t)$	Acceleration time history for r^{th} iteration $[\frac{m}{s^2}]$
$\ddot{u}^{r-1}(t)$	Acceleration time history for $r - 1^{th}$ iteration $[\frac{m}{s^2}]$
b_j	Wavelet magnitude of wavelet j [-]
ψ_j	Wavelet acceleration adjustment function of wavelet j $[\frac{m}{s^2}]$.

The wavelet magnitude b is an array of magnitudes that each wavelet is to be adjusted, and is found from solving a linear set of equations given below in equation (B.4)

$$S_{amisfit} = [C] b \quad (\text{B.4})$$

Where $[C]$ is the matrix for spectral sensitivity whose element c_{ij} gives the acceleration response at time peak t_i of a SDOF system with period T_i due to wavelet acceleration adjustment function $\psi_j(t)$ with period T_j . The acceleration response for element c_{ij} is calculated from equation (B.5)

$$c_{ij} = \int_0^{t_i} \psi_j(\tau) h_i(t_i - \tau) d\tau \quad (\text{B.5})$$

h_i is the acceleration impulse response function given in equation (B.6)

$$h_i(t) = \frac{-\omega_i}{\sqrt{1 - \zeta^2}} e^{(-\omega_i \zeta t)} \left[(2\zeta^2 - 1) \sin(\omega'_i t) - 2\zeta \sqrt{1 - \zeta^2} \cos(\omega'_i t) \right] \quad (\text{B.6})$$

where

$$\begin{array}{l|l} \omega_i & \text{Angular frequency of } i^{\text{th}} \text{ system } [\frac{\text{rad}}{\text{s}}] \\ \zeta & \text{Damping ratio } \zeta = 0.05 \\ \omega'_i & \text{Damped angular frequency } \omega'_i = \omega_i \sqrt{1 - \zeta^2}. \end{array}$$

The remaining parameter that is needed to modify the acceleration time history is the wavelet function ψ_j . The wavelet function is used to modify the acceleration time series and therefore appropriate choice of wavelet function is essential to produce a spectrum compatible acceleration time history and that the velocity and displacement history both tend towards 0. *SeismoMatch* uses the Corrected Tapered Cosine Wavelet function proposed by [L. and N.A., 2010], where the wavelet function is given in equation (B.7).

$$\psi_j = e^{-\left[\frac{t-t_j+\Delta t_j}{\gamma_j}\right]^2} \cos(\omega_{j'}(t-t_j+\Delta t_j)) \quad (\text{B.7})$$

Where Δt_j is the difference between time peak response of wavelet with a reference time t_j and γ_j is the correction factor the variables are calculated as shown below:

$$\Delta t_j = \frac{\tan^{-1}\left[\frac{\sqrt{1-\xi^2}}{\xi}\right]}{\omega'_j}$$

$$t_j = 3.9223 f^{-0.845}$$

$$\gamma_j = 1.178 f^{-0.93}$$

Step 5

Repeat steps 2-5 until the maximum spectral misfit $S_{amisfit}$ does not exceed 30%. The Miyagi-Oki 2003-05-26 Japan earthquake matched to the target spectrum is illustrated in figure B.11

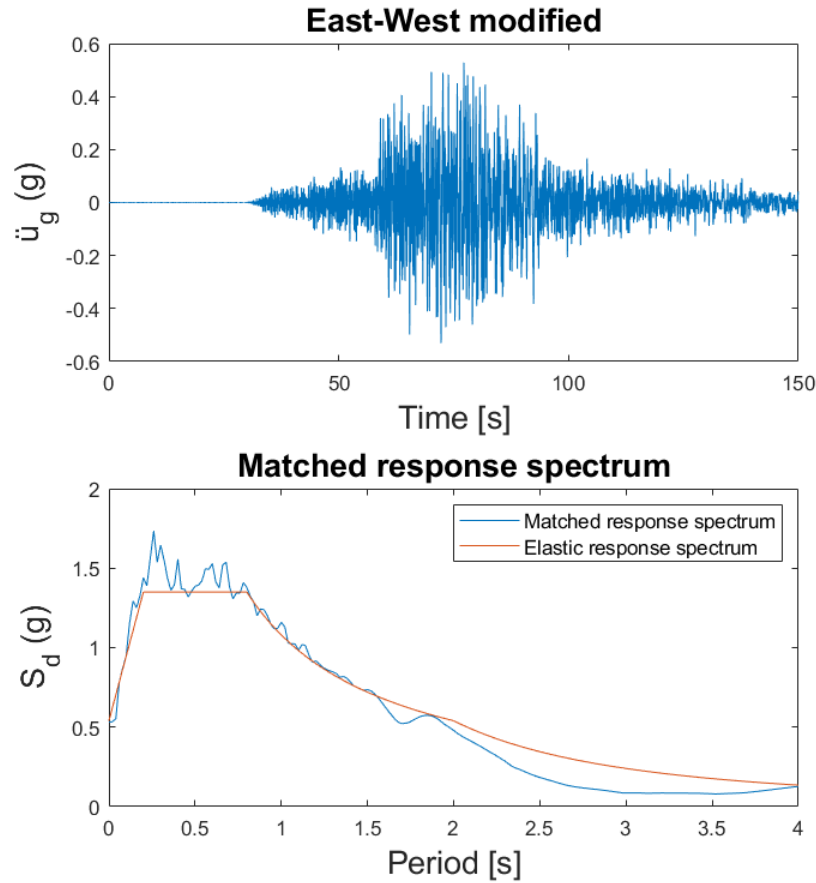


Figure B.11: Modified accelerogram and response spectrum for the earthquake Miyagi-Oki, 2003-05-26 Japan. Software program: *SeismoMatch*.

B.4.2 Artificial Accelerograms

Artificial accelerograms are accelerograms generated from the elastic response spectrum. The generation of an artificial accelerogram can be done in the program *SeismoArtif* using the code specific elastic response spectrum and other predefined and randomly generated variables. The procedure for generation and adjustment of an artificial accelerogram in *SeismoArtif* is as follows:

Step 1

Construct the code specific elastic response spectrum $SRT(\omega)$ for acceleration and velocity, based on the known parameters from the given site.

Step 2

Construct an artificial accelerogram and construct the response spectrum of the artificial accelerogram $SR(\omega)$. The artificial accelerogram is constructed as a series of sinusoidal waves given in equation (B.8)

$$Z(t)_i = I(t) \sum_n A_n \sin(\omega_n t + \phi_n) \quad (\text{B.8})$$

where

$Z(t)_i$	Artificial ground motion for the i^{th} iteration [g]
$I(t)$	Intensity function [-]
A_n	Amplitude of n^{th} sinusoidal wave [g]
ω_n	Angular frequency of n^{th} sinusoidal wave [$\frac{rad}{s}$]
ϕ_n	Phase angle of n^{th} sinusoidal wave [-]
t	Time [s].

The intensity function $I(t)$ is a functional envelope shape which helps dictate the amplitude of the seismic motion over time, as standard input *SeismoArtif* uses the "Saragoni & Hart" function cf. [G.R. and G.C., 1974] illustrated in figure B.12.

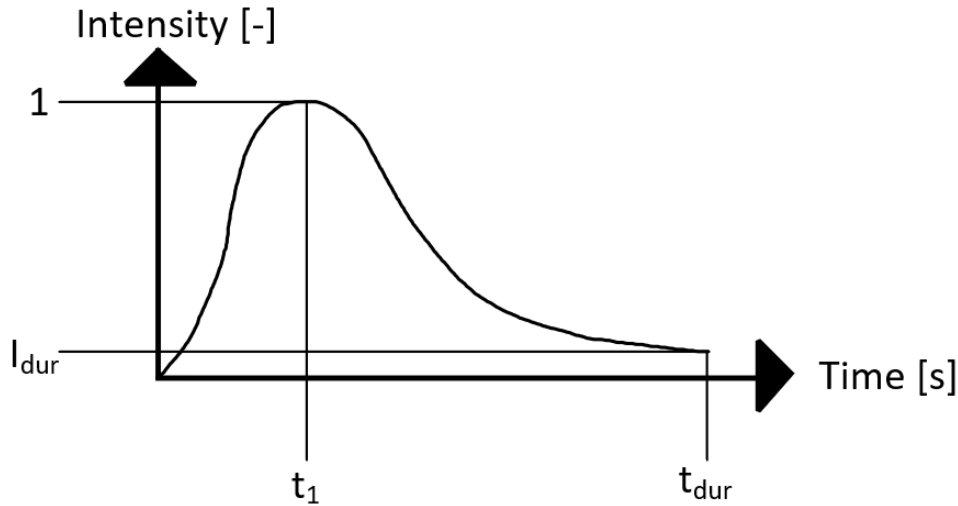


Figure B.12: Saragoni & Harts intensity function.

Where t_1 is the time of peak intensity, I_{dur} is the intensity at the end of the earthquake duration and t_{dur} is the duration of the earthquake. The amplitude A_n is obtained using the Power Spectral Density Function (PSDF) $G(\omega)$ which is calculated from the velocity target spectrum defined in step 1. Using the PSDF the amplitude is obtained from equation (B.9)

$$G(\omega)\Delta\omega = \frac{A_n^2}{2} \quad (\text{B.9})$$

The angular frequency ω_n is an array of n angular frequencies. The last parameter is the phase angle ϕ_n , which is generated through a random process, generated in the interval $[0; 2\pi]$.

Step 3

Perform a Fourier Transformation on the artificial ground motion $Z(t)$. The Fourier transformation for a continuous time history is defined in equation (B.10).

$$F(\omega)_i = \int_{-\infty}^{\infty} Z(t) e^{-i\omega t} dt \quad (\text{B.10})$$

where

$F(\omega)$		Acceleration value in frequency domain [g]
e		Euler number $e = 2.718$
ω		Angular frequency

Step 4

Correction process in the frequency domain. The correction process is performed by following an iterative procedure using equation (B.11).

$$F(\omega)_{i+1} = F(\omega)_i \left(\frac{SRT(\omega)}{SR(\omega)} \right) \quad (\text{B.11})$$

Where $F(\omega)_{i+1}$ and $F(\omega)_i$ are the values of the acceleration time history in the frequency domain for the current and previous iteration.

Step 5

Perform an inverse Fourier Transformation on the artificial ground motion in the frequency domain $F(\omega)$. The inverse Fourier Transformation for a continuous time history is defined in equation (B.12)

$$Z(t) = \frac{1}{2\pi} \int_{-\infty}^{\infty} F(\omega)_{i+1} e^{i\omega t} d\omega \quad (\text{B.12})$$

Step 6

Repeat steps 3-5 until convergence between the code specified target spectrum and earthquake response spectrum.

Appendix C | Principles of Seismic Design According to EN 1998-1

In this appendix some principles within seismic design methods according to EN 1998-1 are presented. These principles include regularity criteria, capacity design and the behaviour factor.

C.1 Structural Regularity

Within seismic design structures can be categorised as being regular or irregular. Whether a structure is classified as regular or irregular has an impact on whether or not a planar or spatial model should be used, whether or not the lateral force method or the modal response spectrum analysis can be used or whether or not the reference value for the behaviour factor should be decreased or not, see table C.1.

Table C.1: Consequences of structural regularity, [EN1998-1, 2004].

Regularity		Allowed simplification		Behaviour factor
Plan	Elevation	Model	Linear analysis	(For linear analysis)
Yes	Yes	Planar	Lateral force method	Reference value
Yes	No	Planar	Modal analysis	Decreased value
No	Yes	Spatial	Lateral force method	Reference value
No	No	Spatial	Modal analysis	Decreased value

Different considerations for structural regularity in plan and elevation should be checked.

C.1.1 Regularity in Plan

The regularity in plan criteria determines whether or not a planar model (2D-model) can be used. If the regularity in plan criteria is not satisfied a spatial model (3D-model) should be analysed. The structure is categorised as being regular in plan if the following conditions are satisfied according to [EN1998-1, 2004]:

- Mass distribution and lateral stiffness is approximately symmetrical in the plan with respect to the two horizontal axis.
- Plan configuration is compact, meaning no in plan set-outs are allowed. Furthermore if in plan set-backs (edge recesses or re-entrant cornes) exist regularity in plan is still considered if the area of each setback does not exceed 5% of the total floor area, see figure C.1.

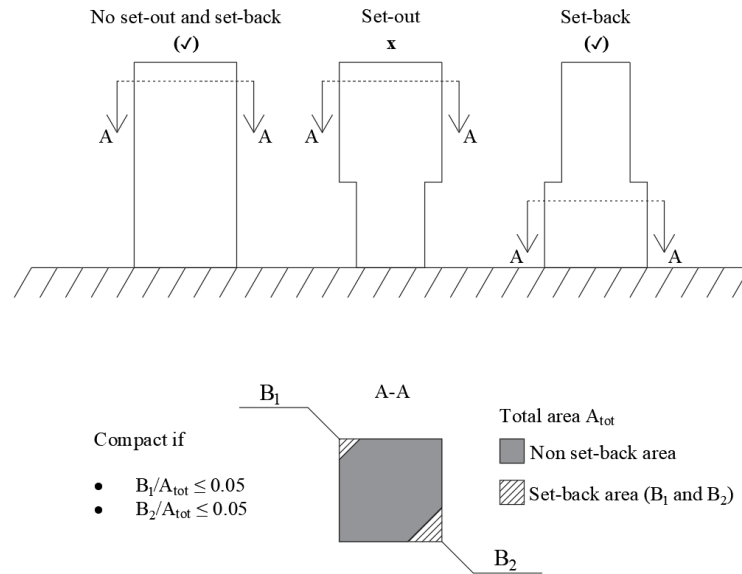


Figure C.1: Regularity plan configuration.

- In plan stiffness of floors is sufficiently large compared to lateral stiffness of vertical elements, meaning deformation of floors have a small effect on distribution of lateral forces.
- The slenderness $\lambda = L_{max}/L_{min} \leq 4$, where L_{max} and L_{min} are the larger and smaller dimension in plan, see figure C.2.

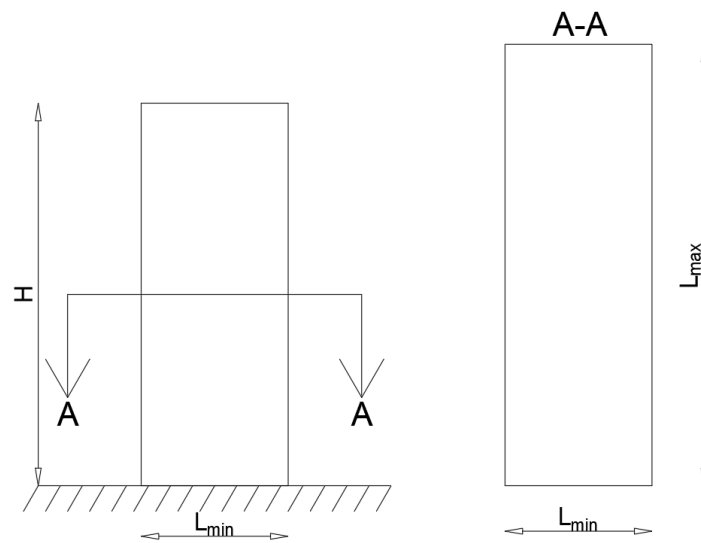


Figure C.2: Regularity in plan slenderness.

- On every level and direction of the analysis x and y the torsional radius r and structural eccentricity e_o and radius of gyration l must satisfy the following conditions:

$$e_{ox} \leq 0.3r_x \text{ and } r_x \geq l_s$$

where

e_{ox}	Distance between the centre of stiffness and the centre of mass, measured along the x direction, which is normal to the direction of analysis considered.
r_x	Torsional radius; square root of the ratio of the torsional stiffness to the lateral stiffness in the y direction
l_s	Square root of the ratio of a) the polar moment of inertia of the floor mass in plan with respect to the centre of mass of the floor to b) the floor mass.

If the above conditions are satisfied it is allowed to perform a linear analysis on a planar model.

C.1.2 Regularity in Elevation

The regularity in elevation determines whether or not the building is uniform in elevation. This is essential as the lateral force method assumes linear distribution of lateral loads from seismic activity. The structure is categorised as being regular in elevation if the following conditions are satisfied according to [EN1998-1, 2004]:

- Lateral load resisting system like cores, frames or structural walls run from their foundation to the top of the building or if setbacks are present to the top of the relevant zone.
- Lateral stiffness and mass of individual storeys remain constant or reduce gradually without sudden changes from base to top
- Ratio of story resistance to needed resistance required by analysis not vary disproportionately between adjacent storeys.
- If setbacks are present the conditions given on figure C.3 should apply.

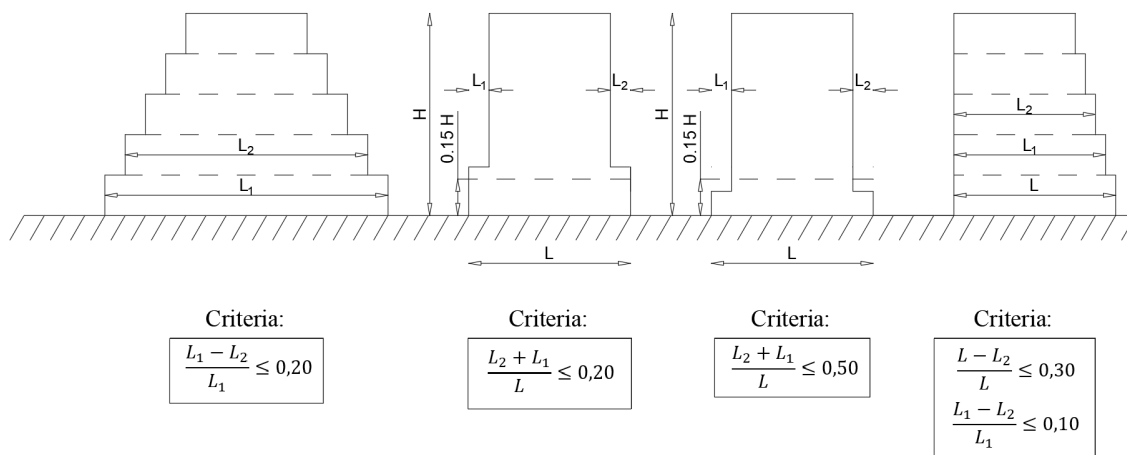


Figure C.3: Regularity in elevation criteria if setbacks are present.

If the above conditions are satisfied it is allowed to perform a linear elastic analysis using the lateral force method.

C.2 Capacity Design

Another important aspect of earthquake engineering is capacity design. Capacity design is the design process where it is decided which elements should be permitted to yield and which elements should remain elastic. In other words the objective of capacity design is to confirm that a building undergoes controlled ductile behaviour such that collapse is avoided during an earthquake. The combination of ductile and elastic behaviour can be illustrated as a chain of ductile and brittle components undergoing tension, see figure C.4.

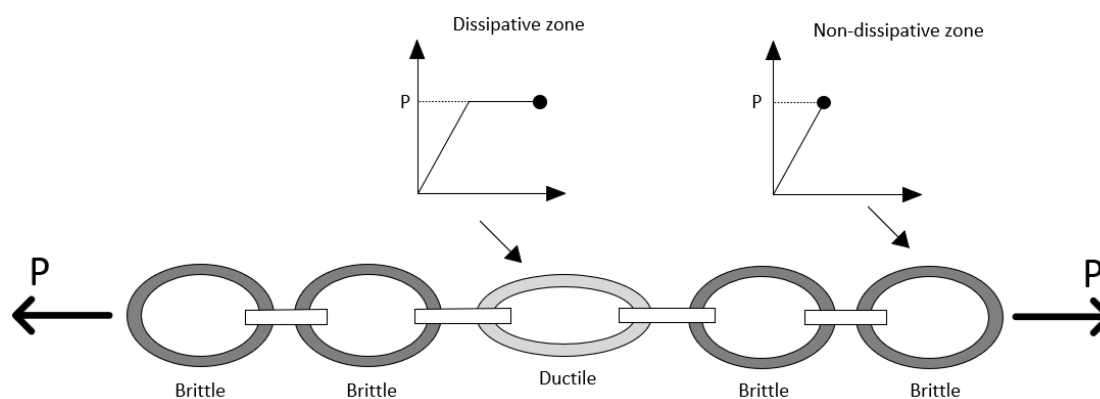


Figure C.4: Principle of capacity design.

According to EN 1998-1 steel structures can be designed as being either dissipative or non-dissipative, meaning whether or not structural elements are allowed to undergo inelastic deformation. When it comes to seismic design in regions of high seismic activity designing the structure as non-dissipative requires indefeasibly large structural elements and therefore structures are usually designed as being dissipative [EN1998-1, 2004]. For simple classical structures the dissipation is incorporated through the behaviour factor q , see section C.3 as the inelasticity can be more easily assumed evenly distributed throughout the structure. In the case of more complicated structures non-linear analysis methods need to be utilised.

Moment resisting frame

A classical structural type, which could be designed against seismic action, is a moment resisting frame structure that ensures dissipative behaviour as well as the desired failure mechanism. The desired failure mechanism for seismic design for a moment resisting frame structure is to develop plastic hinges in the beam ends rather than the column ends. This concept is known as weak beam/strong column (WBSC) design which provides favorable performance in comparison to strong beam/weak column (SBWC) behaviour, see figure C.5 [EN1998-1, 2004].

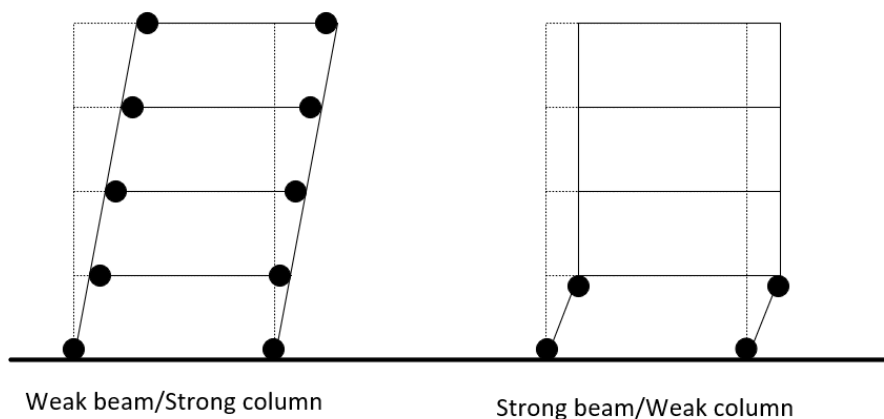


Figure C.5: Weak beam/Strong column and Strong beam/Weak column behaviour

To ensure the WBSBC behaviour the column capacities must be higher than the beam capacities. According to [EN1998-1, 2004] a general requirement to ensure the desired behaviour should be that the sum of the moments of resistance of the columns framing a joint should be 1.3 times higher than the sum of the moment resistance of beam framing that joint, see equation (C.1).

$$\sum M_{Rc} \geq 1.3 \sum M_{Rb} \quad (\text{C.1})$$

Or as the sum of plastic moment of resistance in equation (C.2) if all profiles have the same steel grade.

$$\sum W_{pl,c} \geq 1.3 \sum W_{pl,b} \quad (\text{C.2})$$

Interstory drift

As moment resisting frames are usually flexible structures they are prone to undergo large deformations when exposed to seismic action. Therefore, [EN1998-1, 2004] recommends an ultimate limit state criteria for second order effects (P- Δ effects) through the sensitivity coefficient obtained from equation (C.3).

$$\theta = \frac{P_{tot} d_r}{V_{tot} h} \quad (\text{C.3})$$

Where

P_{tot}	Total gravitational axial force at considered story [N]
d_r	Design inter-story drift [m]
V_{tot}	Seismic shear force at considered story [N]
h	Story height [m].

If the sensitivity coefficient is $\theta \leq 0.10$ second order effects does not need to be taken into account. If $0.10 \leq \theta \leq 0.20$ second order effects can approximately be taken into account be multiplying the fitting seismic action by a factor $1/(1 - \theta)$. Lastly the sensitivity coefficient shall not exceed $\theta \geq 0.30$, otherwise the structure is unstable.

C.3 Structural Behaviour Factor

Another seismic design consideration is the behaviour factor. The behaviour factor is utilised when constructing the design response spectrum which is used in the lateral force method and the modal response spectrum analysis. The behaviour factor in steel design is mainly dependent on the following factors [EN1998-1, 2004]:

- Ductility class for structures
- Structural type
- Ductility class for cross sections.

Ductility class for structures

When designing a building against seismic action the building is designed in accordance to either low-dissipative structural behaviour or dissipative structural behaviour see table C.2.

Table C.2: Design concepts, ductility classes and reference behaviour factor

*Limited by the structural type, [EN1998-1, 2004].

Design concept	Structural ductility class	Reference behaviour q
Low dissipative structural behaviour	DCL (Low)	1.5 – 2.0
Dissipative structural behaviour	DCM (Medium)	$\leq 4^*$
	DCH (High)	*

The reference behaviour factor is an upper limit value and should also be chosen in conjunction with structural type and ductility class for cross sections.

Structural type

The behaviour factor is also highly dependent on the structural type as different types of structures have different energy dissipation capacity. According to [EN1998-1, 2004] steel buildings are assigned to one of the following types:

- Moment resisting frames
- Frames with concentric bracings
- Frames with eccentric bracings
- Inverted pendulum structures
- Structures with concrete cores or concrete walls
- Moment resisting frames combined with concentric bracings
- Moment resisting frames combined with infills

Within the scope of this project the moment resisting frame is considered. For moment resisting frames it is assumed that dissipative zones are located in beam ends or beam-column joints or in base or top columns or the frame building. Examples of moment resisting structures from EN 1998-1 is shown in figure C.6

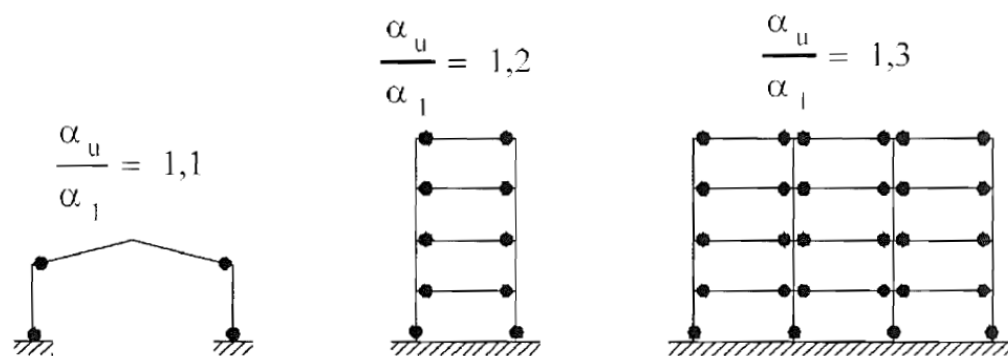


Figure C.6: Examples of moment resisting frames from [EN1998-1, 2004].

The upper limit reference behaviour factor for a moment resisting frame structures is $q = 4$ for DCM and $q = 5 \alpha_u / \alpha_l$ for DCH.

Ductility class for cross sections

For elements undergoing seismic loading action sufficient ductility for elements dissipating energy in bending or compression should be ensured by restricting the width-thickness ratio b/t according to cross sectional classes according to [EN1998-1, 2004]. Therefore the requirements for cross sectional classes depending on ductility class and behaviour factor is given in table C.3.

Table C.3: Requirements for cross sectional classes [EN1998-1, 2004].

Ductility class	Reference behaviour factor q	Required cross-sectional class
DCM	$1.5 < q \leq 2$	class 1, 2 or 3
DCM	$2 < q \leq 4$	class 1 or 2
DCH	$q > 4$	class 1

Appendix D | Seismic Analysis

Methods According to EN 1998-1

This appendix describes the different methods utilised for seismic analysis within the scope of this project, for both the analysis of the ten-story frame building, see chapter 3 and the analysis of the offshore wind turbine foundation 7.

When performing a seismic analysis the following methods are proposed by [EN1998-1, 2004]

- Lateral force method
- Modal response spectrum analysis
- Non-linear static pushover analysis
- Non-linear time history analysis.

The methods are sorted in terms of complexity and computational demands such that the Lateral Force Method is the least complex and computationally demanding method, and Non-linear Time History Analysis is the most complex and computationally demanding method. When designing the structure using the above mentioned methods the structure must be able to withstand seismic loads from both horizontal directions individually and not simultaneously, see figure D.1.

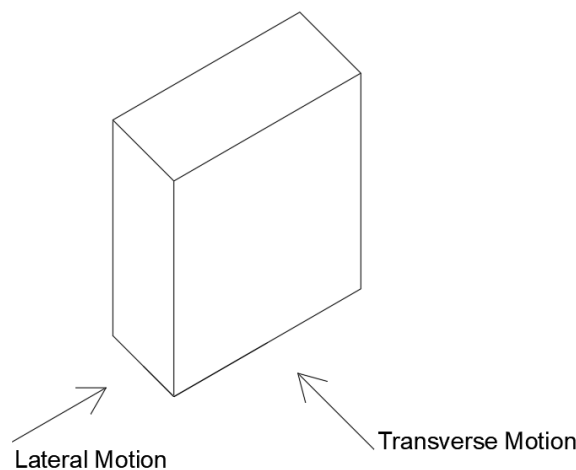


Figure D.1: Lateral and transverse motion directions on a structure.

D.1 Lateral Force Method

The lateral force method also called the equivalent static method is a simplified technique substituting the dynamic effect of an earthquake by a static force, which is laterally distributed on a structure. The method assumes the structure responds to its fundamental horizontal eigenmode, to ensure this the fundamental horizontal period in the two main directions must be smaller than the following values.

$$T_1 \leq \begin{cases} 4 T_C \\ 2.0 \text{ s} \end{cases} \quad (\text{D.1})$$

where

T_1	First eigen period
T_C	Upper limit of the period of the constant spectral acceleration, EN1998 [EN1998-1, 2004] table 3.2 and 3.3.

Furthermore the structure must satisfy the criteria for regularity in elevation for the lateral force method to be utilised, which is shown in table C.1. The lateral force method has the following procedure:

- Approximate/calculate the first eigen period T_1
- Obtain the spectral value from the design spectrum at period T_1
- Calculate the base shear force and distribution of the horizontal forces.

Approximate/calculate the first eigen period T_1

The first eigen period T_1 can either be found from solving the eigenvalue problem or by an approximation equation in EN 1998-1. Within this project the eigenvalue problem is solved. The eigenvalue problem is solved by performing an undamped free eigenfrequency analysis. This is often done for an undamped system due to a decreased computational cost as a damped structure will lead to a complex solution, which is computationally more demanding. The equation of motion is shown in equation (D.2).

$$[\mathbf{M}]\{\ddot{\mathbf{u}}\} + [\mathbf{K}]\{\mathbf{u}\} = \mathbf{0} \quad (\text{D.2})$$

where

$[\mathbf{M}]$	Mass matrix
$[\mathbf{K}]$	Stiffness matrix
$\{\mathbf{u}\}$	Displacement vector.

Vibrations are harmonic and all degree of freedoms are in phase and therefore the displacement vector as a function of time can be written in equation (D.3).

$$\{\mathbf{u}(\mathbf{t})\} = \{\phi_{\mathbf{n}}\} \cos(\omega_n t) \quad (\text{D.3})$$

where

$$\left. \begin{array}{l} \{\phi_{\mathbf{n}}\} = \{\phi_{1n} \ \phi_{2n} \ \dots\}^T \\ \omega_n \\ n \end{array} \right| \begin{array}{l} \text{Modeshape vector for mode } n \\ \text{Eigenfrequency of the system for mode } n \text{ [rad/s]} \\ \text{Mode number } (n = 1, 2, \dots \text{ number of DOF}). \end{array}$$

By substituting the expression above into equation (D.2) gives the following expression in equation (D.4).

$$([\mathbf{K}] - \omega_n^2[\mathbf{M}])\{\phi_{\mathbf{n}}\} = \mathbf{0} \quad (\text{D.4})$$

The equation is a linear eigenvalue problem, which has as many non-trivial solutions ($([\mathbf{K}] - \omega_n^2[\mathbf{M}]) = \mathbf{0}$) as the system has degrees of freedom and an infinite amount of trivial solutions $\{\phi_{\mathbf{n}}\} = \mathbf{0}$, therefore the non-trivial solutions are sought. Each solution has an associated eigenfrequency ω_n and eigenmode $\{\phi_{\mathbf{n}}\}$. At first the eigenfrequencies are obtained from the following expression in equation (D.5).

$$\det([\mathbf{K}] - \omega_n^2[\mathbf{M}]) = 0 \quad (\text{D.5})$$

After obtaining the eigenfrequencies ω_n the associated eigenmodes $\phi_{\mathbf{n}}$ are obtained from equation (D.4). An eigenmode is referred to as the deformed shape of the structure subjected to harmonic loading at the corresponding eigenfrequency. A structures response can be quantified as the sum of the modal response, where each eigenmode represents a part of the total structural mass called modal mass. The eigenfrequency can then be expressed in either frequency f or period T from the expressions below:

$$f = \frac{\omega}{2\pi}, \quad T = \frac{1}{f}$$

In some cases solving the eigenvalue may be too computationally demanding, which is why [EN1998-1, 2004] has proposed that the first eigenperiod T_1 may be approximated using the following expression for buildings with a height up to 40 m:

$$T_1 = C_t H^{3/4} \quad (\text{D.6})$$

Where C_t is 0.085 for moment resistant space steel frames and H is the height of the building from its foundation or rigid base [EN1998-1, 2004].

Obtain the spectral value from the design spectrum at period T_1

After obtaining the first eigenperiod T_1 the spectral acceleration S_d is obtained at that period from the design response spectrum, illustrated on figure E.1.

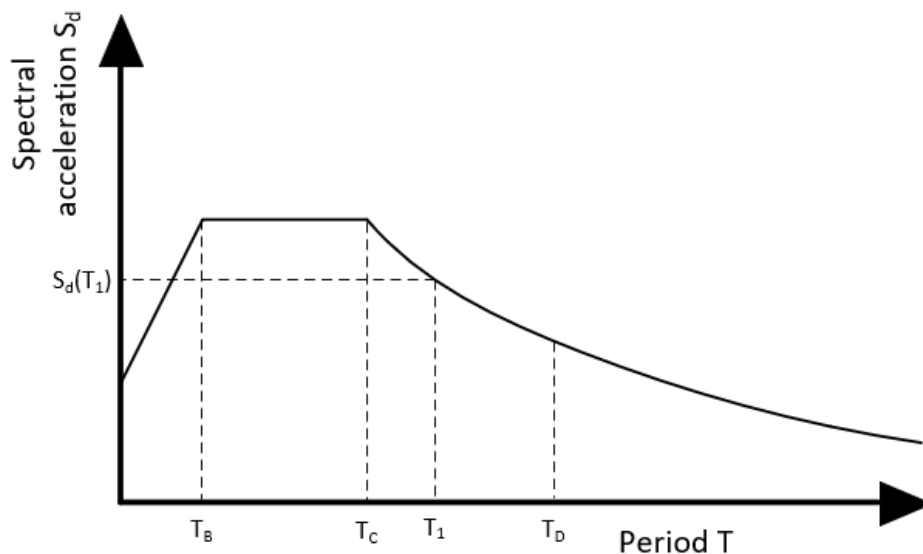


Figure D.2: Illustration of finding the spectral acceleration $S_d(T_1)$ for first eigenperiod.

Calculate the base shear force and distribution of the horizontal forces

Lastly the seismic base shear force is obtained from equation (D.7).

$$F_b = S_d(T_1) m \lambda \quad (\text{D.7})$$

where

$S_d(T_1)$	Design spectrum value at period T_1
λ	Correction factor
m	Total mass

The correction factor takes into account that for a building with at least three stories with a horizontal translation in each story, the effective modal mass of the first mode is smaller, on average by 15% than the total mass. The value is 0.85 for both horizontal directions if $T_1 < 2T_C$ and for buildings with more than 2 stories, and 1 otherwise.

The horizontal story forces are found by equation (D.8).

$$F_i = F_b \frac{\phi_i m_i}{\sum_{i=1}^j \phi_i m_i} \quad (\text{D.8})$$

where

F_i	Horizontal seismic force in story i
m_i	Mass in story i
ϕ_i	The modal displacement of story i in the first modeshape
j	The number of stories.

When the horizontal forces are obtained a static analysis is performed to determine the response such as displacements and reactions.

D.2 Modal Response Spectrum Analysis

An alternative method of estimating equivalent static forces is the modal response spectrum analysis. This analysis is more computationally demanding compared to the lateral force method as it requires a combination of the response of several eigenmodes. When applying this analysis method the following demands of how many modes that should be included in the analysis are given according to [EN1998-1, 2004].

- Response of all modes contributing significantly to the global response in both horizontal directions are used, this requirement is fulfilled if either of the following is upheld
 1. The sum of the effective modal masses for modes included amounts to at least 90% of structure total mass
 2. Every mode with effective modal mass greater 5% of total structure mass are included.

The modal response spectrum analysis is made up of the following procedure:

- Obtain the eigenfrequencies and eigenmodes by performing an undamped free eigenfrequency analysis
- Determine an appropriate number of eigenmodes to include in the analysis
- Obtain the spectral acceleration from the design response spectrum
- Calculate the base shear force and storey forces for each mode
- Combine the modal forces into total force acting on the structure.

Obtain the eigenfrequencies and eigenmodes by performing an undamped free eigenfrequency analysis

The procedure for performing an eigenfrequency analysis is identical to the one shown in appendix D section D.1.

Determine an appropriate number of eigenmodes to include in the analysis

When determining an appropriate number of modes it is essential to know how the choice will impact the solution computational demand. If a few number of modes are included the method is less computationally demanding however the result will be less accurate, and vice versa by included a large number of modes the computational will increase as well as the accuracy of the result. Therefore, [EN1998-1, 2004] deems an appropriate amount modes included if the prior demands are upheld. To determine the effective modal masses equation (D.9), which calculates modal participation factor γ_n , and equation (D.10), which calculates the effective modal mass M_{eff} , are used.

$$\gamma_n = \{\phi_n^T\} [M] \{D\} \quad (D.9)$$

and

$$M_{eff,n} = \gamma_n^2 \quad (D.10)$$

where

$\{\phi_n\}$	Modeshape vector for mode n
$[\mathbf{M}]$	Global mass matrix
$\{\mathbf{D}\}$	Excitation direction vector.

Here the modeshapes $\{\phi_n\}$ are determined from the eigenfrequency analysis. The excitation direction vector $\{\mathbf{D}\}$ represents the direction the participation factor is calculated in, [Ansys, 2020]. Within the scope of this project the participation factor is calculated in the horizontal directions and therefore the vector would contain 1's in the horizontal direction and 0's in all other directions.

Obtain the spectral acceleration from the design response spectrum

Once an appropriate amount of modes are included and the criteria for effective modal mass is checked the spectral acceleration, S_d , for each mode is found using the design response spectrum, as illustrated in appendix D section D.1.

Calculate the base shear force and story forces for each mode

Now that the modal properties are clarified the base shear force can be found from EN1998 [EN1998-1, 2004]. The base shear force for each mode is found using equation (D.11).

$$F_{bn} = S_{dn}(T_n) m_n \quad (\text{D.11})$$

where

T_n	Eigen period for mode n
m_n	Modal mass for mode n .

The modal mass for each mode is determined from equation (D.12).

$$m_n = \{\phi_n^T\} [\mathbf{M}] \{\phi_n\} \quad (\text{D.12})$$

The story forces are obtained by distributing the base shear force on each story. The base shear force is distributed based on the mode shape, meaning the stories that deflect the largest is assumed to have the largest force acting on that story. The story forces for every mode is calculated using equation (D.13).

$$F_{in} = F_{bn} \frac{\phi_{in} m_{in}}{\sum_{i=1}^j (\phi_{in} m_{in})} \quad (\text{D.13})$$

where

F_{in}	Horizontal seismic force in story i for mode n
F_{bn}	Base shear for mode n
m_{in}	Mass in story i for mode n
ϕ_{in}	The modal displacement of story i for mode n
j	The number of stories.

Combine the modal responses into total response acting on the structure

Lastly the responses in each separate mode are combined into a total response acting on the structure. There are several methods for combining modal responses, within the scopes of this project the Square-Root of Sum of Squares rule (SRSS) is applied. This method provides good estimates of total response, however the method assumes each mode is independent of its adjacent modes. EN1998 [EN1998-1, 2004] proposes that the value of adjacent eigenperiods must deviate 10% or more to be considered independent, see equation (D.14).

$$T_j \leq 0.9 T_i \quad (D.14)$$

where

T_j and T_i | Eigenperiods for lower period j and higher period i

If the above conditions is upheld for all modes the responses can be combined using the SRSS method from equation (D.15)

$$r_o = \sqrt{\sum_{n=1}^N r_{io}^2} \quad (D.15)$$

where

r_o | Total response
 r_{io} | Response from mode i .

If the criteria from EN1998 [EN1998-1, 2004] in equation (D.14) is not upheld, meaning the modes are not independent of each other, the complete quadratic combination rule (CQC) should be applied for modal combination. The CQC combination takes into account the correlation between the different modes, and the total response is obtained from equation (D.16)

$$r_o = \left(\sum_{i=1}^N \sum_{n=1}^N \rho_{in} r_{io} r_{no} \right)^{\frac{1}{2}} \quad (D.16)$$

where

r_{io} and r_{no} | Response from mode i and response from mode n
 N | Total number of modes
 ρ_{in} | correlation coefficient between modes i and n

The correlation coefficient is a coefficient between 0 and 1 which gives an indication of how much correlation there is between each mode, the closer to 1 the closer two modes are to be fully correlated. The correlation coefficient is obtained from equation D.17 according to [Chopra, 2007].

$$\rho_{in} = \frac{8 \xi^2 (1 + \beta_{in}) \beta_{in}^{\frac{3}{2}}}{(1 - \beta_{in}^2)^2 + 4 \xi^2 \beta_{in} (1 + \beta_{in})^2} \quad \beta_{in} = \frac{\omega_i}{\omega_n} \quad (D.17)$$

where

ξ | Damping coefficient
 ω_i and ω_n | Angular frequencies for mode i and n .

D.3 Non-linear Static (Pushover) Analysis

D.3.1 Lateral Load Pattern

There must according to EN 1998-1 be performed two analyses with different load patterns, and the most unfavorable result must be used for design. The load patterns are:

1. Uniform load pattern, i.e. acceleration is assumed constant in height.

$$\text{Inertia force distribution: } F_i = \frac{m_i}{\sum_{i=1}^j m_i} F_b.$$

2. Modal load pattern, i.e. the acceleration distribution is assumed proportional to the mode shape.

$$\text{Inertia force distribution: } F_i = \frac{m_i \Phi_i}{\sum_{i=1}^j m_i \Phi_i} F_b.$$

where

F_i		Inertia force in story i
m_i		Mass in story i
j		The number of stories.

For the modal load pattern it can either be for the first modeshape or for the first and higher modeshapes, depending on the dynamic properties of the structure. For low and very stiff structures the load pattern can be assumed to follow an inverted triangle shape or more precise the first modeshape. For more flexible structures can several modes be taken into account as shown in figure D.3.

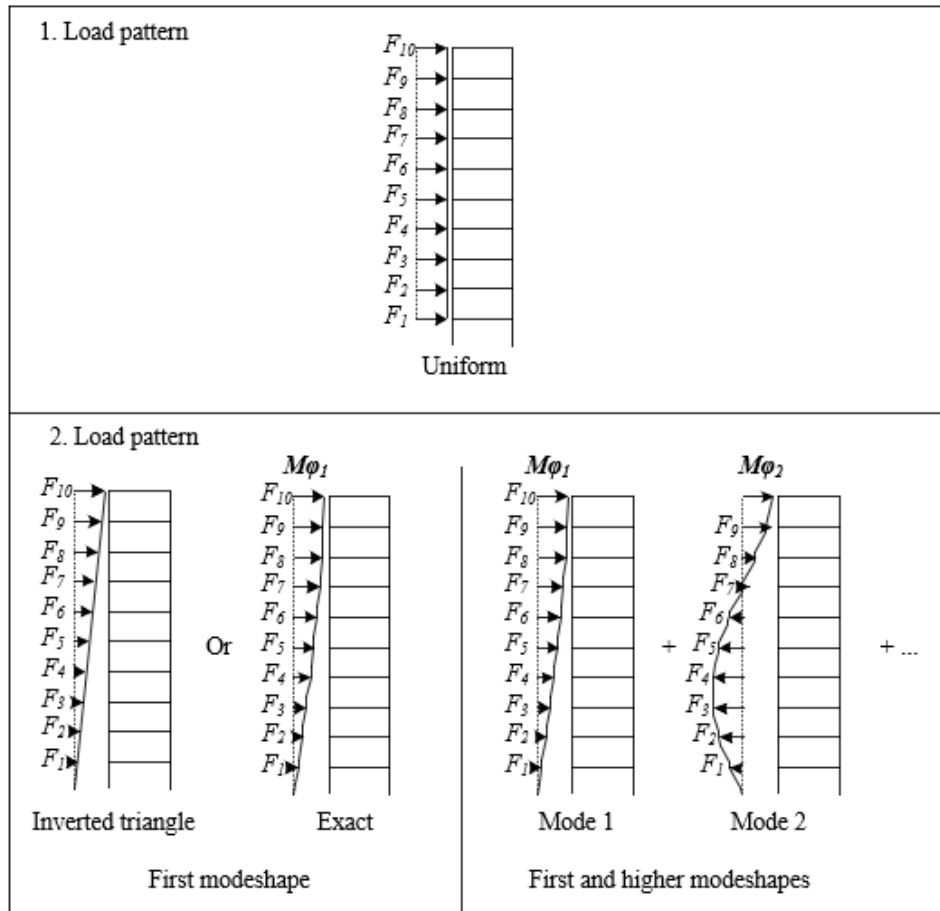


Figure D.3: Different load patterns.

The lateral loads are applied to the model where the load increases by a load factor λ for each time, $F_i = \lambda F_{init}$.

D.3.2 Capacity Curve

For each load step the lateral displacement at a control node is calculated, where the control node should be the node with the largest displacement for the considered load pattern, which is at the roof. The base shear force can then be calculated and the relation between base shear force and lateral roof displacement can be plotted and form the capacity curve illustrated at figure D.4.

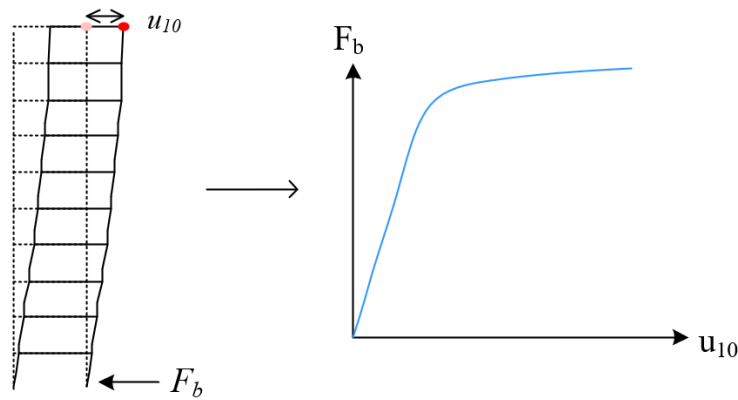


Figure D.4: Base shear force and lateral roof displacement give the capacity curve.

D.3.3 MDOF to SDOF and Idealized Elastic-plastic Relation Curve

The capacity curve at figure D.4 is for a multi degree-of-freedom (MDOF) system, but the purpose is to apply the capacity curve together with the response spectrum, which is based on a single degree-of-freedom (SDOF) system. The capacity curve must then be converted from a MDOF system to an equivalent SDOF system representation, which is done through modal expansion by the following equations:

$$F^* = \frac{F_b}{\Gamma}$$

$$d^* = \frac{d_n}{\Gamma}$$

where

F^*	Force of the equivalent SDOF system
F_b	Base shear force of the MDOF system
d^*	Displacement of the equivalent SDOF system
d_n	Displacement of the MDOF system
Γ	Transformation factor.

The transformation factor can be calculated by:

$$\Gamma = \frac{m^*}{\sum_{i=1}^j m_i \phi_i^2} = \frac{\sum_{i=1}^j \bar{F}_i}{\sum_{i=1}^j \left(\frac{\bar{F}_i^2}{m_i} \right)} \quad (\text{D.18})$$

where

m^*	The mass of an equivalent SDOF system equation (D.19)
m_i	The mass in the i-th story
ϕ_i	Modeshape displacement in the i-th story
j	Number of stories.

And the mass of the equivalent SDOF system can be calculated by:

$$m^* = \sum_{i=1}^j m_i \Phi_i = \sum_{i=1}^j \bar{F}_i \quad (\text{D.19})$$

Furthermore, the capacity curve for the equivalent SDOF system has to be converted into an idealized elastic perfectly-plastic curve where the areas under the curves are equal, as illustrated on figure D.5.

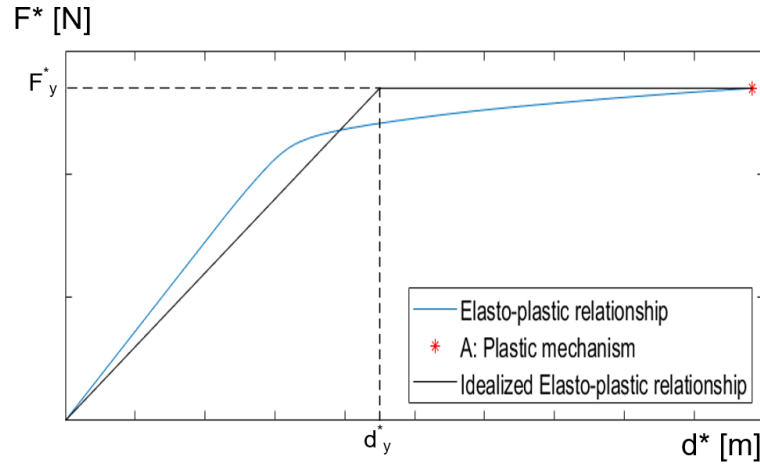


Figure D.5: Idealized elasto-perfect plastic relation curve

The yield displacement of the idealised SDOF system can be calculated by:

$$d_y^* = 2 \left(d_m^* - \frac{E_m^*}{F_y^*} \right)$$

where

E_m^* | The actual deformation energy.

D.3.4 Response Spectrum and Acceleration-displacement Response Spectrum

The next step is to determine the seismic demands on the structure by future earthquakes, which is done through demand curves constructed from the response spectra with specified return periods according to limits states (initial damage, significant damage or near collapse). The response spectra can be converted into acceleration-displacement response spectra (ADRS) which are the demand curves. The fundamental requirements in [EN1998-3, 2005] refer to the state of damage in the structure, which is defined through the three limit states:

- **Damage Limitation (DL):** the structure is only lightly damaged, with structural elements prevented from significant yielding and retaining their strength and stiffness properties. Permanent drifts are negligible. The structure does not need any repair. Return period of 225 years, corresponding to a probability of exceedance of 20% in 50 years.
- **Significant Damage (SD):** the structure is significantly damaged, with some residual lateral strength and stiffness, and the vertical elements are capable of sustaining vertical loads.

Moderate permanent drifts are present. The structure is uneconomic to repair. Return period of 475 years, corresponding to a probability of exceedance of 10% in 50 years.

- Near Collapse (NC): the structure is heavily damaged, with low residual lateral strength and stiffness, and the vertical elements are still capable of sustaining vertical loads. Large permanent drifts are present. The structure is near collapse. Return period of 2.475 years, corresponding to a probability of exceedance of 2% in 50 years.

The response spectrum to be used is the elastic response spectrum as previously shown on figure B.4 which corresponds to significant damage. The elastic response spectrum for soil type D is used to get the response spectra for damage limitation and near collapse limit states by calculating a new importance factor by the following equation:

$$\gamma_I \approx \frac{T_{LR}^{-1/k}}{T_R}$$

where

T_{LR}	Years for which the reference seismic action is defined (=475 years)
k	Exponent dependent on seismicity equal to 3, [EN1998-1, 2004]
T_R	Return period for the limit state (=225, 475 or 2.475 years).

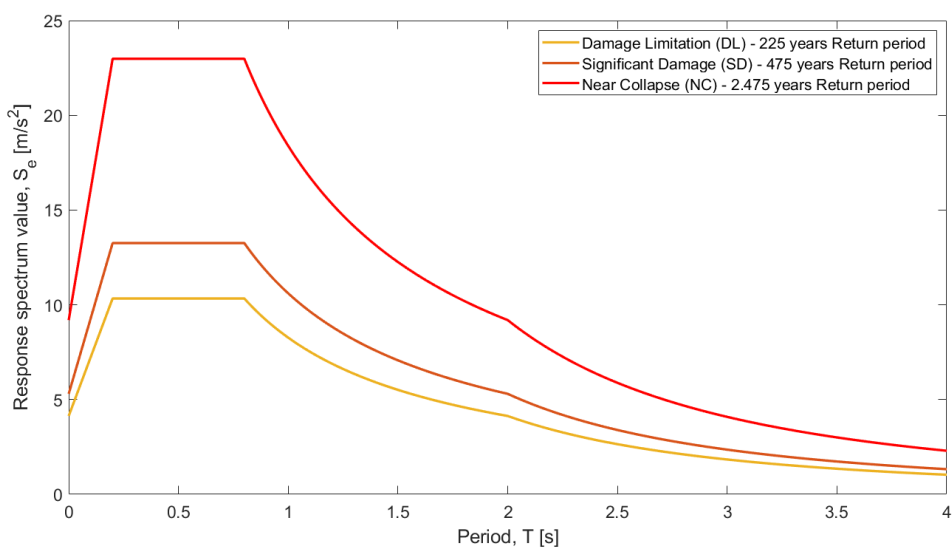


Figure D.6: Response spectra with return periods according to limit state.

Now the response spectra can be converted into the acceleration-displacement format (ADRS) rather than the normal acceleration-period format which is done through changing the period to displacement by the following equation:

$$d^* = S_e(T) \left(\frac{T}{2\pi} \right)^2 \quad (D.20)$$

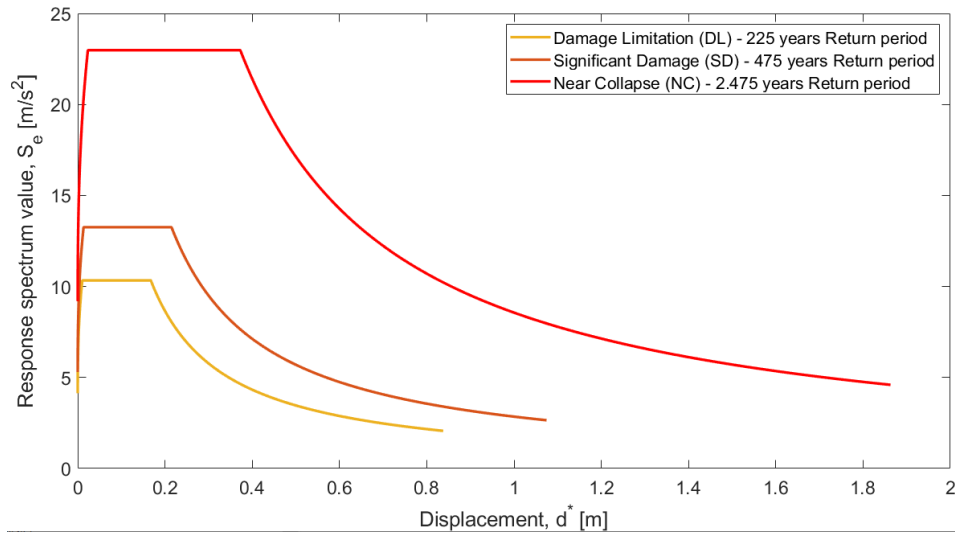


Figure D.7: Demand curves - acceleration-displacement response spectra (ADRS).

Now the ADRS demand curve and the capacity curve can be used together to get the target displacement.

D.3.5 Target Displacement

The target displacement is the result of the pushover analysis, which corresponds to the likely peak inelastic displacement of the control node (roof node) during the earthquake. Dependent on the period of the idealized equivalent SDOF system, the target displacement can be determined by the capacity spectrum and demand curve as shown in figure D.8.

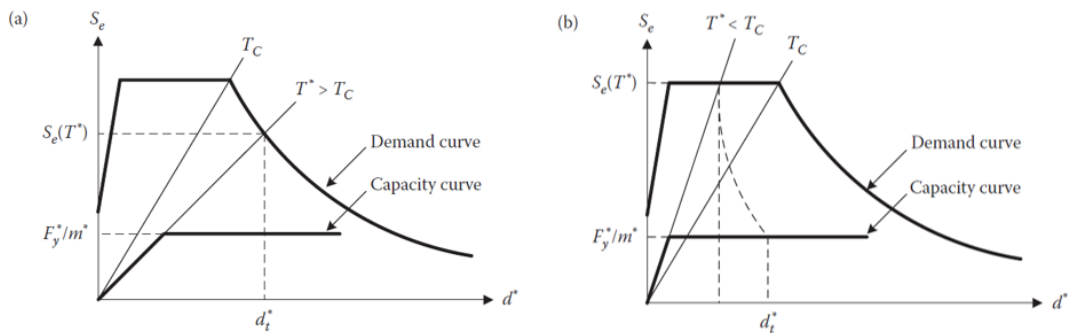


Figure D.8: Determination of target displacement in pushover analysis, [Elghazouli, 2017].
 a) Long-period structures, b) short-period structures.

For long-period structures with $T^* \geq T_c$ in figure D.8 a) the target displacement is based on the equal displacement rule for elastic and inelastic systems and can be found as:

$$d_t^* = d_{et}^*$$

where d_{et}^* is target displacement of the structure with period T^* and unlimited elastic behaviour,

which can be calculated from:

$$d_{et}^* = S_e(T^*) \left(\frac{T^*}{2\pi} \right)^2$$

and T^* is the period of the idealized equivalent SDOF system, which are calculated from:

$$T^* = 2\pi \sqrt{\frac{m^* d_y^*}{F_y^*}}$$

For short-period structures with $T^* < T_c$ in figure D.8 b) the target displacement is based on the equal displacement rule for elastic and inelastic systems but now with a correction applied to account for more complex interaction between behaviour factor and ductility and can be found as:

$$d_t^* = d_{et}^* \quad \text{if } F_y^*/m^* \geq S_e(T^*)$$

and

$$d_t^* = \frac{d_{et}^*}{q_u} \left(1 + (q_u - 1) \frac{T_c}{T^*} \right) \geq d_{et}^* \quad \text{if } F_y^*/m^* < S_e(T^*)$$

where q_u is the ratio between acceleration in the structure with unlimited elastic behaviour and in the structure with limited strength.

$$q_u = \frac{S_e(T^*) m^*}{F_y^*}$$

The above procedure to find target displacement can be applied for the all limit states as illustrated on figure D.9.

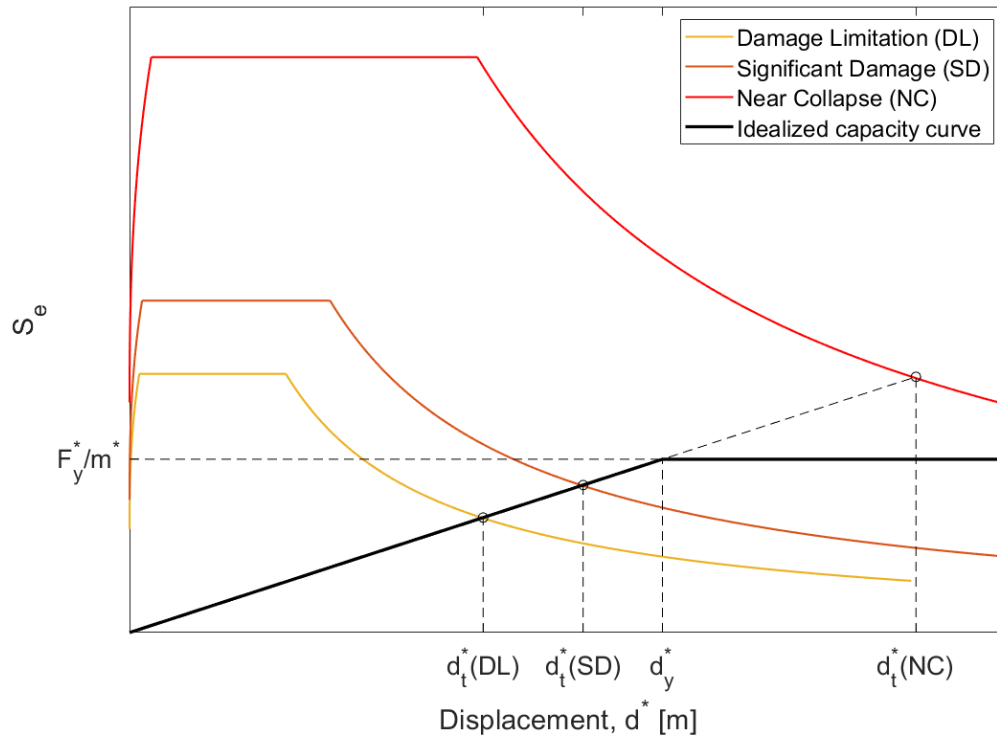


Figure D.9: Target displacement from demand curves and capacity curve.

Now that the target displacement can be calculated for the equivalent SDOF system, by use of the demand curves and capacity curve the last part is to transform the target displacement back to a MDOF system by equation (D.21) and then the target displacement can be plotted on the MDOF capacity curve to evaluate the structural integrity which are shown at figure D.10.

$$d_t = \Gamma d_t^* \quad (\text{D.21})$$

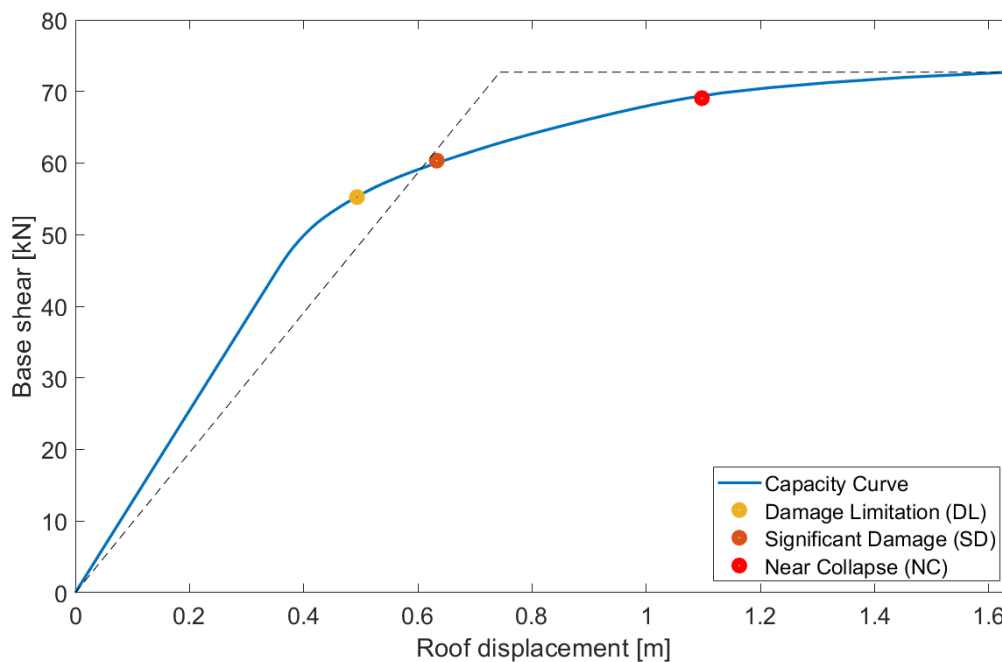


Figure D.10: Target displacement at capacity curve from pushover analysis.

Now a non-linear static analysis can be performed for the model at each limit state as shown in figure D.10 and the story forces and displacements equating to the base shear limit state can be found in a static analysis. Since the purpose is to compare the different methods of analysis from EN 1998-1, the results that will be compared is for the limit state corresponding to significant damage which is for response from a earthquake with 475 years return period, which is also the same as used in the lateral force method analysis and modal response spectrum analysis.

D.4 Non-linear Time History Analysis

The most computationally demanding method is the time history analysis. The time history analysis makes use a ground motion acceleration time history, which frequency content matches the design spectrum. The purpose is to obtain a solution for the dynamic equation where stiffness depend on the deformation, [Cook et al., 2002] shown in equation (D.22):

$$[\mathbf{M}]\{\ddot{\mathbf{u}}\} + [\mathbf{C}]\{\dot{\mathbf{u}}\} + [\mathbf{K}(\mathbf{u})]\{\mathbf{u}\} = \{\mathbf{P}(\mathbf{u},t)\} \quad (\text{D.22})$$

where

$[\mathbf{M}]$	Mass matrix [kg]
$[\mathbf{C}]$	Damping matrix [Ns/m]
$[\mathbf{K}]$	Stiffness matrix [N/m]
$\{\ddot{\mathbf{u}}\}, \{\dot{\mathbf{u}}\}, \{\mathbf{u}\}$	Vector of nodal acceleration [m/s ²], velocity [m/s] and displacement [m]
$\{\mathbf{P}\}$	Global load vector [N].

Within the scope of the non-linear analyses the software program *SeismoStruct* has been used with the following assumptions:

- Consistent mass matrix
- Rayleigh damping model
- Implicit time integration method with time integration parameters
- Modified Newton Raphson iteration scheme

Rayleigh damping also called viscous damping is a commonly used damping model as the global damping matrix is proportional to the global mass and stiffness, which is shown in equation (D.23)

$$[\mathbf{C}] = \alpha [\mathbf{M}] + \beta [\mathbf{K}(\mathbf{u})] \quad (\text{D.23})$$

The mass proportional α and stiffness proportional β coefficients are computed in the software program using the eigenperiod T and damping values ξ of the first and last mode of interest, using equation (D.24).

$$\alpha = 4\pi \frac{\xi_1 T_1 - \xi_2 T_2}{T_1^2 - T_2^2} \quad \text{and} \quad \beta = \frac{T_1 T_2}{\pi} \frac{\xi_2 T_1 - \xi_1 T_2}{T_1^2 - T_2^2} \quad (\text{D.24})$$

Where T_1 and T_2 are the eigenperiods of first and last mode of interest respectively. ξ_1 and ξ_2 are the damping ratios of the first and last mode of interest, but within the scope of this project a damping ratio of 5% is used for all modes. The advantage of this damping model is that it is computationally easy to construct even though it is not directly related to any physical process, however in this project it is used to take total damping effects into account.

D.4.1 Implicit Time Integration Method

The solution is obtained using a stepwise procedure called direct integration method. For this analysis Newmark's integration method is used to solve the differential equation of motion. The Newmark integration method is an implicit time integration method meaning that the method interpolates from both the start n and end state $n + 1$. In this project a constant average acceleration between each time step is assumed, and the displacement and velocity at step $n + 1$ is shown in equation (D.25) and (D.26).

$$\{\mathbf{u}_{n+1}\} = \{\mathbf{u}_n\} + \frac{\Delta t}{2} (\{\dot{\mathbf{u}}_n\} + \{\dot{\mathbf{u}}_{n+1}\}) \quad (\text{D.25})$$

$$\{\dot{\mathbf{u}}_{n+1}\} = \{\dot{\mathbf{u}}_n\} + \frac{\Delta t}{2} (\{\ddot{\mathbf{u}}_n\} + \{\ddot{\mathbf{u}}_{n+1}\}) \quad (\text{D.26})$$

where Δt is the time step which is 0.01 seconds. Substitution of displacement, velocity and acceleration from equations (D.25) and (D.26) into the dynamic equation, yields the following:

$$[\mathbf{K}^{\text{eff}}] \{\mathbf{u}_{n+1}\} = \{\mathbf{P}_{n+1}^{\text{eff}}\} \quad (\text{D.27})$$

where

$$[\mathbf{K}^{\text{eff}}] = \frac{4}{\Delta t^2} [\mathbf{M}] + \frac{2}{\Delta t} [\mathbf{C}] + [\mathbf{K}(\mathbf{u})]$$

$$\{\mathbf{P}_{n+1}^{\text{eff}}\} = \{\mathbf{P}_{n+1}\} + [\mathbf{M}] \left(\frac{4}{\Delta t^2} \{\mathbf{u}_n\} + \frac{4}{\Delta t} \{\dot{\mathbf{u}}_n\} + \{\ddot{\mathbf{u}}_n\} \right) + [\mathbf{C}] \left(\frac{2}{\Delta t} \{\mathbf{u}_n\} + \{\dot{\mathbf{u}}_n\} \right)$$

Then the velocity $\{\dot{\mathbf{u}}_{n+1}\}$ and acceleration $\{\ddot{\mathbf{u}}_{n+1}\}$ is obtained from equation (D.25) and (D.26) respectively and the procedure is repeated for every time step within the analysis. The advantage of using the implicit time integration is its unconditional stability regardless of time step size.

D.4.2 Modified Newton Raphson Method

In the case of geometric, material or contact non-linearities, the stiffness matrix $[\mathbf{K}]$ is dependent on the displacement vector $\{\mathbf{u}\}$, and therefore the stiffness matrix is updated between every time step, which is done using the modified Newton Raphson method. The procedure is illustrated on figure D.11.

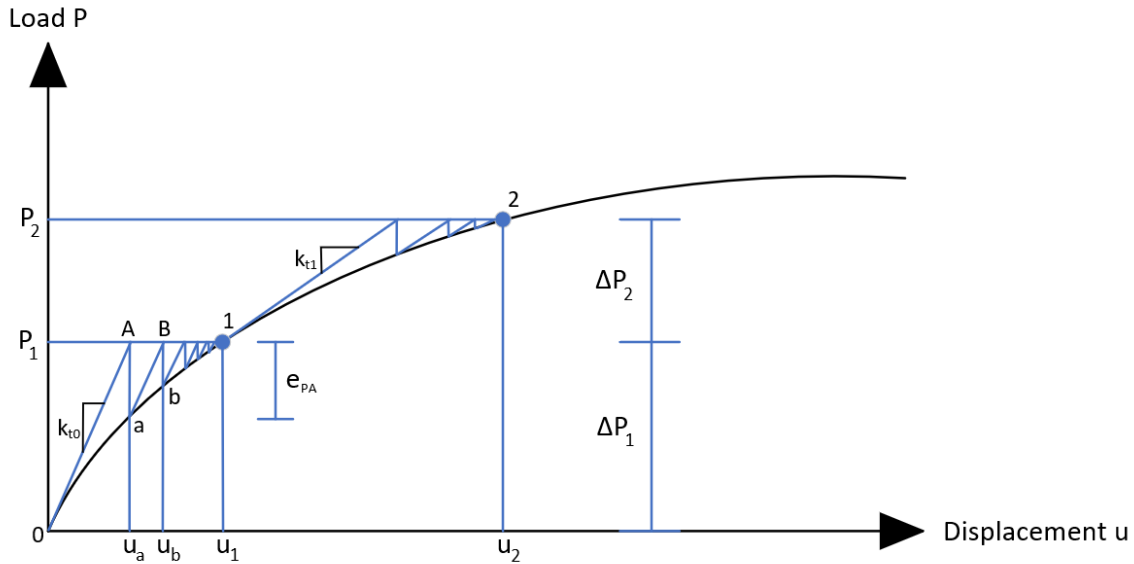


Figure D.11: Updating stiffness matrix between each time step using the procedure of Newton Raphson Method.

The purpose of the method is to construct the load P versus displacement curve u shown above and update the stiffness matrix. If an initial displacement $u = 0$ and a load P_1 is applied the corresponding displacement u_1 is sought, [Cook et al., 2002]. The initial tangent stiffness at point 0, k_{t0} is used and obtained from the material model. Then the displacement increment is calculated and the solution is updated in equation (D.28) and (D.29) respectively.

$$k_{t0} \Delta u = \Delta P_1 \implies \Delta u = k_{t0}^{-1} \Delta P_1 \quad (\text{D.28})$$

$$u_A = 0 + \Delta u \quad (\text{D.29})$$

u_A is the current estimate of u_1 , however this estimate is not exact as the equivalent force for the first estimate does not fully equilibriate the load P_1 , [Cook et al., 2002]. The current load

imbalance is calculated using equation (D.30).

$$e_{PA} = P_1 - k u_A \tag{D.30}$$

The stiffness k is obtained as the stiffness at the current estimate u_A . This process is then repeated until convergence of the load imbalance. For the modified Newton Raphson method the initial tangent stiffness is used until convergence.

Appendix E | Response of Multistorey Steel Frame Building

In this appendix the response of the multistorey steel frame building for each EN 1998-1 method is presented.

E.1 Results Lateral Force Method

For the lateral force method and modal response spectrum method the design response spectrum is utilised to obtain the spectral acceleration for the structures eigenperiods. The spectral acceleration is found for the given site conditions and illustrated in figure E.1.

- Ground type D
- Reference peak ground acceleration of $a_{gR} = 0.4g$ (10% exceedance in 50 years)
- Importance class II with a importance factor of $\gamma_1 = 1$
- Type 1; location of high seismic activity
- 5% structural damping.
- Behaviour factor $q = 4$.

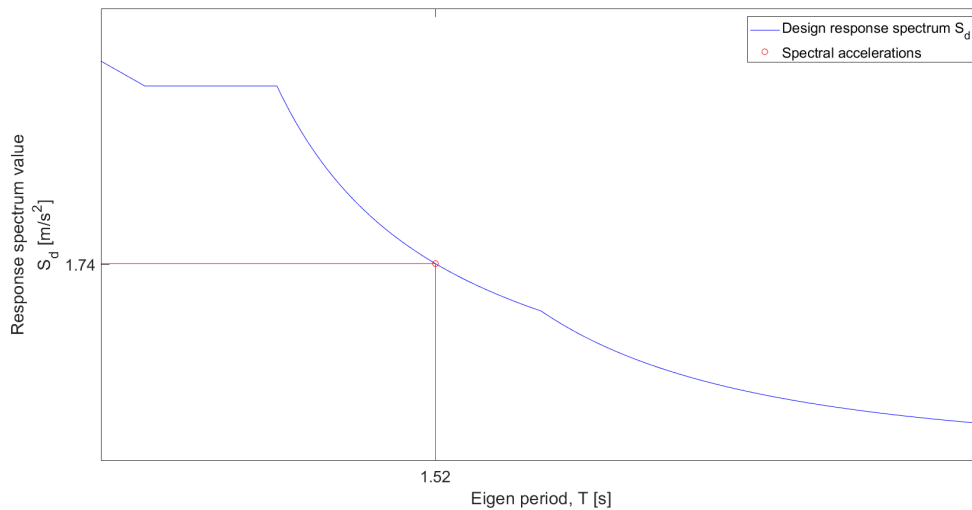


Figure E.1: Reading of spectral accelerations from the design response spectrum.

In table E.1 is the base shear force is shown as well as the variables used to obtain it.

Table E.1: Parameters and results for base shear force.

Description	Symbol	Unit	Value
First eigenperiod	T_1	[s]	1.52
Spectral acceleration	S_{de}	[m/s ²]	1.74
Total mass	m	[kg]	13,536
Correction factor	λ	[-]	0.85
Base shear force	F_b	[N]	20,069

Whether or not P-Δ effects shall be considered are examined by the sensitivity coefficient θ .

$$\theta = \frac{P_{tot,i} d_{r,i}}{F_{tot,i} h} \leq 0.1 \tag{E.1}$$

where

$P_{tot,i}$	Total gravity load at and above the story considered
$d_{r,i}$	Interstory drift
$F_{tot,i}$	Total story shear
h	Story height.

If equation (E.1) is fulfilled for every story then P-Δ effects can be neglected, and if not, the effects can be approximated by increasing every relevant story force by a factor equal to $1/(1-\theta)$.

The results from the lateral force method are listed in table E.2.

Table E.2: Results from lateral force method.

Story	Total gravity load at and above the story considered	Story displacement	Interstory drift $u_i - u_{i-1}$	Story force	Total story shear	Sensitivity coefficient
	$P_{tot,i}$ [N]	u_i [m]	$d_{r,i}$ [m]	F_i [N]	$F_{tot,i}$ [N]	θ_i [-]
1	129,816	0.0096	0.0096	216	20,069	0.021
2	116,537	0.0292	0.0196	622	19,853	0.038
3	103,258	0.0518	0.0226	1,136	19,231	0.041
4	89,980	0.0745	0.0226	1,623	18,095	0.038
5	76,701	0.0955	0.0211	2,083	16,472	0.033
6	63,422	0.1142	0.0186	2,489	14,389	0.027
7	50,144	0.1297	0.0156	2,840	11,901	0.022
8	36,865	0.1419	0.0121	3,111	9,060	0.016
9	23,586	0.1505	0.0086	3,300	5,950	0.011
10	10,308	0.1562	0.0057	2,650	2,650	0.007

Base shear [N]	Base moment [Nm]
20,069	66,718

E.2 Results Modal Response Spectrum Method

The first four eigenmodes are considered and the modeshapes are shown in figure E.2.

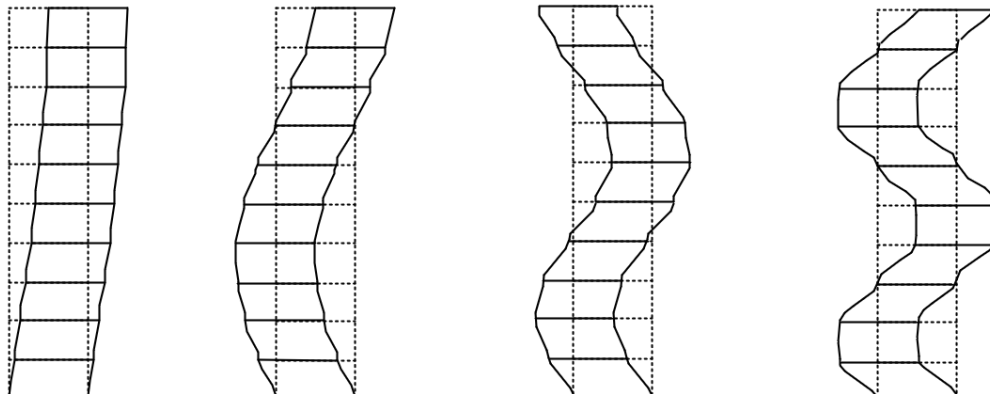


Figure E.2: The first four modeshapes.

The eigenfrequencies and modal masses in the horizontal direction are listed in table E.3.

Table E.3: Modal analysis properties.

Description	Symbol	Unit	Value
Eigenperiod	T_1		1.52
	T_2	[s]	0.47
	T_3		0.25
	T_4		0.16
Modal mass	m_1		10,414
	m_2	[kg]	1,406
	m_3		550
	m_4		356
Modal mass	m_1		76.94
	m_2	[%]	10.39
	m_3		4.06
	m_4		2.63
Total modal mass	m_{tot}	[kg]	12,726
Total modal mass	m_{tot}	[%]	94.02

From table E.3 it is concluded that a sufficient number of eigenmodes are considered as the total mass is above 90 %. It would even have been sufficient to include the three first eigenmodes, however to increase the accuracy of the results additional an additional mode is included as the computational time is not compromised too much.

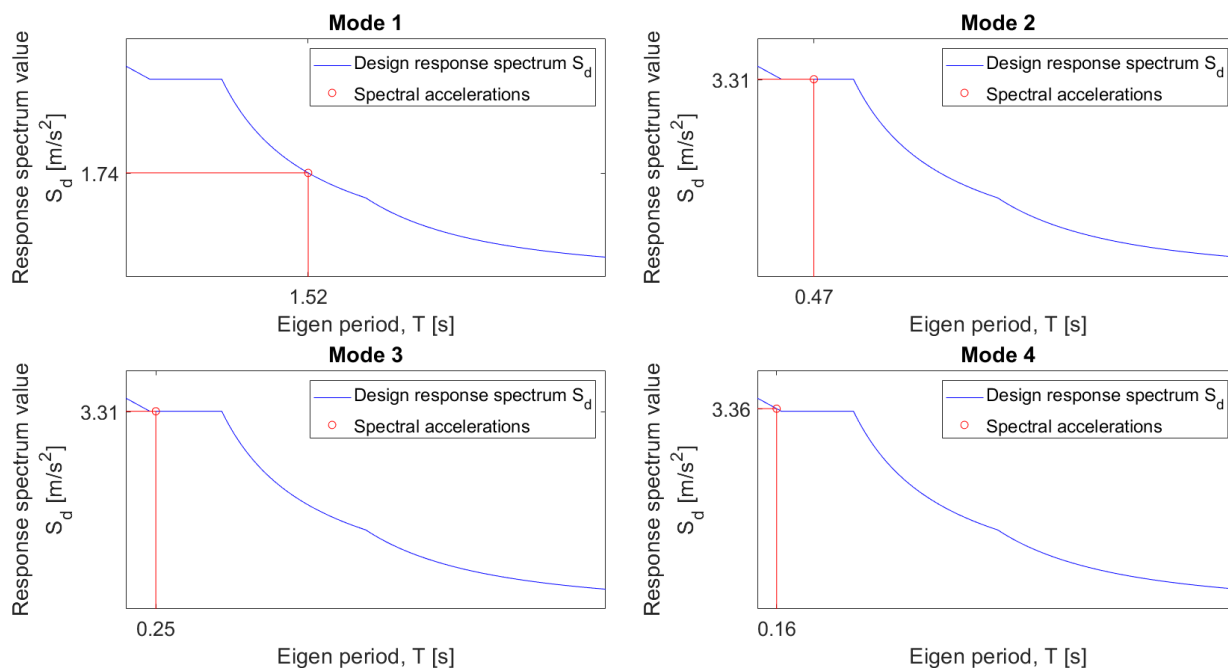


Figure E.3: Reading of spectral accelerations from the design response spectrum.

The spectrum values and base shear are shown in table E.4.

Table E.4: Spectrum values for modes.

Description	Symbol	Unit	Value
Spectrum value	S_{de1}		1.74
	S_{de2}	[m/s ²]	3.31
	S_{de3}		3.31
	S_{de4}		3.36
Base shear force	F_{b1}		[N]
	F_{b2}	4,659	
	F_{b3}	1,823	
	F_{b4}	1,197	

The force acting on each story and the total story force are listed in table E.5 and the results from the modal response spectrum method is shown in table E.6.

Table E.5: Horizontal story forces.

F_i [N]	Mode 1	Mode 2	Mode 3	Mode 4
1	193	383	560	514
2	587	1,062	1,308	912
3	1,041	1,624	1,432	436
4	1,496	1,855	752	-484
5	1,922	1,671	-359	-881
6	2,301	1,107	-1,253	-335
7	2,620	284	-1,400	567
8	2,873	-616	-703	852
9	3,056	-1,411	466	183
10	2,076	-1,300	1,019	-566

Table E.6: Results from modal response spectrum analysis.

Story	Total gravity load at and above the story considered	Story displacement	Interstory drift $u_i - u_{i-1}$	Total story shear	Sensitivity coefficient
	$P_{tot,i}$ [N]	u_i [m]	$d_{r,i}$ [m]	$F_{tot,i}$ [N]	θ_i [-]
1	129,816	0.0088	0.0088	18,879	0.020
2	116,537	0.0268	0.0179	18,529	0.038
3	103,258	0.0472	0.0205	17,681	0.040
4	89,980	0.0675	0.0202	16,501	0.037
5	76,701	0.0862	0.0187	15,018	0.032
6	63,422	0.1025	0.0164	13,222	0.026
7	50,144	0.1162	0.0136	11,118	0.020
8	36,865	0.1268	0.0106	8,717	0.015
9	23,586	0.1342	0.0075	6,003	0.010
10	10,308	0.1391	0.0048	2,713	0.006

Base shear [N]	Base moment [Nm]
18,879	61,806

E.3 Results Non-linear Static Pushover Analysis

For the non-linear static pushover analysis two cases of load patterns have been analysed; one for a "uniform" load pattern and one for a "modal" load pattern that follows the four first modeshapes. From both cases of load patterns the capacity curve has been constructed and the base shear and target displacement corresponding to the earthquake with 10 % prob. of exceedance in 50 years are obtained through the procedure in appendix D section D.3. The capacity curve and results from the "uniform" load pattern are shown at figure E.4 and results from the "modal" load patterns are shown at figure E.5.

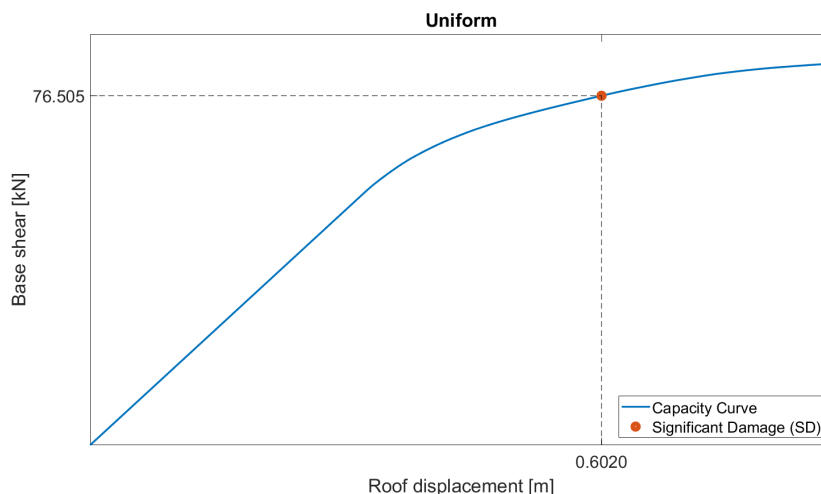


Figure E.4: Base shear and target displacement on capacity curve for "uniform" load pattern.

The results from the "uniform" load pattern are story displacement and force, base shear and base moment and are shown in table E.7.

Table E.7: Results from non-linear static pushover analysis for "uniform" load pattern.

Story	Story displacement u_i [m]	Story force F_i [N]
1	0.0430	7,737
2	0.1360	7,737
3	0.2455	7,737
4	0.3484	7,737
5	0.4319	7,737
6	0.4933	7,737
7	0.5371	7,737
8	0.5681	7,737
9	0.5889	7,737
10	0.6020	6,871
Base shear in [N]		Base moment in [Nm]
76,505		286,016

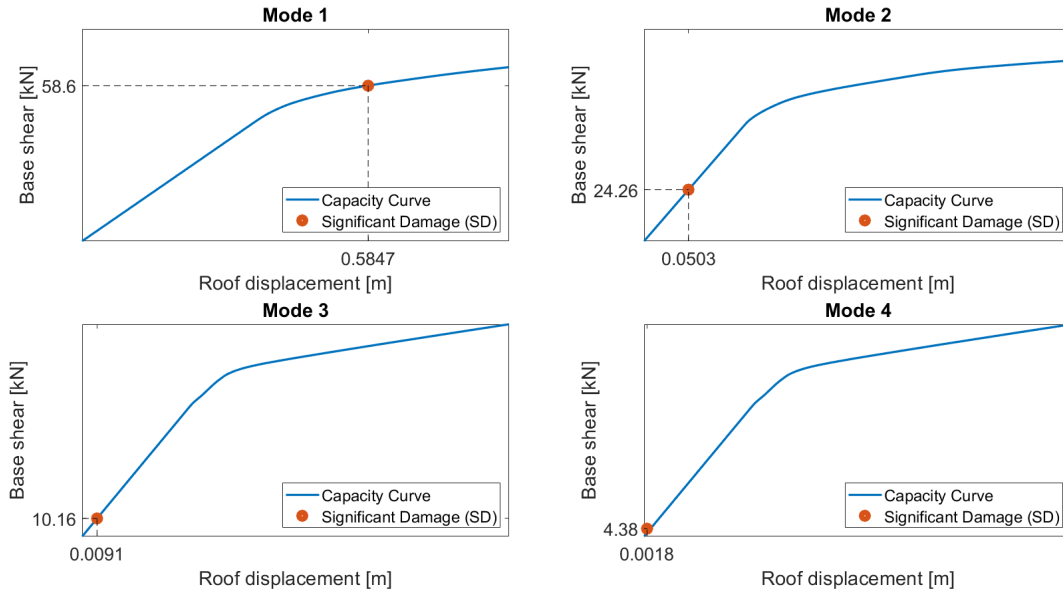


Figure E.5: Base shear and target displacement on capacity curves for "modal" load patterns.

The results from the "modal" load patterns are modal story forces, modal combined story displacement, base shear and base moment through SRSS and are shown in table E.8.

Table E.8: Results from non-linear static pushover analysis for "modal" load patterns.

Story	Mode 1	Mode 2	Mode 3	Mode 4	Story	SRSS
	F_{i1} [N]	F_{i2} [N]	F_{i3} [N]	F_{i4} [N]		u_i [m]
1	619.5	2,217	2,629	2,279	1	0.0338
2	1,780	6,119	6,057	4,054	2	0.1090
3	3,252	9,401	6,629	1,943	3	0.2028
4	4,646	10,731	3,486	-2,144	4	0.2978
5	5,962	9,667	-1,657	-3,920	5	0.3819
6	7,124	6,386	-5,829	-1,508	6	0.4492
7	8,130	1,685	-6,515	2,513	7	0.5004
8	8,904	-3,548	-3,257	3,786	8	0.5390
9	9,447	-8,159	2,172	804.2	9	0.5670
10	8,734	-10,240	6,446	-3,422	10	0.5859

Base shear	Base moment
in [N]	in [Nm]
64,381	231,141

E.4 Results Non-linear Time History Analysis

The original and matched accelerograms and response spectra for the three selected earthquakes in Japan are seen in figure E.6 and E.7.

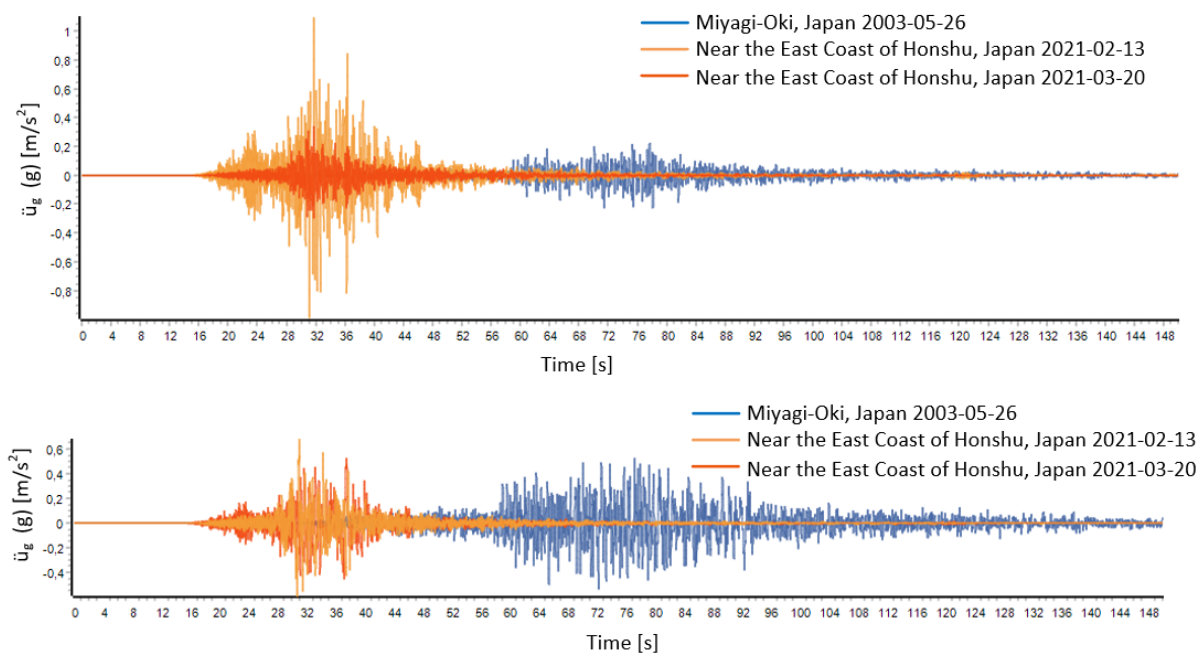


Figure E.6: Upper figure: Original accelerograms.
 Lower figure: Matched accelerogram.

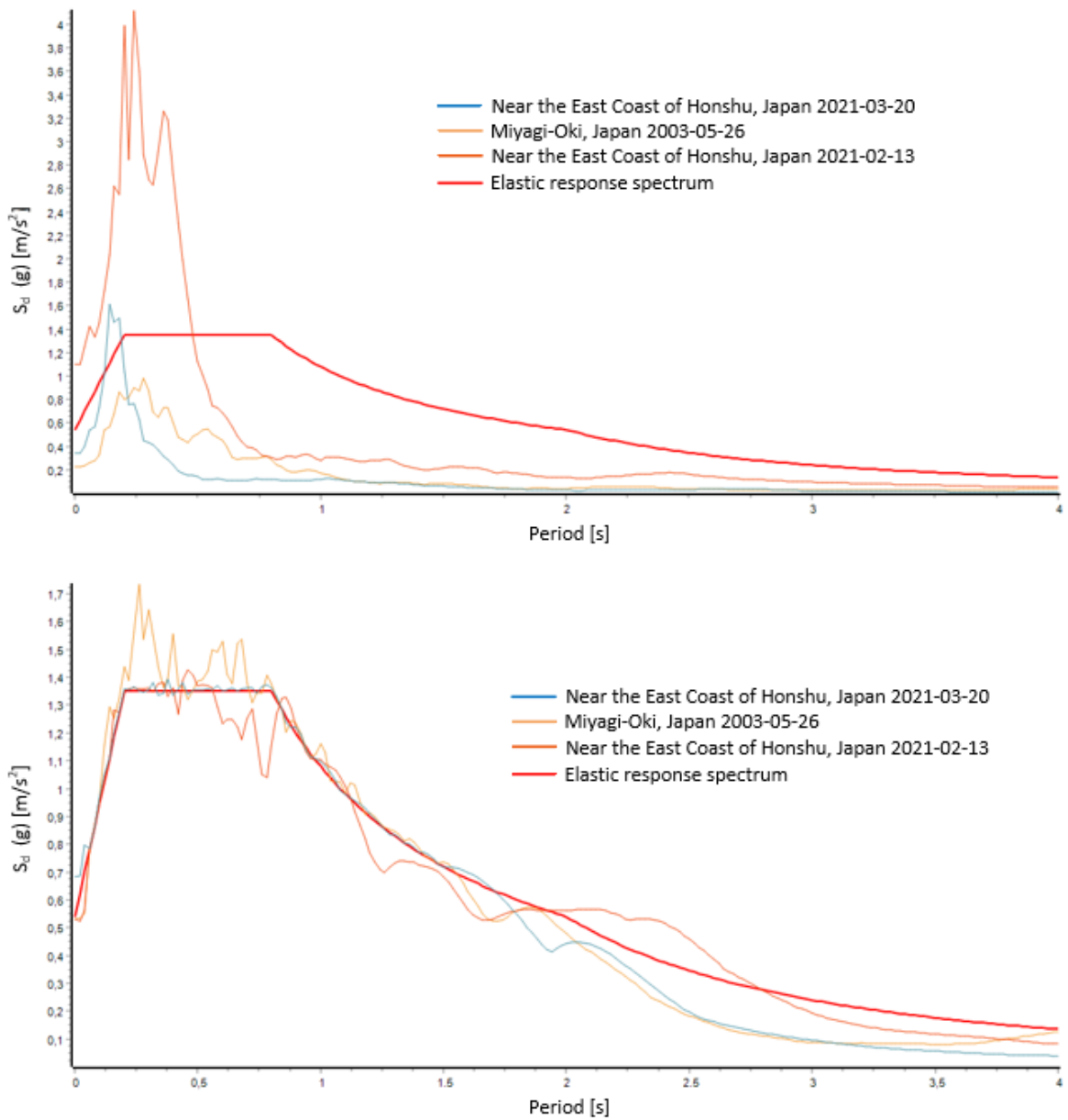
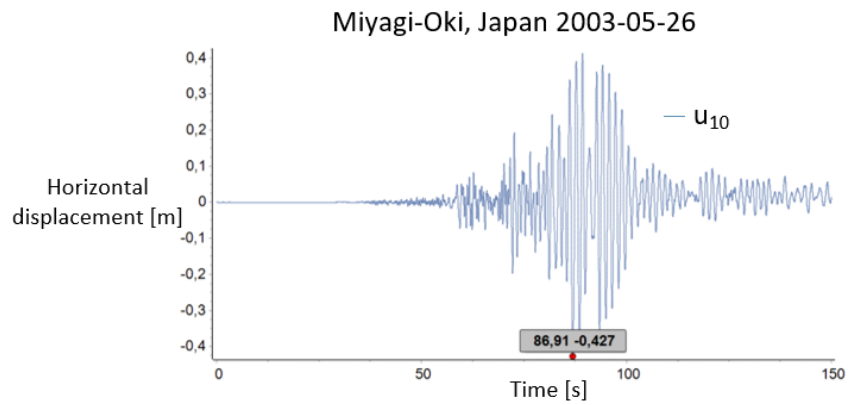


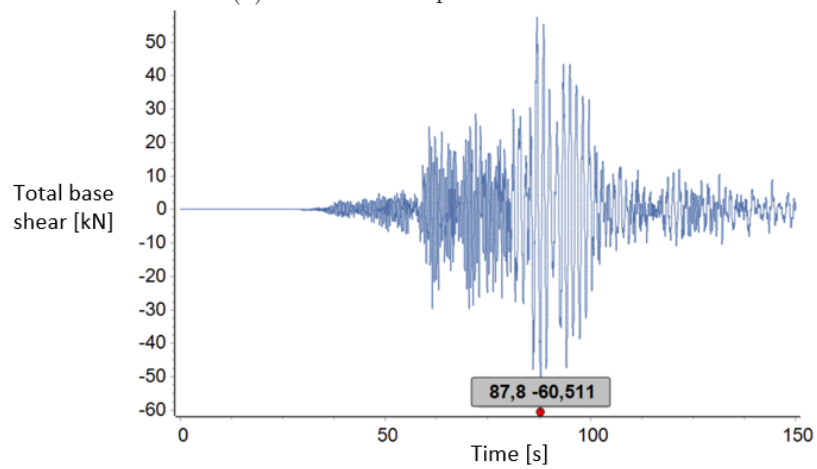
Figure E.7: Upper figure: Original response spectra.

Lower figure: Matched response spectra.

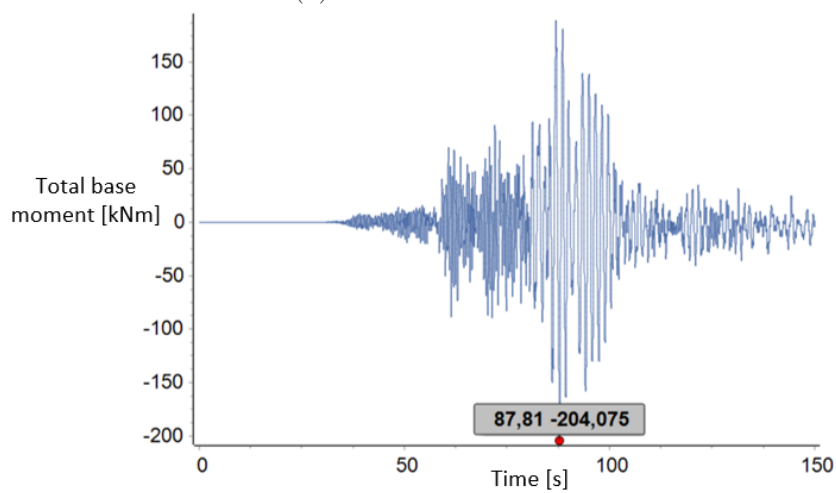
Within the scope of this analysis horizontal acceleration are applied to the restrained nodes and the response from each earthquake is illustrated in the following figures.



(a) Horizontal displacement.



(b) Total base shear.



(c) Total base moment.

Figure E.8: Response time histories for Miyagi-Oki earthquake.

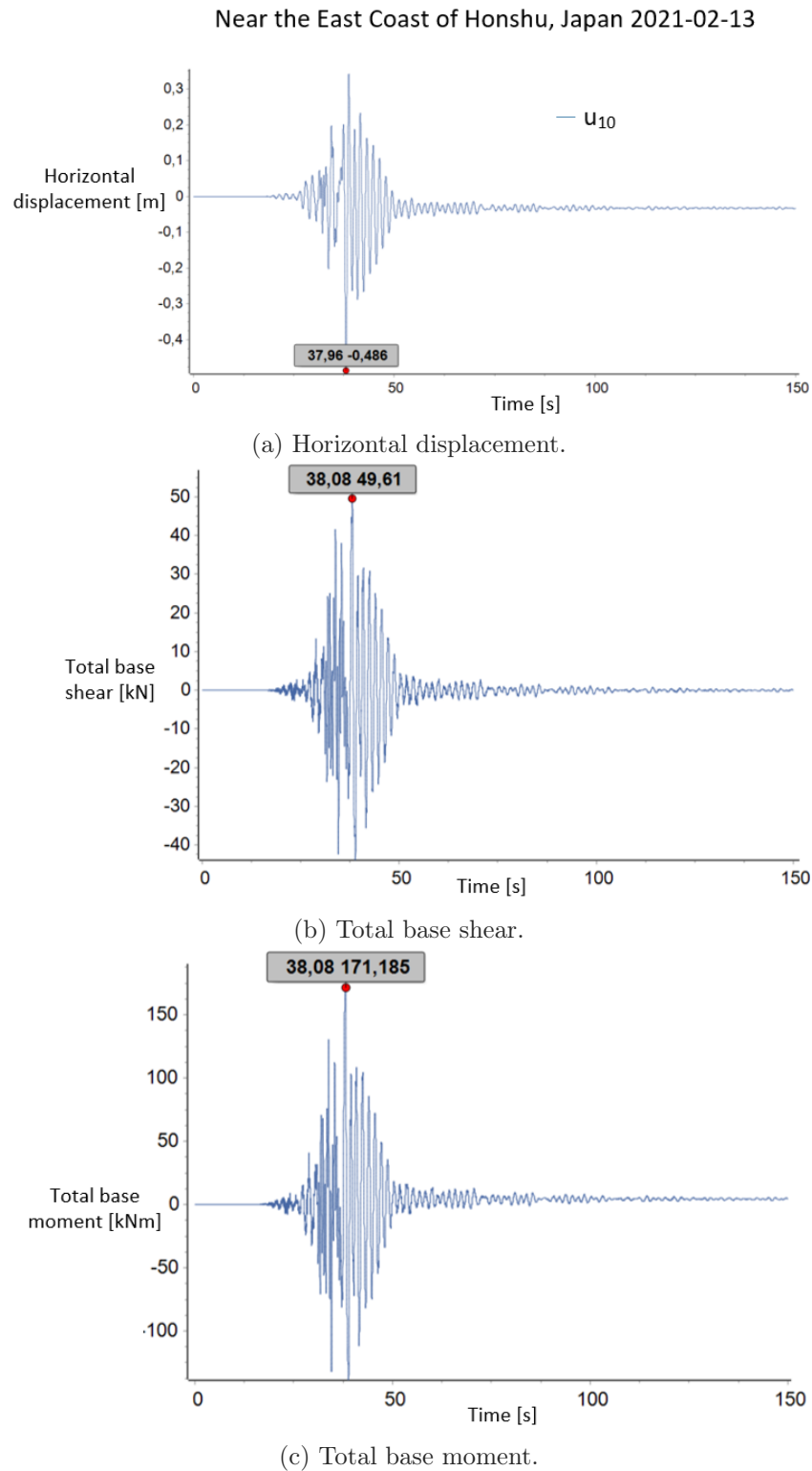
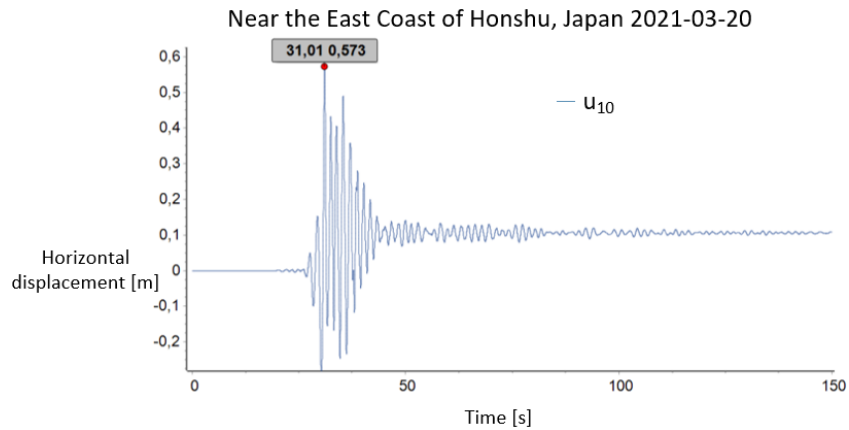
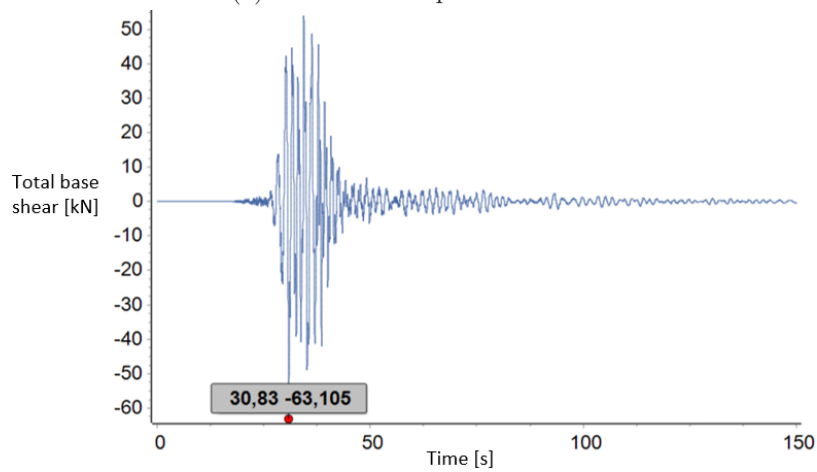


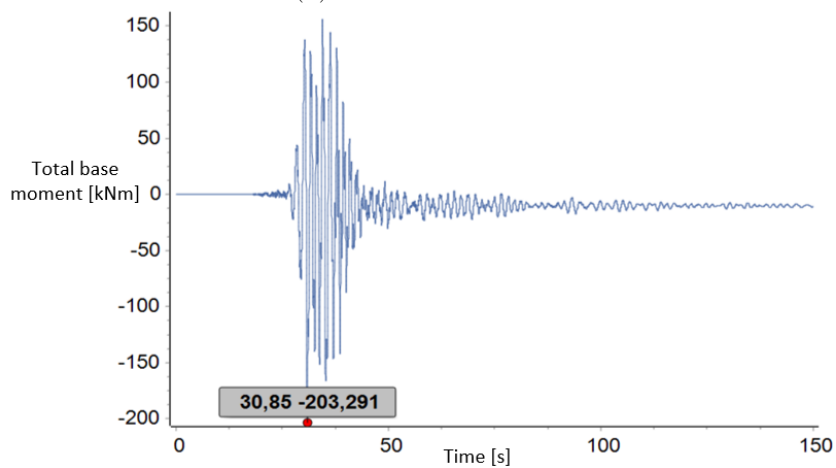
Figure E.9: Response time histories Near the East Coast of Honshu 2021-02-13 earthquake.



(a) Horizontal displacement.



(b) Total base shear.



(c) Total base moment.

Figure E.10: Response time histories Near the East Coast of Honshu 2021-03-20 earthquake.

The maximum response is summarised in table E.9 and the earthquake near the east coast of Honshu, 2021-03-20 gives the most onerous response.

Table E.9: Results from non-linear time history analysis.

	Miyagi-Oki, Japan 2003-05-26	Near the East Coast of Honshu, Japan 2021-02-13	Near the East Coast of Honshu, Japan 2021-03-20
Maximum displacement in top floor [m]	0.427	0.486	0.573
Total base shear force [N]	60,511	49,610	63,105
Total base moment [Nm]	204,075	171,185	203,291

The maximum displacement, base shear and moment reaction for the worst earthquake is summarised in table E.10.

Table E.10: Results from non-linear time history analysis.

Story	Maximum story displacement u_i [m]
1	0.029
2	0.094
3	0.176
4	0.264
5	0.349
6	0.426
7	0.486
8	0.528
9	0.556
10	0.573

Base shear in [N]	Base moment in [Nm]
63,105	203,291

Appendix F | Seismic Hazard Analysis

In this appendix the seismic hazard analysis is presented which is used to predict site-specific ground motions based on past earthquake events. The output from the analysis is a target earthquake moment magnitude and a source-to-site distance in which an appropriate earthquake accelerogram is chosen to design the wind turbine foundation.

According to [DNV-RP-0585, 2021] the seismic design of an offshore wind turbine requires site-specific ground motions, with the relevant earthquake characteristics such as magnitude and distance which is obtained by performing a seismic hazard analysis where ground shaking hazards at a particular area is quantitatively estimated. There are two broad methods for performing site-specific seismic hazard analysis:

- Deterministic seismic hazard analysis (DSHA)
- Probabilistic seismic hazard analysis (PSHA)

F.1 Deterministic Seismic Hazard Analysis (DSHA)

DSHA was prevalent in the early years of earthquake engineering, [Kramer, 1996] and is the original analysis as the framework is straightforward. A single, specific earthquake is represented and assumptions of how big the earthquake is going to be and where it will occur are made so that the ground motions are conservative. DSHA represents each single earthquake source at a time and the worst earthquake is selected. An earthquake source could be a point source (volcano), fault/line source, area source (when the fault location is unknown but assumed to be anywhere in the area). The process in DSHA is described in steps and shown in figure F.1.

1. step: Identify all earthquake sources that are capable of producing strong ground motions at the site and their magnitude.
2. step: Identify the shortest source-to-site distances
3. step: Select controlling earthquake (earthquake that is expected to produce the largest ground motions)
4. step: The seismic hazard is defined in terms of different ground motion parameters (peak acceleration, peak velocity, response spectrum).

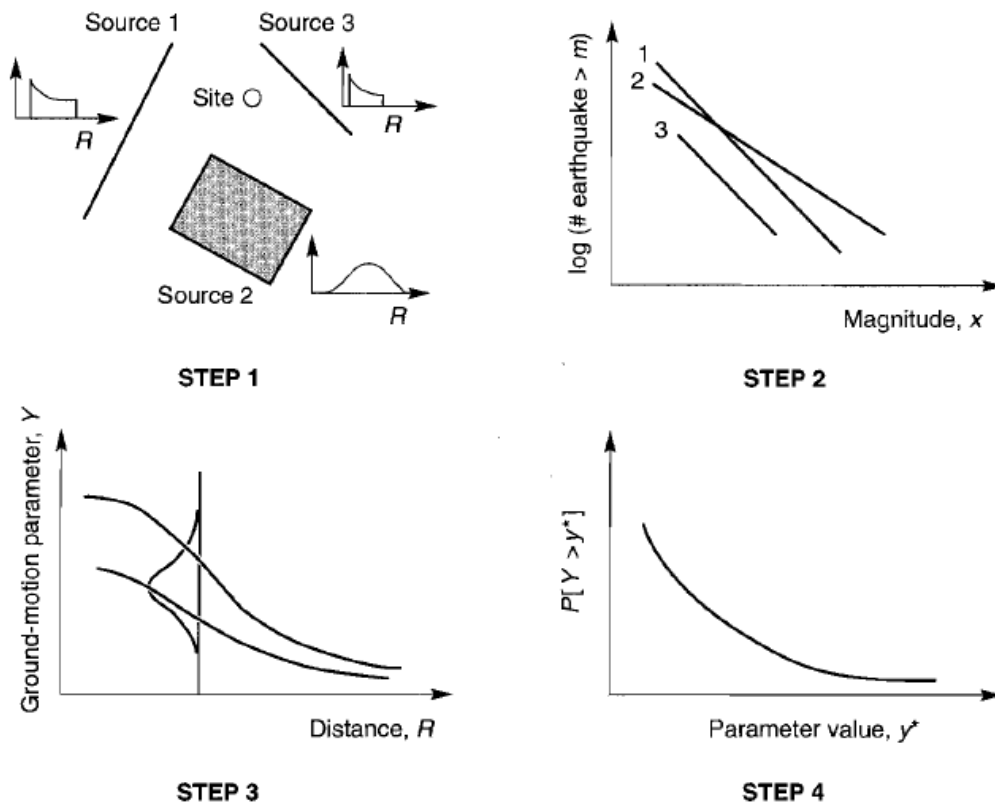


Figure F.1: Steps of deterministic seismic hazard analysis, [Kramer, 1996].

The limitations of the DSHA analysis is that it does not consider uncertainties in regards to earthquake size to source distance, size, intensity and when the earthquake occurs. The DSHA simply considers a single earthquake scenario chosen as the most conservative possible scenario, which as a result will give the worst scenario earthquake without considering the probability of occurrence and uncertainties of said earthquake. To account for this the PSHA can be utilised.

F.2 Probabilistic Seismic Hazard Analysis (PSHA)

The PSHA acknowledges that a number of things are uncertain in regards to determining the design earthquake, these uncertainties includes:

- Where the earthquake will occur (there are multiple seismic sources that the earthquake can occur on and on the seismic source there are different locations where the earthquake can occur).
- How big the earthquake will be
- The intensity of the ground motions at the site
- When the earthquake will occur.

The process of performing a PSHA is described in steps and shown in figure F.2.

1. step: Is related to the uncertainty of where the earthquake will appear. Identical to step 1 in DSHA except that the probability of potential earthquake locations on the source is characterized; typically a uniform probability distribution is assigned to each location on the seismic source.

2. step: Is related to the uncertainty of how big the earthquake will be. The distribution of the earthquake recurrence is found, i.e. how often will an earthquake magnitude repeat itself or in a given year what is the likelihood of exceeding a given magnitude.
3. step: Is related to the uncertainty of the intensity of the ground motions at the site. All possible ground motions are accounted for and weighted accordingly to their likelihood of being exceeded.
4. step: When the uncertainties in earthquake location, earthquake size and intensity of the ground motions are found these are combined to obtain the probability that the ground motion parameter will be exceeded during a particular time period, [Kramer, 1996].

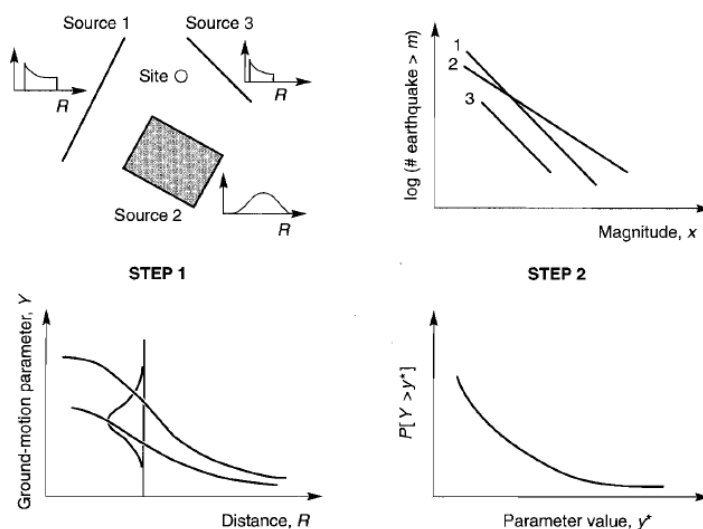


Figure F.2: Steps of probabilistic seismic hazard analysis, [Kramer, 1996].

F.2.1 Step 1: Uncertainty of earthquake location

When the earthquake sources are identified the uncertainty of where the earthquake will occur on the source shall be examined which is referred to as spatial uncertainty. It is typically assumed that the earthquake has uniform likelihood of occurring in every possible location on the seismic source (unless evidence suggests otherwise), see figure F.3. For a point source the probability is associated with one source-to-site distance. For a line source and an area source there is a minimum and a maximum source-to-site distance and the probability function will range between these two distances and will be zero outside those distances. For a rectangular area source the area is split into smaller squares and the probability function will range between the minimum and maximum source-to-site distance to the center of each square.

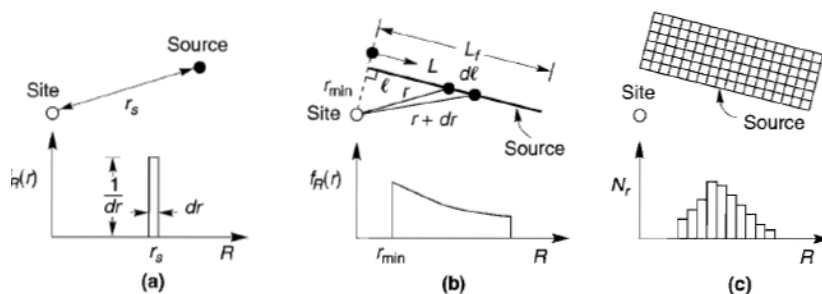


Figure F.3: Source-to-site distances for different earthquake sources, [Kramer, 1996].

The way to obtain the probability density function (PDF) for source-to-site distances for a line or area source is explained in the following steps and illustrated in figure F.4.

1. Identify the closest and farthest possible source-to-site distances, r_{min} and r_{max} , and the difference between them, $D = r_{max} - r_{min}$.
2. Select a number of bins, i , in the PDF and compute the bin size, D/i .
3. Divide the source into a number of sub-segments, n . Find the distance to each midpoint, r_n .
4. Assign each sub-segment, n , to its bin based on the distance from midpoint i to the bin n .
5. The number of sub-segments in each bin is divided by the total number of sub-segments n to create the PDF for that bin.
6. Plot each bin probability as a function of distance to get the PDF.

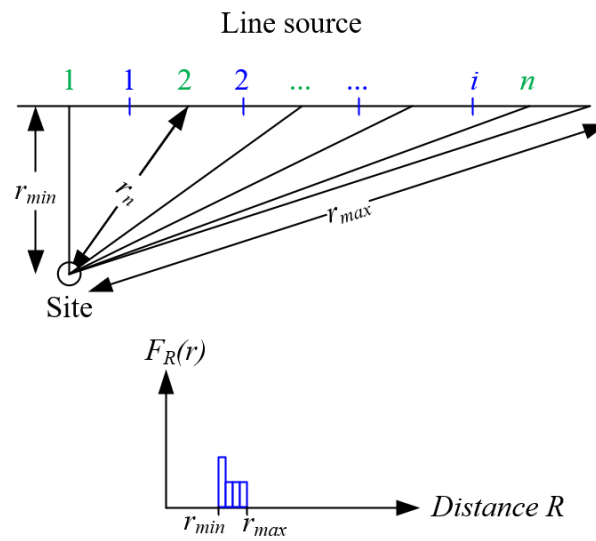


Figure F.4: Example of how a line source is divided into n sub-segments and illustration of source-to-site distances on that source.

F.2.2 Step 2: Uncertainty of earthquake size

The recurrence laws deals with the uncertainty of an earthquake's size. In recurrence laws terms as annual rate of exceedance, λ_m , and return period, T_R , are introduced. The annual rate of exceedance is the average number of earthquakes larger than a specified magnitude that occurs each year. The return period is the number of years between each earthquake that produces a magnitude larger than the specified magnitude $T_R = 1/\lambda_m$. It is assumed that recurrence law obtained from past earthquakes is appropriate for prediction of future earthquakes, [Kramer, 1996]. Commonly, Gutenberg-Richter Recurrence Laws are used which state that there is a linear relationship between the logarithm to the annual rate of exceedance and the earthquake magnitude for a given source as shown in equation (F.1) and figure F.5.

$$\begin{aligned} \log \lambda_m &= a - b m \\ \lambda_m &= 10^{a-bm} = \exp(\alpha - \beta m) \end{aligned} \tag{F.1}$$

where

λ_m	Mean annual rate of exceedance magnitude m
10^a	Mean yearly number of earthquakes of magnitude greater than or equal to zero
b	Slope of the line
α	2.303 a
β	2.303 b.

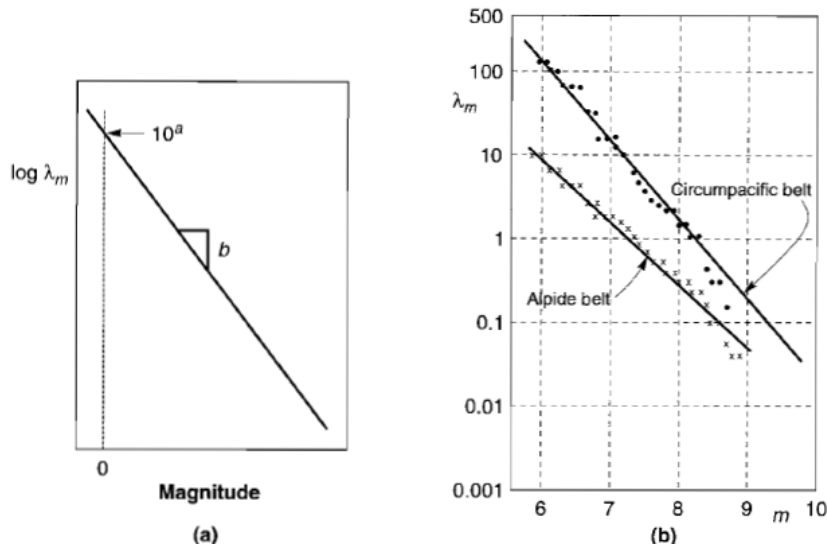


Figure F.5: Gutenberg-Richter recurrence law, [Kramer, 1996].

The Gutenberg-Richter recurrence laws have been developed to account for a minimum and a maximum magnitude, as it is only interesting to consider earthquakes with a magnitude larger than 4.0 or 5.0, [Kramer, 1996], as smaller earthquakes simply will not produce any significant damage. Likewise, some seismic sources cannot produce earthquake magnitudes above a certain limit as an earthquakes magnitude is dependent on the area of the ruptured zone. For example the Circumpacific belt do not producing earthquakes with magnitudes larger than approximately 8.7, see figure F.5, and when using the standard Gutenberg-Richter with no bounds there will be predicted likelihoods for magnitudes that physically cannot happen. The bounded Gutenberg-Richter recurrence law can be seen in figure F.6.

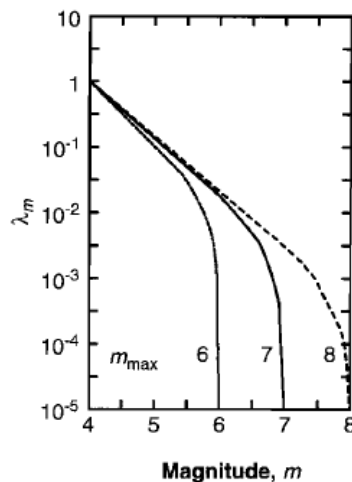


Figure F.6: Bounded Gutenberg-Richter recurrence law, [Kramer, 1996].

The mean annual rate of exceedance of magnitude m when accounting for lower and upper bound m_{min} and m_{max} is found by equation (F.2) [Kramer, 1996].

$$\lambda_m = \nu \frac{\exp[-\beta(m - m_{min})] - \exp[-\beta(m_{max} - m_{min})]}{1 - \exp[-\beta(m_{max} - m_{min})]} \quad m_{min} \leq m \leq m_{max} \quad (\text{F.2})$$

where ν is the mean annual rate of exceeding the minimum earthquake magnitude given by:

$$\nu = \exp[\alpha - \beta m_{min}] = 10^{a - b m_{min}} \quad (\text{F.3})$$

The PDF and cumulative distribution function (CDF) are found by:

$$PDF = f_M(m) = P[M = m] = \frac{\beta \exp[-\beta(m - m_{min})]}{1 - \exp[-\beta(m_{max} - m_{min})]}$$

$$CDF = F_M(m) = P[M < m] = \frac{1 - \exp[-\beta(m - m_{min})]}{1 - \exp[-\beta(m_{max} - m_{min})]}$$

F.2.3 Step 3: Uncertainty of the intensity of the ground motions at the site

Even if the location and size of the earthquake is known it is still unknown what the ground motions will be at the site which relates to the scatter and uncertainty even with recorded ground motions as shown in figure F.7.

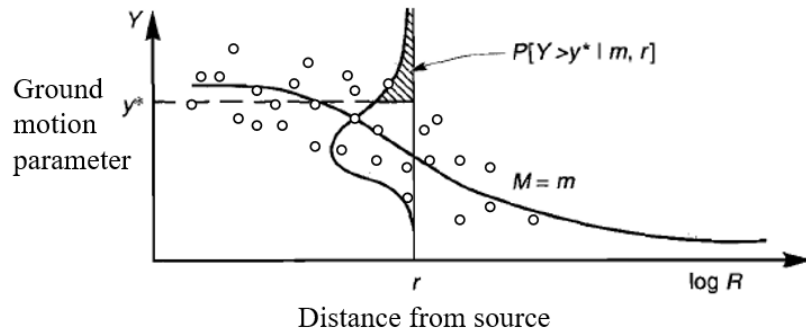


Figure F.7: Probability of exceeding a particular ground motion parameter for a given earthquake and distance, [Kramer, 1996]. The fitted line tends to attenuate the ground motion parameter with the source-to-site distance.

The scatter is related to the randomness of the rupture and from variability of the source, travel path and site conditions, [Kramer, 1996].

Predicting ground motions at the site

Attenuation relationships or ground motions prediction equations are used to predict future earthquake ground motions using collected ground motions data from the past. Attenuation relationships typically produce ground motions in terms of spectral accelerations, i.e. the response of a SDOF system. Attenuation relationships account among others for

- Fault type (e.g. strike-slip, normal or reverse faulting, see appendix A.3)
- Site characteristics (soil conditions). [Kramer, 1996].

There have been developed different attenuation relationship over time and within this project the predicted PGA is calculated from [Kanno et al., 2006] as shown in equation (F.4).

$$\begin{aligned}
 \log \text{pre} &= a_1 M_w + b_1 X - \log(X + d_1 \cdot 10^{e_1 M_w}) \\
 &\quad + c_1 + \varepsilon_1 \quad \text{for shallow earthquake event } (D \leq 30 \text{ km}) \\
 \log \text{pre} &= a_2 M_w + b_2 X - \log(X) \\
 &\quad + c_2 + \varepsilon_2 \quad \text{for deep earthquake event } (D > 30 \text{ km})
 \end{aligned} \tag{F.4}$$

where

pre	Predicted PGA (cm/s ²), PGV (cm/s), or 5% damped response spectral acceleration (cm/s ²)
$a_1, b_1, c_d, d_1, a_2, b_2, c_2$	Regression coefficient as seen in figure F.8
M_w	Earthquake moment magnitude
X	Source-to-site distance
D	Focal depth [km], see appendix A.3 for explanation
e_1	Coefficient of 0.5
$\varepsilon_1, \varepsilon_2$	Errors between predicted and observed values.

Regression Coefficients for Shallow Event Model of PGA, PGV, and 5% Damped Acceleration Response Spectra						Regression Coefficients for Deep Event Model of PGA, PGV, and 5% Damped Acceleration Response Spectra				
Period	a_1	b_1	c_1	d_1	e_1	Period	a_2	b_2	c_2	e_2
PGA	0.56	-0.0031	0.26	0.0055	0.37	PGA	0.41	-0.0039	1.56	0.40
5% Damped Acceleration Response Spectra (sec)						5% Damped Acceleration Response Spectra (sec)				
0.05	0.54	-0.0035	0.48	0.0061	0.37	0.05	0.39	-0.0040	1.76	0.42
0.06	0.54	-0.0037	0.57	0.0065	0.38	0.06	0.39	-0.0041	1.86	0.43
0.07	0.53	-0.0039	0.67	0.0066	0.38	0.07	0.38	-0.0042	1.96	0.45
0.08	0.52	-0.0040	0.75	0.0069	0.39	0.08	0.38	-0.0042	2.03	0.45
0.09	0.52	-0.0041	0.80	0.0071	0.40	0.09	0.38	-0.0043	2.08	0.46
0.10	0.52	-0.0041	0.85	0.0073	0.40	0.10	0.38	-0.0043	2.12	0.46
0.11	0.50	-0.0040	0.96	0.0061	0.40	0.11	0.38	-0.0044	2.14	0.46
0.12	0.51	-0.0040	0.93	0.0062	0.40	0.12	0.38	-0.0044	2.14	0.46
0.13	0.51	-0.0039	0.91	0.0062	0.40	0.13	0.38	-0.0044	2.13	0.46
0.15	0.52	-0.0038	0.89	0.0060	0.41	0.15	0.39	-0.0044	2.12	0.46
0.17	0.53	-0.0037	0.84	0.0056	0.41	0.17	0.40	-0.0043	2.08	0.45
0.20	0.54	-0.0034	0.76	0.0053	0.40	0.20	0.40	-0.0042	2.02	0.44
0.22	0.54	-0.0032	0.73	0.0048	0.40	0.22	0.40	-0.0041	1.99	0.43
0.25	0.54	-0.0029	0.66	0.0044	0.40	0.25	0.41	-0.0040	1.88	0.42
0.30	0.56	-0.0026	0.51	0.0039	0.39	0.30	0.43	-0.0038	1.75	0.42
0.35	0.56	-0.0024	0.42	0.0036	0.40	0.35	0.43	-0.0036	1.62	0.41
0.40	0.58	-0.0021	0.26	0.0033	0.40	0.40	0.45	-0.0034	1.49	0.41
0.45	0.59	-0.0019	0.13	0.0030	0.41	0.45	0.46	-0.0032	1.33	0.41
0.50	0.59	-0.0016	0.04	0.0022	0.41	0.50	0.47	-0.0030	1.19	0.40
0.60	0.62	-0.0014	-0.22	0.0025	0.41	0.60	0.49	-0.0028	0.95	0.40
0.70	0.63	-0.0012	-0.37	0.0022	0.41	0.70	0.51	-0.0026	0.72	0.40
0.80	0.65	-0.0011	-0.54	0.0020	0.41	0.80	0.53	-0.0025	0.49	0.40
0.90	0.68	-0.0009	-0.80	0.0019	0.41	0.90	0.56	-0.0023	0.27	0.40
1.00	0.71	-0.0009	-1.04	0.0021	0.41	1.00	0.57	-0.0022	0.08	0.41
1.10	0.72	-0.0007	-1.19	0.0018	0.41	1.10	0.59	-0.0022	-0.08	0.41
1.20	0.73	-0.0006	-1.32	0.0014	0.41	1.20	0.60	-0.0021	-0.24	0.41
1.30	0.74	-0.0006	-1.44	0.0014	0.41	1.30	0.62	-0.0020	-0.40	0.41
1.50	0.77	-0.0005	-1.70	0.0017	0.40	1.50	0.64	-0.0020	-0.63	0.41
1.70	0.79	-0.0005	-1.89	0.0019	0.39	1.70	0.66	-0.0018	-0.83	0.40
2.00	0.80	-0.0004	-2.08	0.0020	0.39	2.00	0.68	-0.0017	-1.12	0.40
2.20	0.82	-0.0004	-2.24	0.0022	0.38	2.20	0.69	-0.0017	-1.27	0.40
2.50	0.84	-0.0003	-2.46	0.0023	0.38	2.50	0.71	-0.0017	-1.48	0.39
3.00	0.86	-0.0002	-2.72	0.0021	0.38	3.00	0.73	-0.0017	-1.72	0.39
3.50	0.90	-0.0003	-2.99	0.0032	0.37	3.50	0.75	-0.0017	-1.97	0.38
4.00	0.92	-0.0005	-3.21	0.0045	0.38	4.00	0.77	-0.0016	-2.22	0.37
4.50	0.94	-0.0007	-3.39	0.0064	0.38	4.50	0.79	-0.0016	-2.45	0.36
5.00	0.92	-0.0004	-3.35	0.0030	0.38	5.00	0.82	-0.0017	-2.70	0.35
PGV	0.70	-0.0009	-1.93	0.0022	0.32	PGV	0.55	-0.0032	-0.57	0.36

Figure F.8: Regression coefficients from [Kanno et al., 2006].

Additional correction terms from site effects are applied:

$$\log \text{pre}_G = \log \text{pre} + G \tag{F.5}$$

where

pre_G	Predicted ground motion value after applying site effects
G	Additional correction term corresponding to site effects

$$G = \log(\text{obs}/\text{pre}) = p \log \text{AVS30} + q \tag{F.6}$$

where

log(obs/pre)	Residual between the observed amplitude of PGA, PGV, and spectral acceleration (obs) and the values predicted (pre) by the base model in equation (F.4)
AVS30	Average shear wave velocity in 30 m depth of 800 m/s
p, q	Coefficients derived by regression analysis on the residuals averaged at intervals of every 100 m/s in AVS30 as seen in figure F.9.

Period	p	q
PGA	-0.55	1.35
5% Damped Acceleration Response Spectra (sec)		
0.05	-0.32	0.80
0.06	-0.26	0.65
0.07	-0.24	0.60
0.08	-0.26	0.64
0.09	-0.29	0.72
0.10	-0.32	0.78
0.11	-0.35	0.84
0.12	-0.39	0.94
0.13	-0.43	1.04
0.15	-0.53	1.28
0.17	-0.61	1.47
0.20	-0.68	1.65
0.22	-0.72	1.74
0.25	-0.75	1.82
0.30	-0.80	1.96
0.35	-0.85	2.09
0.40	-0.87	2.13
0.45	-0.89	2.18
0.50	-0.91	2.25
0.60	-0.92	2.30
0.70	-0.96	2.41
0.80	-0.98	2.46
0.90	-0.97	2.44
1.00	-0.93	2.32
1.10	-0.92	2.30
1.20	-0.91	2.26
1.30	-0.88	2.20
1.50	-0.85	2.12
1.70	-0.83	2.06
2.00	-0.78	1.92
2.20	-0.76	1.88
2.50	-0.72	1.80
3.00	-0.68	1.70
3.50	-0.66	1.64
4.00	-0.62	1.54
4.50	-0.60	1.50
5.00	-0.59	1.46
PGV	-0.71	1.77

Figure F.9: Obtained coefficients from [Kanno et al., 2006].

Once the mean ground motion parameter (e.g. the peak ground acceleration PGA or spectral acceleration SA) is found from the chosen attenuation relationship the probability that an earthquake with magnitude m with a source-to-site distance, r , would cause a PGA or SA, Y , greater than a certain ground motion parameter (PGA or SA) value, y^* , can be found by equation (F.7) and is shown in figure F.7.

$$P[Y > y^* | m, r] = 1 - F_Y(y^*) \tag{F.7}$$

where

Y	Mean PGA or SA found from attenuation relationships
y^*	PGA or SA value of interest to be exceeded
m	Earthquake moment magnitude
r	Source-to-site distance
$F_Y(y)$	The value of the CDF of Y at m and r .

The value of the $F_Y(y)$ is determined using the expressions below, where ϵ is the error between predicted and observed values shown in figure F.8:

$$F_Y(y^*) = \Phi(z) \quad z = \frac{X - X_{mean}}{\epsilon} \quad X_{mean} = \log(Y) \quad X = \log(y^*) \quad (\text{F.8})$$

F.2.4 Step 4: Combining all uncertainties

It is of interest to obtain the mean spectral acceleration for a wide range of earthquakes so that all the uncertainties (earthquake location, size and intensity of ground motions) are accounted for. To do so, the Total Probability Theorem is used where

1. The probability of exceeding a certain PGA or SA value for all possible magnitudes and source-to-site distances is found and multiplied with
2. The probability of having those magnitudes and distances:

$$P[Y > y^*] = \sum_{j=1}^{N_m} \sum_{k=1}^{N_r} P[Y > y^* | m_j, r_k] P[m = m_j] P[r = r_k] \quad (\text{F.9})$$

where

N_m	Number of different earthquake magnitudes
N_r	Number of different source-to-site distances

If equation (F.9) is multiplied by the mean annual rate of exceeding the minimum earthquake magnitude ν given in equation (F.3) the mean annual rate λ_{y^*} of exceeding any PGA or SA at the site y^* is found:

$$\lambda_{y^*} = \sum_{i=1}^{N_s} \nu_i \sum_{j=1}^{N_m} \sum_{k=1}^{N_r} P[Y > y^* | m_j, r_k] P[m = m_j] P[r = r_k] \quad (\text{F.10})$$

where

N_s	Number of different earthquake sources.
-------	---

To obtain the seismic hazard curve a number of λ_{y^*} values should be found and plotted against their corresponding PGA or SA y^* as shown in figure F.10.

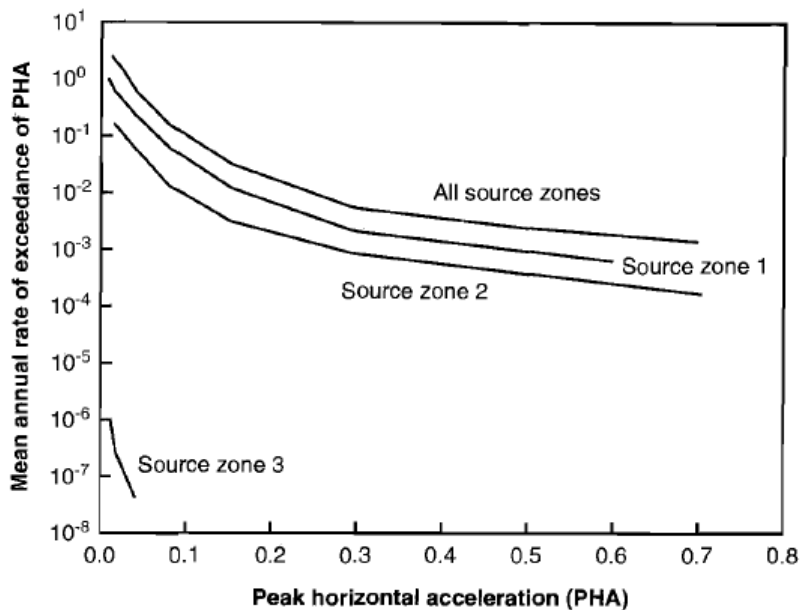


Figure F.10: Seismic hazard curve for different earthquake sources and the total seismic hazard curve from aggregating the different sources, [Kramer, 1996].

The last uncertainty to be accounted for is when an earthquake with a given size will occur. This can be modelled by The Poisson Probability Model which deals with random and independent processes as every single earthquake is unrelated to the previous earthquakes that happened on a fault. The Poisson Model gives the probability of exceeding a PGA of y^* in a specified time T :

$$P [Y_T > y^*] = 1 - \exp^{-\lambda_{y^*} T} \tag{F.11}$$

where

$P [Y_T > y^*]$	The probability of exceeding y^* in time T
T	Lifetime of structure
λ_{y^*}	Mean annual rate of exceeding PGA value y^* .

F.2.5 Deaggregation

According to [DNV-RP-0585, 2021] the earthquake event that contributes the most to the seismic hazard at the site shall be found by deaggregating the data down to individual earthquake events. This is important as an existing ground motion accelerogram with a relevant magnitude (± 0.5 of target magnitude) and similar site-to-source distance shall be selected to design the wind turbine foundation. An example of deaggregation is illustrated in figure F.11 where the red bin represents an earthquake with a target magnitude and source-to-site distance that is most likely to occur at the site.

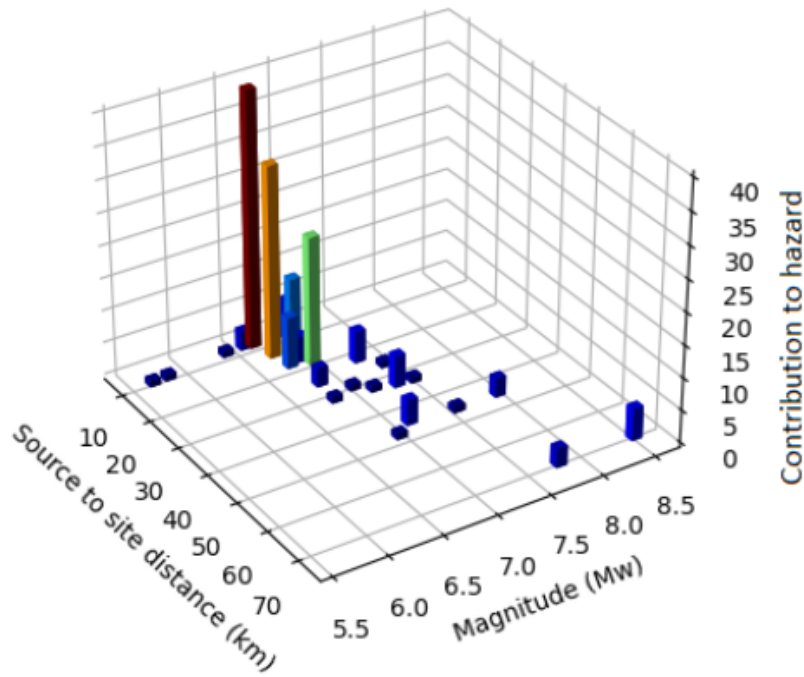


Figure F.11: Example of deaggregation, [DNV-RP-0585, 2021].

Deaggregation is done by equation (F.12) and (F.13), [Baker, 2013]. The probability of exceeding a PGA y^* given a magnitude of m_j and a source-to-site distance r_k :

$$P(Y > y^* | m = m_j, r = r_k) = \frac{\lambda_{y^*}(m = m_j, r = r_k)}{\lambda_{y^*}(Y > y^*)} \quad (\text{F.12})$$

The numerator is found using equation (F.10) but without summing over magnitudes m and source-to-site distances r :

$$\lambda_{y^*}(m = m_j, r = r_k) = \sum_{i=1}^{N_s} \nu_i P(Y > y^* | m_j, r_k) P[m = m_j] P[r = r_k] \quad (\text{F.13})$$

F.2.6 Generation of design response spectrum with target return period

The seismic hazard curve in figure F.10 is found for a number of periods and the spectral accelerations SA corresponding to each period with a selected target return period are plotted in a design response spectrum. The process is shown in figure F.12

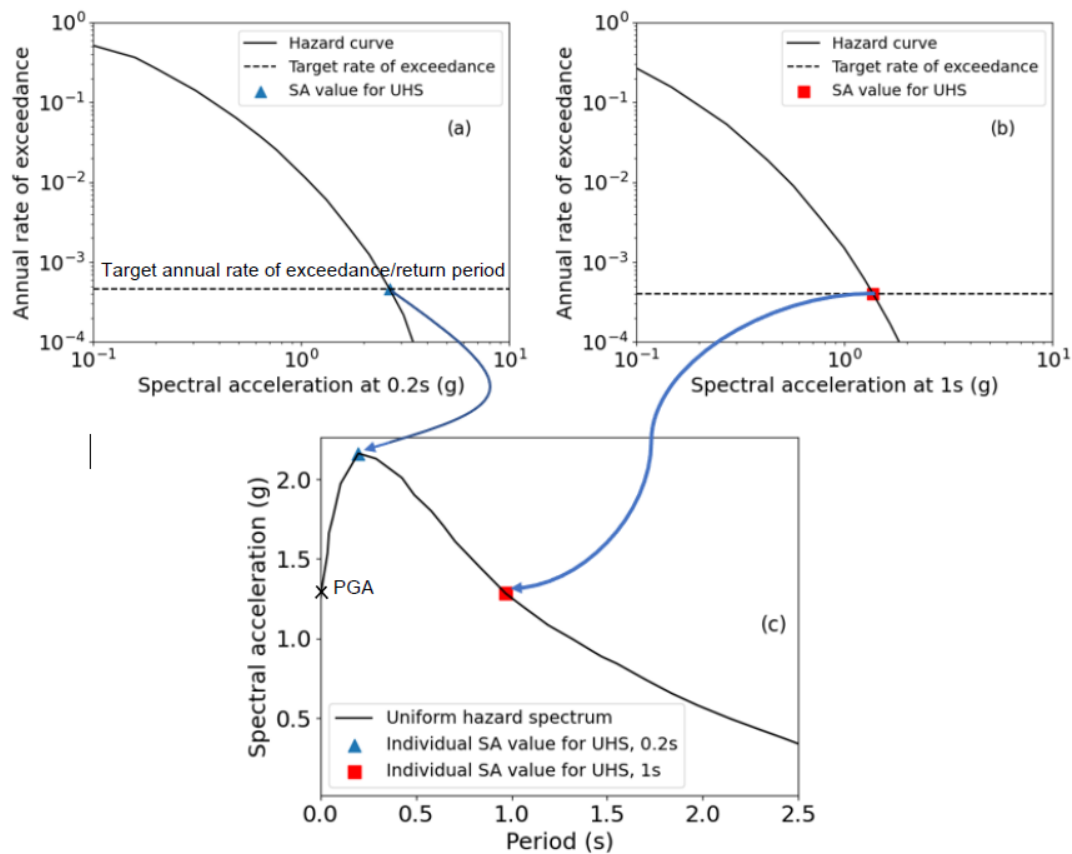


Figure F.12: Design response spectrum is obtained by combining seismic hazard curves with individual periods and selected target return period, [DNV-RP-0585, 2021].

The selected accelerogram with target magnitude and source-to-site distance found from deaggregation shall be generated so it matches the design response spectrum. By generating an accelerogram that matches the design response spectrum in shape and spectral content, a wide range of earthquakes are represented in the accelerogram.

According to [DNV-RP-0585, 2021] the design response spectrum shall be generated for a set of locations; 1 location at the centre of the wind farm and 4 locations in each corner. If the resulting spectral acceleration difference in 1 s intervals is less than 0.05 g the design spectral acceleration is found by enveloping the five curves. Otherwise, it should be considered to zone the site.

Appendix G | Site Seismic Response Analysis

In this appendix the purpose and theory behind one-dimensional "Site Seismic Response Analysis" SSRA are presented, as well as the linear, equivalent linear and non-linear approach.

Within the discipline of geotechnical earthquake engineering evaluation of ground response due to seismic excitation is essential to know, this is often determined through a SSRA. SSRA are used to determine ground motions, stresses and strains for evaluation of liquefaction hazards as well as seismic forces which could lead to instability of the soil. Within the scope of this project the techniques of one-dimensional SSRA is utilised and described below.

G.1 1D SSRA

When a fault ruptures beneath the earth's surface seismic waves travel away from the source in every direction. As the waves reach different materials they are refracted. Since shallower materials generally have lower wave propagation velocities than materials beneath, when seismic waves strike the horizontal boundaries the waves are refracted in a more vertical direction [Kramer, 1996]. By the time the seismic waves nearly have reached the surface the seismic waves have been refracted in a nearly vertical direction, see figure G.1.

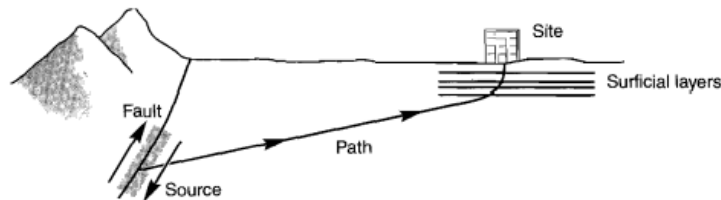


Figure G.1: Refraction process of seismic waves from earthquake source to site [Kramer, 1996].

One-dimensional SSRA are based on the assumption that all boundaries are horizontal and the soil response is mainly caused by shear-waves which is assumed to propagate vertically from the bedrock. Furthermore, the soil and bedrock surfaces are assumed to extend infinitely in the horizontal direction. When utilising the one-dimensional SSRA it is essential to determine whether or not the motion of the bedrock is unaffected by the motion of the overlaying soils and if that is not the case the SSRA the bedrock is modelled as a rigid rock and if not it is modelled as an elastic rock, see figure G.2.

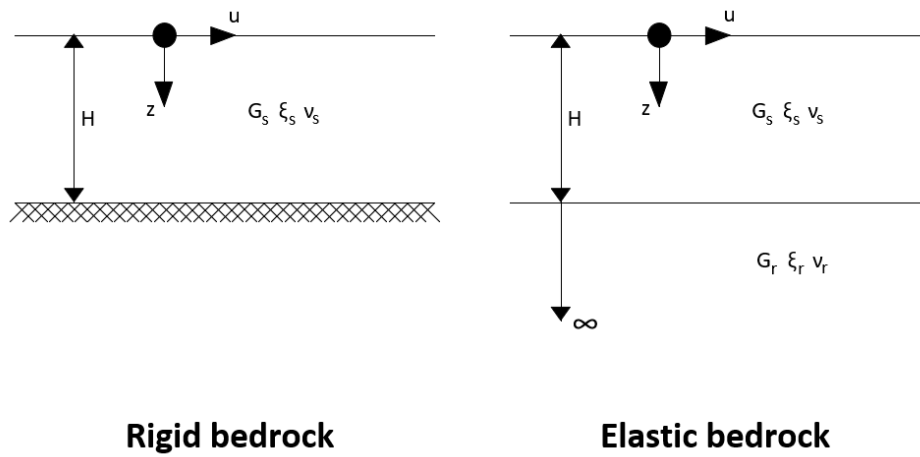


Figure G.2: Illustration of rigid and elastic bedrock.

Where

G_s and G_r	Shear modulus of soil and bedrock [kPa].
ξ_s and ξ_r	Damping ratio of soil and bedrock $[-]$.
ν_s and ν_r	Shear wave velocity of soil and bedrock [$\frac{m}{s}$].
ρ_s and ρ_r	Density of soil and bedrock [ρ].

When the model and soil/bedrock parameters are established either a linear, equivalent linear or non-linear approach is used to obtain the ground response. The choice of an appropriate approach is based on available information such as strain level and purpose of the analysis. The approaches are named after whether or not the material parameters for the soil change as a function of shear strain γ . For the linear approach the initial tangent shear modulus G_{max} is used to obtain ground response, for the equivalent linear approach the secant shear modulus G_{sec} is used throughout the entire analysis, and lastly for the non-linear approach the tangent shear modulus G_{tan} is used which varies as a function of shear strain, see figure G.3.

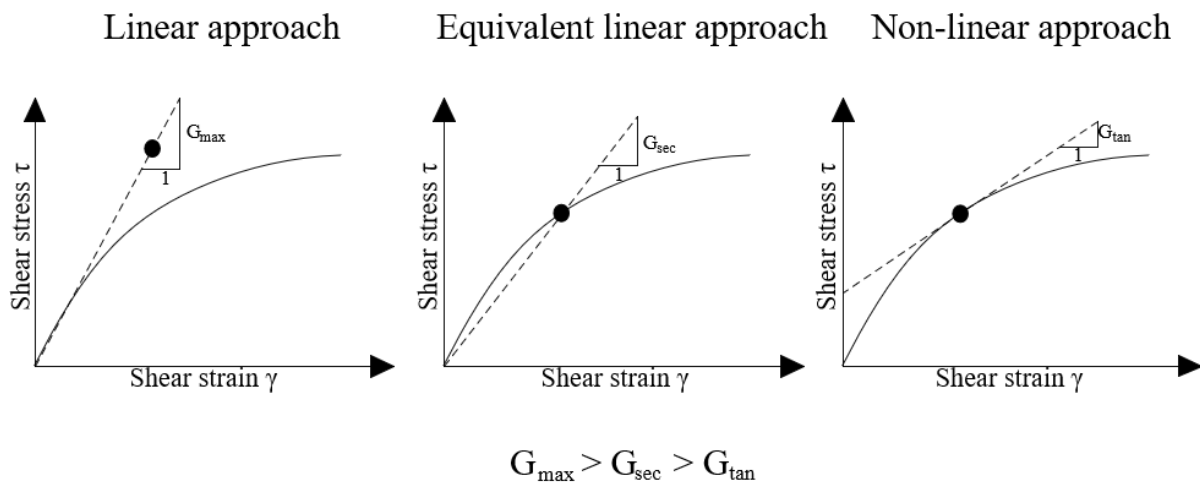


Figure G.3: Approaches for SSRA to obtain shear modulus.

As illustrated in figure G.3 the higher the complexity of the method chosen the smaller the shear modulus obtained. The approaches are described in details in the following:

G.1.1 Linear Approach

The simplest and computationally fastest approach to obtain ground response is the linear approach. For the linear approach transfer functions are utilised to obtain ground response, by expressing ground response parameters such as shear strain, shear stress, displacement, velocity and acceleration to an input bedrock acceleration. As the method uses the superposition principle it is limited to linear systems meaning dynamic soil parameters, such as shear modulus G , damping ratio ξ and shear wave velocity ν_s , doesn't change as a function of shear strain γ . In reality this is seldom the case however the approach is usually fine for very small strains, see figure G.4.

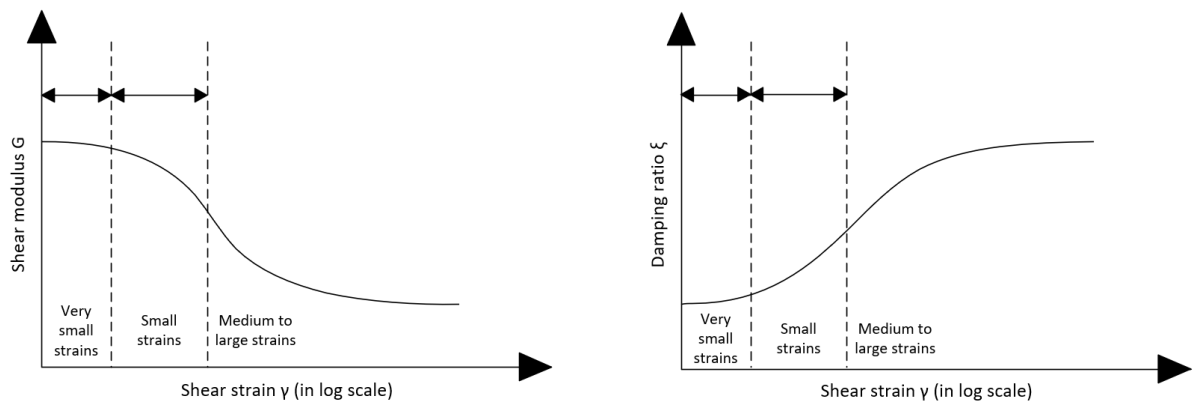


Figure G.4: Illustration of shear modulus G and damping ratio ξ as a function of shear strain

The shear wave velocity is obtained as an expression based on the shear modulus G and soil density ρ from equation (G.1)

$$\nu_s = \sqrt{\frac{G}{\rho}} \quad (\text{G.1})$$

The ground response is obtained by multiplying the bedrock response spectrum by a transfer function $|F(\omega)|$, see figure G.5. The bedrock response spectrum is obtained from the input motion illustrated in figure G.2. The input motion is converted into a response spectrum through a fast fourier transformation. The ground response can afterwards be converted to a time history through an inverse fast fourier transformation.

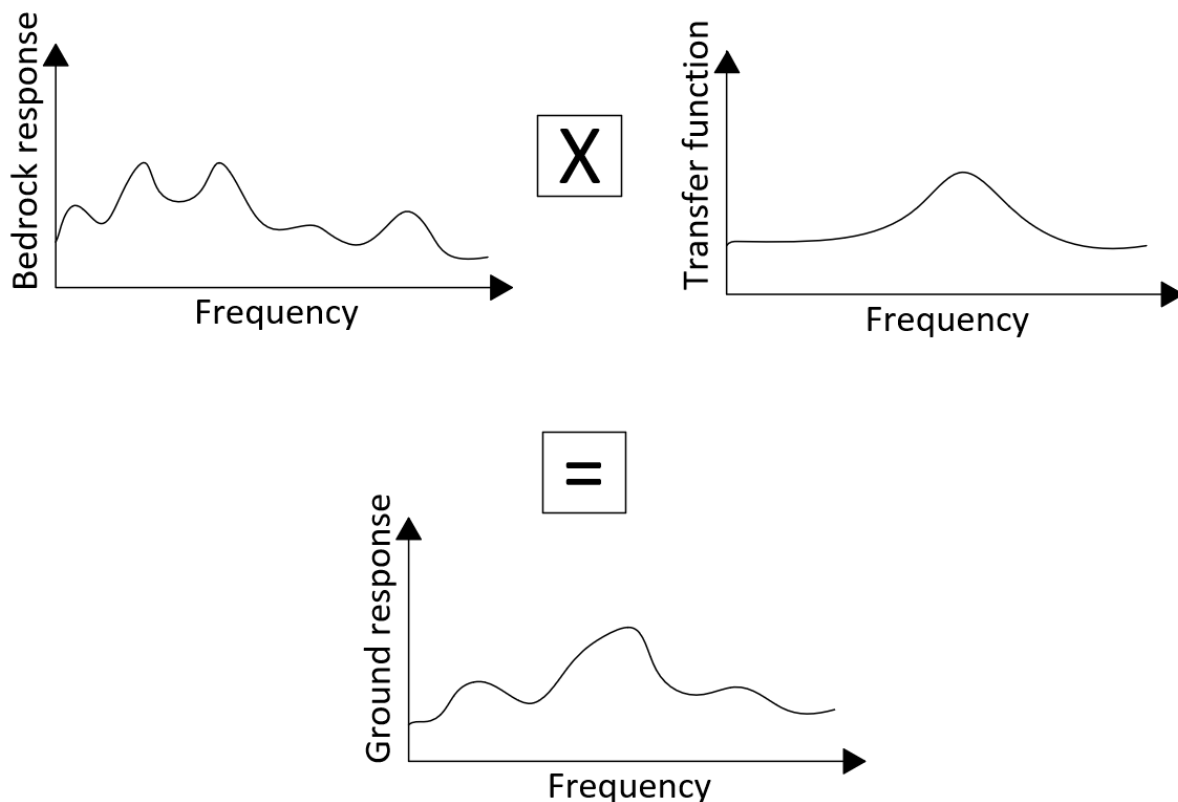


Figure G.5: Illustration of linear approach to obtaining the ground response.

The most realistic case within a SSRA is the case of a multilayered soil profile on top of an elastic bedrock as bedrock seldom can be treated as rigid as this would require a very large shear modulus and density of the bedrock. As an example a multilayered soil profile on top of elastic bedrock is shown in figure G.6.

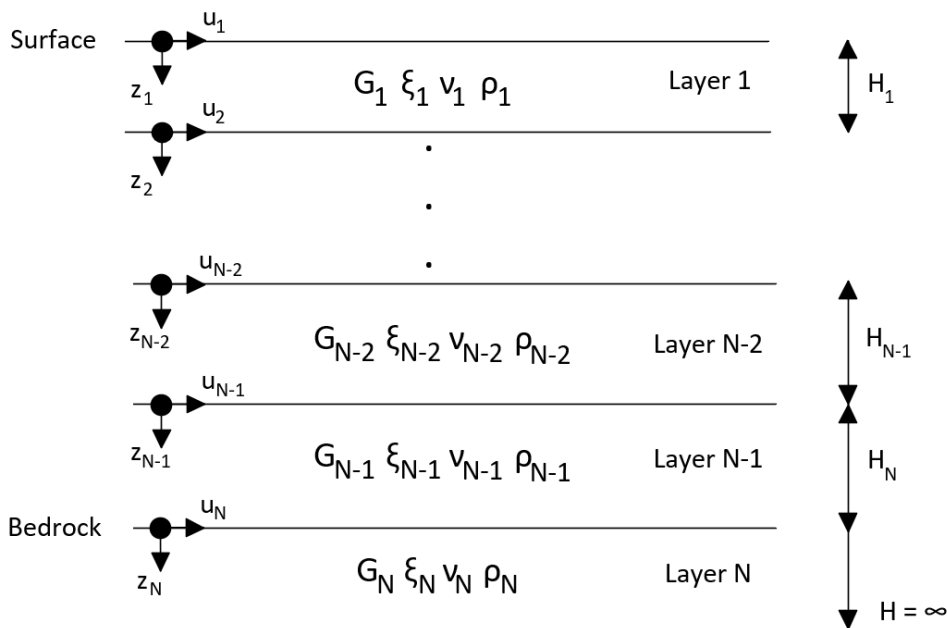


Figure G.6: Illustration of multilayered soil profile on top of elastic bedrock.

The first step to obtaining ground response is obtained from the wave equation of a damped soil which is assumed to behave like a Kelvin-Voight solid in equation (G.2) [Kramer, 1996].

$$\rho \frac{\partial^2 u}{\partial t^2} = G \frac{\partial^2 u}{\partial z^2} + \eta \frac{\partial^3 u}{\partial z^2 \partial t} \quad (\text{G.2})$$

where

u		Displacement [m]
z		Depth [m]
t		Time [s]
G		Shear modulus [kPa]
ρ		Soil density [kg/m ³]
η		Soil viscosity [-].

Furthermore, the shear stress τ is obtained by multiplying the shear strain γ by the complex shear modulus G^* due to the inclusion of damping in equation (G.3).

$$\tau(z,t) = G^* \frac{\partial u}{\partial z} \quad (\text{G.3})$$

where the complex shear modulus G^* , complex shear wave velocity ν^* and complex wave number k^* is expressed based on the assumption of frequency independent damping as:

$$G^* = G (1 + 2i\xi), \quad \nu_s^* = \nu_s (1 + i\xi), \quad k^* = k (1 - i\xi)$$

The ground response $u(z,t)$ is obtained by solving the wave equation (5.1) which is expressed in equation (G.4)

$$u(z,t) = A e^{i(\omega t + k^* z)} + B e^{i(\omega t - k^* z)} \quad (\text{G.4})$$

Where A and B are the amplitude of the seismic waves travelling in upward and downward direction. As an example of the procedure the transfer function is obtained the transfer function which relates displacements between layer N and $N - 1$ is shown. Given the solution for the wave equation the displacements at the top of layer N and bottom of layer $N - 1$ is given below:

$$\begin{aligned} u_N(z_N = 0, t) &= (A_N + B_N) e^{i \omega t} u_{N-1}(z_{n+1} = H_{N-1}, t) \\ &= (A_{N-1} e^{i k_{N-1}^* H_{N-1}} + B_{N-1} e^{i k_{N-1}^* H_{N-1}}) e^{i \omega t} \end{aligned}$$

Displacements at layer boundaries must be compatible, in this case $u_N(z_N = 0, t) = u_{N-1}(z_{n+1} = H_{N-1}, t)$, which yields equation (G.5)

$$A_N + B_N = A_{N-1} e^{i k_{N-1}^* h_{N-1}} + B_{N-1} e^{-i k_{N-1}^* h_{N-1}} \quad (\text{G.5})$$

In a similar way the shear stresses at the top of layer N and bottom of layer $N - 1$ is given below using the equation (G.3):

$$\begin{aligned}\tau_N(z_N = 0, t) &= i k_N^* G_N^* (A_N - B_N) e^{i \omega t} \tau_{N-1}(z_{n+1} = H_{N-1}, t) \\ &= i k_N^* G_N^* (A_{N-1} e^{i k_{N-1}^* H_{N-1}} - B_{N-1} e^{-i k_{N-1}^* H_{N-1}}) e^{i \omega t}\end{aligned}$$

Since stresses at layer boundaries must also be compatible which leads to $\tau_N(z_N = 0, t) = \tau_{N-1}(z_{n+1} = H_{N-1}, t)$ which yields equation (G.6)

$$A_N - B_N = \frac{k_{N-1}^* G_{N-1}^*}{k_N^* G_N^*} \left(A_{N-1} e^{i k_{N-1}^* h_{N-1}} - B_{N-1} e^{-i k_{N-1}^* h_{N-1}} \right) \quad (\text{G.6})$$

Combining equation (G.5) and (G.6) the recursion formulas obtained in equation (G.7) and (G.8) are found

$$A_N = \frac{1}{2} A_{N-1} (1 + \alpha_{N-1}^*) e^{i k_{N-1}^* h_{N-1}} + \frac{1}{2} B_{N-1} (1 - \alpha_{N-1}^*) e^{-i k_{N-1}^* h_{N-1}} \quad (\text{G.7})$$

$$B_N = \frac{1}{2} A_{N-1} (1 - \alpha_{N-1}^*) e^{i k_{N-1}^* h_{N-1}} + \frac{1}{2} B_{N-1} (1 + \alpha_{N-1}^*) e^{-i k_{N-1}^* h_{N-1}} \quad (\text{G.8})$$

Where α_m^* is the complex impedance ratio between layers $N - 1$ and N

$$\alpha_m^* = \frac{k_m^* G_m^*}{k_{m+1}^* G_{m+1}^*} \quad (\text{G.9})$$

The transfer function which relates displacement amplitude at layer i to layer j is obtained in equation (G.10)

$$F_{ij}(\omega) = \frac{|u_i|}{|u_j|} \quad (\text{G.10})$$

As $|\ddot{u}| = \omega |\dot{u}| = \omega^2 |u|$ for harmonic motions the transfer function also describes amplification in acceleration and velocity between layer i and j . Even though the linear approach is simple and computationally fast it should be used with caution and is generally meant for preliminary analysis or analysis with very small strains, therefore an alternative approach is to estimate the non-linearity through the equivalent linear approach.

G.1.2 Equivalent Linear Approach

Soil non-linearity is usually the case and strains are rarely so small that the assumption of linear behaviour is very accurate. Therefore, the equivalent linear approach has been developed as a modification of the linear approach to provide better estimates of soil damping ratio ξ and shear modulus G . The equivalent linear approach also uses one shear modulus and one damping ratio for each soil layer throughout the entire time history as is the case for the linear approach, however with strain appropriate soil parameters.

To utilize the equivalent linear approach shear modulus reduction and damping curves should be known, which can be determined from laboratory tests by applying cyclic harmonic loading to the soil, and characterising the shear modulus or damping ratio at the peak shear strain.

However earthquake time histories are irregular and may only reach peak shear strain γ_{max} a few times within its duration and therefore a cyclic harmonic loading with the same peak as the transient loading is way more crucial. Therefore the strain level of a transient record is characterised using an effective shear strain γ_{eff} , see figure G.7.

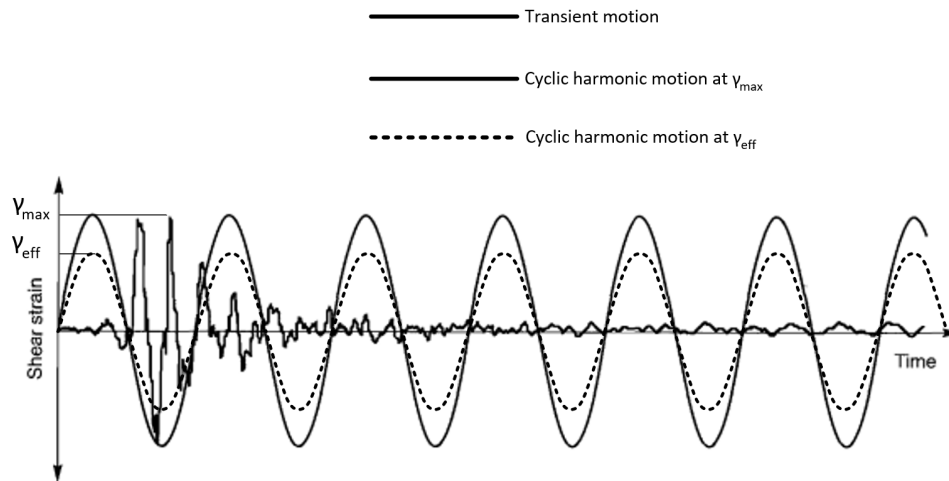


Figure G.7: Illustration of transient earthquake motion along with a cyclic harmonic motion with peak strain γ_{max} and an equivalent cyclic harmonic motion to the transient motion with peak strain γ_{eff} [Kramer, 1996].

The iterative procedure to ensure strain compatible shear modulus G and damping ratio ξ is given below and shown on figure G.8.

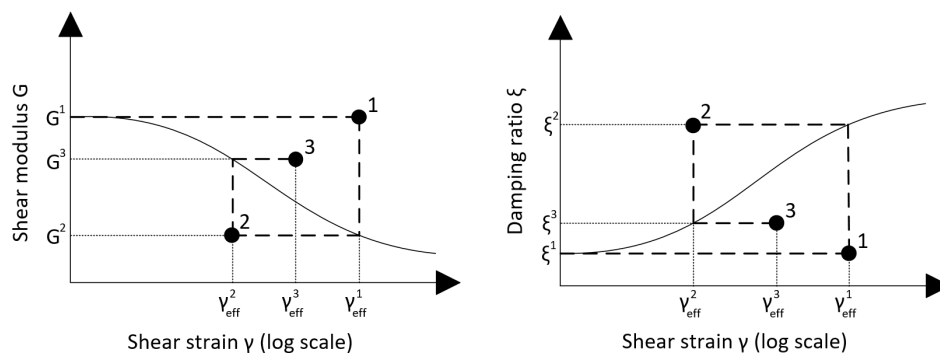


Figure G.8: Illustration of iterative procedure to obtain strain-compatible shear modulus and damping ratio.

Step 1:

Initial estimates of shear modulus G^1 and damping ratio ξ^1 is made for each layer based on zero strain values for every soil layer, see figure G.9.

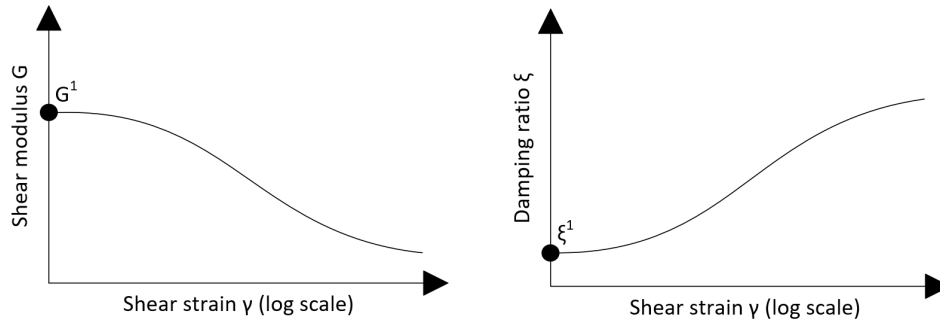


Figure G.9: Illustration of initial estimate of damping ratio ξ and shear modulus G .

Step 2:

Perform linear SSRA for the model to obtain shear strain time histories for every layer. The maximum shear strain γ_{max} is identified for every layer.

Step 3:

Effective shear strain γ_{eff} in every layer is determined from the maximum shear strain γ_{max} obtained from the shear strain time history analysis

$$\gamma_{eff}^i = R_\gamma \gamma_{max}^i \quad (\text{G.11})$$

where i refers to the iteration number and R_γ is the ratio between effective and maximum shear strain which is estimated from the empirical expression below, which depends on the earthquake magnitude M :

$$R_\gamma = \frac{M - 1}{10} \quad (\text{G.12})$$

This value of R_γ is often set to 0.65 which is valid for an earthquake magnitude of 7.5.

Step 4:

The effective shear strain value γ_{eff} is used to obtain new estimates for shear modulus G and damping ratio ξ for the next iteration.

Step 5:

Repeat steps 2-4 until convergence of shear modulus G and damping ratio ξ .

Using the equivalent linear analysis non-linear soil behaviour can be approximated, however the obtained shear modulus G and damping ratio ξ is then used throughout the entire analysis so soil behaviour is still linear. Furthermore the equivalent linear method doesn't tell anything about the development of soil stiffness and excess porewater which is crucial for soils undergoing large strains. Therefore the equivalent linear method is best suited for low strains, stiff soils with insignificant development of excess porewater pressure. For high strain, soft soils with significant development of excess porewater pressure the equivalent linear approach is no longer sufficient and the non-linear approach should be applied.

G.1.3 Non-linear Approach

Even though the equivalent linear method is computationally fast and gives reasonable results it estimates material parameters which are used throughout the entire analysis and furthermore the equivalent does not take into account the change in material parameters or development of excess porewater pressure, hence in such cases the non-linear approach should be used.

The non-linear approach requires shear modulus reduction and damping curves described in section G.2, soil constitutive model in section G.3, loading-reloading rule in section G.4 and if required a model describing development of excess porewater pressure under cyclic loading in section G.5.

The non-linear approach analyses ground response through direct integration in the time domain of the equation of motion, in equation (G.13). Using this stepwise procedure the non-linear inelastic stress-strain relationship of the soil is followed in a set of incrementally linear steps.

$$[\mathbf{M}]\{\ddot{\mathbf{u}}\} + [\mathbf{C}(\mathbf{u})]\{\dot{\mathbf{u}}\} + [\mathbf{K}(\mathbf{u})]\{\mathbf{u}\} = -[\mathbf{M}]\{\mathbf{1}\}\ddot{u}_g \quad (\text{G.13})$$

where

$[\mathbf{M}]$	Mass matrix [kg]
$[\mathbf{C}]$	Damping matrix [Ns/m]
$[\mathbf{K}]$	Stiffness matrix [N/m]
$\{\ddot{\mathbf{u}}\}, \{\dot{\mathbf{u}}\}, \{\mathbf{u}\}$	Vector of nodal acceleration [m/s ²], velocity [m/s] and displacement [m]
$\{\mathbf{1}\}$	Unit vector with ones in nodes where ground motion is applied and in the direction of acceleration [-]
\ddot{u}_g	Input ground motions [m/s ²].

Equation (G.13) is solved in each time increment Δt using the Newmark β time integration assuming average constant acceleration $\gamma = 0.5$ and $\beta = 0.25$, where $\{\mathbf{u}_t\}$, $\{\dot{\mathbf{u}}_t\}$ and $\{\ddot{\mathbf{u}}_t\}$ represent the response at time increment t and $\{\mathbf{u}_{t+1}\}$, $\{\dot{\mathbf{u}}_{t+1}\}$ and $\{\ddot{\mathbf{u}}_{t+1}\}$ is the response at the next time increment.

$$\{\mathbf{u}_{t+1}\} = \{\mathbf{u}_t\} + \frac{\Delta t}{2}(\{\dot{\mathbf{u}}_t\} + \{\dot{\mathbf{u}}_{t+1}\}) \quad (\text{G.14})$$

$$\{\dot{\mathbf{u}}_{t+1}\} = \{\dot{\mathbf{u}}_t\} + \frac{\Delta t}{2}(\{\ddot{\mathbf{u}}_t\} + \{\ddot{\mathbf{u}}_{t+1}\}) \quad (\text{G.15})$$

By substitution the equation of motion, (5.2) in time step $t + 1$ displacement, velocity and acceleration from equations (G.14) and (G.15) the following expression is obtained

$$[\mathbf{K}^{\text{eff}}]\{\mathbf{u}_{t+1}\} = \{\mathbf{R}_{t+1}^{\text{eff}}\} \quad (\text{G.16})$$

where

$$[\mathbf{K}^{\text{eff}}] = \frac{4}{\Delta t^2} [\mathbf{M}] + \frac{2}{\Delta t} [\mathbf{C}] + [\mathbf{K}] \quad (\text{G.17})$$

$$\{\mathbf{R}_{t+1}^{\text{eff}}\} = -[\mathbf{M}]\{\mathbf{1}\}\ddot{u}_g + [\mathbf{M}] \left(\frac{4}{\Delta t^2} \{\mathbf{u}_t\} + \frac{4}{\Delta t} \{\dot{\mathbf{u}}_t\} + \{\ddot{\mathbf{u}}_t\} \right) + [\mathbf{C}] \left(\frac{2}{\Delta t} \{\mathbf{u}_t\} + \{\dot{\mathbf{u}}_t\} \right) \quad (\text{G.18})$$

The first step in the analysis is to represent the soil column profile as a lumped mass system with propagation in the horizontal direction an example of representation of soil column profile to lumped mass system is shown in figure G.10.

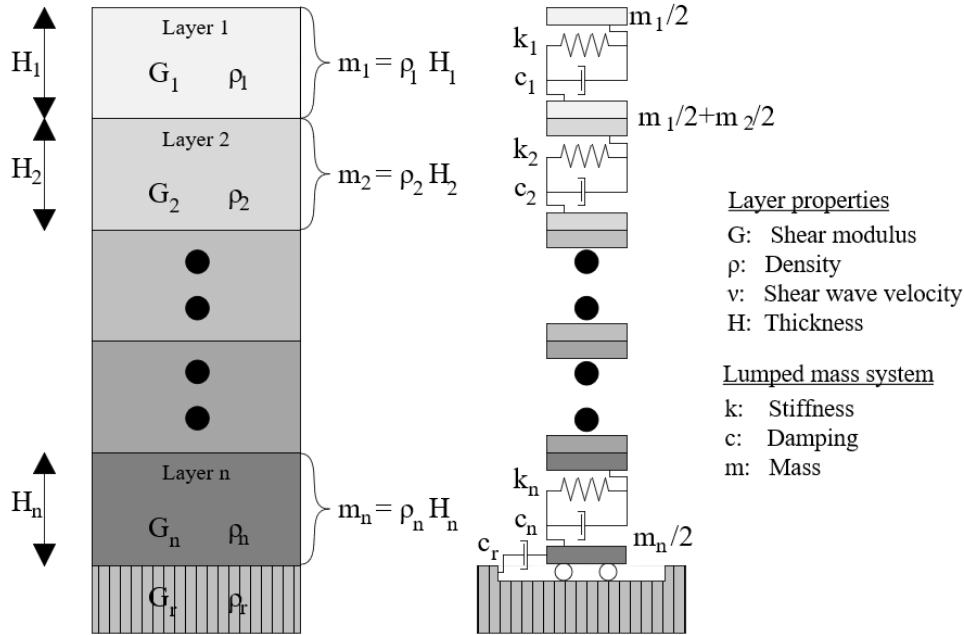


Figure G.10: Illustration of lumped mass model for a soil model.

The model utilises spring stiffnesses k , which are a function of shear strain as well as frequency independent damping c . The spring stiffnesses are obtained directly as shear strain dependent shear modulus of the soil layer G_s in equation (G.19)

$$k = \frac{G_s(\gamma)}{H} \quad (\text{G.19})$$

The damping matrix $[\mathbf{C}]$ of the model is obtained based on the formulation for frequency independent in equation (G.20)

$$[\mathbf{C}] = [\mathbf{M}] a_1 [\Phi] [\omega_n] [\Phi]^{-1} \quad (\text{G.20})$$

where $[\omega_n]$ is a diagonal matrix of the natural frequencies and $[\Phi]$ is the modal matrix of the system. $[\omega_n]$ and $[\Phi]$ are calculated as the eigenvalues and eigenvectors of $[\mathbf{M}]^{-1}[\mathbf{K}]$, [Carlton, 2014]. a_1 is a coefficient computed using the shear strain dependent damping ratio in equation (G.21)

$$\xi_n(\gamma) = 0.5 a_1 \quad (\text{G.21})$$

The non-linear analysis can be summarised as a stepwise procedure through which the ground response is obtained, the procedure consists of the following steps:

Step 1:

Initial motions in each nodal coordinate and boundary conditions are obtained for the beginning of the first time step as well as the first input motions at the bedrock \ddot{u}_g .

Step 2:

The displacement in each node is used to calculate the shear strain γ in each node, from equation (G.22)

$$\gamma_t = \frac{u_t^{i+1} - u_t^i}{\Delta z} \quad (\text{G.22})$$

Where the superscript i refers to the node starting from the top layer and the subscript t refers to the time step and Δz is the vertical distance between the two nodes considered.

Step 3:

The stiffness K and damping C matrix are calculated/updated based on the newly obtained strains using the constitutive soil model to determine an updated shear modulus G as well as the damping curves to obtain an updated damping ratio ξ .

Step 4:

Solve the equation of motion using equations (G.16), (G.17) and (G.18) obtained using the Newmark β method assuming constant average acceleration to calculate the ground response such as displacements u_{t+1} , velocity \dot{u}_{t+1} and acceleration \ddot{u}_{t+1} .

Step 5:

Repeat steps 2-4 through every time increment until the end of input motion time history.

G.2 Shear Modulus Reduction and Damping Curves

Soil is known to behave non-linearly, as soil parameters change as a function of shear strain γ . In the non-linear 1D SSRA four soil parameters are needed to run the analysis; soil density ρ_s , shear wave velocity ν_s , shear modulus G_s and damping ratio ξ_s . Among these parameters the soil density ρ_s is the only parameter which remains independent of shear strain and as a relationship has previously been established between the shear wave velocity ν_s and shear modulus G_s in equation (G.23), it is only necessary to obtain the shear modulus G_s .

$$\nu_s = \sqrt{\frac{G_s}{\rho_s}} \quad (\text{G.23})$$

Therefore a relationship has to be established between the shear modulus and shear strain as well as a relation between damping ratio and shear strain, these are respectively named shear modulus reduction and damping curves. The curves are usually determined from empirical relationships, within the context of this project the relationship proposed by [Roblee and Chiou,

2004] is used, which proposes the relation for shear modulus reduction and damping ratio given in equation (G.24) and (G.25) respectively.

$$\frac{G}{G_{max}} = \frac{1}{1 + \left(\frac{\gamma(\%)}{\gamma_{ref}}\right)^\alpha} \quad (\text{G.24})$$

$$\xi(\%) = D_{min} + \beta D_{Masing} \left(\frac{G}{G_{max}}\right)^{0.1} \quad (\text{G.25})$$

Where

$\frac{G}{G_{max}}$	Shear reduction [-]
γ_{ref}	Reference shear strain [-]
$\gamma(\%)$	Shear strain in percent [%]
$\xi(\%)$	Damping ratio in percent [%]
D_{min}	Minimum damping ratio [-]
D_{Masing}	Masing damping ratio [-]
β	Coefficient [-] .

The Masing damping ratio D_{Masing} is the ratio of dissipated energy and stored energy of a hysteresis loop [Roblee and Chiou, 2004]. According to [Roblee and Chiou, 2004] D_{Masing} can be approximated using the polynomial expression in equation (G.26)

$$D_{Masing} = c_1 D_{Masing,\alpha=1.0} + c_2 D_{Masing,\alpha=1.0}^2 + c_3 D_{Masing,\alpha=1.0}^3 \quad (\text{G.26})$$

Where

$$D_{Masing,\alpha=1.0} = \frac{100}{\pi} \left[4 \frac{\gamma - \gamma_{ref} \ln\left(\frac{\gamma + \gamma_{ref}}{\gamma_{ref}}\right)}{\frac{\gamma^2}{\gamma + \gamma_{ref}}} - 2 \right] \quad (\text{G.27})$$

And

$$c_1 = 0.2523 + 1.8618 \alpha - 1.1143 \alpha^2$$

$$c_2 = -0.0095 - 0.0710 \alpha + 0.0805 \alpha^2$$

$$c_3 = 0.0003 + 0.0002 \alpha - 0.0005 \alpha^2$$

The remaining parameters that are left to be determined is γ_{ref} , α , D_{min} and β , which are determined based on soil classification according to passing percentage of sieve 200 with a 0.05 mm wire diameter and plasticity index, and the depth see tables G.1 and G.2 respectively

Table G.1: Soil classification according to [Roblee and Chiou, 2004].

GeoIndex Model	Primarily coarse All plactisity values	Passing #200	Plasticity Index
1 - PCA	Fine-Grained Lower Plasticity	$\leq 30\%$	All
2 - FML	Fine-Grained Lower Plasticity	$> 30\%$	$\leq 15\%$
3 - FMH	Fine-Grained Higher Plasticity	$> 30\%$	$> 15\%$

Table G.2: Recommended coefficients for GeoIndex Model [Roblee and Chiou, 2004].

GeoIndex Model Depth [m]	1-PCA Soil				2-FML Soil				3-FMH Soil			
	γ_{ref}	α	D_{min}	β	γ_{ref}	α	D_{min}	β	γ_{ref}	α	D_{min}	β
0-10 m	0.032	0.85	1.30	0.62	0.057	0.90	1.30	0.62	0.085	0.98	1.30	0.62
10-20 m	0.044	0.85	1.15	0.62	0.065	0.90	1.15	0.62	0.097	0.98	1.15	0.62
20-40 m	0.061	0.85	1.02	0.62	0.074	0.90	1.02	0.62	0.111	0.98	1.02	0.62
40-80 m	0.085	0.85	0.90	0.62	0.085	0.90	0.90	0.62	0.126	0.98	0.90	0.62
80-160 m	0.130	0.85	0.80	0.62	0.130	0.90	0.80	0.62	0.130	0.98	0.80	0.62
>160 m	0.200	0.85	0.70	0.62	0.200	0.90	0.70	0.62	0.200	0.98	0.70	0.62

What is obtained from these relationships is the shear modulus reduction and damping curve as illustrated in figure G.11

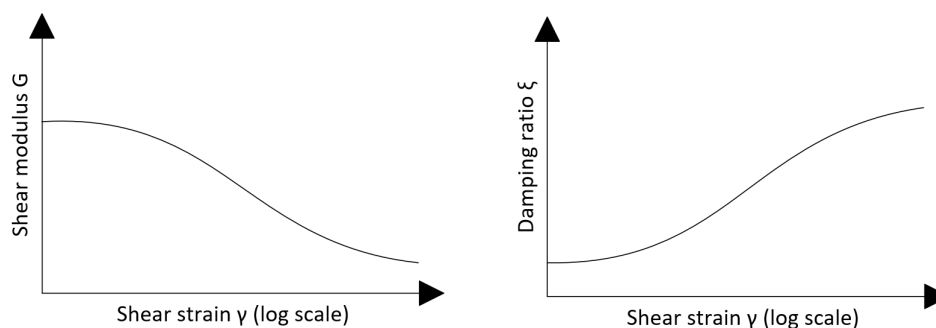


Figure G.11: Illustration of shear modulus reduction and damping curve.

G.3 Soil Constitutive Model

The characterization of soil non-linear behaviour under cyclic loading is dependent on the unloading-reloading behaviour and the generation of excess porewater pressure, Groholski et al. [2015]. The non-linear stress-strain relationship (also called the backbone curve) can be modelled by different hyperbolic models which can be fitted to the shear modulus reduction and damping curves, within the scope of this project the "Hyperbolic / Pressure-Dependent Hyperbolic (MKZ)" model by [Matasovic and Vucetic, 1993] and "Generalized Quadratic/Hyperbolic (GQ/H) Model with Shear Strength Control" by [Groholski et al., 2015] are implemented to compare the non-linear stress-strain behaviour of a soil.

The constitutive model for MKZ is shown equation (G.28).

$$\tau = \frac{G_{max}\gamma}{1 + \beta \left(\frac{\gamma}{\gamma_r}\right)^s} \quad (G.28)$$

Where

G_{max}		Initial shear modulus [kPa]
β, γ_r, s		Model parameters [-]
γ		Shear strain [-]
γ_r		Model parameter [-].

The model parameter γ_r is a confining pressure dependent parameter which is obtained using equation (G.29) according to [DeepSoil, 2020].

$$\gamma_r = \gamma_{ref} \frac{\sigma'_{v0}}{\sigma_{ref}} \quad (G.29)$$

where

γ_{ref}		Reference strain [-]
σ'_{v0}		Effective overburden pressure [kPa]
σ_{ref}		Reference stress $\sigma_{ref} = 100\text{kPa}$.

This model characterizes the small-strain behaviour sufficiently while the large-strain behaviour often develops unrealistic shear stresses, which either may be under- or overestimated. This means that if the shear stresses are overestimated as shown in figure G.12, it could lead to generating shear stresses that exceed the soil shear strength and therefore the soil will fail and the shear stresses produced could be incorrect.

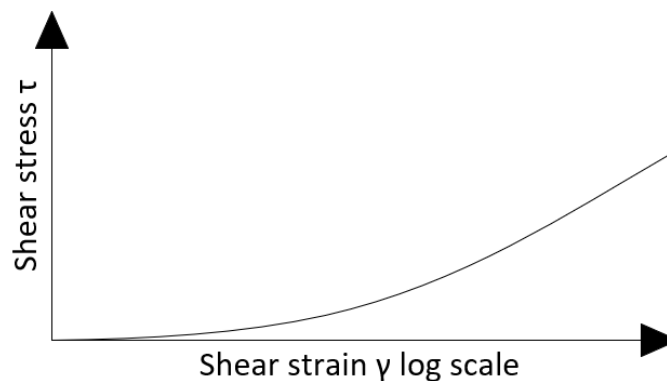


Figure G.12: Illustration of stress-strain curve for the MKZ soil constitutive model.

It is also possible for this soil constitutive model to incorporate excess pore pressure generation and dissipation through the degradation of stiffness and strength through the modulus δ_G and stress δ_τ degradation index factors. The degradation parameters are included in the constitutive

model as shown in equation (G.30) based on [Oscar Moreno-Torres and Olson, 2010].

$$\tau = \frac{G_{max} \gamma \delta_G}{1 + \beta \left(\frac{\delta_G}{\delta_\tau}\right)^s \left(\frac{\gamma}{\gamma_r}\right)^s} \quad \text{MKZ soil model} \quad (\text{G.30})$$

where

$$\begin{array}{l} \delta_G \mid \text{Degradation parameter for stiffness [-]} \\ \delta_\tau \mid \text{Degradation parameter for strength [-]} \end{array}$$

The degradation index parameters are obtained differently whether or not a cohesionless or a cohesive soil is considered, and are given below:

For cohesionless soils

For a cohesionless soils the degradation parameters are defined based on the excess pore pressure ratio r_u and curve fitting parameter v . Within the scope of this project the fitting parameter v is set equal to 1 taking inspiration from table G.4. The stiffness δ_G and stress δ_τ degradation index factors are found in equation (G.31) based on [DeepSoil, 2020] user manual.

$$\begin{array}{l} \delta_G = \sqrt{1 - r_u} \\ \delta_\tau = 1 - (r_u)^v \end{array} \quad (\text{G.31})$$

where

$$\begin{array}{l} r_u = \frac{\Delta u}{\sigma'_{v0}} \mid \text{Porewater pressure ratio [-]} \\ v \mid \text{Curve fitting parameter } v = 1 \text{ G.4 [-].} \end{array}$$

For cohesive soils

For cohesive soils the degradation parameters are found in equation (G.32) based on [Matasovic and Vucetic, 1995]

$$\begin{array}{l} \delta_G = \delta_\tau = N^{-t} \\ t = s (\gamma - \gamma_{tv})^r \end{array} \quad (\text{G.32})$$

where

$$\begin{array}{l} N \mid \text{Number of cycles [-]} \\ s, r \mid \text{Degradation parameter, see equation (G.37) [-]} \\ \gamma \mid \text{Shear strain after } N \text{ load cycles [-]} \\ \gamma_{tv} \mid \text{Cyclic shear strain threshold, below which no excess pore water pressure develop} \\ \text{regardless of the number of applied load cycles [-].} \end{array}$$

In the GQ/H model it is possible to implement shear strength corrections where a maximum shear strength at failure is defined to control the shear stresses at large strains. The constitutive

model for GQ/H model is given in equation (G.33).

$$\tau = \tau_{\max} \left[\frac{1}{\theta_{\tau}} \left\{ 1 + \left(\frac{\gamma}{\gamma_r} \right) - \sqrt{\left\{ 1 + \frac{\gamma}{\gamma_r} \right\}^2 - 4\theta_{\tau} \frac{\gamma}{\gamma_r}} \right\} \right] \quad \text{GQ/H soil model} \quad (\text{G.33})$$

where θ_{τ} is the curve fitting parameter:

$$\theta_{\tau} = \theta_1 + \theta_2 \frac{\theta_4 \left(\frac{\gamma}{\gamma_r} \right)^{\theta_5}}{\theta_3^{\theta_5} + \theta_4 \left(\frac{\gamma}{\gamma_r} \right)^{\theta_5}}$$

where θ_1 - θ_5 are curve fitting constants that provide the best fit of shear modulus reduction curves in a defined strain range.

G.4 Loading-reloading Rule

The soil constitutive model in section G.3 is a model which gives the stress-strain curve relationship, however this curve is only followed for soils exposed to continuously increased shearing. However for typical seismic loading this is never the case as seismic loading is usually transient and therefore loading-reloading rules are established for the soils. Within the scope of this project it is assumed the soils can follow Masing and non-Masing behaviour. The Masing model dictates that soil behaviour follows the following four rules, which are based on the soil constitutive model also called the backbone curve F_{bb} , see figure G.13:

1. At initial loading the stress-strain curve follows the backbone curve F_{bb}
2. When a stress reversal happens at a point defined by (γ_r, τ_r) the stress strain curve follows the path given by:

$$\frac{\tau - \tau_r}{2} = F_{bb} \left(\frac{\gamma - \gamma_r}{2} \right)$$

3. If the unloading or reloading curve surpasses the maximum past strain and crosses the backbone curve it follows the backbone curve F_{bb} until next stress reversal
4. if an unloading or reloading curve intersects an unloading or reloading curve from the cycle before the stress strain curve follows it.

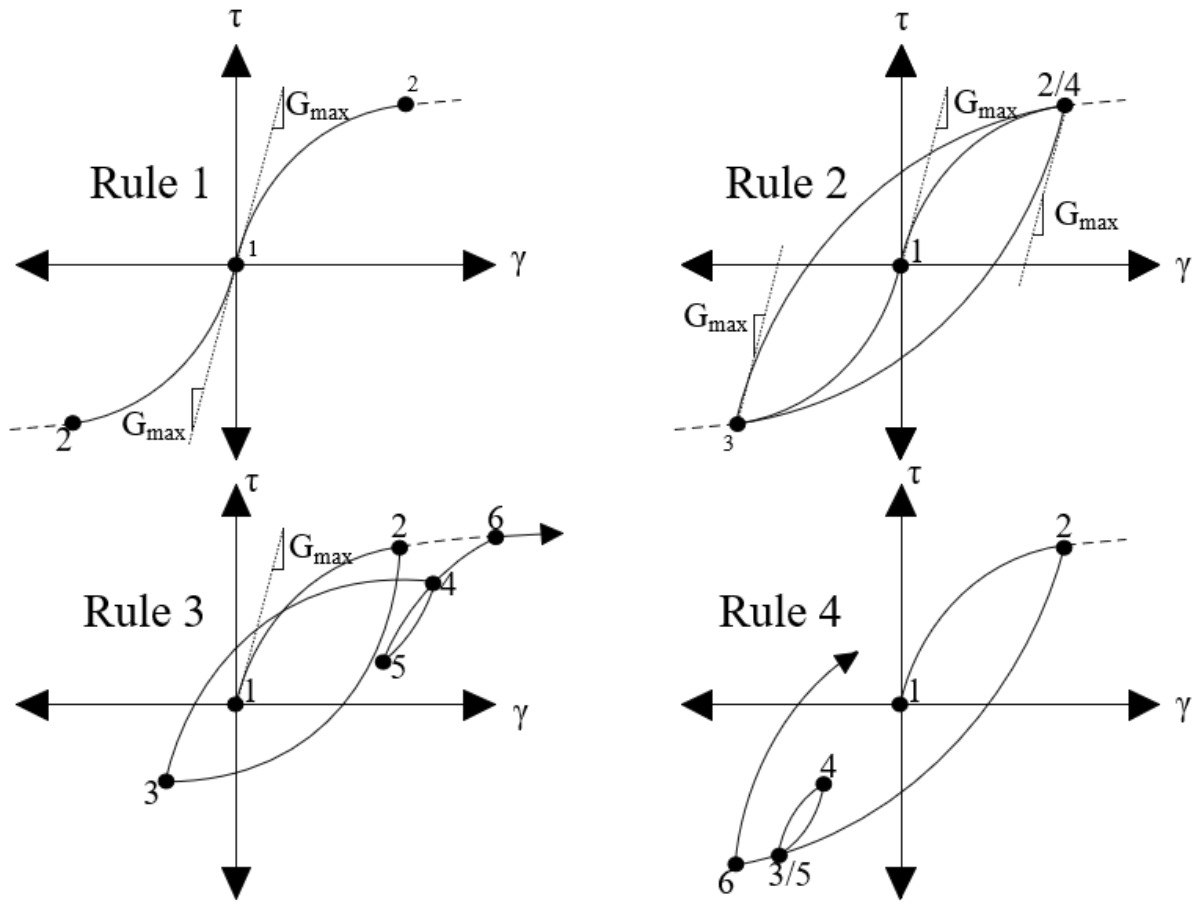


Figure G.13: Extended Masing rules for loading reloading behaviour of material.

For large strains the hysteretic damping in Masing rules is known to be overestimated compared to laboratory measured damping. The non-Masing behaviour can be applied to better capture the real behaviour of soil damping at large strains because non-Masing controls the hysteretic damping at large strains.

G.5 Porewater Pressure Generation Model

Liquefaction is initiated when a loose saturated soil is mixed with water and the porewater pressure increases. As a consequence the effective stress in the soil decreases, thus the soil stiffness and strength also decreases as they depend on the effective stress. It is therefore very important to model the porewater pressure generation in the soil realistically during ground shaking as misinterpretation of porewater pressure (PWP) generation can underestimate the damages induced by liquefaction. There are three PWP generation models; the stress-based, strain-based and energy-based. The stress-based PWP model is a relation between porewater ratio and number of applied uniform (constant amplitude) cycles that cause liquefaction based on stress-controlled tests on clean sands. The disadvantage is that the input ground motion shall be converted into an equivalently damaging number of uniform cycles as shown on figure G.7. The energy-based PWP model is a relation between porewater ratio and dissipated shear energy in the soil developed for sands and silts from cyclic shear tests. The strain-based PWP model is used for both sand and clay layers and table G.3 summarizes the required input parameters in *DeepSoil*.

Table G.3: Chosen PWP generation models in *DeepSoil* and program input parameters.

Strain-based PWP Model	Pore pressure dissipation parameter	Pore pressure degradation parameters						
Sand - Vucetic/Dobry	Cv	f	p	F	s	γ_{tv}	v	-
Clay - Matasovic	Cv	s	r	A	B	C	D	γ_{tv}

In the following are the strain-based PWP model and required parameters for sand and clay layers presented.

G.5.1 Strain-based PWP Generation Model for Sand

It was shown by [Dobry et al., 1982] that the applied shear strain is correlated with the excess porewater pressure ratio, $r_u = \frac{\Delta u}{\sigma'_{v0}}$, from strain-controlled cyclic shear tests in undrained clean sands as shown in figure G.14.

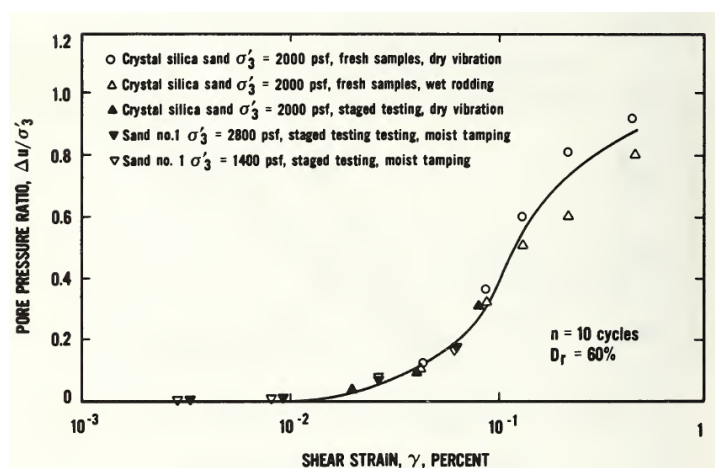


Figure G.14: Strain-controlled cyclic triaxial tests: Measured pore water pressure in saturated sands after ten loading cycles, [Dobry et al., 1982].

Where Δu is the excess porewater pressure and $\sigma'_{v0} = \sigma'_3$ is the effective initial vertical stress. The strain-based porewater pressure generation model by Vucetic and Dobry 1993 builds on the strain-controlled cyclic shear tests in undrained clean sands:

$$r_u = \frac{p f N F (\gamma - \gamma_{tv})^s}{1 + f N F (\gamma - \gamma_{tv})^s} \quad (\text{G.34})$$

where

r_u	Excess porewater pressure ratio after N cycles of applied loading
N	Number of load cycles
f	Factor that accounts for loading in multiple directions. $f = 1$ for 1D, $f = 2$ for 2D
p, s and F	Curve fitting parameters
γ	Shear strain at N load cycles
γ_{tv}	Cyclic shear strain threshold, below which no excess pore water pressure develop regardless of the number of applied load cycles.

It is assumed that the porewater pressure ratio can reach a maximum value of $r_u = 0.95$ (i.e., excess porewater pressure up to 95% of the initial confining pressure) before the soil layer has liquefied.

Pore Pressure Generation and Cyclic Degradation Parameters for Sand

According to [Carlton, 2014] the SSRA program D-MOD2000 manual [Matasovic and Ordóñez, 2011] the best database for reported parameters which are shown in table G.4.

Table G.4: Parameters for Matasovic and Vucetic (1993) sand porewater pressure generation model, [Matasovic and Ordóñez, 2011].

Material	Reference	Parameters					Shear strain threshold γ_{tv} [%]
		v	f	p	F	s	
Bangding Sand (BS); poorly-graded commercially available sand $D_r=40\%$; $D_{50}=0.19$; $C_c=0.9$; $C_u=1.4$ $\gamma_{d,min}=14.138$ kN/m ³ ; $\gamma_{d,max}=16.651$ kN/m ³	Dobry et al. (1985)	1	1	1	10.9	1	0.017
Wildlife Site Sand A (WSA); $e=0.84-0.85$; $FC=37\%$; $N \approx 5$; $\nu_s \approx 107$ m/s	Vucetic and Dobry (1988)	1	2	1.04	2.6	1.70	0.020
Wildlife Site Sand B (WSB); $e=0.74-0.76$; $FC=25\%$; $N \approx 6-13$; $\nu_s \approx 137-152$ m/s	Vucetic and Dobry (1988)	1	2	1.04	2.6	1.70	0.020
Heber Road Site Sand PB; $e=0.7$; $FC=15\%$; $\nu_s \approx 152-183$ m/s	Vucetic and Dobry (1989)	1	2	1.05	1.706	1.09	0.024
Heber Road Site Sand PB; $e=0.7$; $FC=22\%$; $\nu_s \approx 122-142$ m/s	Vucetic and Dobry (1990)	1	1	1.071	1.333	1.08	0.022
Santa Monica Beach Sand (SMB); clean uniform beach sand similar to Monterey No. 0; $e=0.56$; $FC=0\%$; dense; $\nu_s \approx 264$ m/s	Matasovic (1993)	3.8	1	1.00	0.73	1.00	0.020
Owi Island sand at depths from 6-14 m below ground surface; silty fine sand placed as hydraulic fill; $18\% < FC < 35\%$	Thilakaratne and Vucetic (1987)	1	2	1.005	3.0	1.80	0.025
Owi Island silt at depths of 6 m; placed as hydraulic fill; $50\% < FC < 85\%$	Thilakaratne and Vucetic (1987)	1	2	0.95	2.5	1.60	0.015

where

D_r	Relative density [%]
D_{50}	Mean grain diameter [mm]
C_c	Curvature coefficient [-]
C_u	Uniformity coefficient [-]
γ_d	Dry unit weight of the soil [kN/m ³]
e	Void ratio [-]
N	Recorded blow counts needed to advance through a 150 mm interval of soil
ν_s	Shear wave velocity [m/s]
FC	Fine content [%].

However, the sand layers used in this project differ from the sands and silts in table G.4 and

therefore are correlation equations [Matasovic and Ordóñez, 2011] used. The fitting parameters F and s developed by [Carlton, 2014] are shown in equation (G.35) and figure G.15.

$$\begin{aligned} F &= 3810 \cdot \nu_s^{-1.55} \\ s &= (FC + 1)^{0.1252} \end{aligned} \quad (\text{G.35})$$

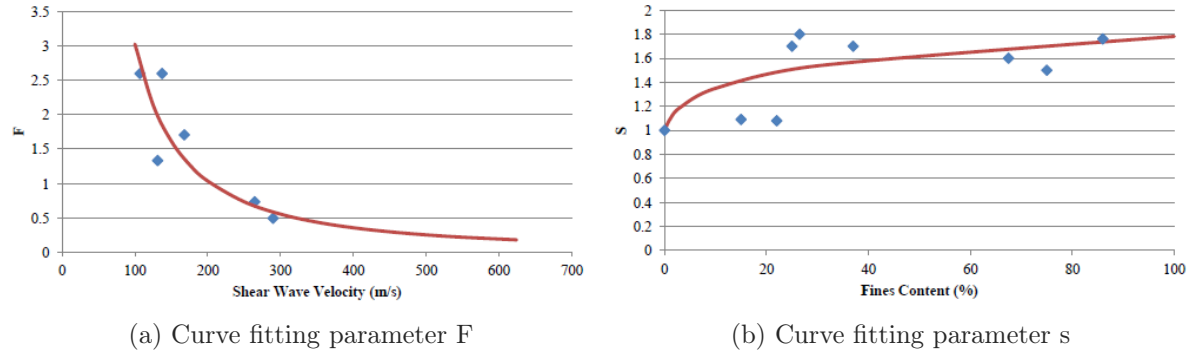


Figure G.15: Comparison of given values of s from sands and silts in table G.4 (blue dots) and the correlation equation used in [Carlton, 2014] (red line).

The fine content for all sand layers is chosen to be $FC=10\%$.

The parameters $f = p = v = 1$ is chosen for all cohesionless soils. The values of v in table G.4 are all equal to 1 except for Santa Monica Beach Sand and the values for p in table G.4 are all close to 1. f accounts for loading in multiple directions and a 1D SSRA in this project is considered. The cyclic shear strain threshold is chosen to be consistent with the work done by Vucetic (1994) that found that an average value of γ_{tv} was about the same shear strain as when $G/G_{max} = 0.65$, [Carlton, 2014]. For both sand and clay layers γ_{tv} are found from the shear modulus reduction curves generated in *DeepSoil* as the strain value at $G/G_{max} = 0.65$.

G.5.2 Strain-based PWP Generation Model for Clay

Based on the model of Dobry et al. (1985) [Matasovic and Vucetic, 1995] developed a pore pressure generation model for clays:

$$\begin{aligned} r_u &= A \delta^3 + B \delta^2 + C \delta + D \\ \delta &= N^{-t} \\ t &= s (\gamma - \gamma_{tv})^r \end{aligned} \quad (\text{G.36})$$

where

$$\begin{array}{l|l} \delta & \text{Degradation parameter} \\ A, B, C, D, r, s & \text{Curve fitting parameters.} \end{array}$$

Pore pressure generation and cyclic degradation parameters for clay

The listed parameters in table G.5 from D-MOD2000 Manual [Matasovic and Ordóñez, 2011] are the best reported according to [Carlton, 2014].

Table G.5: Parameters for Matasovic and Vucetic (1995) clay porewater pressure generation model, [Matasovic and Ordóñez, 2011].

Material	Shear strain threshold	Curve fitting parameters					
	γ_{tw} [%]	s	r	A	B	C	D
Marine Clay OCR=1.0	0.1	0.075	0.495	7.6451	-14.7174	6.3800	0.6922
Marine Clay OCR=1.4	0.1	0.064	0.520	14.6202	-30.5124	18.4265	-2.5343
Marine Clay OCR=2.0	0.1	0.054	0.480	12.9495	-26.3287	15.3736	-1.9944
Marine Clay OCR=4.0	0.1	0.042	0.423	11.263	-21.4595	11.2404	-1.0443

It would be incorrect to use parameters from table G.5 for all clay layers as the clay in this project differ and correlation equations by [Carlton, 2014] are used to obtain s, r, A, B, C and D :

$$\begin{aligned}
 s &= 1.6374 \cdot PI^{-0.802} \cdot OCR^{-0.417} \\
 r &= 0.7911 \cdot PI^{-0.113} \cdot OCR^{-0.147} \\
 A &= \begin{cases} 7.6451 & \text{for } OCR < 1.1 \\ 15.641 \cdot OCR^{-0.242} & \text{for } OCR \geq 1.1 \end{cases} \\
 B &= \begin{cases} -14.714 & \text{for } OCR < 1.1 \\ -33.691 \cdot OCR^{-0.33} & \text{for } OCR \geq 1.1 \end{cases} \\
 C &= \begin{cases} 6.38 & \text{for } OCR < 1.1 \\ 21.45 \cdot OCR^{-0.468} & \text{for } OCR \geq 1.1 \end{cases} \\
 D &= \begin{cases} 0.6922 & \text{for } OCR < 1.1 \\ -3.4708 \cdot OCR^{-0.857} & \text{for } OCR \geq 1.1 \end{cases}
 \end{aligned} \tag{G.37}$$

Where

$$\begin{array}{l|l}
 OCR & \text{Over consolidation ratio [-]} \\
 PI & \text{Plasticity index [-].}
 \end{array}$$

Pore pressure dissipation parameters for sand

For the PWP pressure dissipation model in *DeepSoil* the coefficient of consolidation, C_v , is needed for each soil layer.

For sand layers the coefficient of consolidation is estimated based on [Carlton, 2014]:

$$C_v = \frac{k}{m_v \cdot \gamma_w} \tag{G.38}$$

Where

$$\begin{array}{l|l}
 C_v & \text{Coefficient of consolidation [m}^2\text{/s]} \\
 k & \text{Coefficient of hydraulic conductivity [m/s]} \\
 m_v & \text{Coefficient of volumetric compressibility [m}^2\text{/kN]} \\
 \gamma_w & \text{Unit weight of water = 10kN/m}^3\text{.}
 \end{array}$$

The coefficients of hydraulic conductivity and volumetric compressibility for sand layers are based on table G.6 and G.7 from [Carlton, 2014].

Table G.6: Coefficient of hydraulic conductivity k of granular soils (after Terzaghi and Peck 1948) (From Pestrana et al. 1997) [Carlton, 2014].

Soil type	Coefficient of hydraulic conductivity k [m/s]
Very fine sand	0.00001-0.00005
Fine sand	0.00005-0.0001
Medium sand	0.0001-0.001
Coarse sand	0.001-0.01
Small pebbles	0.01-0.05

A coefficient of hydraulic conductivity is chosen as $k=0.0001$ m/s for all sand layers for medium sand.

Table G.7: Typical values of volumetric compressibility m_v of granular soils (modified from PHRI 1997) (From Pestrana et al. 1997) [Carlton, 2014].

Type of sand	Coefficient of volumetric compressibility m_v [m ² /kN]	Mean particle diameter D_{50} [mm]
Sacramento river sand	$2 \cdot 10^{-5}$	0.2
El monte sand (D)	$2 \cdot 10^{-5}$	0.22
El monte sand (E)	$2 \cdot 10^{-5}$	0.1
Akita port sand	$3 - 4 \cdot 10^{-5}$	0.15
El monte sand (C)	$4 \cdot 10^{-5}$	0.65
Monterey sand	$4 \cdot 10^{-5}$	0.6
Fuji river sand	$6 \cdot 10^{-5}$	0.4
El monte sand (B)	$8 \cdot 10^{-5}$	3.0
Ogishima sand	$10 \cdot 10^{-5}$	0.32

An average value of $m_v = 5 \cdot 10^{-5}$ m/s for the volumetric compressibility for all sand layers is chosen.

Pore pressure dissipation parameters for clay

The coefficient of consolidation for clay layers is found from the correlation from NAVFAC 7.01 (1986):

$$C_v = 0.79861 \cdot LL^{-2.7905} \quad (\text{G.39})$$

where

LL | Liquid limit [%].

Appendix H | Geotechnical Site Conditions

In this appendix the geotechnical site conditions achieved from a standard penetration test (SPT) are presented where the test procedure and results are shown. Furthermore the number of blows (N) in the SPT will be corrected for field procedure and overburden pressure and the necessary soil parameters are obtained using the SPT data.

H.1 Standard Penetration Test

The standard penetration test (SPT) is a field test and is performed by driving a split spoon sampler into the ground by blows from a drop hammer of mass 63.5 kg falling 760 mm. The split spoon sampler is first driven 152 mm into the soil at the bottom of the borehole, this is to avoid seating errors, and the number of blows (N) required to drive the split spoon sampler further 304 mm into the soil is counted and is the SPT- N result, [Budhu, 2010]. The procedure for a SPT is shown at figure H.1 and the results used in this project is shown at figure H.2.

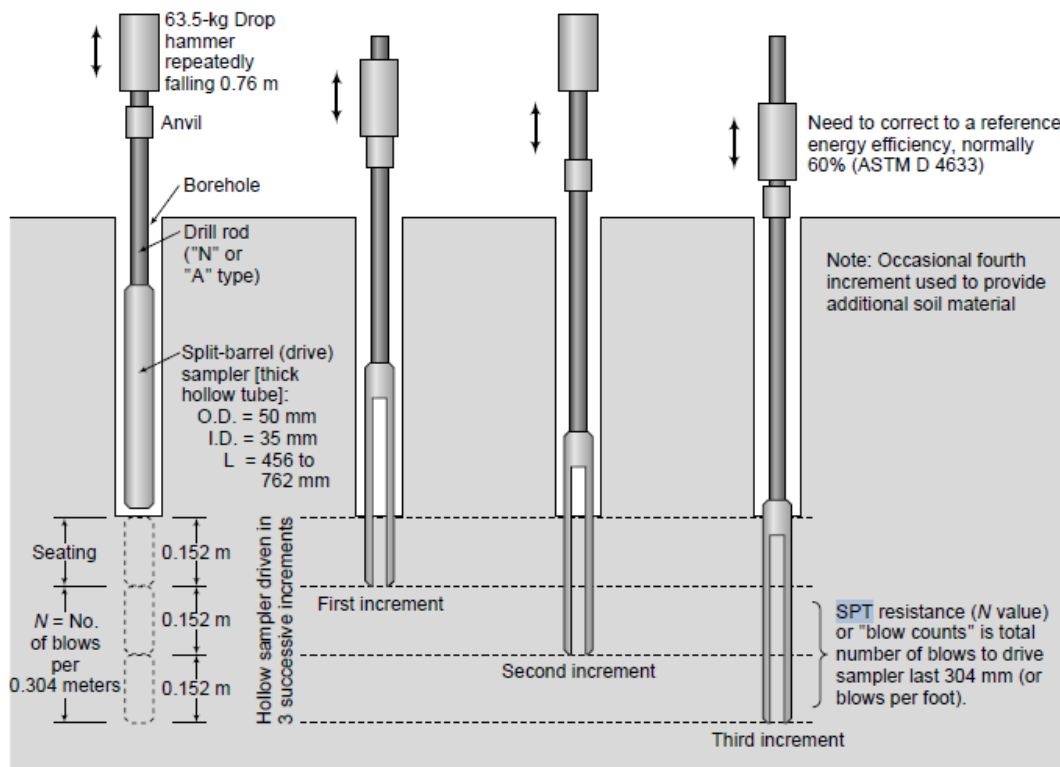


Figure H.1: Procedure for SPT, [Budhu, 2010].

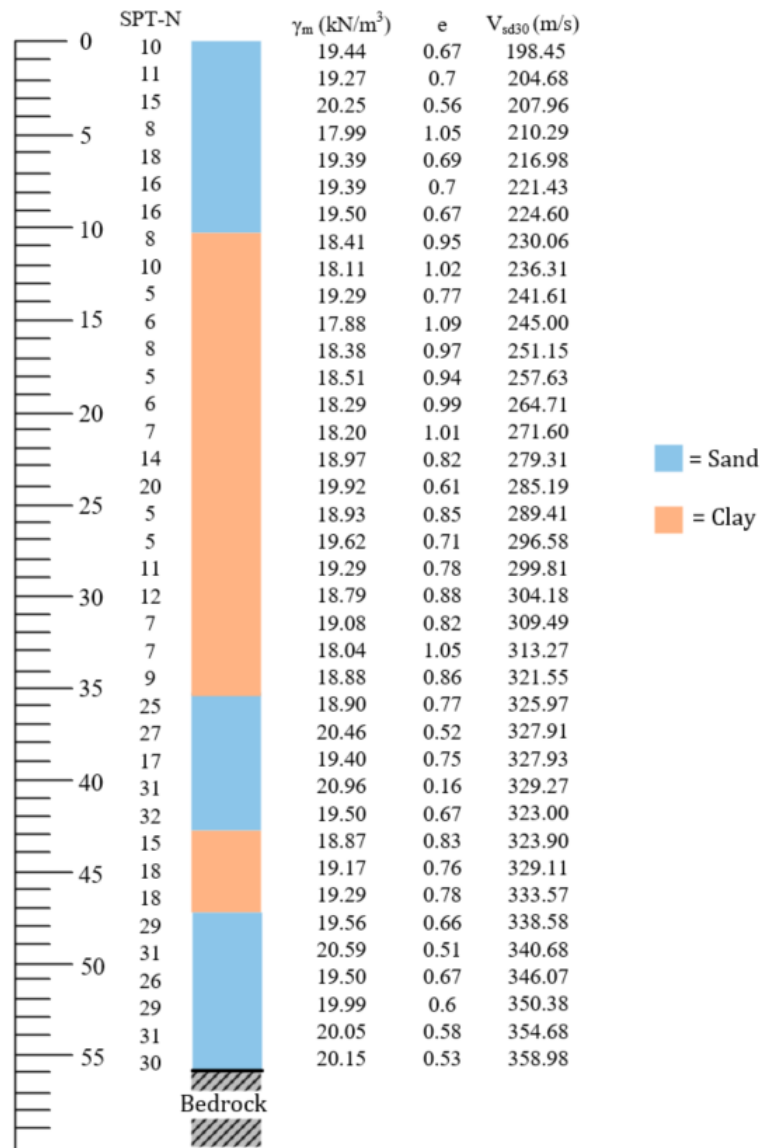


Figure H.2: Results for standard penetration tests [Kuo et al., 2021]

H.2 Correction of SPT-N for Field Procedure and Overburden Pressure

The SPT-N values need to be corrected to account for energy losses, overburden pressure, rod length, sampler type, borehole diameter and hammer equipment. The purpose of this is to have a corrected value that is general and not influenced of which equipment and country the test have been made in.

For correction of energy losses, overburden pressure, rod length, sampler type, borehole diameter and hammer equipment the following equation are used.

$$N_{60} = N C_R C_S C_B C_E \quad (\text{H.1})$$

where

C_R	Rod length correction
C_S	Sampler correction
C_B	Borehole correction
C_E	60 % rod energy ration correction factor and equipment.

Furthermore, for correction for overburden pressure which normalises the SPT value to a overburden pressure is calculated by the following equation, and is only applied for sand layers.

$$C_N = \left(\frac{P_a}{\sigma'_{v0}} \right)^n \quad (\text{H.2})$$

where

C_N	Overburden pressure correction
P_a	Atmospheric pressure of 100 kPa
σ'_{v0}	Effective overburden pressure
n	n = 0.5

Then the corrected SPT value becomes:

$$(N_1)_{60} = C_N N_{60} \quad (\text{H.3})$$

The correction factors for SPT value can be found in table H.1.

Table H.1: Correction factors for rod Length, sampler type and borehole size, [Budhu, 2010].

Correction factor	Item	Correction factor
C_R	Rod length (below anvil)	$C_R = 0.05L + 0.61; 4m < L \leq 6m$ $C_R = -0.0004L^2 + 0.017L + 0.83; 6m < L < 20m$ $C_R = 1; L \geq 20m$ L = rod length
C_S	Standard sampler	$C_S = 1.0$
	U.S. sampler without liners	$C_S = 1.2$
C_B	Borehole diameter:	
	65 mm to 115 mm	$C_B = 1.0$
	152 mm	$C_B = 1.05$
	200 mm	$C_B = 1.15$
C_E	Equipment:	
	Safety hammer (rope, without Japanese "throw" release)	$C_E = 0.7 - 1.2$
	Donut hammer (rope, without Japanese "throw" release)	$C_E = 0.5 - 1.0$
	Donut hammer (rope, with Japanese "throw" release)	$C_E = 1.1 - 1.4$
	Automatic-trip hammer (donut or safety type)	$C_E = 0.8 - 1.4$

For the SPT in this project the correction factors are:

- C_R = Depend on the depth of the $SPT - N$
- Standard sampler, $C_S = 1.0$
- Borehole diameter: 65 mm to 115 mm, $C_B = 1.0$
- Equipment: Automatic-trip hammer, $C_E = 0.8$

By use of the correction factors in table H.1 and from equation (H.2) and equations (H.3) and (H.1) the SPT-N values are corrected where the results can be seen in table H.2.

Table H.2: SPT values and corrected SPT values, N_{60} and $(N_1)_{60}$.

Layer no	Soil type	Depth [m]	SPT-N	N_{60}	$(N_1)_{60}$
1	Sand	0.73	10	6	13
		2.21	11	7	14
		3.69	15	10	15
		5.17	8	6	8
		6.65	18	13	16
		8.13	16	12	13
		9.62	16	12	12
		11.10	8	6	6
		12.58	10	8	8
		14.06	5	4	4
		15.54	6	5	5
		17.02	8	6	6
		18.51	5	4	4
		19.99	6	5	5
2	Clay	21.47	7	6	6
		22.95	14	11	11
		24.43	20	16	16
		25.91	5	4	4
		27.39	5	4	4
		28.88	11	9	9
		30.36	12	10	10
		31.84	7	6	6
		33.32	7	6	6
		34.80	9	7	7
3	Sand	36.28	25	20	11
		37.76	27	22	12
		39.25	17	14	7
		40.73	31	25	13
		42.21	32	26	13
4	Clay	43.69	15	12	12
		45.17	18	14	14
5	Sand	46.65	18	14	14
		48.14	29	23	11
		49.62	31	25	12
		51.10	26	21	10
		52.58	29	23	10
		54.06	31	25	11
		55.54	30	24	11

H.3 Soil Parameters

Besides the SPT-N value, unit weight and shear wave velocity for the soil layers there are additional soil parameters that have to be calculated which are obtained from the SPT.

Relative density, D_r :

The relative density can be obtained for sand by use of the following equation, [Mujtaba et al., 2017], where the relative density is related to the corrected SPT-N value:

$$D_r(\%) = 1.96N_{60} - 19.2 \left(\frac{p_a}{\sigma_{v'}} \right)^{0.23} + 29.2 \quad (\text{H.4})$$

where p_a is the atmospheric pressure.

Table H.3: Mean values of relative density for sand layers.

Layer no	D_r
1	24.6 %
2	-
3	56.8 %
4	-
5	61.9 %

Friction angle, ϕ' :

The friction angle is found based on the N_{60} value where linear interpolation is used for intermediate N_{60} -values:

Table H.4: Correlation of N , N_{60} , D_r , and ϕ' for coarse-grained soils, [Budhu, 2010].

N	N_{60}	Compactness	D_r [%]	ϕ' [°]
0-4	0-3	Very loose	0-20	26-28
4-10	3-9	Loose	20-40	29-34
10-30	9-25	Medium dense	40-70	35-40*
30-50	25-45	Dense	70-85	38-45*
>50	>45	Very dense	>85	>45*

*These values correspond to ϕ'_p

The mean value for each layer is found:

Table H.5: Mean values of friction angle for sand layers.

Layer no	ϕ' [°]
1	34.1
2	-
3	38.1*
4	-
5	38.9*

*These values correspond to ϕ'_p

Undrained shear strength, s_u :

The undrained shear strength for clay are determined from the relations between undrained shear strength and corrected N values, where for clay $N_{60} = (N_1)_{60}$, the relations are given in table H.6 and mean values for the clay layers are shown in table H.7.

Table H.6: Relation of N_{60} and s_u for clay, Budhu [2010].

N_{60}	Description	s_u [kPa]
0 – 2	Very soft	< 10
3 – 5	Soft	10 – 25
6 – 9	Medium	25 – 50
10 – 15	Stiff	50 – 100
15 – 30	Very stiff	100 – 200
> 30	Extremely stiff	> 200

Table H.7: Mean values of undrained shear strength for clay layers.

Layer no	s_u [kPa]
1	-
2	34.51
3	-
4	83.33
5	-

Overconsolidation ratio, OCR :

The OCR describes the soil's consolidation history, where the current vertical effective stress is less than its past maximum vertical effective stress.

$$OCR = \frac{\sigma'_p}{\sigma'_{v0}} \quad (\text{H.5})$$

The OCR for clay is calculated by equation (H.6), based on [Kulhawy and Mayne, 1990]

$$OCR = 0.58N \frac{P_a}{\sigma'_{v0}} \quad (\text{H.6})$$

where

N	Uncorrected SPT-N value.
P_a	Atmospheric pressure of 100 kPa.
σ'_{v0}	Current vertical effective stress.

The mean values for the clay layers are shown in table H.8.

Table H.8: Mean values of overconsolidation ratio for clay layers.

Layer no	OCR
1	-
2	2.51
3	-
4	2.36
5	-

Plasticity index, PI and Liquid limit, LL :

For clay the plasticity index and liquid limit are needed in the porewater pressure generation

model, the plasticity index is the range of water content where the soil behaves plastic and the liquid limit is the water content at which the soil changes from a plastic state to a liquid state.

The plasticity index is calculated by equation (H.7), based on [Caicedo et al., 2018] where the relation is assumed to apply:

$$PI = \frac{s_u}{14w^{-1.8}P_a} \tag{H.7}$$

where

- s_u | Undrained shear strength.
- w | Water content in %.
- P_a | Atmospheric pressure of 100 kPa.

The water content can be found from the void ratio, specific gravity and degree of saturation from equation (H.8). The void ratio is known from the SPT, the specific gravity is assumed to be 2.7 and the soil is fully saturated so the degree of saturation is 1.

$$w = \frac{e S}{G_s} \tag{H.8}$$

where

- e | Void ratio.
- S | Degree of saturation (= 1).
- G_s | Specific gravity (= 2.7).

The liquid limit are found based on the relation to the plasticity index, where the diagram at figure H.3 are used to determine the liquid limit for the clay.

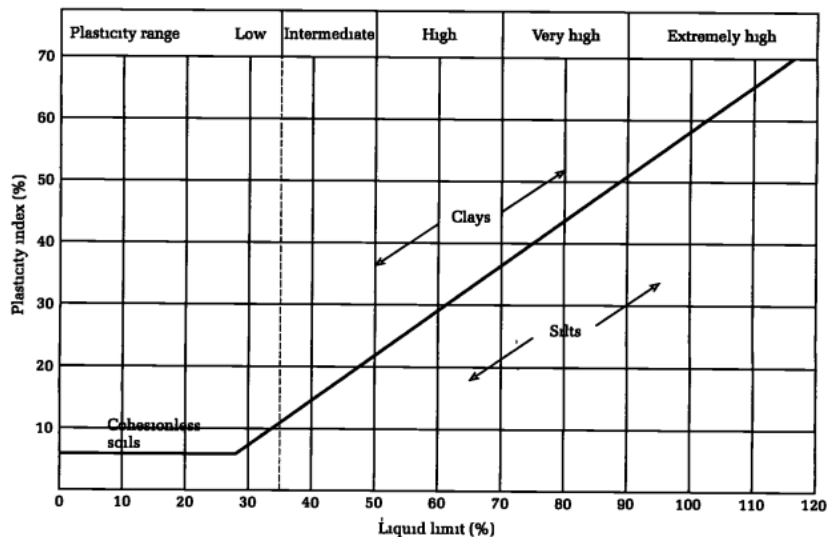


Figure H.3: Diagram for liquid limit and plasticity index, [Tomlinson and Boorman, 2001].

The plasticity index and liquid limit for the clay layers are shown in the following table:

Table H.9: Mean values of plasticity index and liquid limit for clay layers.

Layer no	PI [%]	LL [%]
1	-	-
2	13.3	38.3
3	-	-
4	25.9	55.7
5	-	-

In general the soil parameters can be calculated as outlined in the above procedures. In the SSRA the reduction and damping curves for the GeoIndex Model accounts for the confining pressure as shown in section G.2, this results in sub-division of soil layer 2 and 3 according to the depth intervals in table H.10 at 20 m and 40 m. The mean soil parameters are calculated and shown in table H.10.

Table H.10: Soil parameters.

Layer no	Soil type	Depth [m]	Description	γ_m [kN/m ³]	e [-]	V_{sd30} [m/s]	D_r [%]	ϕ' [°]	s_u [kPa]	OCR [-]	PI [%]	LL [%]
1	Sand	0 - 10	Loose	19.32	0.72	212	24.6	34.1	-	-	-	-
2.1	Clay	10 - 20	Medium stiff	18.43	0.96	258	-	-	25.3	3.02	11.1	35.3
2.2		20 - 35.5	Medium stiff	18.91	0.85	281	-	-	39.5	2.24	14.1	39.4
3.1	Sand	35.5 - 40	Medium dense	19.59	0.68	310	51.4	38.0*	-	-	-	-
3.2		40 - 43	Medium dense	20.23	0.42	320	65.1	38.2*	-	-	-	-
4	Clay	43 - 47	Stiff	19.11	0.79	329	-	-	83.3	2.36	25.9	55.7
5	Sand	47 - 55.65	Medium dense	19.94	0.59	348	61.9	38.9*	-	-	-	-
-	Bedrock	55.65 -				>360						

*These values correspond to ϕ'_p

Appendix I | Input Parameters for Numerical Models

In this appendix the input parameters for the numerical models for investigation of soil response as well as response of the jacket substructure are given

I.1 SSRA

For the SSRA the "Generalized Quadratic/Hyperbolic (GQ/H) Model with Shear Strength Control" by [Groholski et al., 2015] is used for all soil layers with the input parameters defined in table G.2

Table I.1: Input parameters for soil constitutive model in *DeepSoil*. Reference: table G.2.

Layer	Soil type	Soil model	Shear strength [kPa]	γ_{ref}	α	D_{min}	β
1	Sand	GQ/H MRDF	9.84	0.032	0.85	1.30	0.62
2.1	Clay	GQ/H MRDF	25.3	0.065	0.90	1.15	0.62
2.2	Clay	GQ/H MRDF	39.5	0.074	0.90	1.02	0.62
3.1	Sand	GQ/H MRDF	67.84	0.061	0.85	1.02	0.62
3.2	Sand	GQ/H MRDF	75.05	0.085	0.85	0.90	0.62
4	Clay	GQ/H MRDF	83.3	0.126	0.98	0.90	0.62
5	Sand	GQ/H MRDF	93.12	0.085	0.85	0.90	0.62

For every soil layer are the shear modulus reduction and damping curves, which are fitted using the input parameters shown in table G.2.

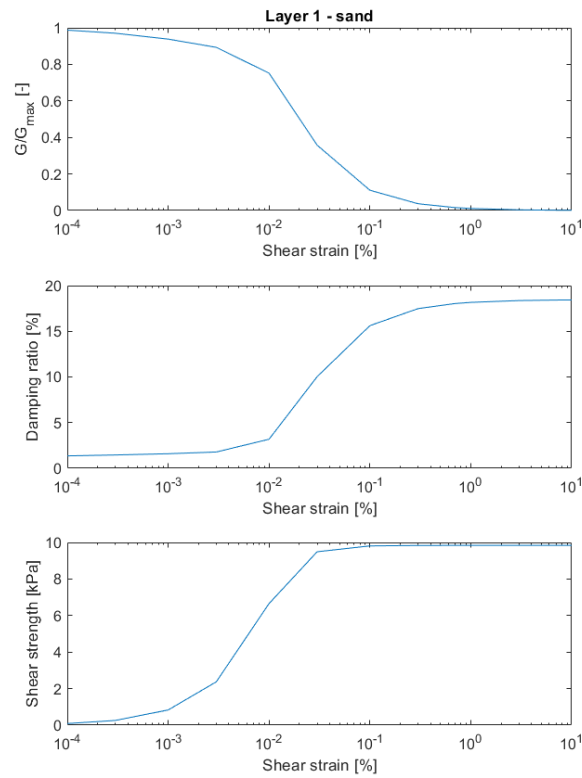
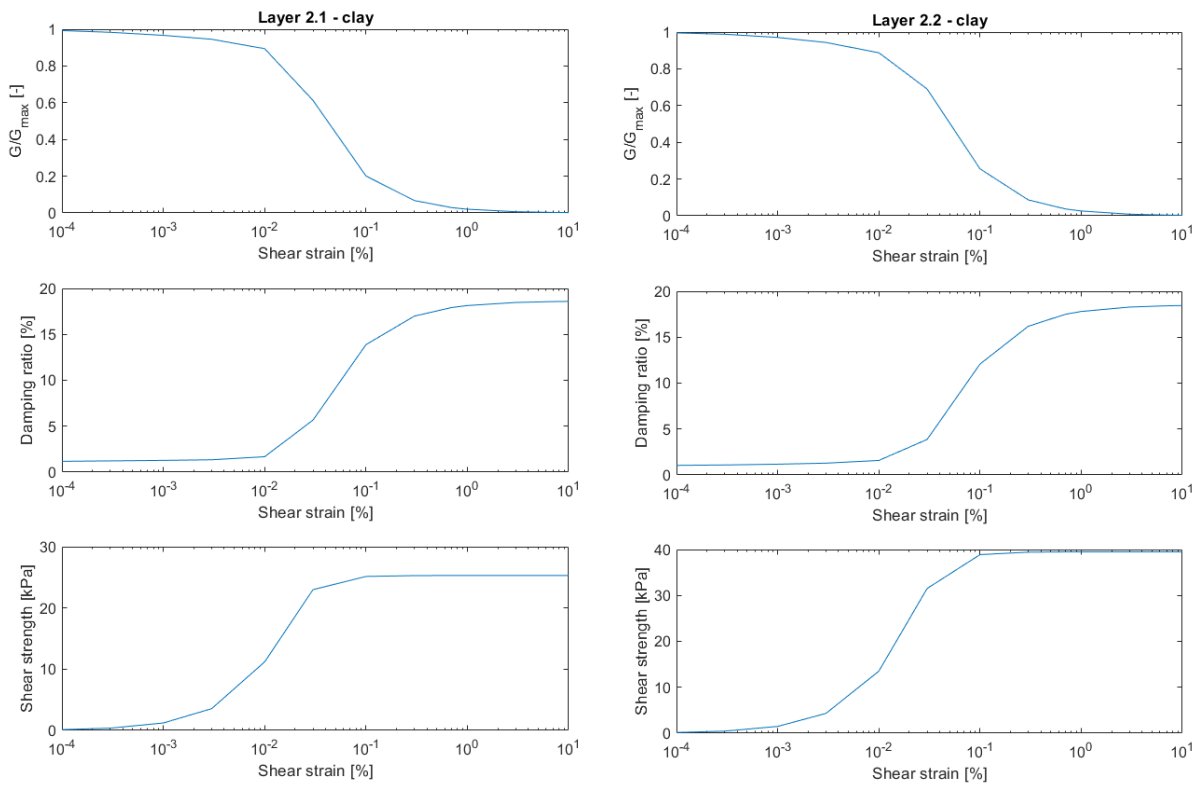


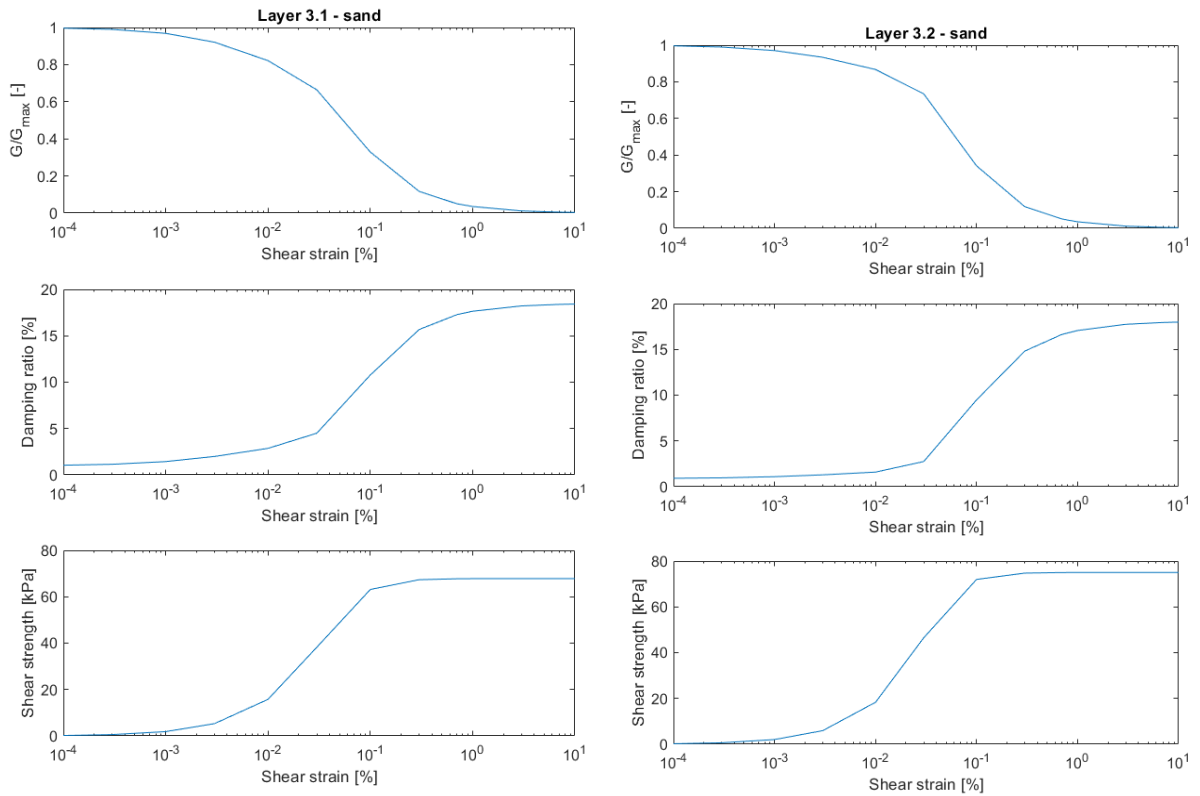
Figure I.1: Fitted shear modulus reduction and damping curve - layer 1 sand.



(a) Layer 2.1 clay

(b) Layer 2.2 clay

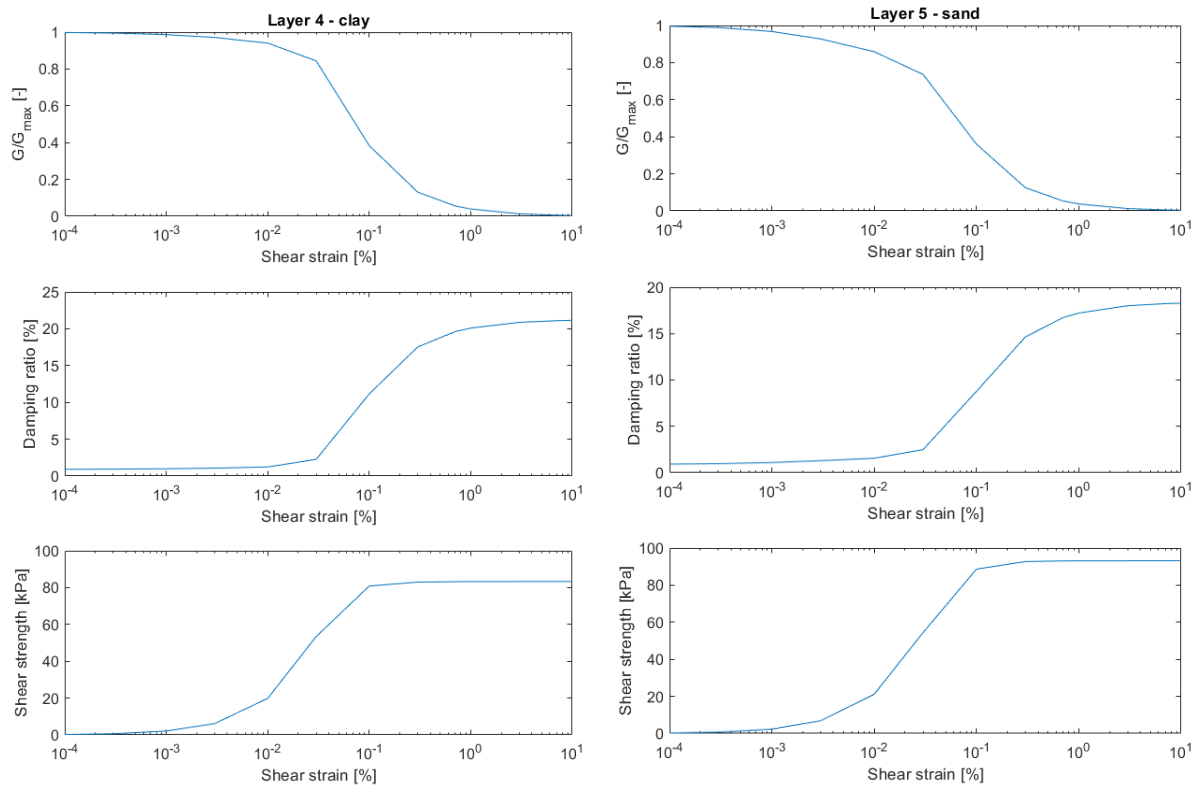
Figure I.2: Fitted shear modulus reduction and damping curves.



(a) Layer 3.1 sand

(b) Layer 3.2 sand

Figure I.3: Fitted shear modulus reduction and damping curves.



(a) Layer 4 clay

(b) Layer 5 sand

Figure I.4: Fitted shear modulus reduction and damping curves.

Lastly an appropriate porewater pressure generation model is necessary to model the increase of excess porewater pressure and for the project a strain based porewater pressure generation model for sand by [Dobry et al., 1982] and clay by [Matasovic and Vucetic, 1995]

Table I.2: Input parameters in PWP generation model in *DeepSoil*.

Layer	Soil type	PWP model	Dissipation parameters			Degradation parameters						
			Max ru	Cv	Cv exponent	f/s	p/r	F/A	s/B	γ_{tw}/C	v/D	γ_{fv}
1	Sand	Vucetic/Dobry	0.95	0.200	0	1	1	0.944	1.350	0.015	1	-
2.1	Clay	Matasovic	0.95	3.831E-05	0	0.150	0.512	11.970	-23.394	12.787	-1.346	0.033
2.2	Clay	Matasovic	0.95	2.819E-05	0	0.140	0.521	12.868	-25.819	14.707	-1.739	0.037
3.1	Sand	Vucetic/Dobry	0.95	0.200	0	1	1	0.524	1.350	0.029	1	-
3.2	Sand	Vucetic/Dobry	0.95	0.200	0	1	1	0.499	1.350	0.041	1	-
4	Clay	Matasovic	0.95	1.073E-05	0	0.084	0.483	12.706	-25.378	14.352	-1.663	0.067
5	Sand	Vucetic/Dobry	0.95	0.200	0	1	1	0.438	1.350	0.041	1	-

Sand
Clay
ref

I.2 Numerical Model of Jacket Substructure

In section I.3 and I.4 the numerical modelling parameters for the soil and soil-pile interaction are showed and explained. In this section the numerical modelling parameters for the jacket substructure are presented, the jacket substructure are modelled with the same parameters in both model 2 in *SeismoStruct* and model 3 in *Plaxis*. The structural members in the substructure are shown at figure I.5 and the parameters are shown in table I.3 where the structural members are circular hollow sections (CHS).

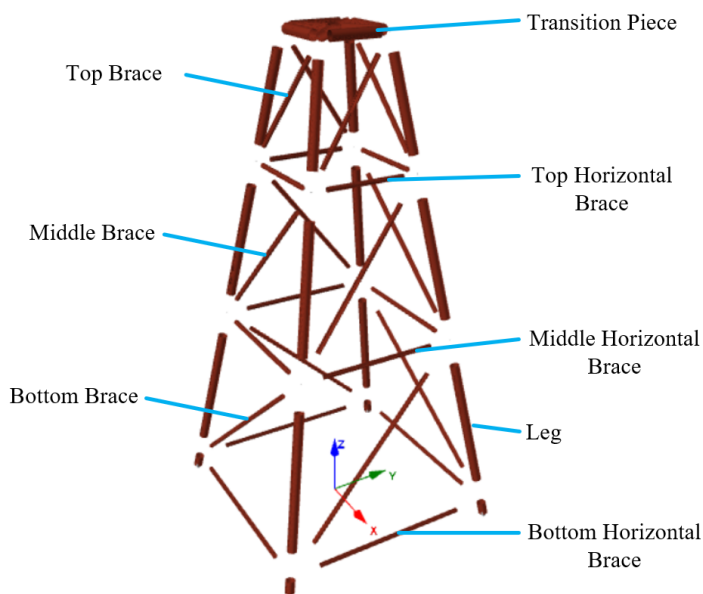


Figure I.5: Structural member in jacket substructure, the model is expanded.

Table I.3: Structural members parameters.

Parameters	Legs	Horizontal Braces	Braces	Transition Piece
Cross section	CHS1800x40	CHS900x30	CHS900x30	CHS1800x40
Diameter [mm]	1,800	900	900	1,800
Wall thickness [mm]	40	30	30	40
Area [mm ²]	221,168	81,996	81,996	221,168
Moment of inertia [mm ⁴]	85,681 10 ⁶	7,767 10 ⁶	7,767 10 ⁶	85,681 10 ⁶
Specific weight [kN/m ³]	78.50	78.50	78.50	78.50
Modulus of elasticity [MPa]	210,000	210,000	210,000	210,000
Yield strength [MPa]	275	275	275	275

I.3 Numerical Model 2: Jacket Substructure on Embedded Piles with Soil-pile Springs

I.3.1 Soil-pile Interacts as Non-linear Springs

In the numerical model in *SeismoStruct* the p-y curves are fitted to 4 segments (1, 2, 3 and 4) that describe the non-linear behaviour of the soil in a linearized way, as shown in figure I.6. The curve fitting is done by first finding the ultimate soil strength corresponding to that point where the slope of the p-y curve approaches zero, named point U. Then, the p-y curve is fitted into 3 segments with a minimum deviation between the linear segments and the non-linear p-y curve.

The soil yield strength F_y is then defined as point Y and the initial stiffness K_0 is the slope of segment 1.

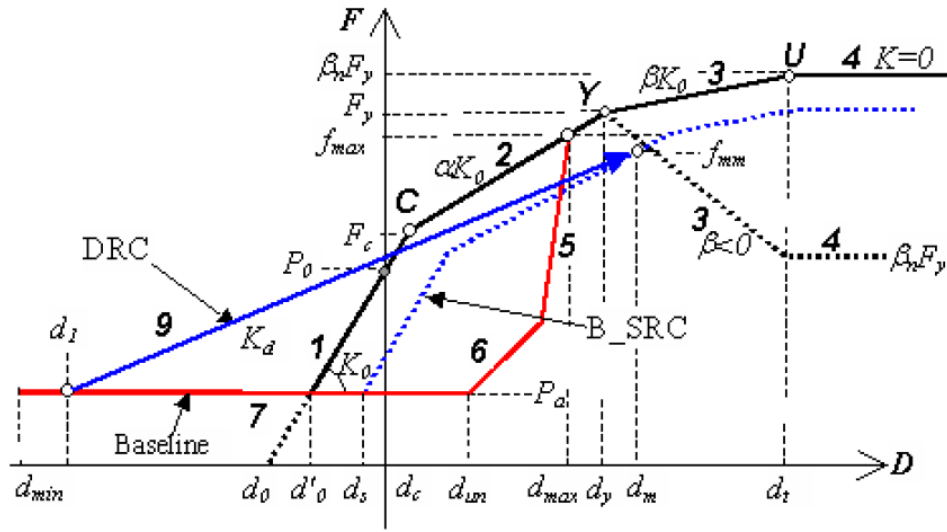


Figure I.6: Fitting of p-y curve to 4 linear segments, [SeismoStruct, 2022] user manual.

The model takes into account the initial horizontal earth pressure on the pile by shifting the fitted p-y curve in figure 7.6 leftwards, i.e. the pile is pre-stressed at zero pile displacement, named P_0 at the intercept with the y-axis. The initial horizontal earth pressure is found as $\sigma'_{h0} = 0.5\sigma'_{v0}$ where the earth pressure coefficient K_0 is set to 0.5 as a simplification for all layers. The input parameters for soil-pile interaction can be seen in table I.4 and parameters are obtained for every 1 m.

Table I.4: Input parameters for non-linear soil-pile springs in *SeismoStruct*.

p-y curve parameters			
Initial stiffness [kN/m]	K_0		
Soil strength ratio at first turning point [-]	F_c		
Yield soil strength [kN]	F_y		
Initial horizontal earth pressure ratio [-]	P_0		
Minimum force ratio at baseline [-]	P_a		0
Stiffness ratio after 1st turning point [-]	α		
Yielding stiffness ratio [-]	β		
Ultimate soil strength factor [-]	β_N		
Cyclic curve parameters			
DRC stiffness ratio [-]	e_{p1}	$X < L/3$	0:linear:1
		$X > L/3$	1
Gap force parameter [-]	p_1		1
Soil cave-in parameter [-]	p_2	$X < L/3$	0:linear:5
		$X > L/3$	5
Degradation parameters			
Stiffness degradation/hardening [-]	δ_k, e_k		
Strength degradation/hardening [-]	δ_t, e_t		
Slope of S-N curve [-]	k_s		
Soil stress corresponding to point S1 in S-N curve [kN]	f_0		

I.3.2 S-N Curves

The S-N curves are obtained by exciting a 10 meter soil layer by an acceleration time series of different amplitudes with a frequency of 0.1 Hz in *DeepSoil*. The maximum shear stress versus the number of load cycles until failure are plotted which give the corresponding S-N curve for the specific soil layer as shown in figure 7.8. The input ground motions and corresponding response of layer 1 - sand in order to obtain the SN curve can be seen in figure I.7-I.10.

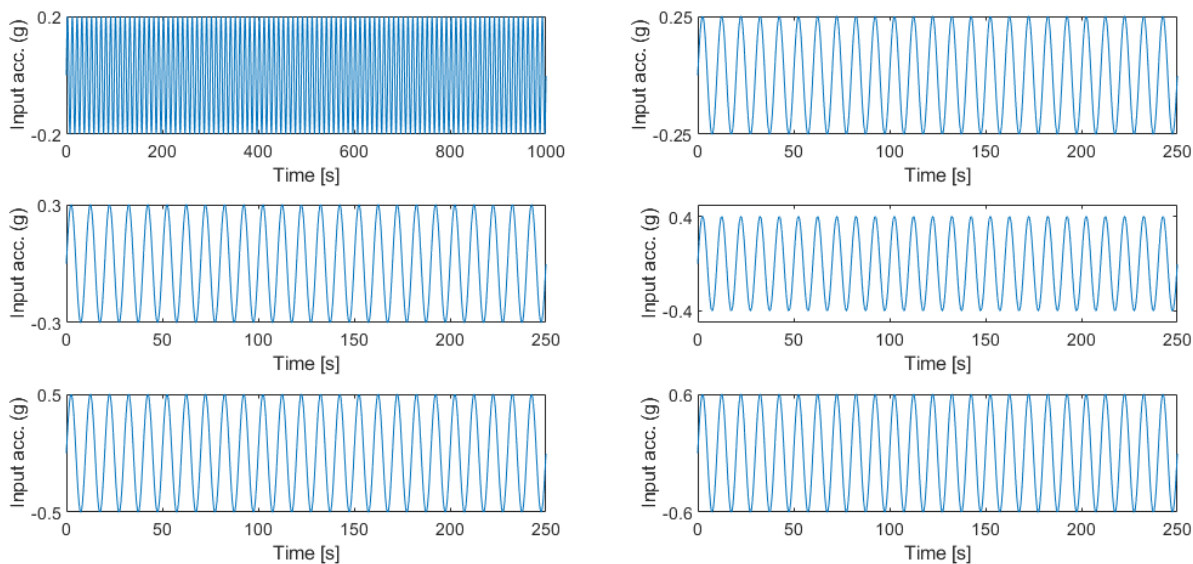


Figure I.7: Input ground motions with different amplitudes with frequency of 0.1 Hz for layer 1 - sand.

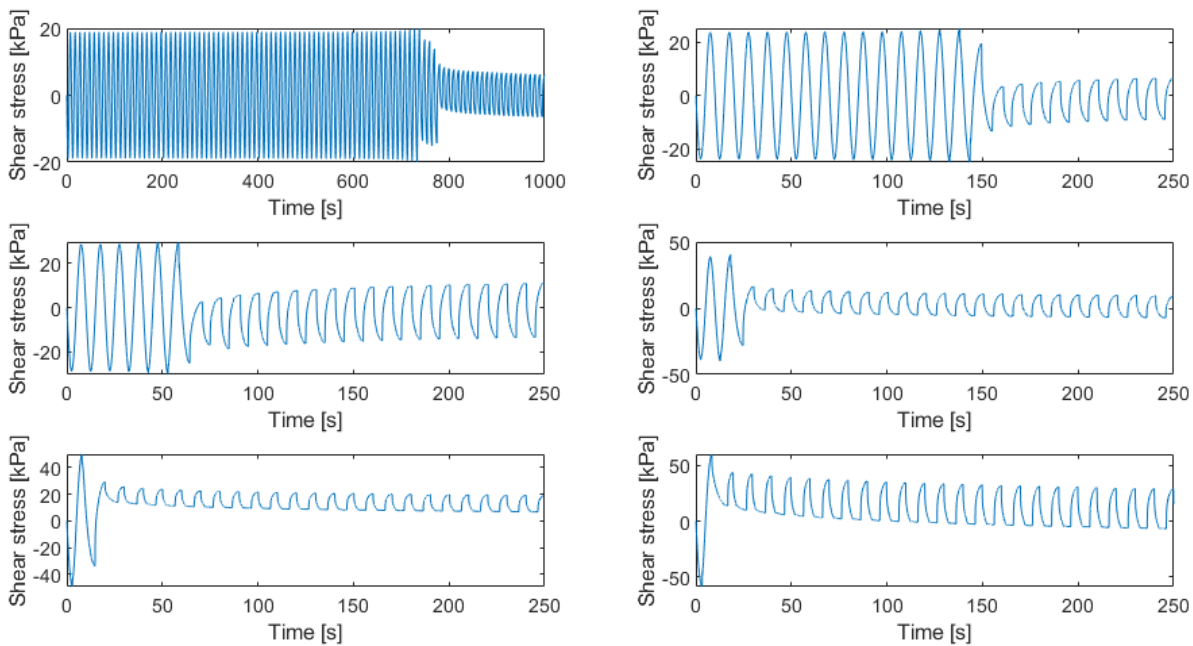


Figure I.8: Shear stress for layer 1 - sand.

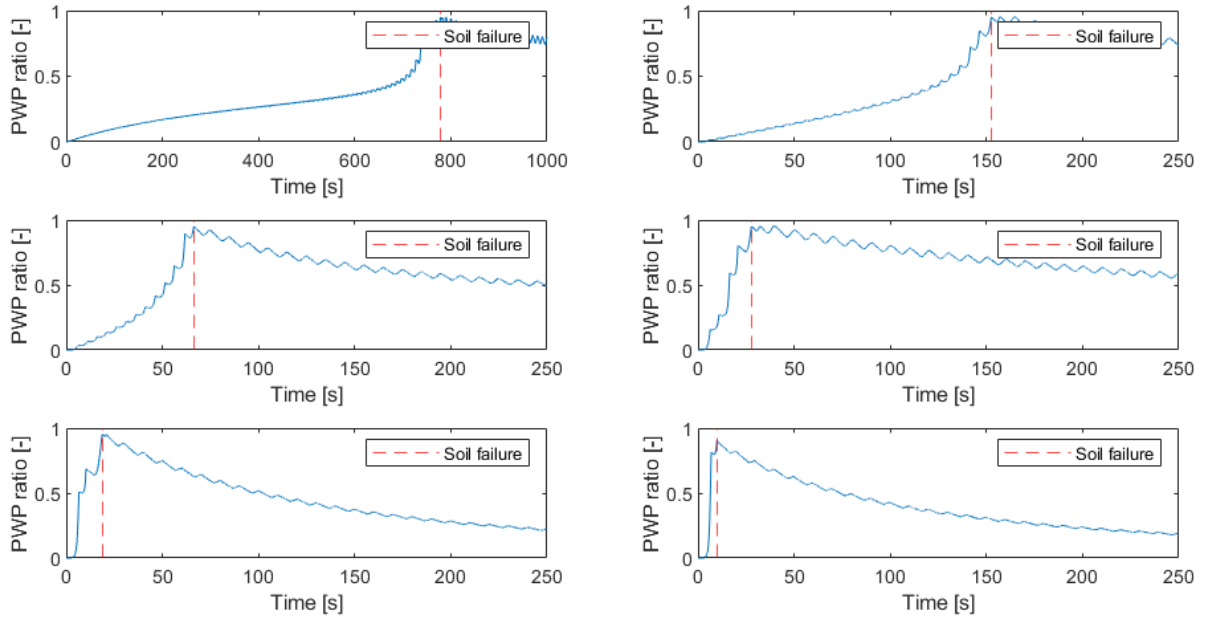


Figure I.9: Porewater pressure ratio for layer 1 - sand. Soil failure at PWP ratio $r_u = 0.95$.

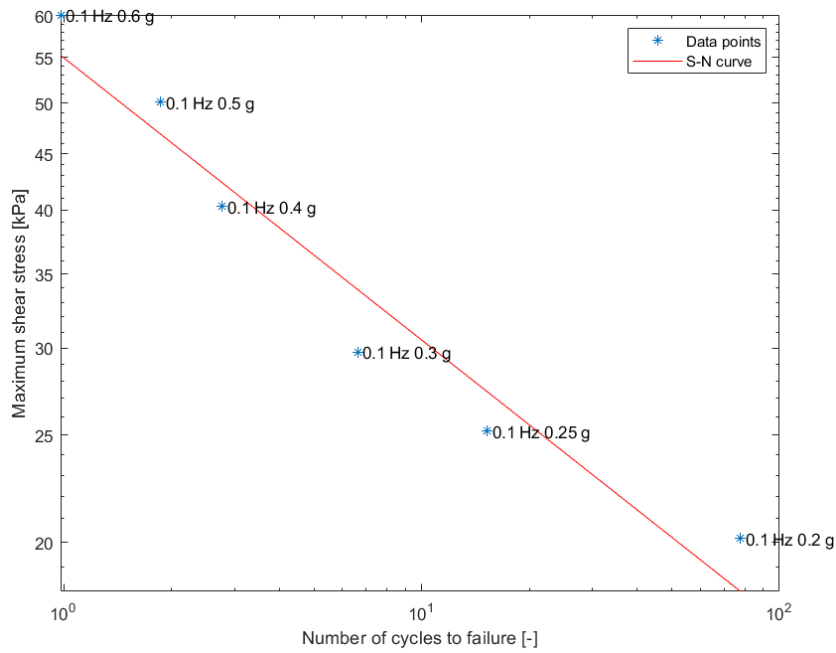


Figure I.10: S-N curve for layer 1 - sand.

In the soil-pile model in *SeismoStruct* are the required S-N curve parameters given in table I.5.

Table I.5: S-N curve parameters.

Layer number	Soil type	Slope of S-N curve [-]	Shear stress after first cycle [kPa]
1	Sand	0.256	55
2.1	Clay	0.129	113
2.2		0.111	147
3.1	Sand	0.183	163
3.2		0.185	232
4	Clay	0.079	279
5	Sand	0.236	322

I.3.3 Radiation Damping

The horizontal radiation damping, ζ_{HH} , assigned for every 1 m along the embedded piles is a stiffness proportional damping obtained from table I.6. Sand layers are assumed to have a parabolic stiffness distribution and clay layers are assumed to have a constant stiffness distribution as shown in figure I.11.

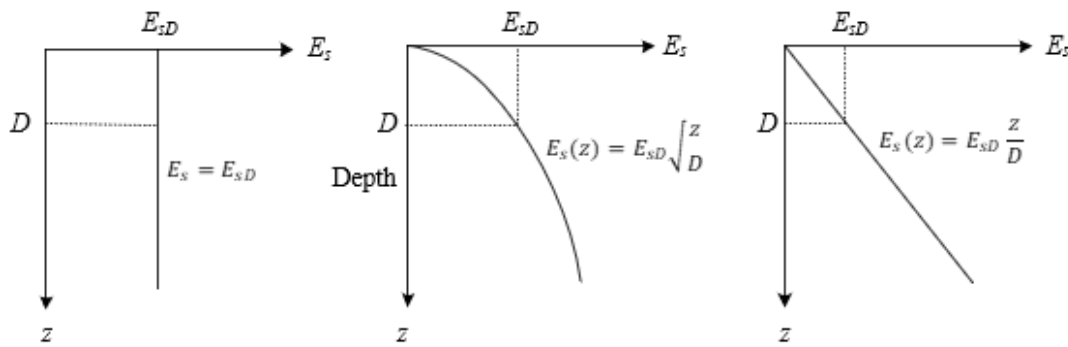


Figure I.11: Idealised soil stiffness profiles. Constant stiffness (typical of OC clay), parabolic stiffness (typical of sand), linear stiffness (typical of soft clay). [Elghazouli, 2017]

Table I.6: Pile-head hysteretic (left hand term) and radiation (right hand term) damping for flexible piles, [Gazetas, 1991].

Damping ratio [%]	Soil stiffness profile		
	Constant - OC clay	Parabolic - sand	Linear - soft clay
ζ_{HH}	$0.8\beta + \frac{1.10fD}{v_s} \left(\frac{E_p}{E_{sD}} \right)^{0.17}$	$0.7\beta + \frac{1.20fD}{v_s} \left(\frac{E_p}{E_{sD}} \right)^{0.08}$	$0.6\beta + \frac{1.8fD}{v_s}$

*Radiation damping is only applicable when the natural frequency of soil is below exciting frequency ($f_n < f$), otherwise radiation damping is negligibly.

where

β	Hysteretic damping ratio [%], see figures I.1-I.4b
f	Exciting frequency [Hz]
D	Pile diameter [m]
E_p	Pile Young's modulus [kPa]
E_{sD}	Soil Young's modulus at a depth equal to pile diameter = $3G_{max}$ [kPa]
ν_s	Shear wave velocity [m/s].

As hysteretic damping is already accounted for in the non-linear p-y curves with unloading-reloading, radiation damping (the right hand term in table I.6) is found for each soil layer. The exciting frequency is taken as different frequencies in the range as shown in figure I.12 and radiation damping is shown in table I.7.

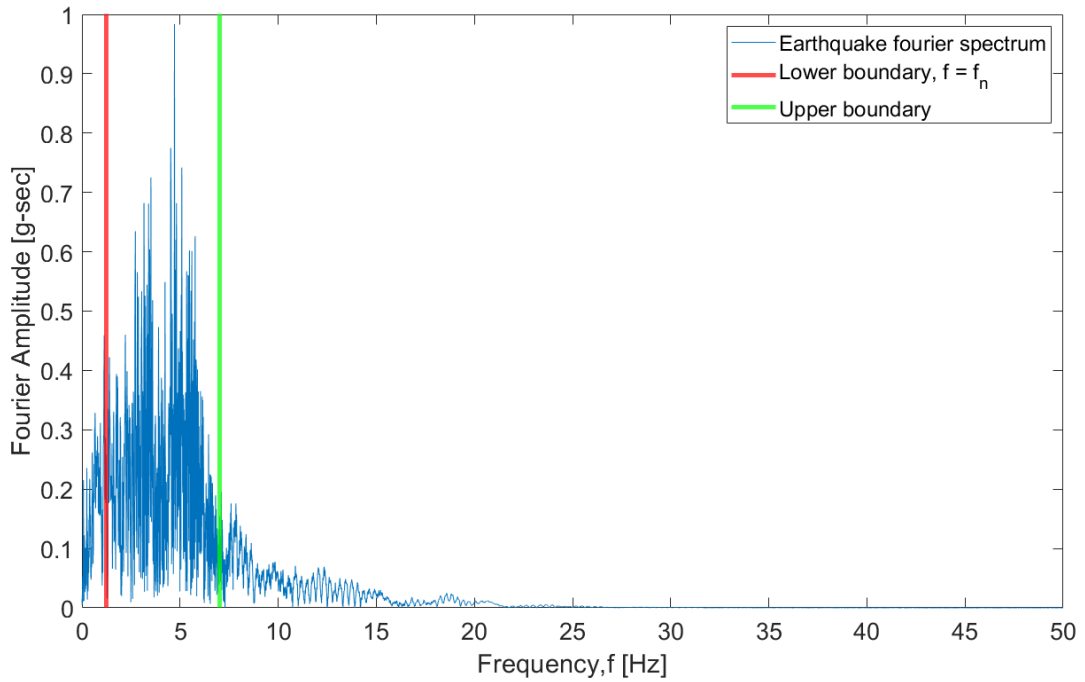


Figure I.12: Spectrum of exciting frequency for design earthquake in North-South. Lower limit equals soil profile frequency $f_n = 1.238$ Hz and upper limit is taken as 7 Hz.

Table I.7: Horizontal radiation damping ζ_{HH} for soil layers along the embedded piles.

f [Hz]	ζ_{HH} [%]		
	Layer 1 - sand	Layer 2.1 - clay	Layer 2.2 - clay
	Parabolic stiffness profile	Constant stiffness profile	
1.238	0.0239	0.0310	0.0275
2.977	0.0574	0.0744	0.0661
4.715 (peak)	0.0910	0.1179	0.1047
5.858	0.1130	0.1464	0.1300
7	0.1351	0.1750	0.1554

It can be concluded that radiation damping is insignificant compared to hysteretic damping.

I.4 Numerical Model 3: Jacket Substructure on Embedded Piles with Soil Volume

I.4.1 Liquefaction Constitutive Soil Model

Sand layers are modelled by the liquefaction implemented soil model UBC3D-PLM in *Plaxis* which is based on the original UBCSAND model. The model suggests SPT based input parameters:

Table I.8: Input parameters for sand layers in liquefaction model UBC3D-PLM in *Plaxis*.

Stiffness parameters									
Layer	Elastic shear modulus factor [-]	Elastic bulk modulus factor [-]	Plastic shear modulus factor [-]	Rate of stress-dependency of elastic shear modulus [-]	Rate of stress-dependency of bulk modulus [-]	Rate of stress-dependency of plastic shear modulus [-]	Atmospheric pressure [kN/m ²]		
	k_G^{se}	k_B^{se}	k_G^{sp}	me	me	np	P _{ref}		
1	1016	711	644	0.5	0.5	0.4	100		
3.1	979	686	490	0.5	0.5	0.4	100		
3.2	1020	714	617	0.5	0.5	0.4	100		
5	960	672	440	0.5	0.5	0.4	100		

Strength parameters			
Layer	Constant volume friction angle [°]	Peak friction angle [°]	Tensile strength [kN/m ²]
	$\phi_{cv} = \phi'$	ϕ'_p	σ_t
1	34.1	35.2	0
3.1	36.9	38.0	0
3.2	36.8	38.2	0
5	37.7	38.9	0

Advanced parameters			
Layer	Failure ratio R_f	Corrected SPT value $(N_1)_{60}$	Post-liquefaction factor f_{Epost}
			f_{dens}
1	0.99	13	0.2
3.1	0.99	10	0.2
3.2	0.99	13	0.2
5	0.99	11	0.2

Stiffness modulus factors

Plaxis uses the elastic, k_G^e and k_K^e , and plastic, k_G^p , stiffness factors to calculate the elastic shear and bulk modulus and the plastic shear modulus as shown in figure I.13.

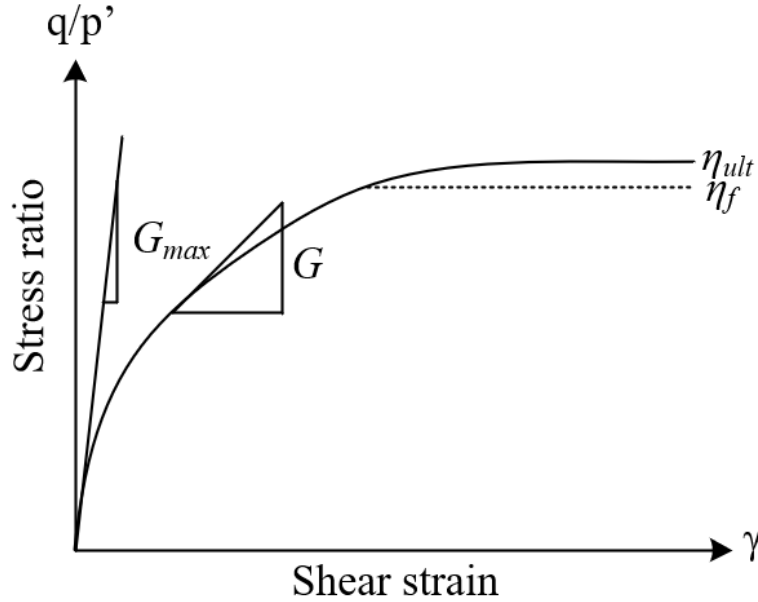


Figure I.13: The original UBCSAND hardening rule.

η_f	Stress ratio at failure
η_{ult}	Asymptotic stress ratio
G	Plastic shear modulus
G_{max}	Elastic shear modulus.

The stiffness modulus factors are obtained based on SPT, [Plaxis, 2021a]:

$$\begin{aligned}
 k_G^e &= 21.7 \times 20 \times (N_1)_{60}^{0.3333} \\
 k_B^e &= 0.7 \times k_G^e \\
 k_G^p &= k_G^e \times (N_1)_{60}^2 \times 0.003 + 100
 \end{aligned}
 \tag{I.1}$$

The suggested default values for $m_e = n_e = 0.5$ and $n_p = 0.4$, [Plaxis, 2021a].

Strength parameters

The peak friction angle, ϕ'_p , and the constant volume friction angle at critical state, $\phi_{cv} = \phi'$ are correlated based on the SPT, [Plaxis, 2021a]:

$$\phi'_p = \phi_{cv} + \frac{(N_1)_{60}}{10} + \max\left(0; \frac{(N_1)_{60} - 15}{5}\right)
 \tag{I.2}$$

The cohesion of sand layers are $c = 0$.

Advanced parameters

The densification factor, f_{dens} , controls the plastic shear modulus, G , during reloading. It is recommended to use $f_{dens} = 1.0$ because the densification does not significantly affect liquefaction triggering, [Plaxis, 2021a].

Post-liquefaction behaviour is adjusted by f_{Epost} where 0.2 - 1 is recommended, [Plaxis, 2021a].

The failure ratio is based on the SPT, [Plaxis, 2021a]:

$$R_f = \frac{\eta_f}{\eta_{ult}} \approx 1.1 ((N_1)_{60})^{-0.15} < 0.99 \quad (\text{I.3})$$

I.4.2 Hardening Soil Model with Small-Strain Stiffness

Clay layers are modelled by the hardening soil model with small-strain stiffness (HS small) in *Plaxis* where input parameters are based on drained triaxial and oedometer test:

Table I.9: Input parameters in hardening soil model HS small in Plaxis.

Mohr-Coulomb failure parameter			
Layer	Effective cohesion c	Friction angle $[\circ]$	Dilatancy angle $[\circ]$
		ϕ	ψ
2.1	10	28	0
2.2	10	28	0
4	10	28	0

Stiffness parameters			
Layer	Secant stiffness in standard drained triaxial test [kPa]	Tangent stiffness for primary oedometer loading [kPa]	Unloading/reloading stiffness [kPa]
	E_{50}^{ref}	E_{oed}^{ref}	E_{ur}^{ref}
2.1	13750	13750	137500
2.2	19091	19091	190909
4	33333	33333	333333

Advanced parameters			
Layer	Poisson's ratio for unloading-reloading $[-]$	Reference stress for stiffnesses kN/m^2	K0-value for normal consolidation $[-]$
	ν_{ur} (default = 0.2)	$p_{\text{-ref}}$ (default = 100)	$K_0^{nc} = 1 - \sin \phi$ (default = 0.5)
2.1	0.2	100	0.5
2.2	0.2	100	0.5
4	0.2	100	0.5

Layer	Power for stress-level dependency of stiffness $[-]$	Small strain shear modulus [kPa]	Shear strain at which the shear modulus is reduced to about 70% of G_{max} $[\%]$
	m	G_{max}	$\gamma_{0.7}$
2.1	0.8	125053	0.0225
2.2	0.8	152207	0.0256
4	0.8	210855	0.0476

Stiffness parameters

The stiffness properties E_{50}^{ref} , E_{ur}^{ref} and E_{oed}^{ref} can be obtained from drained triaxial and oedometer tests as shown in figure I.14.

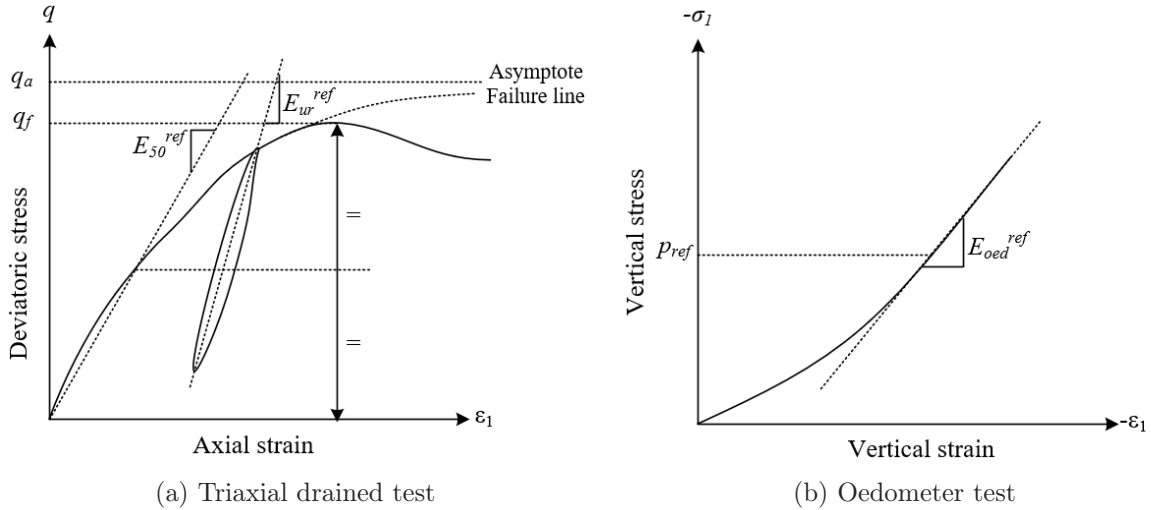


Figure I.14: Input parameters from laboratory tests.

E_{50}^{ref} is the secant stiffness of 50% of the maximum deviatoric stress at a cell pressure of $-\sigma_3 = p^{ref}$.

In lack of triaxial and oedometer tests a paper by [Phien-wej et al., 2012] of hard Bangkok clay with empirical correlation equations between stiffness input properties and SPT-N values is used:

$$\begin{aligned}
 E_{50}^{ref} &= 2500N_{60} \\
 E_{ur}^{ref} &= 10E_{50}^{ref} \\
 E_{oed}^{ref} &\approx E_{50}^{ref}
 \end{aligned}
 \tag{I.4}$$

The shear strain, $\gamma_{0.7}$, at which the shear modulus is reduced to 70% of G_{max} is found from the relation of shear modulus reduction in equation (G.24).

I.5 Numerical Model 3 with Ground Improvements

The top sand layer is made denser with an increase in SPT blow count. An average $N_{1.60}$ value for the top sand layer is chosen to be 45 which according to table H.2 corresponds to a very dense sand. The input parameters in the liquefaction model are updated:

Table I.10: Input parameters in liquefaction model UBC3D-PLM in Plaxis with ground improvements.

Stiffness parameters						
Layer	Elastic shear modulus factor [-]	Elastic bulk modulus factor [-]	Plastic shear modulus factor [-]	Rate of stress-dependency of elastic shear modulus [-]	Rate of stress-dependency of elastic bulk modulus [-]	Rate of stress-dependency of plastic shear modulus [-]
	k_G^{*e}	k_B^{*e}	k_G^{*p}	me	ne	np
1	1544	1081	9478	0.5	0.5	0.4
3.1				Unchanged		
3.2				Unchanged		
5				Unchanged		100
Strength parameters						
Layer	Constant volume friction angle [°]	Peak friction angle [°]	Cohesion [kN/m ²]	Tensile strength [kN/m ²]		
	ϕ_{cv}	ϕ_p	c	σ_t		
1	34.1	44.6	0	0		
3.1			Unchanged			
3.2			Unchanged			
5			Unchanged			
Advanced parameters						
Layer	Failure ratio R_f	Corrected SPT value $(N_1)_{60}$	Densification factor f_{dens}	Post-liquefaction factor f_{Epost}		
1	0.99	45	1	0.2		
3.1			Unchanged			
3.2			Unchanged			
5			Unchanged			

Appendix J | P-y Curves for Laterally Loaded Piles

In this appendix the p-y curves utilised for seismic analysis are presented for soft clay and sand. Furthermore the limitations and applications of the p-y curves are presented.

J.1 Soft Clay

The ultimate lateral resistance in [kN/m] for static loading is according to [DNV-RP-0126, 2016] calculated as:

$$p_u = \begin{cases} (3s_u + \gamma'X)D + Js_uX & \text{for shallow depth } 0 < X \leq X_R \\ 9s_uD & \text{for great depth } X > X_R \end{cases} \quad (\text{J.1})$$

where

X	Depth below soil surface [m]
X_R	Transition between shallow and great depth [m]
D	Pile diameter [m]
s_u	Undrained shear strength [kPa]
γ'	Effective soil unit weight [kN/m ³]
J	Empirical constant between 0.25-0.5, 0.5 for soft NC clay.

The reason why the ultimate strength is different for shallow and great depth is due to the difference in failure mechanism because of increased overburden pressure. In shallow depth the soil will move to the surface during failure whereas in great depth the soil will move around the pile.

The p-y curve for cyclic loading can be calculated as:

$$p = \begin{cases} \frac{p_u}{2} \left(\frac{y}{y_c} \right)^{1/3} & \text{for } y \leq 3y_c \\ 0.72p_u \left(1 - \left(1 - \frac{X}{X_R} \right) \frac{y-3y_c}{12y_c} \right) & \text{for } 3y_c < y \leq 15y_c \quad \text{for moderate depth} \\ 0.72p_u \frac{X}{X_R} & \text{for } y > 15y_c \end{cases} \quad (\text{J.2})$$

$$p = \begin{cases} \frac{p_u}{2} \left(\frac{y}{y_c} \right)^{1/3} & \text{for } y \leq 3y_c \\ 0.72p_u & \text{for } y > 3y_c \end{cases} \quad \text{for great depth} \quad (\text{J.3})$$

where

p, y	Lateral soil resistance p in [kN/m] when pile has deflected laterally y in [m]
y_c	$2.5\varepsilon_c D$
ε_c	Strain which occurs at one-half the maximum stress in laboratory undrained compression tests of undisturbed soil samples set equal to 0.007.

J.2 Sand

The ultimate lateral resistance for static loading is:

$$p_u = \begin{cases} (C_1 X + C_2 D) \gamma' X & \text{for shallow depth } 0 < X \leq X_R \\ C_3 D \gamma' X & \text{for great depth } X > X_R \end{cases} \quad (\text{J.4})$$

where

C_1, C_2, C_3 | Coefficients dependent on friction angle φ .

The fitted coefficients are:

$$\begin{aligned} C_1 &= 0.115 \cdot 10^{0.0405\varphi} \\ C_2 &= 0.571 \cdot 10^{0.022\varphi} \\ C_3 &= 0.646 \cdot 10^{0.0555\varphi} \end{aligned} \quad (\text{J.5})$$

The p-y curve is found as:

$$p = A p_u \tanh\left(\frac{kX}{A p_u} y\right) \quad (\text{J.6})$$

where

k | initial modulus of subgrade reaction and depends on the friction angle φ , found from figure F-5 in [DNV-RP-0126, 2016]
 A | Factor equal to 0.9 that accounts for cyclic loading.

J.3 Applications and Limitations

When applying the p-y curves for analysis considerations about application and limitations of these curves are crucial, as improper use of or negligence of its limitations may lead to incorrect or unrealistic results. Some of the applications and limitations of the p-y curves are listed below:

Applications

When applying the non-linear p-y curves for analysis of pile in sand and/or clay according to [DNV-RP-0126, 2016], the following points ought to be considered.

- The non-linear p-y curves for clay and sand are primarily used for evaluation of lateral pile capacity in the ULS analysis and caution must be exercised when p-y curves are utilised for any other purpose
- p-y curves must be used with caution whether or not the non-linear p-y curves of piece-wise linear approximations are used.
- When p-y curves for clay and sand are used in analysis where the initial slope of the is crucial a piece-wise linear approximation between carefully selected discretization points illustrated in figure J.1

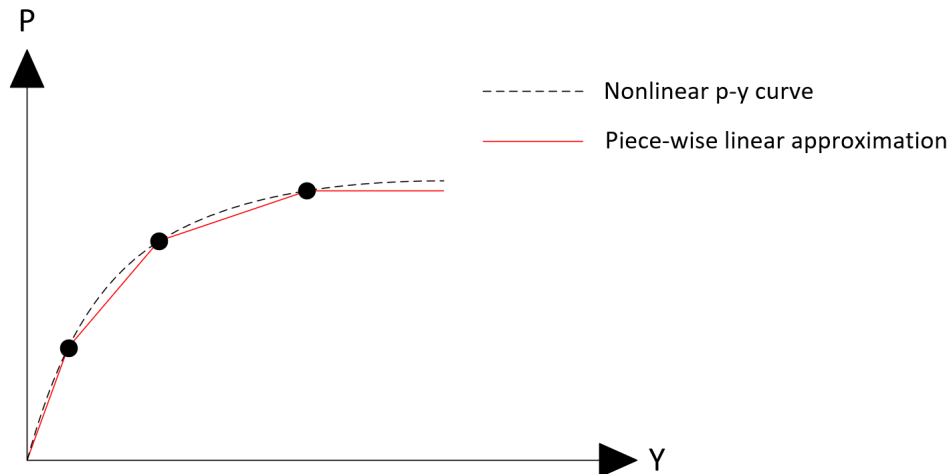


Figure J.1: Non-linear p-y curve and piece-wise linear approximation of the p-y curve.

Limitations

When utilising the p-y curves for analysis om embedded piles according to [DNV-RP-0126, 2016], some of the limitations ought to be considered are listed below:

- The p-y curves from [DNV-RP-0126, 2016] have been calibrated for long slender piles with diameters up to 1.0 m. However according to [Międlarz and Bałachowski, 2018] the curves can be applied to piles with diameters of up to 2.5 m.
- Another limitation of using the p-y curves from [DNV-RP-0126, 2016] is group effects should be considered if the spacing between the piles is less than eightfold the pile diameter.

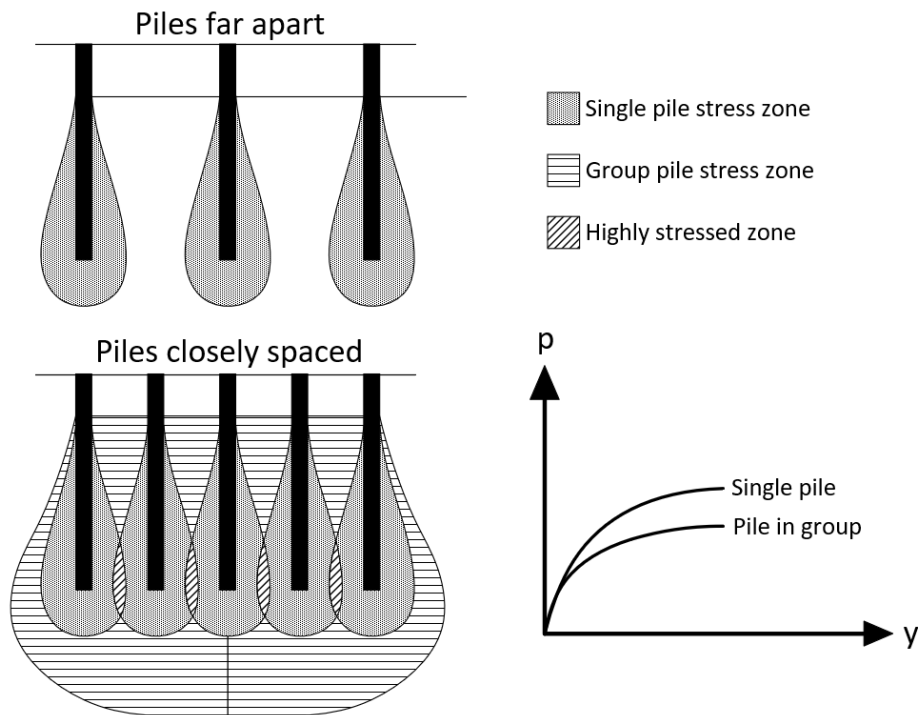


Figure J.2: Pile group behaviour.

Appendix K | Liquefaction Hazard Analysis

Within the context of geotechnical engineering the liquefaction phenomena is one of the most important, complex and interesting topics, [Kramer, 1996]. The term liquefaction is used to describe soil deformations caused by repeated disturbance which results in the development of excess porewater pressure of cohesionless saturated soils under undrained conditions. When cohesionless, saturated soil is exposed to repeated shearing which is the case under an earthquake soil particles rearranges and the soil behaviour heavily depends on whether porewater can drain or not, see figure K.1.

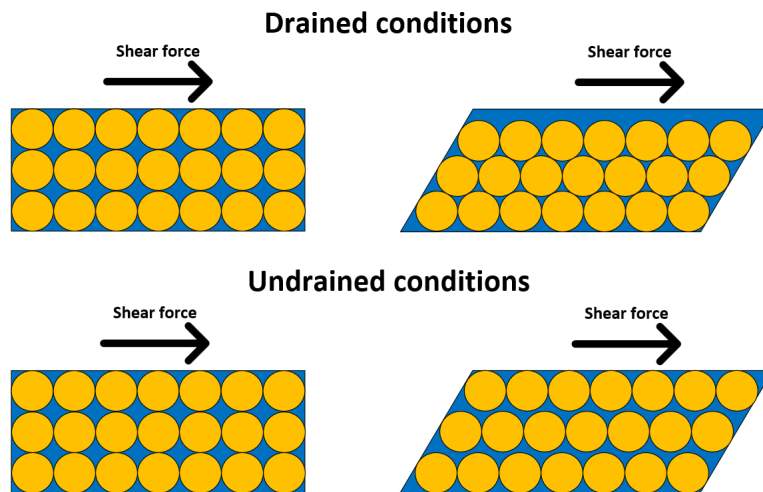


Figure K.1: Illustration of soil particle rearrangement for cohesionless soils in drained and undrained conditions.

Under drained conditions porewater is allowed to escape resulting in the soil consolidating and retaining its strength. However, in undrained conditions porewater is not allowed to escape resulting in soil particles hydroplaning and having little to no strength temporarily. In undrained conditions this results in development of excess porewater pressure as well as a decrease of effective stresses, which can cause soil liquefaction.

K.1 Liquefaction Types

Liquefaction phenomena that results from the development of excess porewater pressure can be classified as either *flow liquefaction* or *cyclic mobility*, [Kramer, 1996]. Whether or not the soil will experience either flow liquefaction or cyclic mobility solely depends on the stress state of the soil, see figure K.2.

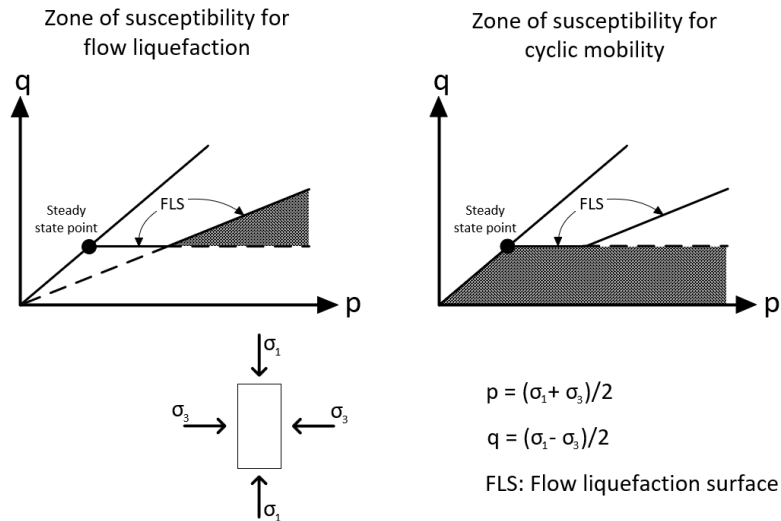


Figure K.2: Zone of susceptibility for flow liquefaction and cyclic mobility.

K.1.1 Flow Liquefaction

Flow liquefaction is among the two types of liquefaction the most damaging type of liquefaction, but also occurs less frequently compared to cyclic mobility, [Kramer, 1996]. Flow liquefaction can occur when the static shear stress is greater than the steady state shear strength, S_{su} , see figure K.2. The reason flow liquefaction is the most damaging and dangerous type of liquefaction phenomena is due to the speed and large rapid movements. Flow liquefaction for soils exposed to cyclic loads mainly consists of two phases AB and BC respectively as shown in figure K.3.

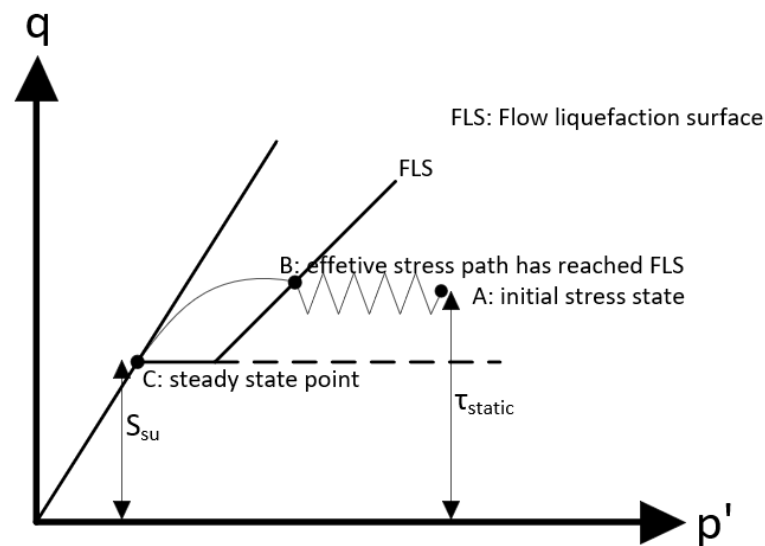


Figure K.3: Flow liquefaction due to cyclic loading.

Under process AB the soil undergoes cyclic loading where excess pore pressure is developed until the soil reaches the FLS, where the soil becomes unstable and flow liquefaction has initiated at this point B. In process BC the soil has become unstable from previous cyclic loading causing the soil strength to drop significantly at which point large soil deformations are solely dictated by static shear stresses. If the soil is disturbed to the FLS process BC is inevitable. Flow

liquefaction however can only occur in loose cohesionless soils.

K.1.2 Cyclic Mobility

Cyclic mobility is the less damaging but more frequent liquefaction phenomena compared to flow liquefaction, [Kramer, 1996]. Cyclic mobility can occur if the static shear stress is lower than the steady state shear strength. Unlike flow liquefaction there is no point at which the soil becomes unstable when undergoing continuous cyclic loading as permanent deformations are accumulated incrementally [Kramer, 1996]. The magnitude of permanent strains and deformations depend on static shear stress and duration of the ground motions. Development of cyclic mobility of a soil undergoing cyclic loading is illustrated in figure K.4.

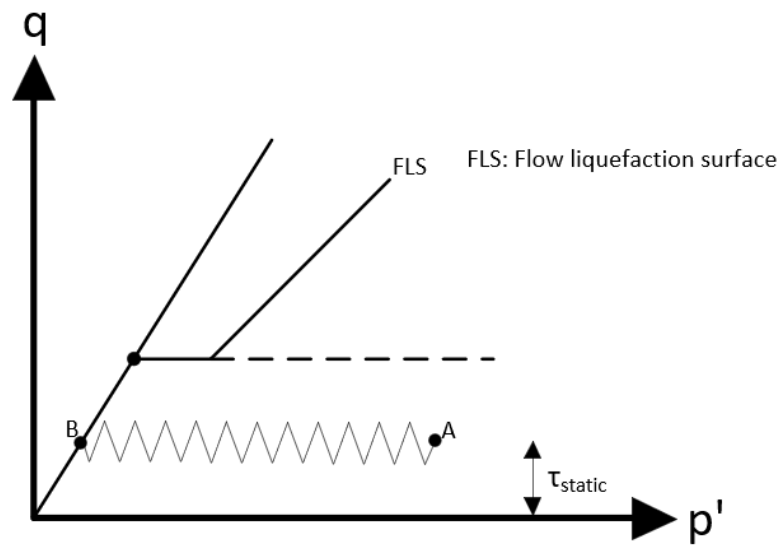


Figure K.4: Cyclic mobility due to cyclic loading.

When a soil undergoes cyclic mobility the deformations caused by cyclic mobility develop incrementally in process AB, and deformations are driven by static shear stresses caused by gravity and dynamic shear stresses caused by the earthquake. Cyclic mobility can develop in both loose and medium dense cohesionless soils unlike flow liquefaction which only occurs in loose cohesionless soils [Kramer, 1996].

K.2 Liquefaction Evaluation

When a structure is located on a site exposed to seismic action it is crucial to perform an evaluation on whether or not liquefaction should be included in the analysis by considering the following aspects:

- Liquefaction susceptibility
- Liquefaction initiation
- Liquefaction effects.

When performing the liquefaction evaluation it can be composed of three questions which remain to liquefaction susceptibility, initiation and effects are answered, the process is illustrated on figure K.5.

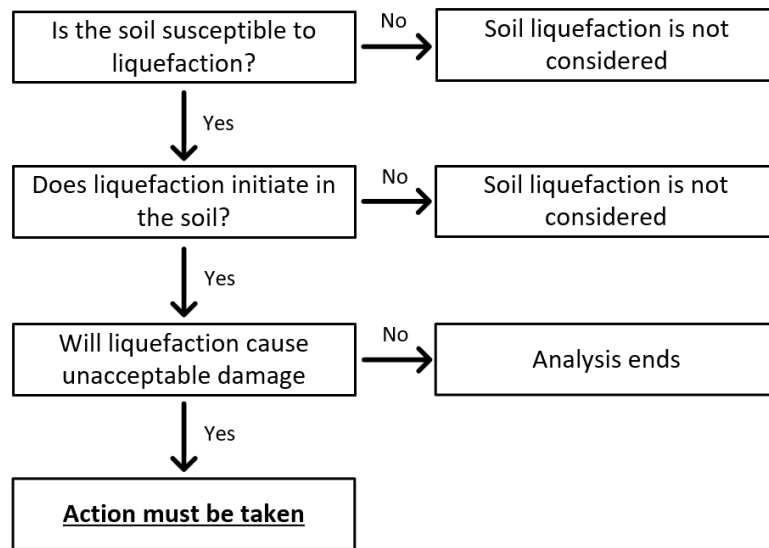


Figure K.5: Liquefaction evaluation process diagram.

The first question is whether or not the soil is susceptible to liquefaction, if the answer is no soil liquefaction is not considered, however if the answer is yes you move on to the next question. The next question is whether or not liquefaction will initiate or not, if the answer is no soil liquefaction will not be triggered and the evaluation ends, however if the answer is yes you move on to the last question. If the soil is susceptible to liquefaction and liquefaction initiates the last question to be answered is whether or not damage caused by liquefaction is unacceptable if the answer is no the liquefaction evaluation ends, if the answer is yes necessary preventive measures must be taken.

Each of the aspects previously listed are thoroughly explained, as well as ways of answering the questions on the liquefaction evaluation process diagram in figure K.5.

K.2.1 Susceptibility

Not all soils are susceptible to liquefaction, therefore it is essential to determine whether or not the soils on a specific site is susceptible to liquefaction. If a soil is not susceptible liquefaction hazards do not exist and the evaluation is ended [Kramer, 1996]. However if the soil is susceptible to liquefaction, initiation and effects must be handled, when evaluating susceptibility there are criteria which are evaluated to assess whether or not the soil is susceptible these include historical, geological, compositional and state criteria.

Historical criteria

The historical criteria is about evaluation of whether or not the soil at the given site has liquefied in the past as a great deal of post-earthquake field investigations have shown that liquefaction reoccurs at the same location if groundwater and soil conditions are unchanged [Kramer, 1996]. Therefore past liquefaction cases can be used to identify sites where liquefaction is likely to reoccur. To evaluate this criteria a map of past liquefaction sites is used to identify whether or not liquefaction will reoccur, for this case a liquefaction map of earthquake induced liquefaction sites in the period 1885-1997 is shown in figure K.6.

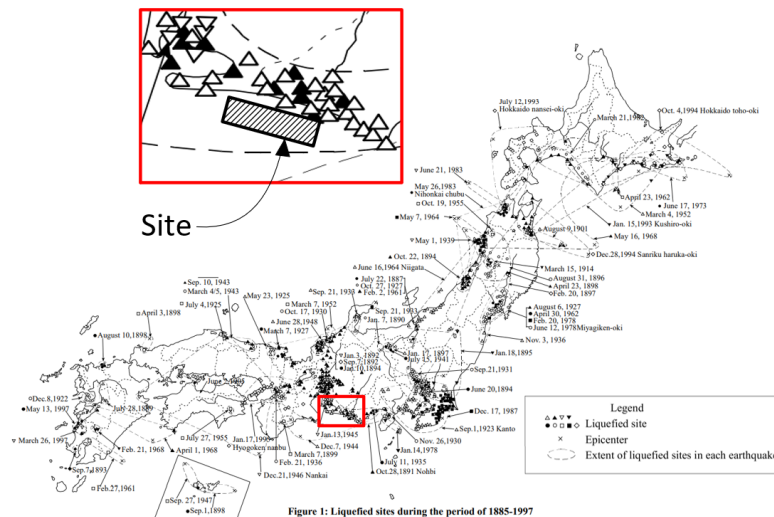


Figure 1: Liquefied sites during the period of 1885-1997

Figure K.6: Map of liquefied sites in Japan in the period 1885-1997, [Wakamatsu, 1997]. The site investigated in this project is zoomed in.

Geological criteria

Another criteria to evaluate liquefaction susceptibility is the geologic criteria which evaluates the geological processes through which soil particles are sorted and deposited. Geological processes which sort soil into uniform grain sizes as well as loose deposits tend to be highly susceptible to liquefaction [Kramer, 1996].

The susceptibility of soils is also dependent on the age in which it was deposited, the older the age the less likely a soil is to liquefy, with soils deposits preceding the Pleistocene epoch rarely liquefy [Kramer, 1996].

Lastly in reference to the geological criteria the liquefaction occurs only in saturated soils, which means the depth of the groundwater table influences liquefaction susceptibility. Liquefaction susceptibility decreases with an increase in groundwater depth and liquefaction is mostly observed at sites where the groundwater depth is within a few meters of the ground surface [Kramer, 1996].

Compositional criteria

Compositional criteria revolves around the soil characteristic which influence volume change, these characteristics include particle size, shape and gradation [Kramer, 1996]. The particle size heavily influences liquefaction susceptibility as sands are more susceptible to liquefaction than heavily grained soils such as gravel and fine-grained soils such as silts or clay [Kramer, 1996]. However, sensitive clays are susceptible to significant strength loss (strain softening) if the following criteria are meet according to [Wang, 1979].

$$\text{Fraction finer than } 0.005 \text{ mm} \leq 15\%$$

$$\text{Liquid Limit, } LL \leq 35\%$$

$$\text{Natural water content} \geq 0.9 LL$$

$$\text{Liquidity index} \leq 0.75$$

State criteria

The last criteria which dictates whether or not a soil liquefies is the state criteria, even though a soil is indicated by all the previous criteria that it will liquefy the state criteria must also be satisfied. The initial state of the soil dictates whether or not the soil is in a loose contractive state or a dense dilative state, which dictates whether or not the soil is susceptible to flow liquefaction [Kramer, 1996]. This is done by identifying the initial state of soil in comparison to the critical void ratio line, see figure K.7.

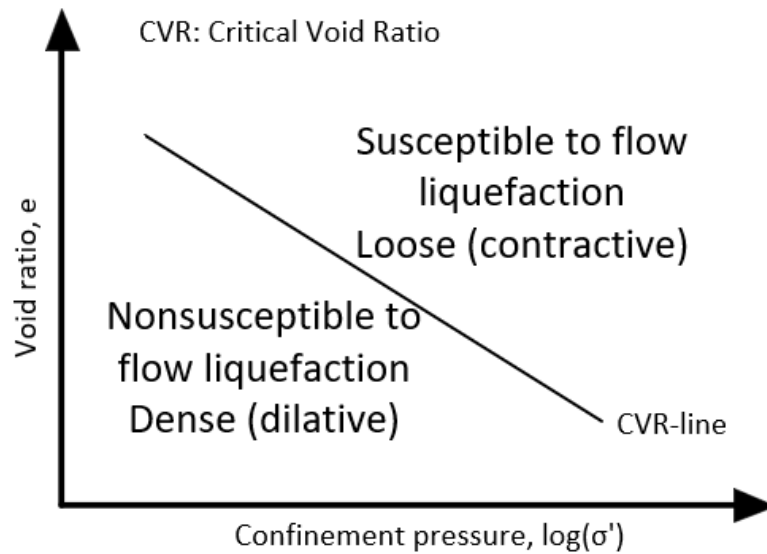


Figure K.7: State criteria for flow liquefaction and definition of soil initial state.

Whether or not a soil behaves as a loose contractive soil or a dense dilative soil entirely depends on its positioning in comparison to the critical void ratio line. Furthermore its initial state also tells us how the soil will behave in a drained or undrained condition, see figure K.8.

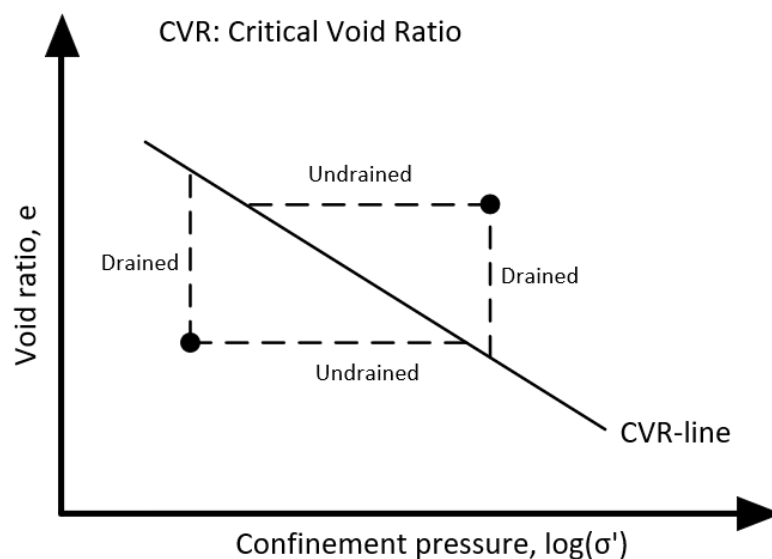


Figure K.8: Soil drained and undrained behaviour for loose contractive and dense dilative soils.

K.2.2 Initiation

Even though a soil layer has been evaluated to be susceptible to liquefaction, this does not necessarily entail that liquefaction is initiated. To evaluate liquefaction initiation a simplified cyclic stress-based approach is utilised where the factor of safety FS against liquefaction initiation is evaluated, using equation (K.1)

$$FS = \frac{CRR}{CSR} \quad (\text{K.1})$$

Where CSR is the cyclic stress ratio, which is a measure of the cyclic stress which is applied to the soil and CRR is a measure of soil resistance to liquefaction. According to [DNV-RP-0585, 2021] when using a simplified stress-based method to evaluate liquefaction a minimum factor of safety against liquefaction of 1.25 meaning if the CSR value reaches 80% of the CRR liquefaction is considered to be initiated, see equation (K.1)

$$FS = \frac{0.8 CRR}{CSR} \quad (\text{K.2})$$

Using (K.2) liquefaction is considered initiated when the factor of safety reaches a value of 1. The CSR and CRR value respectively can be found using different approaches given below.

Cyclic stress ratio

The first step to evaluating liquefaction initiation is estimating the CSR value, which can be estimated using either a Site Seismic Response Analysis $SSRA$ or a simplified approach, see figure K.9

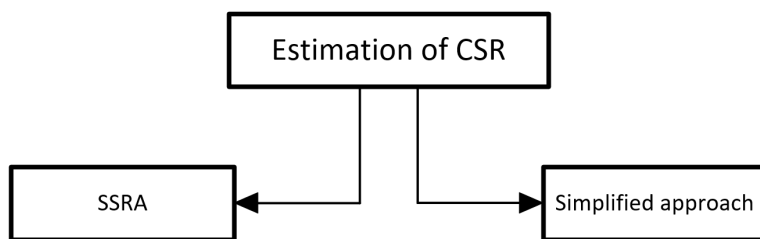


Figure K.9: Estimation of cyclic stress ratio, CSR value.

Within the scope of this project site seismic response analysis have been performed and are utilised to find the cyclic stress ratio based on the shear stress history at different depths in the soil profile. The CSR value is calculated using the cyclic shear stress τ_{cyc} and the average effective vertical stress σ'_v as well as correcting for moment magnitude and overburden pressure using factors MSF and K_σ , see equation (K.3) [Kramer, 1996]:

$$CSR = \frac{\tau_{cyc}}{\sigma'_v} \frac{1}{MSF} \frac{1}{K_\sigma} \quad (\text{K.3})$$

where

MSF	Factor that account for moment magnitude correction
K_σ	Factor that accounts for overburden pressure.

However shear stress histories imposed from earthquakes are usually transient shear stress histories and therefore a cyclic shear stress τ_{cyc} , which generates similar excess porewater pressure is calculated as 65 % of the maximum shear stress τ_{max} from the shear stress time history [Seed et al., 1975].

$$\tau_{cyc} = 0.65 \tau_{max}$$

Combining this with equation (K.3) the equation can be rewritten as

$$CSR = 0.65 \frac{\tau_{max}}{\sigma'_v} \frac{1}{MSF} \frac{1}{K_\sigma} \quad (K.4)$$

Cyclic resistance ratio

The last parameter needed to perform evaluation of liquefaction initiation is estimating the CRR value, which is done based on either a field-based approach or a lab-based approach, see figure K.10.

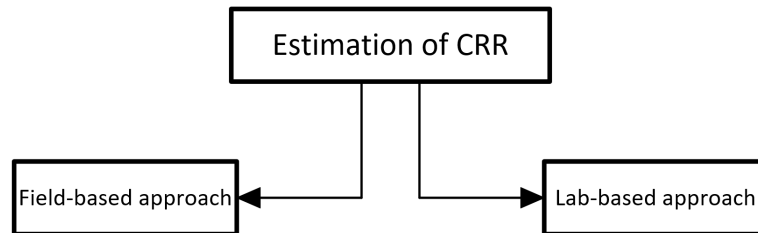


Figure K.10: Estimation of cyclic resistance ratio, CRR value.

Within the scope of this project the field-based approach is utilised, which includes estimation of the soils resistance to liquefaction based on either SPT or CPT field testing results. In this project SPT tests have been performed at the future windturbine site location where SPT blow counts N_m have been obtained. The corrected blow count is shown in equation (K.5)

$$(N_1)_{60} = C_N C_E C_R C_B C_S N_m \quad (K.5)$$

Where

$(N_1)_{60}$	Corrected SPT blow count [-].
C_N	Overburden correction factor [-].
C_E	Delivered energy over theoretical free fall energy [-].
C_R	Rod correction factor [-].
C_B	Nonstandard borehole diameter correction factor [-].
C_S	Liner correction factor [-].
N_m	Measured SPT blow count [-].

The corrected SPT blow count $(N_1)_{60}$ is used to obtain the soils resistance to liquefaction. To do this the following expression according to [Idriss and Boulanger, 2010] is used, see equation (K.6)

$$CRR = \exp \left(\frac{(N_1)_{60cs}}{14.1} + \left(\frac{(N_1)_{60cs}}{126} \right)^2 - \left(\frac{(N_1)_{60cs}}{23.6} \right)^3 + \left(\frac{(N_1)_{60cs}}{25.4} \right)^4 - C_o + \sigma_{\ln(R)} \cdot \Phi^{-1}(P_L) \right) \quad (K.6)$$

Where

$(N_1)_{60cs}$	Corrected equivalent fine sand SPT blow count [-]
C_o	Fitting parameter $C_o = 2.67$ [Idriss and Boulanger, 2010] [-]
$\sigma_{\ln(R)}$	Standard deviation of log CRR $\sigma_{\ln(R)} = 0.13$ [-]
Φ^{-1}	Inverse standard normal cumulative distribution function
P_L	Probability of liquefaction [-].

Recommended values for probability of liquefaction when evaluating the factor of safety FS is 15%. Therefore the only unknown parameter needed to estimate soil resistance to liquefaction is the corrected equivalent fine sand SPT blow count, which is obtained in equation (K.7) according to [Idriss and Boulanger, 2010]

$$(N_1)_{60cs} = (N_1)_{60} + \Delta(N_1)_{60} \quad (K.7)$$

Where $\Delta(N_1)_{60}$ is the clean sand adjustment value which is used to correlate for the fine content in the sand layers. This value is obtained from the empirical relationship according to [Idriss and Boulanger, 2008], see equation (K.8)

$$\Delta(N_1)_{60} = \exp \left(1.63 + \frac{9.7}{FC + 0.01} - \left(\frac{15.7}{FC + 0.01} \right)^2 \right) \quad (K.8)$$

Within the scope of this project all sands have a fines content of $FC = 10\%$.